UNIVERSITY OF SOUTHAMPTON

FACULTY OF ENGINEERING, SCIENCE & MATHEMATICS

School of Ocean and Earth Science

Joint Elastic-Electrical Properties of Reservoir Sandstones

by

Tongcheng Han

Thesis for the degree of Doctor of Philosophy

November 2010

UNIVERSITY OF SOUTHAMPTON

ABSTRACT

FACULTY OF ENGINEERING, SCIENCE & MATHEMATICS
SCHOOL OF OCEAN & EARTH SCIENCE

Doctor of Philosophy

JOINT ELASTIC-ELECTRICAL PROPERTIES OF RESERVOIR SANDSTONES

by Tongcheng Han

Over the last decade, marine controlled source electromagnetic (CSEM), sub-seabed imaging has developed to a state where routine resistivity mapping of hydrocarbon reservoirs is now possible. Co-located marine seismic and electrical resistivity survey data could provide the engineering parameters needed to better assess the economic potential of hydrocarbon reservoirs without the need for drilling, and could provide additional reservoir monitoring capabilities in the future. However, proper exploitation of joint seismic-CSEM datasets will require a much better understanding of the inter-relationships among geophysical (elastic and electrical) and reservoir engineering properties.

This project seeks to study the inter-relationships among the elastic and electrical properties of typical reservoir sandstones for improved insight into wave propagation phenomena in porous rocks.

A high quality joint elastic-electrical dataset has been collected on a set of 67 sandstone samples showing a range of porosities, permeabilities and clay contents. The measurements were simultaneously carried out at differential pressures up to 60 MPa. Elastic properties (compressional and shear wave velocity and attenuation) were measured using a pulse-echo technique; electrical resistivity was recorded at AC frequency of 2 Hz using a circumference resistivity measurement method.

The effects of porosity, permeability, clay content and differential pressure on the low frequency (2 Hz) electrical resistivity properties and the influence of differential pressure and petrophysical parameters on the joint elastic-electrical properties of reservoir sandstones were analyzed. A three-phase (quartz, brine and pore-filling clay) effective medium model based on self-consistent approximation (SCA) and differential effective medium (DEM) for the joint elastic-electrical properties of reservoir sandstones was developed and was found to give a good description of the experimental observations.

List of Contents

List of Figures

List of Tables

DECLARATION OF AUTHORSHIP

I, *Tongcheng Han*, declare that the thesis entitled:

Joint Elastic-Electrical Properties of Reservoir Sandstones

and the work presented in it are my own and has been generated by me as the result of my own original research. I confirm that:

- This work was done wholly or mainly while in candidature for a research degree at this University;
- Where any part of this thesis has previously been submitted for a degree or any other qualification at this University or any other institution, this has been clearly stated;
- Where I have consulted the published work of others, this is always clearly attributed;
- Where I have quoted from the work of others, the source is always given. With the exception of such quotations, this thesis is entirely my own work;
- I have acknowledged all main sources of help;
- Where the thesis is based on work done by myself jointly with others, I have made clear exactly what was done by others and what I have contributed myself;
- Parts of this work have been published as:

Han T., Best A., Sothcott J., MacGregor L. and Minshull T. 2009. Laboratory joint ultrasonic and resistivity measurements on reservoir sandstones. 71st EAGE Meeting, Amsterdam, the Netherlands, Extended Abstracts, Z007.

Han T., Best A.I., MacGregor L., Sothcott J. and Minshull T.A. 2010. Joint velocity-resistivity effective medium models. 72nd EAGE Meeting, Barcelona, Spain, Extended Abstracts, I007.

Signed: .....

Date: .....

Acknowledgements

I would like to acknowledge all those who have helped me throughout my 3-year's PhD work. First, I would like to give my sincere thanks to my supervisors Angus Best, Lucy MacGregor and Tim Minshull for all their distinguished advice, support, encouragement and supervision throughout this project, and for their endless reading and comments on my papers and the thesis. I also wish to thank Baohua Liu and Weigang Zhang for their earlier supervision.

I would like to thank Jeremy Sothcott (I owe him numerous 50Ps) for all his great help in the laboratory. Without his outstanding technology help none of the laboratory measurements would have been possible. I would also like to thank all the rest of the Rock Physics group at NOCS, Michelle Ellis, Laurence North, George Marketos, Philip Tillotson and Nadia Frerichs for their help in various aspects and for making a friendly and harmonic environment to work here.

Thanks are given to Michael Worthington of Oxford University, Jinliang Zhang of Ocean University of China and Cheng Xu of Peking University for providing the borehole core samples. Help from Bob Jones and John Ford for making thin sections, Ross Williams for XRD measurements and analyses and Ian West for the petrophysical analyses is also gratefully acknowledged.

I appreciate the internship opportunity provided by OHM Ltd. at the beginning of this work. With the help from Zhijun Du in doing well logging analysis I initially understood what rock physics is and what rock physics can do. I am grateful to Arthur Cheng and Peter Harris for their knowledgeable suggestions on my data interpretation and for the helpful discussions on model validity.

I thank the financial support from OHM Ltd. and the Engineering and Physical Sciences Research Council of the United Kingdom under the Dorothy Hodgkin Postgraduate Awards scheme.

I wish to thank all my friends in Southampton, especially Yining Chen, Liao Chang, Hao Zuo, Xiang Zhao, Chongyuan Mao, Zongpei Jiang and Tingting Shi, who helped to make the tedious life abroad colourful.

I can not end without thanking my parents, whose love and encouragement are always my spirit guides for the last 28 years.

Chapter 1

Introduction

1.1. Motivation

1.1.1. Marine controlled source electromagnetic (CSEM)

The technique of marine controlled source electromagnetic (CSEM) sounding in the frequency domain was developed first at the Scripps Institution of Oceanography and later at Cambridge University (Young and Cox, 1981; Sinha *et al*., 1990). Their CSEM method uses a high power deep-towed horizontal electric dipole (HED) source to transmit discrete frequency electromagnetic signals to an array of sea-bottom receivers which record two orthogonal components of the horizontal electric field at the seafloor (Figure 1.1). The dipole source is usually towed at a height of about 50 m from the sea bottom to avoid attenuation in the water. By analyzing the variation in the amplitude and phase of the received electric field as a function of source-receiver separation and geometry and the frequency of the signal, the resistivity structure of the underlying formation can be determined.

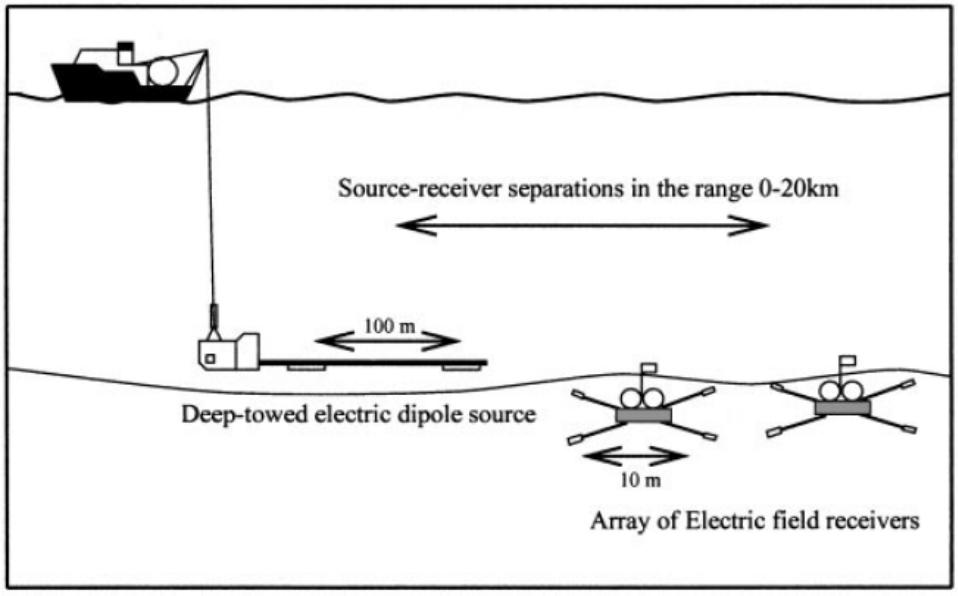

Figure 1.1. Schematic diagram of a controlled source electromagnetic acquisition method of Young and Cox (1981). The source is towed close to the seafloor within an array of receivers which measure two components of the horizontal electric field. In a typical survey, electric fields can be detected to a distance of about 15 km from the source, giving sensitivity to resistivity structure in the upper 5-7 km of the crust (from MacGregor and Sinha, 2000).

There are other CSEM acquisition methods, for example the one developed at the University of Toronto (Edwards and Chave, 1986; Edwards 1997), which uses an electric dipole-dipole transient electromagnetic system with the seafloor array towed

in direct contact with the soft marine sediments by attaching a heavy weight to the forward end of the array. The length of the dipoles is 124 m and 15 m for the transmitter dipole and the receiver dipoles respectively (Schwalenberg *et al*., 2005).

To make use of the vertical electrical field to improve the characterisation and monitoring of the reservoir, Borehole CSEM (BCSEM) has been theoretically and experimentally developed in terms of cross-borehole (source and receiver in boreholes), borehole-to-surface (source in a borehole, receivers on the surface) and surface-to-borehole (source on the surface, receivers in a borehole) although most of these BCSEM surveys were carried out on land (Maxey, 2009).

Frequencies used in a typical commercial marine CSEM survey are 0.05 – 5 Hz. Frequencies lower than this tend to lack resolution and are more likely to be affected by seafloor electromagnetic noise; frequencies higher than this attenuate rapidly and contain little information about the subsurface resistivity structure.

1.1.2. Joint seismic-CSEM inversion

Seismic methods (both reflection and refraction) rely on variations in the elastic properties of geological units which give rise to seismic impedance contrasts that are governed by the seismic velocity and density of those units. Although seismic data are good at imaging geological structures and contain significant information about the elastic properties between different types and porosities of rocks, the hydrocarbon saturation can be difficult to quantify. By contrast, the CSEM method gives relatively poor resolution to the geological structures but is sensitive to the electrical properties of rocks with varying fluids and saturation. Because seismic and CSEM methods measure complementary but independent bulk physical properties of geological formations that are related through rock and pore fluid properties, joint interpretation of co-located seismic and CSEM data can potentially produce much better constraints on the reservoir properties of rocks.

The joint seismic-CSEM method was first developed to study magmatic activity at active spreading centres beneath mid-ocean ridges (Evans *et al*., 1991, 1994; MacGregor *et al*., 1998; Sinha *et al*., 1998). More recently, the joint inversion of seismic and CSEM data was applied successfully to hydrocarbon reservoir characterisation (Hoversten *et al*., 2006; Harris *et al*., 2009). The combined use of

seismic and CSEM methods can give an independent estimate of whether hydrocarbons (oil, gas) are present in a reservoir structure identified by seismic imaging. It can help reduce the likelihood of drilling expensive dry exploration wells. Furthermore a fully coupled joint simultaneous seismic-CSEM inversion could be used to find reservoir rock properties directly if suitably robust rock physics models can be developed. Such rock physics models should link the measured elastic and electrical parameters to the reservoir rock and fluid properties of interest (Du and MacGregor, 2009), e.g., lithology, porosity, permeability, fluid type, saturation, shalyness, etc. These parameters are needed to quantify the economic potential of hydrocarbon reservoir units during the exploration phase, for designing production strategies during reservoir development, and for reservoir monitoring during production.

There are several existing rock physics models describing the elastic (e.g., Gassmann, 1951; Xu and White, 1995; Dvorkin and Nur, 1996) and electrical (e.g., Archie, 1942; Simandoux, 1963) properties of reservoir rocks that are potential candidates for the joint inversion of seismic-CSEM data. There are several examples of joint seismic-CSEM inversions in the literature that used these rock physics models (e.g., Hoversten *et al*., 2006; Harris *et al*., 2009). They showed that combining seismic and CSEM data in an inversion produces better estimates of reservoir parameters with lower variance than either a CSEM inversion or a seismic inversion when performed separately. However the key to success in these cases was the availability of well logging data that could be employed to reduce uncertainty in the rock physics model parameters; this has a significant impact on the estimates of reservoir parameters (Chen and Dickens, 2008). However for exploration regions without well logging data (which is usually the case), unconstrained rock physics models may be invalid and could lead to incorrect estimation of reservoir parameters from the joint inversion. In addition, most of the existing elastic and electrical rock physics models were developed separately with different assumptions. Whether these different sets of assumptions apply to the same reservoir is under question.

It is therefore essential to gain a better understanding of the links between the elastic and electrical properties of reservoir rocks and to use this new knowledge to develop improved rock physics models for joint elastic-electrical inversions of marine seismic-CSEM survey data. In particular, improved knowledge of the links between joint

elastic-electrical properties and the reservoir rock properties of interest, such as lithology, porosity, permeability, fluid type, saturation and shalyness, will provide the required rock physics tools for successful quantitative inversions.

1.1.3. Rock physics

Rock physics addresses the relationships between geophysical observations (e.g., elastic velocity and attenuation and electrical resistivity measured at the surface of the earth, within the borehole environment or in the laboratory) and the underlying reservoir properties of rocks (e.g., lithology, porosity, confining stress and pore pressure, pore fluid type and saturation, anisotropy and degree of fracturing, temperature, and frequency). The relationships can be used to predict the geophysical properties from the geology (rock physics modelling), or to predict geology from the geophysical observations (rock physics inversion, Figure 1.2).

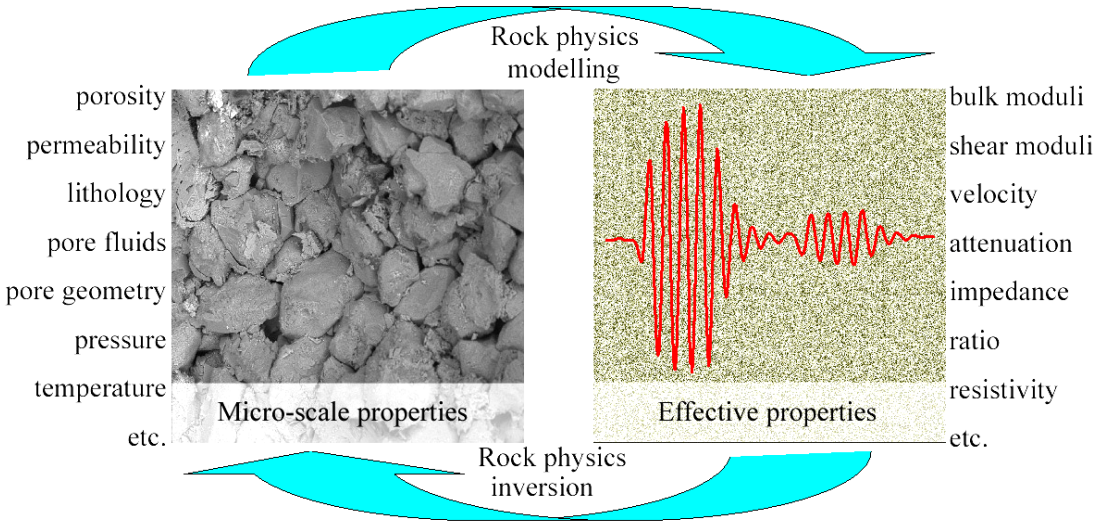

Figure 1.2. Schematic diagram illustrating rock physics as tools that link geophysical properties of rocks to the reservoir properties of the individual rock constituents (adapted from http://www.norsar.no/c-65-Rock-Physics.aspx).

Borehole (well logging) and laboratory measurements are the two main methods for rock physics study. In spite of providing unbiased, continuous and abundant *in situ* information about the physical properties of the rocks, borehole geophysics has its own drawbacks. A significant problem is that borehole measurements, e.g. using the full waveform sonic tool (Goldberg and Zinszner, 1989), give averaged physical values for the rocks between the source and detector in the decimetre range. This can

lead to log values for mixed lithological layers, such as shale stringers in a sand unit, which adds additional complexity to the interpretation. In general, such a measurement scale allows a range of geological heterogeneities (e.g., thin bedding, cross-lamination, mineral veins) to influence the logged value. By contrast, laboratory studies tend to avoid this scale of geological heterogeneity by selection of small cm-sized samples of a definite lithology. This provides a way to precisely define the various physical properties of a particular lithology (sandstone, limestone, shale, etc.) according to standard geological classification systems. Not only do laboratory studies give insight into physical mechanisms, they also offer a way to validate existing rock physics models and to develop new models. The prediction of the geophysical response of multiple layers of different lithologies at the well logging (decimetre) and CSEM (10s metres) scale can then be solved using effective medium theory with knowledge of the component lithologies' behaviour provided through laboratory studies.

Given the uncertainties with well log data, laboratory measurements on small homogenous rock samples offers the best way to build a physical properties database. Such a rock physics database will provide the foundation for developing and testing new reliable mathematical models of the joint elastic-electrical properties of reservoir rocks that are required for the improved inversion of joint seismic-CSEM datasets.

1.1.4. Reservoir lithologies

The world's conventional hydrocarbon reserves are found in two main lithological groups: sandstones and carbonates. According to the Oil and Gas Journal (found on http://www.eia.doe.gov/emeu/international/reserves.html), the world proved reserves of oil and natural gas by January 2009 are about 1342 billion barrels and 169 trillion cubic feet respectively. Approximately half of known hydrocarbon reserves are in sandstones (Tanner *et al*., 1991) which make up the most significant group of reservoir rocks.

Sandstones have a more regular granular geometry than carbonates and therefore can be considered "easier" to study in terms of their physical properties. However, sandstones are often found together with shales and shale stringers or shaly sandstones. Shaly sandstones are commonplace in sedimentary basins and can

degrade overall reservoir quality by their reduced permeability in particular compared to clean sandstones. Shale or clay in sandstones also increases the complexity of rock physics models. However, given the ubiquitousness of shales and clay minerals in sandstone units in the Earth's crust, any rock physics model of sandstones should also account for shalyness if it is to be of practical use in geophysical inversion schemes. This is particularly true for electrical properties which are known to be affected by surface charge conduction on clay mineral double layers.

Hence, the effects of clay on the joint elastic-electrical properties of reservoir sandstone have been chosen as one focus in this study. Any advances in knowledge in this area is likely to have an immediate and significant impact on practical geophysical inversions relevant to conventional hydrocarbon exploration, but also to aquifers, underground carbon dioxide (CO_2) storage and to unconventional hydrocarbon exploration, such as seabed methane gas hydrates.

1.2. Aims and objectives

This thesis aims to study the inter-relationships among the elastic and electrical properties of typical reservoir sandstones for improved insight into wave propagation phenomena in porous rocks, which might aid in improving joint seismic-CSEM inversions. The aim will be achieved through the following objectives:

(1) to collect a comprehensive dataset of accurate elastic velocities, attenuations and electrical resistivities of typical reservoir sandstones measured simultaneously in the laboratory. The sandstones should show a wide range of porosities, permeabilities and clay contents.

(2) to interpret the laboratory data in terms of the cross-property relations between elastic and electrical parameters and the inter-relationships among reservoir petrophysical properties and the joint elastic-electrical properties.

(3) to investigate the validity of available rock physics models against the new dataset and to develop new models where appropriate. The new rock physics models should have the ability to model a three-phase medium (quartz, brine and clay) since most of the sandstone samples contain non-negligible amount of clay minerals.

1.3. Thesis structure

Brief 1-D elastic and electromagnetic wave equations and current knowledge of some key reservoir parameters on the elastic and electrical properties of sandstones are presented in Chapter 2. Knowledge gaps in the joint elastic-electrical properties of reservoir sandstones are highlighted and discussed.

Chapter 3 describes the laboratory experiments carried out in this study. Advanced and reliable joint elastic-electrical equipment, selection of a large number of typical sandstone samples, careful preparation, characterisation and measurement of the samples and precise data processing ensure high quality of the accurate joint elastic-electrical dataset.

Analyses of the dataset and the main results are given in Chapters 4 to 7. In Chapter 4 the relationships among some key reservoir parameters and the low frequency (2 Hz) electrical resistivity are discussed (research paper submitted to *Geophysics*). The main result is that the electrical resistivity of shaly sandstones is primarily controlled by two different types of pore geometries and associated connectivities. For connected porosity greater than about 9%, clay minerals tend to occupy the pores formed by the framework of cemented sand grains and show negligible surface conductive effects; the sandstones behave effectively like clean sandstones even though significant clay minerals (as high as 22%) are present. Here, the size and connectivity of the pores (and hence hydraulic permeability and electrical conductivity) is controlled by the packing of sand grains (e.g. quartz), cementation (e.g., quartz overgrowths) and amount of pore-filling clay mineral assemblages (e.g., illite, kaolinite). By contrast, for connected porosity less than about 9%, clay minerals tend to be dispersed throughout the framework of mineral grains and a small clay surface conductivity effect is seen. Here, pore size and connectivity is controlled by clay mineral assemblages giving relatively low hydraulic permeability and electrical conductivity. The relations established in this chapter may aid directly the interpretation of CSEM data at < 40 Hz (laboratory results for 440 Hz showed little variation in electrical properties from those at 2 Hz).

Chapter 5 presents the effect of differential pressure on the joint elastic-electrical properties of reservoir sandstones (research paper submitted to *Geophysical Prospecting*). It shows that electrical resistivity is more sensitive to low aspect ratio

pores and attenuation is more subject to high aspect ratio pores while elastic velocity shows no apparent dependence on different pore types with varying differential pressure. It also demonstrates the approximate linear relationships between resistivity and velocity, resistivity and attenuation and velocity and attenuation as a function of differential pressure; and the use of the slopes of the above linear trends to discriminate between clean and clay-rich sandstones samples.

Chapter 6 presents the effect of petrophysical parameters (porosity, permeability, clay content) on the joint elastic-electrical properties of reservoir sandstones (research paper submitted to *Geophysical Prospecting*). It shows a linear velocity-resistivity (two groups, clean sandstone group and clay-rich sandstone group) and a bell-shaped resistivity-attenuation (S-wave attenuation shows part of this relation) relationship and provides explanations for the joint relations in terms of clay content. It concludes that the joint elastic-electrical relations can be used to discriminate between sandstones of similar porosities with different clay contents and permeabilities

In Chapter 7 some existing effective medium models for the joint elastic-electrical properties of reservoir sandstones are implemented and compared to the new joint dataset. In addition, a 3-phase (quartz, brine and pore-filling clay minerals) model is developed that gives a good description of the joint dataset (research paper submitted to *Geophysical Prospecting*). This general sandstone model has minimal input parameters and offers a practical means to invert joint elastic-CSEM datasets for estimates of porosity and clay content in exploration areas without borehole information.

In Chapter 8, the main results are summarized and discussed in the context of their likely impact on hydrocarbon exploration and other suitable targets for joint seismic-CSEM surveying. In particular, the likely effect of frequency on elastic properties is discussed as only ultrasonic properties were measured in this study. The resistivity measurements in this study are already at CSEM frequencies, but the likely frequency-dependent effects on borehole logging measurements are discussed.

Chapter 2

Elastic and electrical properties of reservoir sandstones

2.1. Introduction

This chapter reviews the current knowledge of the relationships between key reservoir sandstone parameters and their elastic and electrical properties, generally obtained from controlled laboratory experiments on rock samples. Theories trying to explain the mechanisms of the elastic and electrical behaviours of reservoir sandstones and the limited experimental work on the joint elastic-electrical properties of reservoir sandstones will be excluded from this chapter but introduced in the following chapters where appropriate. The one-dimensional (1-D) elastic and electromagnetic wave equations are introduced in this chapter to provide a theoretical justification for the key physical properties that affect elastic and electromagnetic wave propagation. These parameters need to be measured in any dedicated study of joint properties.

2.2. Theory of 1-D elastic wave equation

2.2.1. Elastic waves in a lossless medium

A 1-D elastic wave propagates along the x axis (medium length L) with elastic velocity v and amplitude u (which generally depends on both propagation distance x and time t). For plane waves in an isotropic, homogeneous medium and for small linear strains, the wave motion can be described by a partial differential equation of second order known as the 1-D wave equation (e.g., Gribben, 1975),

$$\frac{1}{v^2}\frac{\partial^2 u}{\partial t^2} = \frac{\partial^2 u}{\partial x^2}. \tag{2.1}$$

The velocity v depends on the wave mode (compressional or shear) and the properties of the medium through which the wave is moving. Compressional wave velocity v_p and shear wave velocity v_s can be calculated respectively from the expressions

$$v_p = \sqrt{\frac{K + (4/3)G}{d}}, \tag{2.2}$$

$$v_s = \sqrt{\frac{G}{d}}, \tag{2.3}$$

where K is the elastic bulk modulus, G is the elastic shear modulus and d is the density of the medium.

In order to specify a wave, the equation is subject to boundary conditions

$$\begin{aligned} u(0,t) &= 0 \\ u(L,t) &= 0 \end{aligned} \tag{2.4}$$

and initial conditions

$$\begin{aligned} u(x,0) &= f(x) \\ \frac{\partial u}{\partial t}(x,0) &= g(x) \end{aligned}. \tag{2.5}$$

The 1-D wave equation can be solved exactly by d'Alembert's solution, using a Fourier transform method or via separation of variables (e.g., Gribben, 1975; Zavada, 2002). The solutions of the 1-D wave equation are sums of two wave shapes travelling through the medium in opposite directions: f in the positive x direction and g in the negative x direction, of arbitrary functional shapes f and g, in the general form of

$$u(x,t) = f(x - vt) + g(x + vt). \tag{2.6}$$

It can be seen from equations 2.2 and 2.3 that parameters that directly affect the velocity and propagation of an elastic wave include bulk and shear modulus and density of the medium. However all these parameters can depend on other reservoir parameters such as porosity and pressure for reservoir sandstones. The current knowledge of the relationships between some key reservoir parameters and the elastic properties of reservoir sandstones will be reviewed in Section 2.4.

2.2.2. Elastic waves in a porous, attenuating medium

Sedimentary rocks differ from the simple situation described in Section 2.2.1 in two main respects. Firstly, they are generally porous and comprise solid and fluid phases, and secondly, as a consequence of this (see Section 2.2.3), they tend to attenuate propagating elastic waves. Therefore, it is necessary to introduce an attenuation term into the solution of the wave equation.

According to Toksöz and Johnston (1981), the amplitude A of a plane wave propagating in a homogeneous medium in the x direction as a function of time t is given by the solution to the 1-D wave equation

$$A(x,t) = A_0 e^{i(kx-\omega t)}, \tag{2.7}$$

where A_0 is the amplitude at $t = 0$ and $x = 0$, ω is angular frequency ($\omega = 2\pi f$ where f is frequency in Hz, the reciprocal of wave period), and k is the wave number. Attenuation is introduced mathematically by allowing the wavenumber to become a complex number

$$k = k_r + i\alpha, \tag{2.8}$$

where k_r is the real part and α is the imaginary part. This leads to the expression

$$A(x,t) = A_0 e^{-\alpha x} e^{i(k_r x-\omega t)}, \tag{2.9}$$

where α is known as the attenuation coefficient with units of Nepers per metre (inverse length). The phase velocity v is given by

$$v = \frac{\omega}{k_r}. \tag{2.10}$$

Omitting the propagation terms, the attenuation coefficient can be measured between two positions in the medium x_1 and x_2 ($x_1 < x_2$) using the natural logarithm of the amplitude ratio

$$\alpha = \frac{1}{x_2 - x_1} \ln[\frac{A(x_1)}{A(x_2)}]. \tag{2.11}$$

Attenuation coefficient is sometimes expressed in units of dB/m equivalent to

$$\alpha = \frac{1}{x_2 - x_1} 20 \cdot \log[\frac{A(x_1)}{A(x_2)}], \tag{2.12}$$

using the base 10 logarithm. The attenuation coefficient in Nepers/m is equivalent to the attenuation coefficient in dB/m divided by $20 \cdot \log(e) = 8.686$.

Intrinsic attenuation is also commonly expressed in terms of the inverse quality factor Q^{-1} given by (Hamilton, 1972a)

$$\frac{1}{Q} = \frac{\alpha v}{\pi f - \frac{\alpha^2 v^2}{4\pi f}}. \tag{2.13}$$

However, for relatively small signal losses ($Q > 10$) the second order terms are negligible and are usually dropped to give

$$\frac{1}{Q} = \frac{\alpha v}{\pi f}, \tag{2.14}$$

where α is in Nepers/m and v is phase velocity. In this thesis, intrinsic rock attenuation will be expressed in terms of Q^{-1} or $1000/Q$ which is generally dependent on signal frequency.

Several theoretical models have been developed to account for particular intrinsic loss mechanisms in porous rocks, such as the classical Biot theory (Biot, 1956a, b) and its derivatives. These will be discussed in Section 2.2.3.

2.2.3. Attenuation mechanisms

Attenuation is the process by which rocks convert compressional and shear waves into heat and thereby modify the amplitude and phase of the waves (e.g., Klimentos and McCann, 1990). The two most important mechanisms proposed to account for compressional and shear wave attenuation due to viscous interaction between solid rock framework and the pore fluid are the Biot mechanism and the squirt-flow mechanism.

Biot (Biot, 1956a, b) developed a theory of wave propagation in fluid saturated porous media that considered the effects of viscous losses due to the 'global' relative motion between the pore fluid and the solid framework. The theory shows that acoustic waves create relative motion between the fluid and the solid framework due to inertial effects. As the solid framework is accelerated, the fluid lags behind, resulting in viscous attenuation of acoustic waves. At low frequencies the viscous skin depth (viscous skin depth $\delta = \sqrt{2\eta / d\omega}$, where η and d are the viscosity and density of the pore fluid respectively and ω is the angular frequency of the acoustic wave) is much larger than the pore size and the pore fluid moves with the solid framework and there is little attenuation. At high frequencies the viscous skin depth is very small and the viscous coupling is weak compared to the inertia effects; the pore fluid moves relative to the framework, but again the attenuation is small. Attenuation reaches a peak when the viscous skin depth is comparable to the pore size (Murphy III *et al*., 1986; Klimentos and McCann, 1990; Winkler and Murphy III, 1995; Pride *et al*.,

2004). The Biot type attenuation mechanism is also referred to as macroscopic fluid-flow or global fluid-flow.

The squirt-flow mechanism focuses on the loss resulting from the 'local' flow of viscous fluid into and out of microcracks during the passage of acoustic waves (O'Connell and Budiansky, 1977; Mavko and Nur, 1979; Murphy III *et al*., 1986; Klimentos and McCann, 1990). The pore space of a rock is generally very heterogeneous, some regions being very compliant while others are very stiff. This can result in fluid being squeezed out of grain contacts into nearby pores, or squeezed between adjacent cracks having different orientations with respect to a passing stress wave (Winkler and Murphy III, 1995). The squirt-flow mechanism is also called microscopic fluid-flow or local fluid flow.

The two attenuation mechanisms are intimately interconnected and occur in a rock simultaneously, they affect each other as well as influence the process of acoustic energy propagation and attenuation. Dvorkin and Nur (1993) developed a consistent theory dealing simultaneously with the Biot and the squirt-flow mechanisms, known as the BISQ model, which proves to give better descriptions of seismic properties (e.g., Marketos and Best, 2010).

2.3. Theory of 1-D electromagnetic wave equation

2.3.1. Electromagnetic waves in an insulating medium

The electric wave equation for a plane electromagnetic wave (Figure 2.1) travelling in the x direction in a medium is (e.g., Pozar, 1998)

$$\frac{1}{c^2}\frac{\partial^2 E}{\partial t^2} = \frac{\partial^2 E}{\partial x^2}, \tag{2.15}$$

where E is the electric field strength and $c = \frac{1}{\sqrt{\mu\varepsilon}}$ is the electromagnetic wave velocity in the medium, where μ and ε are the magnetic permeability and electrical permittivity of the medium respectively.

The solutions to equation 2.15 (Pozar, 1998) are in the form of

$$E(x,t) = E^{+}\cos(\omega t - kx) + E^{-}\cos(\omega t + kx), \tag{2.16}$$

where E^+ and E^- are real arbitrary amplitude constants, $k = \omega\sqrt{\mu\varepsilon}$ is the wave number and ω is the angular frequency. Similarly to equation 2.6, the solution to the elastic wave equation, equation 2.16 also consists of a wave travelling in the positive x direction (the first term) and one travelling in the negative x direction (the second term).

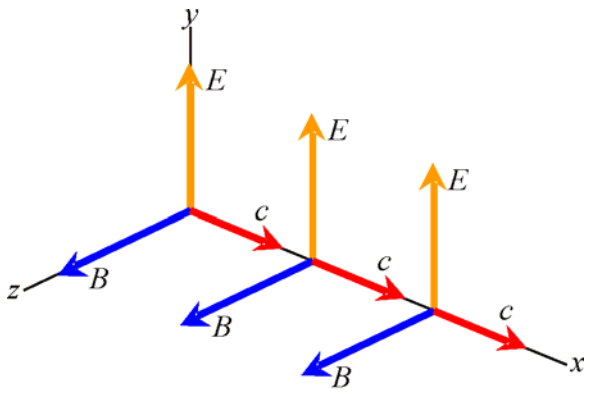

Figure 2.1. A plane electromagnetic wave propagating in the x direction with velocity c, with the electric field E pointing in the y direction and the magnetic field B in the z direction.

2.3.2. Electromagnetic waves in a conductive medium

Sedimentary rocks saturated with brines are not insulating but conductive resulting in progressive loss of energy of the wave as it propagates due to the heating effect associated with the flow of conduction currents.

For practical low frequency CSEM measurements, assuming magnetic permeability μ in geological materials deviates little from its free space value μ_0 compared to the large variations in electrical resistivity, the electromagnetic wave equation (a diffusion equation) can be written as (according to Sinha, 2010)

$$\nabla^2 E + \frac{i\mu_0\omega}{\rho} E = 0, \tag{2.17}$$

where ρ is the electrical resistivity of the medium. The solution to equation 2.17 for a plane wave as shown in Figure 2.1 is

$$E(x,t) = E_0 e^{-\frac{x}{\delta_s}} e^{i(\omega t + \frac{x}{\delta_s})}, \tag{2.18}$$

where E_0 is the initial (t = 0 and x = 0) amplitude of the signal, ω is the angular frequency, x is the distance propagated, t is elapsed time and $\delta_s = \sqrt{\frac{\rho}{\pi f \mu_0}}$ is the skin depth, which is a crucial concept in electromagnetic geophysics. We can estimate the skin depth at the relevant frequency once an electromagnetic signal has propagated a known distance through a medium, and either the resulting propagation delay or the amount by which it has been attenuated can be measured or estimated. We can then estimate the resistivity of the medium through which it has propagated from the estimated skin depth (Sinha, 2010).

The phase velocity u of the electromagnetic signal can be written as

$$u = f\lambda = f \cdot 2\pi \cdot \delta_s = 2\sqrt{\frac{\pi f \rho}{\mu_0}}, \tag{2.19}$$

which shows that the propagation of electromagnetic waves is dispersive. By recording a propagation delay (or 'phase') the electrical resistivity can also be estimated at a particular frequency. This is why marine CSEM method measures both phase and amplitude of electromagnetic signals (see Section 1.1.1).

From the above introduction, it is already clear that the most important physical parameter (providing frequency is known) that affects the propagation of low frequency electromagnetic waves employed by CSEM in the Earth is electrical resistivity. The effects of electrical permittivity are generally negligible at low frequencies although they can be important at high frequencies, for example in ground penetrating radar surveys (e.g., Reppert *et al*., 2000). This is why I chose to focus on electrical resistivity measurements in the laboratory rather than on other electrical parameters (e.g., electrical permittivity). The current knowledge of the relationships between some key reservoir parameters and electrical resistivity/conductivity of reservoir sandstones will be reviewed in Section 2.5.

2.4. The effect of reservoir parameters on elastic velocity and attenuation

Numerous laboratory investigations have been performed to study the elastic properties (elastic velocity and attenuation) of reservoir sandstones (e.g., Han, 1986;

Klimentos, 1988; Best, 1992; Jones, 1996), from which a fundamental understanding of factors that influence elastic velocity and attenuation has been obtained. Wang (2001) reviewed the progress in studying physical properties of rocks and minerals in relation to seismic exploration and earthquake seismology and summarized the importance of various factors in affecting elastic velocity of reservoir rocks (Table 2.1). This importance is also valid for attenuation since higher elastic velocity is usually associated with lower attenuation (higher quality factor Q) in sandstones (Hamilton, 1972b; Marks *et al*., 1992; Best *et al*., 1994; Shatilo *et al*., 1998). In this section, the relationships between the elastic properties of sandstones and some particular reservoir parameters (i.e., porosity, clay content, pressure, permeability and frequency) that are relevant to this project are reviewed in more depth.

Table 2.1. Factors influencing elastic properties (velocity) of sedimentary rocks with increasing importance from top to bottom (Wang, 2001).

Rock properties	**Fluid properties**	**Environment**
Compaction	Viscosity	Frequency
Consolidation history	Density	Stress history
Age	Wettability	Depositional environment
Cementation	Fluid composition	Temperature
Texture	Phase	Reservoir process
Bulk density	Fluid type	Production history
Clay content	Gas-oil, gas-water ratio	Layer geometry
Anisotropy	Saturation	Net reservoir pressure
Fractures		
Porosity		
Lithology		
Pore shape		

2.4.1. Porosity and clay content

Both compressional and shear wave velocity (V_p and V_s respectively) decrease with increasing porosity in clean, water-saturated sandstones (Wyllie *et al*., 1956; Pickett, 1963; Bourbie and Zinszner, 1985; Tutuncu *et al*., 1994) due to the compressibility of

the pores. Attenuation (the process by which rocks convert compressional and shear waves into heat and which is mainly caused by the viscous interaction between the solid rock framework and the pore fluid, see Section 2.2.3) increases with porosity in saturated sandstone samples (Bourbie and Zinszner, 1985; Shatilo *et al*., 1998).

Many reservoir sands and sandstones contain clay minerals (Wang, 2001), which soften generally the rock grain contacts and reduce the bulk and shear moduli leading to a decrease in V_p and V_s (Castagna *et al*., 1985; Miller and Stewart, 1990; Best *et al*., 1994; Tutuncu *et al*., 1994). On the other hand some researchers (e.g., Best *et al*., 1994; Tutuncu *et al*., 1994) found that both compressional and shear wave attenuation increase with increasing clay content but others (e.g., Shatilo *el al*., 1998) reported no apparent correlation between attenuation and clay content.

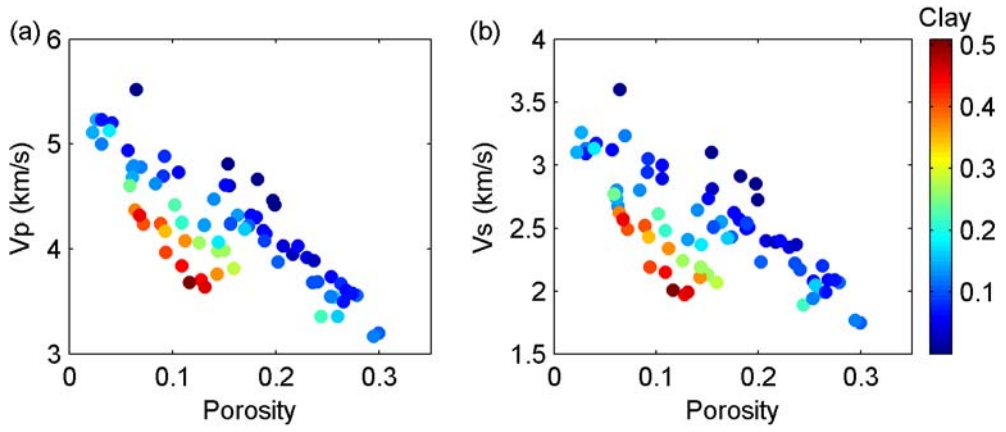

Figure 2.2. Han *et al*. (1986) correlation between compressional (a) shear (b) wave velocity and porosity by colour-coding volumetric clay content at confining pressure of 40 MPa and pore pressure of 1.0 MPa.

However, a systematic correlation between porosity and clay content in sand/clay mixtures has been shown to exist (Marion *et al*., 1992), so efforts have been made to study the combined effects of porosity and clay content on elastic properties (e.g., Tosaya and Nur, 1982; Kowallis *et al*., 1984; Castagna *et al*., 1985). Han *et al*. (1986) studied the porosity-clay effect on compressional and shear wave velocity of 75 consolidated sandstones at a confining pressure of 40 MPa and a pore pressure of 1.0 MPa (Figure 2.2) and found that V_p and V_s decrease linearly with porosity (φ) and volumetric clay content (C) according to

$$V_p(km/s) = 5.59 - 6.93\varphi - 2.18C\,, \tag{2.20}$$

and

$$V_s\,(km/s) = 3.52 - 4.91\varphi - 1.89C\,. \qquad (2.21)$$

Similar work was done by Klimentos (1991) who measured compressional wave velocity (Figure 2.3a) of 42 water-saturated reservoir sandstones at an effective pressure of 20 MPa (confining pressure of 40 MPa and pore pressure of 20 MPa), and found that the effect of porosity on reducing V_p is approximately twice that of the clay content. Freund (1992) concluded, based on 88 dry sandstone samples, that above 120 MPa the effect on reducing velocities is stronger for porosity than for clay content by a factor of 5.6 and 4.9 for V_p and V_s respectively.

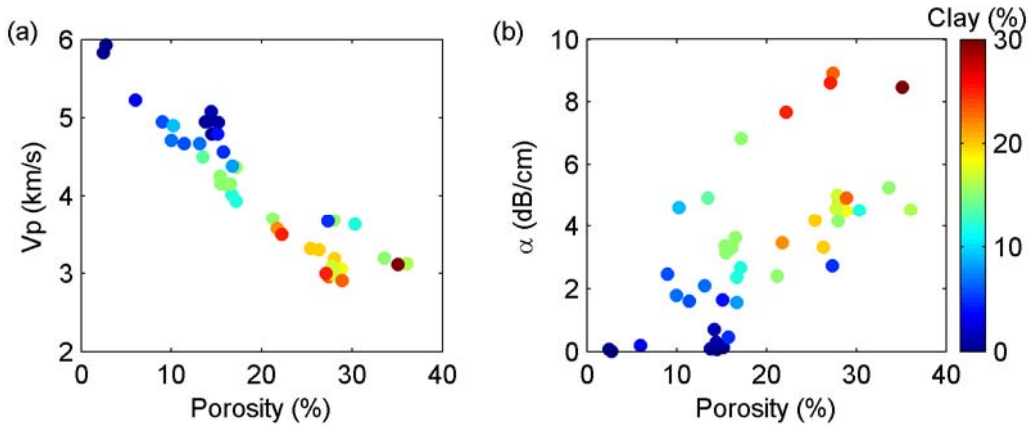

Figure 2.3. Correlation between compressional (a) wave velocity and (b) attenuation coefficient and porosity by colour-coding volumetric clay content at confining pressure of 40 MPa and pore pressure of 20 MPa. Velocity and attenuation data from Klimentos (1991) and Klimentos and McCann (1990) respectively.

On the 42 water-saturated reservoir sandstone samples of Klimentos (1991), Klimentos and McCann (1990) also measured their P-wave attenuation (Figure 2.3b) in terms of porosity-clay effect. They found that attenuation coefficient (α, in dB/cm) is linearly related to both clay content and porosity of the sandstones, but the clay (percentage) effect is an order of magnitude greater than the porosity (percentage) effect given by

$$\alpha = 0.0315\varphi + 0.241C - 0.132\,. \qquad (2.22)$$

Best *et al*. (1994) measured attenuations of both compressional and shear waves in 29 water-saturated samples of sandstones and shales at a differential pressure of 60 MPa in terms of porosity and clay content. Their P-wave results are generally consistent with results form Klimentos and McCann (1990), and S-wave attenuations show similar trends to P-wave attenuations changing with porosity and clay content.

2.4.2. Pressure

Both compressional and shear wave velocity increase with increasing differential pressure (the difference between confining pressure and pore pressure) mainly due to the closure of low aspect ratio pores such as microcracks and compliant grain contacts in the rock skeleton (e.g., Wyllie *et al*., 1958; Todd and Simmons, 1972; Han *et al*., 1986; Winkler and Murphy III, 1995; Best, 1997; Domnesteanu *et al*., 2002).

Eberhart-Phillips *et al*. (1989) analysed the data of Han *et al*. (1986) collected on saturated sandstones at effective pressure (P_e) from 0.02 – 0.49 kbar (1 kbar = 100 MPa), and found the velocity-effective pressure relationship is non-linear and can be characterised by an initial rapid increase in velocity as effective pressure increases from zero, followed by a reduction in the rate of velocity increase with further increase in effective pressure. They found an empirical equation consisting of a constant, a linear part and an exponential part in the form of

$$V = A + KP_e - Be^{-DP_e} \tag{2.23}$$

can be used to simulate the velocity change with pressure. Similar velocity-pressure relationships were also found by Freund (1992) and Jones (1995).

However Khaksar *et al*. (1999) found an empirical equation without the linear part

$$V = A - Be^{-DP_e} \tag{2.24}$$

gives a better, more realistic fit to dry sandstone velocity at higher pressures. They concluded that pore geometry and the nature of grain contacts may be more important than total porosity in describing the pressure sensitivity in sandstones. Also, the distribution and location of clay minerals within the rock framework might be more important than the total volumetric clay content in determining the pressure dependence of velocity in sandstones.

Attenuation is also strongly dependent on effective pressure, decreasing by at least an order of magnitude between ambient and 40 MPa (Winkler and Nur, 1982; Klimentos and McCann, 1990). The compressional and shear wave quality factor (Q_p and Q_s respectively) at ultrasonic frequency increase with increasing effective pressure and reach a limiting value before staying constant (Toksöz *et al*., 1979; Johnston and Toksöz, 1980; Domnesteanu *et al*., 2002; Khazanehdari and McCann, 2005; Mayr and Burkhardt, 2006).

Jones (1995) measured Q_p and Q_s of 16 water-saturated sandstones as a function of differential pressure from 5 MPa to 60 MPa. He found equation 2.24 gives a better fit to the measured Q than using equation 2.23. He concluded that the redundancy of the linear term in equation 2.24 is caused by the microcracks alone in governing the pressure variation of Q whereas velocity is additionally dependent on other factors.

Prasad and Manghnani (1997) measured compressional-wave velocity and quality factor of Berea and Michigan sandstones as a function of confining pressure (P_c) to 55 MPa and pore pressure (P_p) to 35 MPa. They proposed an equation by combining the effects on differential pressure (P_d) and confining pressure in the form of

$$Z^2 = A + BP_d + Ce^{-P_c/D}. \qquad (2.25)$$

They used this equation to perform a least squares regression on both measured V_p and Q_p, and found that the effect of pore pressure on Q_p is greater at higher differential pressures.

In general, elastic velocity is found to increase with pressure while attenuation decreases. Differences between various authors' equations seeking to describe variations in elastic properties as a function of pressure might result from the different pressure ranges employed, differences in rock properties (e.g., rock porosity) or even different types of pore fluids and saturation.

2.4.3. Permeability

Relationships between elastic velocity and permeability have been difficult to establish (Prasad, 2003). Klimentos (1991) showed that P-wave velocity in reservoir sandstones increases slightly with increasing permeability, although with a large scatter of datapoints about the trend. However, this scatter is significantly reduced when the measured P-wave velocity is plotted against permeability for rocks with identical porosities. He concluded that the slight increase of P-wave velocity with permeability arises mainly from the strong dependencies of P-wave velocity and permeability on clay content. The effect of permeability alone on P-wave velocity is negligible in sandstones with small amounts of clay (< 1 percent) or with the same amounts of clay, porosity, lithology, etc. (e.g., grain-size and sorting, pore-size and

shape, etc.). Best *et al*. (1994) similarly showed that there is no significant relationship between velocity and permeability in reservoir sandstones.

Klimentos and McCann (1990) found that P-wave quality factor increases with increasing permeability in 42 water-saturated, high clay content sandstones. They attributed this dependence of attenuation on permeability to the strong dependence of permeability on clay content. The P-wave experimental results of Best *et al*. (1994) are generally consistent with the results from Klimentos and McCann (1990), and their S-wave attenuation data show similar trends to those of P-wave attenuation against permeability.

On the other hand, Shatilo *et al*. (1998) measured ultrasonic P-wave attenuation on 29 low clay content sandstone samples showing increasing attenuation (decreasing quality factor) with increasing permeability. A similar attenuation-permeability correlation was demonstrated by Khazanehdari and McCann (2005) who measured the ultrasonic quality factors of 19 low-shale sandstones, and concluded that the response of the ultrasonic attenuation to changes in permeability depends on variations in mineralogy and rock fabric. When permeability decreases because of an increase in clay content, attenuation also increases because of the increased heterogeneity of the rock; when permeability decreases because of a decrease in porosity the quality factor can increase (attenuation decreases).

2.4.4. Frequency

Most of the relationships established above are through laboratory measurements in the ultrasonic frequency range (0.1 – 2 MHz). However, since surface seismic exploration and borehole sonic measurements use frequency bands of 10 – 200 Hz and 2 – 20 kHz respectively (Goldberg and Zinszner, 1989; Wang, 2001), care must be taken when applying the relationships obtained in the laboratory to the interpretation of seismic field surveys (King and Marsden, 2002).

It is generally accepted that velocity dispersion in dry porous rocks is negligible over the frequency range from seismic to ultrasonic (Gist, 1994), whereas velocities in fluid saturated rocks vary with frequency (Winkler, 1986). Experimental evidence confirms that velocities measured on fluid saturated rocks at logging frequencies are slightly higher than those measured at seismic frequency (Goetz *et al*., 1979), and

velocities of saturated rock at ultrasonic frequencies are significantly higher than at seismic frequency (Winkler, 1985; Best and Sams, 1997).

Pre-1980 observations of attenuation indicated that Q^{-1} is independent of frequency over a wide range of frequencies (Stacey *et al*., 1975; Kjartansson, 1979; Toksöz *et al*., 1979; Johnston and Toksöz; 1980) implying attenuation coefficient is linearly proportional to frequency. In addition to the study of velocity and attenuation dispersion within each frequency band, i.e., seismic, sonic logging and ultrasonic respectively (Wuenschel, 1965; Jones and Nur, 1983; Winkler, 1983; Tutuncu *et al*., 1994) efforts have also been made to address the discrepancies of velocity and attenuation between these frequency bands. Notably, Sams *et al*. (1997) carried out a series of experiments at a shallow (~ 300 m) borehole test site and on core samples in the laboratory to determine the elastic properties of a sequence of saturated sedimentary rocks over a wide range of frequencies: 30 – 280 Hz for vertical seismic profiles (VSPs), 0.2 – 2.3 kHz for crosshole surveys, 8 – 24 kHz for sonic logging and 300 – 900 kHz for laboratory ultrasonic measurements. The data show velocity dispersion of both compressional and shear waves over the frequency range and attenuation of compressional waves is frequency dependent with a peak in the attenuation in the sonic frequency band.

Best and Sams (1997) measured ultrasonic (about 1 MHz) compressional wave velocity and attenuation on clean sandstones taken from the test borehole and compared the ultrasonic velocity with those from the full waveform sonic log at about 10 kHz. Significant velocity dispersion was found over this frequency range. Based on the fact that clean sandstones are highly attenuating at about 1 MHz, they deduced that the sandstones must also be highly attenuating over a significant part of the frequency range 10 kHz to 1 MHz to account for the magnitude of the observed velocity dispersion.

Best and McCann (1995) investigated frequency dependence of seismic velocity and attenuation in a suite of clay-rich reservoir sandstones. By varying the viscosity (0.3 to 1000 centipoise) of the fluids saturating the samples, the equivalent frequencies were calculated to be 2.6 MHz to 780 Hz for a water-saturated sandstone assuming a global-flow loss mechanism (Biot, 1956a, b). They found that high permeability sandstones show small velocity dispersions and variable Q_p and Q_s with changing pore-fluid viscosity (equivalent to varying frequency); whereas low permeability

sandstones show relatively large increases in velocity with increasing viscosity (equivalent to increasing frequency if a local fluid flow loss mechanism is inferred in these rocks, the opposite behaviour to Biot theory) and almost constant Q_p and Q_s in the viscosity (frequency) range.

Batzle *et al*. (2006) used a forced deformation system in conjunction with pulse transmission to study elastic properties at seismic strain amplitude (10^{-7}) from 5 Hz to 800 kHz. Their measurements over the broad frequency band demonstrate that velocity dispersion can be significant and is strongly influenced by fluid mobility (defined as ratio of rock permeability to fluid viscosity). They concluded that for most sedimentary rocks (e.g., shales, tight sandstones and carbonates, heavy oil sands and evaporates) and even permeable rocks saturated with viscous oil, seismic, sonic logging, and ultrasonic measurements can yield consistent velocity values (excluding issues with heterogeneity) because of lower fluid mobility. This increases the relaxation time needed for fluid equilibration, thus lowering the dispersion frequency; in contrast the velocity dispersion in porous and permeable sands may be larger.

McCann and Sothcott (2009) measured the quality factor of 2 sandstones at sonic and ultrasonic frequency using resonant-bar equipment and an ultrasonic pulse-echo technique. Their data show that the energy absorption in the two sandstones is variable in magnitude (Q_p ranges from less than 50 to greater than 300, at reservoir pressures) and arises from a combination of poroelastic (through global viscous fluid flow within the pores) and viscoelastic (arising from local viscous fluid flow) loss mechanisms.

In summary, various methods and assumptions (e.g., constant Q^{-1}) have been applied over the years to analyse variations in elastic properties with elastic wave frequency. The results sometimes contradict themselves and some results may be compromised by flawed experimental procedures. Hence, there is to date no consensus on the true frequency dependence of velocity and attenuation in reservoir sandstones. The most direct and convincing way to demonstrate this would be to conduct experiments on samples with continuously changing frequency from seismic to ultrasonic. However, there have been no such measurements due to insurmountable practical problems. Seismic pulse transmission measurements in the laboratory under simulated pressures would require rock samples that are far too big (dimensions in the magnitude of 10 metres) for any practical experimental apparatus. Thus, laboratory experimentalists

have been forced to use resonance and stress-strain methods to achieve seismic and sonic frequency measurements on reasonably sized core samples up to 30 cm long. Problems in calibration of these methods make it difficult to compare results from different methods with absolute confidence.

2.5. The effect of reservoir parameters on electrical resistivity/conductivity

Electrical resistivity (the reciprocal of electrical conductivity) is another useful geophysical parameter measured routinely in boreholes (Erickson and Jarrard, 1998) and increasingly by marine CSEM surveys. Since the electrical conductivity of clean reservoir sandstones results dominantly from the pore fluids saturating the rocks, higher electrical resistivities could indicate the presence of hydrocarbons which behave like insulators compared to ionic-conducting brines. However, the reality is often more complicated because lower porosities and/or brine saturations may also result in higher observed resistivities. Also, there are many other parameters that affect electrical resistivity, such as pressure and temperature. Therefore, a thorough understanding of the inter-relationships between electrical resistivity and these other parameters is required for the valid interpretation of resistivity data in terms of reservoir characteristics.

This section reviews the current knowledge of the effects of some of these parameters (i.e., porosity & saturation, clay content & salinity, pressure, permeability and frequency) on the electrical properties of reservoir sandstones. Further discussion of these established relationships and comparisons with novel experimental data will be presented in Chapter 4.

2.5.1. Porosity and saturation

Electrical properties are usually measured to determine the porosity and hydrocarbon saturation of reservoir rocks (Jing *et al*., 1992). Based on the laboratory measurements of electrical resistivity on a large number of brine-saturated cores from various sand formations, Archie (1942) related resistivity to porosity empirically by

$$\frac{\rho_0}{\rho_w} = \varphi^{-m}, \tag{2.26}$$

where ρ_0 is the resistivity of a rock sample fully saturated with a brine of resistivity ρ_w, φ is the porosity fraction and the exponent m is known as the cementation coefficient. For samples partially saturated with brine, Archie (1942) found the resistivity (ρ) to decrease as a function of brine saturation (S) according to

$$\rho = \frac{\rho_0}{S^n}, \tag{2.27}$$

where n is the saturation exponent and found to be close to 2.

Archie's equation is usually expressed for rocks of varying saturation as

$$\rho = a\varphi^{-m}\rho_w S^{-n}, \tag{2.28}$$

where the coefficient a is tortuosity factor which is regarded as a reservoir constant that can depart from unity (Carothers, 1968; Porter and Carothers, 1970; Timur *et al*., 1972; Gomez-Rivero, 1977; Worthington, 1993; Khalil and Monterio Santos, 2009). Some researchers (e.g., Glover, 2009) argue that the tortuosity factor $a \neq 1$ does not have a physical or theoretical meaning and therefore should always be unity.

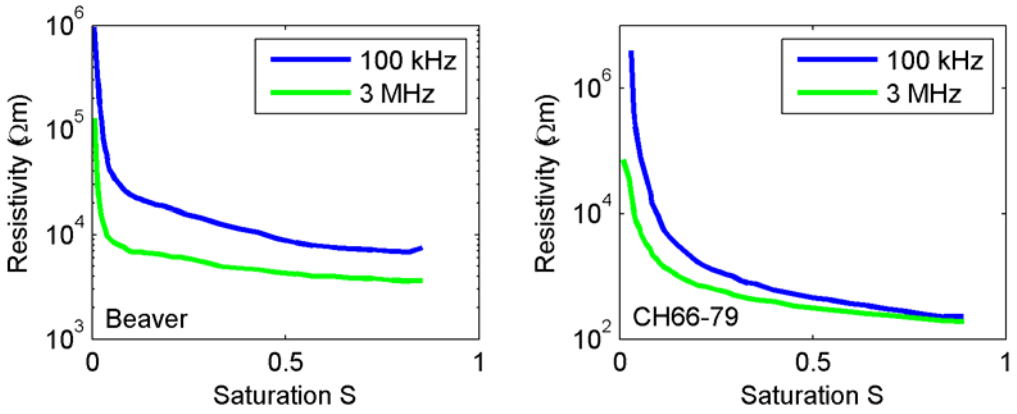

Figure 2.4. An example showing the variation of electrical resistivity with water saturation S and measurement frequency. Data digitized from Knight and Dvorkin (1992).

Other researchers (e.g., Keller, 1953; Alvarez, 1973) found experimentally that the electrical resistivity of a dry sandstone decreases significantly with the addition of a small amount of water. However, the decrease in resistivity with water content at higher levels of water saturation is more gradual and linear (Figure 2.4), distinctly different from that at the lower saturations (Knight and Dvorkin, 1992; Taylor and

Barker, 2002; Gomaa, 2009). The differences in the saturation dependence are interpreted to reflect the differences in the nature of the water present in the rock, i.e., a surface adsorbed phase and a bulk water phase for low saturation and high saturation respectively (Knight and Dvorkin, 1992).

In addition to affecting the overall resistivity of sandstones, Longeron *et al*. (1989) noticed hysteresis in the electrical resistivity of sandstone samples when saturated with a mixture of oil and brine which was varied by imbibition (increasing brine saturation) and drainage (reducing brine saturation). Knight (1991) measured the resistivity of three sandstone samples during imbibition and drainage and found that the resistivity measured during imbibition is consistently less than that measured during drainage at the same saturation. She attributed this to the presence of conduction at the air/water interface, an effect that is enhanced by fluid geometries associated with the imbibition process in partially saturated samples.

2.5.2. Clay content and salinity

Archie's equation (equation 2.26) is known to work well for clean sandstones, but it fails to predict the electrical properties of shaly sandstones (Waxman and Smits, 1968; Cohen, 1981; Sen *et al*., 1988; Glover *et al*., 1994; de Lima *et al*., 2005; Leroy *et al*., 2008). The conductivity of shaly sandstones results not only from conduction through the bulk solution occupying the interconnected pores but also from surface conduction occurring in the vicinity of the clay/electrolyte interface (Bussian, 1983; Revil and Glover, 1997, 1998; Revil *et al*., 1998). It has been demonstrated through experiments and theory that the surface conductivity depends on both clay type and content and the salinity of the electrolyte saturating the sandstones (e.g., Worthington, 1982; Revil *et al*., 1998; Rabaute *et al*., 2003).

Experimental measurements (e.g., Patnode and Wyllie, 1950; Wyllie and Southwich, 1954; Waxman and Smith, 1968; Barker and Worthington, 1973; Rink and Schopper, 1974; Glover *et al*., 1994; Chan *et al*., 2000; Deng *et al*., 2006) on shaly sandstones with varying clay content and electrolyte salinity show that two salinity regions exist for the conductivity of shaly sandstones. At high electrolyte salinities the conductivity of the saturated sandstones is linearly proportional to the electrolyte conductivity on a logarithmic scale. This indicates that conductivity is controlled by the movement of

ions in the electrolyte, and that surface conductivity is negligible compared with this high electrolyte conduction. At low electrolyte salinities the conductivity of saturated shaly sandstones is no longer linearly correlated to the electrolyte conductivity; at very low electrolyte salinities it tends to be a constant equal to the value of surface conductivity. Glover *et al*. (1994) concluded that the effect of surface conduction in shaly sandstones becomes noticeable when the electrolyte conductivity is approximately equal to the surface conductivity of a shaly sandstone.

2.5.3. Pressure

The electrical resistivity of saturated sandstone samples generally increases with increasing differential pressure due to reductions in pore size and changes to the tortuosity of the current flow paths during sample compression (Fatt, 1957; Brace *et al*., 1965; Brace and Orange, 1968; Timur *et al*., 1972).

Jing *et al*. (1992) showed experimentally that the increase of electrical resistivity in the lower pressure range (e.g. < 10 MPa) is greater than that in the higher pressure range. Also, as pressure increases further, the resistivity will eventually converge on a constant value due to the closure of pressure sensitive pores (Jing, 1990; Jing *et al*., 1990). This is attributed to the greater compressibility of low aspect ratio pores at lower confining pressures.

The effect of pressure on electrical resistivity is found to be greater for less porous, less permeable samples than that for more porous, more permeable samples. This can be explained by the higher proportion of microcracks and/or low aspect ratio pores in the less porous and permeable samples (Glanville, 1959; Xu *et al*., 1990; Jing *et al*., 1992).

Glover *et al*. (2000) showed that, as triaxial stress increases, low aspect ratio pore spaces are initially closed perpendicular to the principal stress. Later, at higher axial stresses, new low aspect ratio fractures are formed along the samples axis. The interaction of these two sets of factures can lead to extremely well connected pores and low electrical resistivities when the differential pressure is reduced.

2.5.4. Permeability

There is conflicting evidence for the true relationship between permeability and electrical resistivity in reservoir sandstones. Laboratory measurements on artificial and real rocks by Wong *et al*. (1984) showed a negative correlation between permeability and formation factor (see Figure 2.5). This relation is approximately satisfied by $k \propto F^{-2}$, where k and F correspond to permeability and formation factor respectively, with $F = \rho_0 / \rho_w$. The results of Heigold *et al*. (1979) and Frohlich *et al*. (1996) also showed negative correlations between permeability and electrical resistivity.

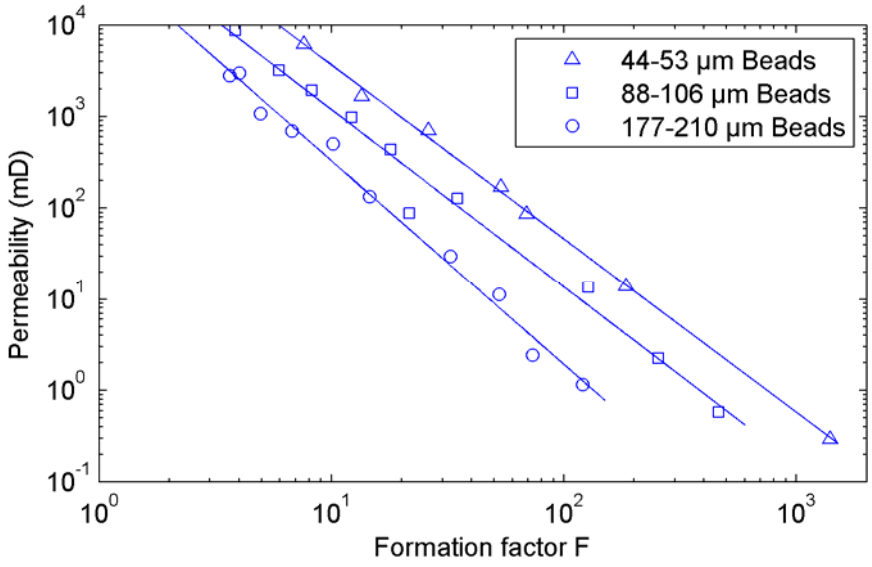

Figure 2.5. An example showing the negative correlation between permeability and electrical formation factor obtained on artificial sandstones. Data digitized from Wong *et al*. (1984).

By contrast, the experiments of Jones and Buford (1951) on sandstones saturated with low salinity brine demonstrated permeability is positively correlated with electrical resistivity (see Figure 2.6). The work of Worthington (1977), Urish (1981), Kosinski and Kelly (1981) and Ponzini *et al*. (1983) also supports this positive correlation.

However, experiments on sandstones by Huntley (1986) showed only weak relations between permeability and formation factor (for constant fluid conductivity only). He also observed a strong (positive) correlation between permeability and matrix conductivity.

Purvance and Andricevic (2000) summarized the permeability-resistivity relations, and attributed the negative or positive correlations to the salinity of the brines

saturating the rocks: for conducting pore fluids (brines), bulk rock electrical conductivity is predominantly through these pore volumes. This causes electrical resistivity to decrease with permeability, resulting in a negative permeability-resistivity relation. However, in freshwater saturated, clay-rich sandstones, the predominant mode of electrical conduction is along the pore surfaces. This causes electrical resistivity to decrease with permeability as a function of clay content and therefore giving a positive permeability-resistivity correlation.

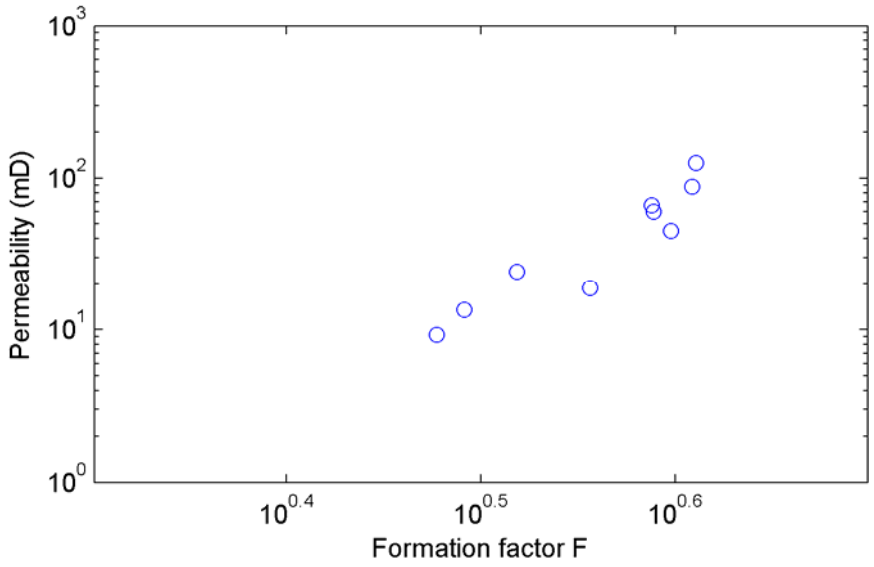

Figure 2.6. An example showing the positive correlation between permeability and electrical formation factor. Data from Jones and Buford (1951).

2.5.5. Frequency

Dry sandstones without a metallic component in a vacuum at room temperature are good dielectrics and resistivity is independent of frequency (Chelidze *et al*., 1999; Gomaa, 2009). Frequency dependence can be related to chemical and physical reactions taking place between the solid rock framework and conductive fluid or solid phases (e.g., brine pore fluid, clay minerals) with different electrical properties (Rink and Schopper, 1974; Sen, 1980; Olhoeft, 1985; Sen *et al*., 1988; Knight and Endres, 1991; Denicol and Jing, 1998). At low frequencies (less than 1 Hz), chemical interactions such as adsorption and cation exchange at the solid-fluid interface play an important role. At higher frequencies (10 Hz to 10 MHz), ionic double-layer polarisations at the solid-fluid interface become significant (Garrouch and Sharma,

1994), resulting in a slowly decreasing electrical resistivity as a function of frequency (de Lima and Sharma, 1992).

Various parameters have been found to affect the frequency dependence of the electrical resistivity of reservoir sandstones. Denicol and Jing (1998) systematically studied the effects of water salinity, saturation and clay content on resistivity of sandstone samples from 10 Hz to 2 MHz. They demonstrated that the frequency dependence of resistivity increases with decreasing brine concentration, increases when brine is displaced with oil, increases consistently with increasing clay content and decreases with brine saturation. These results are generally consistent with work of Garrouch and Sharma (1994) who studied the influence of clay content, salinity and stress on the dielectric properties of brine-saturated rocks in the frequency range 10 Hz to 10 MHz. They showed that stress is relatively unimportant in determining the frequency dependent resistivity of brine-saturated sandstones.

Other experiments investigating the effects of brine salinity (e.g., Börner and Schön, 1995; Saltas *et al*., 2007), saturation (e.g., Knight and Dvorkin, 1992; Garrouch, 2000; Su *et al*., 2000; Gomaa, 2009) and clay content (e.g., Al-Mjeni *et al*., 2002; Moss *et al*., 2002) on the frequency dependence of resistivity show similar results.

2.6. Summary

This chapter reviewed some key sandstone reservoir parameters that affect elastic velocity and attenuation, and electrical resistivity, and hence the propagation of elastic and electromagnetic waves in sandstones. It turns out that porosity, clay content, permeability and pressure influence both elastic and electrical properties of reservoir sandstones under constant brine salinity and temperature of interest to this study (see following chapters). Measurement frequency also affects both elastic and electrical properties, although elastic frequency and electrical frequency are two different parameters and should be dealt with separately.

Despite the scientific progress made by researchers over several decades, knowledge of some aspects of the elastic and electrical behaviours of reservoir sandstones still remain elusive:

(1) There are apparently conflicting observations of the effect of clay content and permeability on seismic wave attenuation in porous rocks;

(2) Although there are theoretical models that seek to describe variations in elastic wave velocity and attenuation with frequency, the available experimental data is inconclusive because of the practical difficulties in carrying out low frequency measurements on rock samples in the laboratory;

(3) Electrical resistivity is sensitive to rock porosity, clay content, water saturation and salinity and measurement frequency. The combined effects of these variables on electrical resistivity need further investigation;

(4) So far, elastic and electrical properties of sandstones have been studied separately although there is a growing interest in joint geophysical inversions for application to borehole and surface measurements. In fact, there are no published laboratory datasets of simultaneous measurements of both elastic and electrical properties on reservoir sandstones under simulated reservoir pressures, although many *in situ* borehole logging datasets exist. Such an internally consistent laboratory dataset is needed (thus avoiding complications of comparing measurements made at different times on different samples under different conditions) with which to conduct a systematic study of the joint elastic-electrical properties of reservoir sandstones. The main advantage of using a laboratory dataset over a borehole logging dataset is that unknown parameters can be minimised, such as rock sample heterogeneity.

(5) It is possible that some unexpected relationships may emerge when joint elastic-electrical properties are studied in detail. An unambiguous dataset would provide insight into key physical processes and help establish robust rock physics models that could be used in a range of geophysical inversion problems.

This project will address some of these deficiencies.

Chapter 3

Laboratory experiments

3.1. Introduction

Laboratory experimentation is one of the most important steps in rock physics studies. The establishment of new inter-relationships between physical and reservoir properties and validation of rock physics models are only possible following the collection of an accurate rock physics dataset. To achieve this, the experimental apparatus needs to be robust and suitably advanced, the samples have to be representative of geological formations, the experimental procedure must be carefully designed and consistently performed, and the data should finally be precisely processed and calculated with error bars.

This chapter describes how a comprehensive joint elastic-electrical dataset was successfully collected on 67 reservoir sandstone samples in the laboratory. It starts by introducing the apparatus which allows elastic and electrical properties of the samples to be measured almost simultaneously under elevated differential pressures, followed by the descriptions of the sandstone samples, the experimental procedure, and how the raw data were processed to get the required parameters. It ends with a summary of how the newly collected joint elastic-electrical dataset will be used in the analyses given in the following chapters.

3.2. Apparatus

Joint elastic-electrical measurements were made on brine saturated sandstone samples in an adapted Wykeham Farrance high pressure rig (Figure 3.1). The rig was originally developed for ultrasonic measurements but was recently adapted for electrical resistivity as part of a laboratory gas hydrates study (see Sothcott *et al*., 2007; Ellis, 2008). The rock sample was kept isolated from the surrounding hydraulic oil, which was used to apply confining pressure up to 65 MPa, by a rubber sleeve. A ram was used to apply a uniaxial confining pressure equal to the surrounding confining pressure to the top and base of the sample assembly; the resulting confining pressure on the sample was equal in all directions. Pore fluid pressure was controlled via a pore fluid inlet at the base of the sample (Figure 3.2).

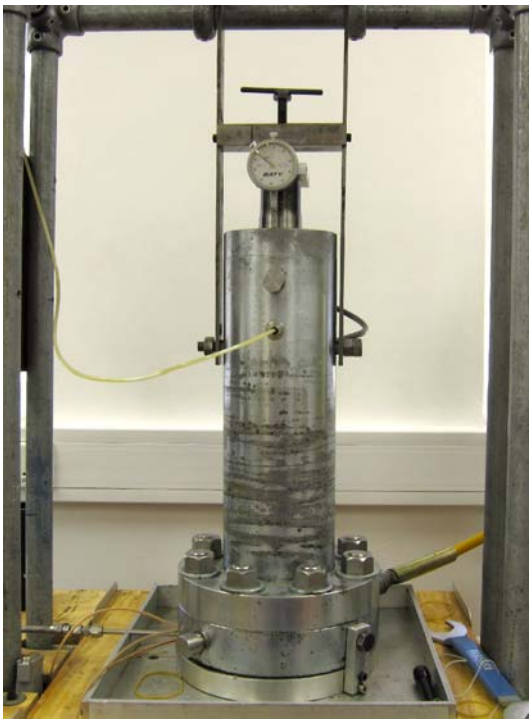

Figure 3.1. The adapted Wykeham Farrance high pressure rig for the joint elastic-electrical measurements.

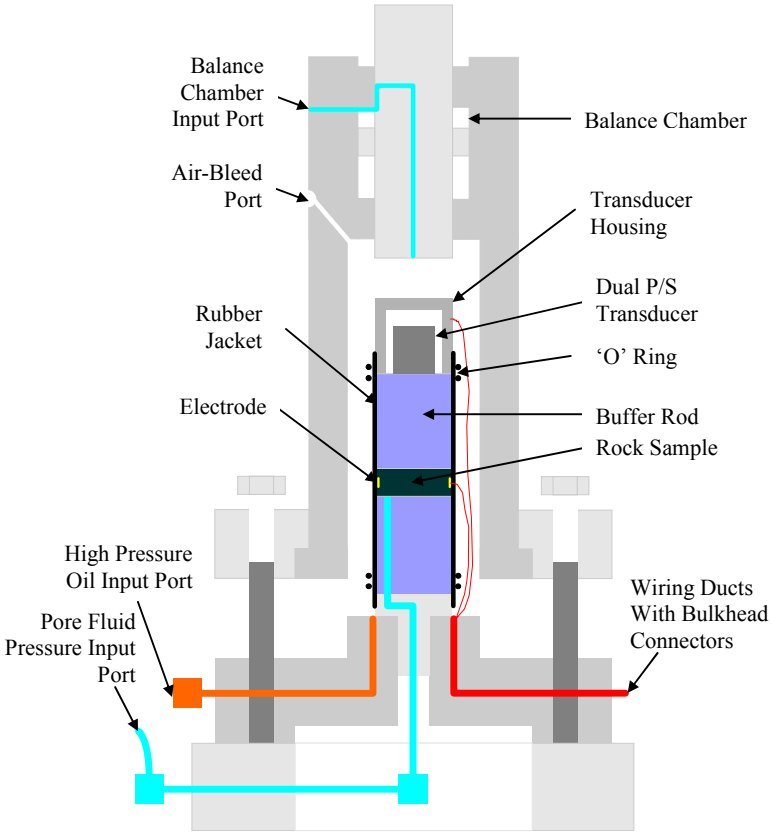

Figure 3.2. Schematic diagram of the adapted Wykeham Farrance high pressure rig for joint elastic-electrical measurements (adapted from Ellis, 2008).

3.2.1. Ultrasonic reflection system

Elastic (both compressional and shear wave velocity and attenuation) properties were measured using an ultrasonic reflection technique first developed by Winkler and Plona (1982) and adapted by Klimentos and McCann (1990) and Best *et al*. (1994) in which the system was described in detail. A 5 cm diameter sandstone sample was sandwiched between two Perspex buffer rods while a dual P/S wave transducer was used to transmit an ultrasonic pulse through the upper buffer rod and into the sample. The pulse was partly reflected back from the top of the sandstone sample and then from the base of the sample (Figure 3.3). The reflected signals were detected by the same transducer and digitally recorded. The velocity of the sample was calculated from the time difference between the two reflection arrivals and the thickness of the sample, and the attenuation was determined by comparing the amplitudes of the two reflected pulses.

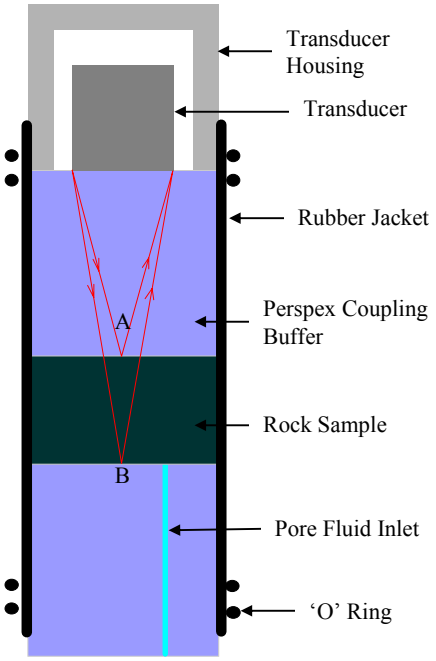

Figure 3.3. The ultrasonic reflection system used for elastic wave velocity and attenuation measurements. A and B are reflections from the top and base of the sample respectively (adapted from Best *el al*., 1994).

3.2.2. Circumference resistivity system

The circumference resistivity system for measuring electrical resistivity of sedimentary rocks was first introduced and used by Ellis (2008). Twelve electrodes

were incorporated into the rubber sleeve and arranged at equal spacings around the circumference of the sandstone sample but were electrically isolated from one another. An alternating current (A/C) was generated using a constant current source (Keithley 6221) and was applied across successive pairs of opposing electrodes. For each pair of current electrodes the voltages were measured at adjacent electrode pairs as shown in Figure 3.4. This electrode configuration was shifted stepwise around the sample so that the resistance could be measured in different orientations. The current was passed through a total of 6 different electrode pairs and voltage was measured 24 times (12 wide electrode pairs and 12 narrow electrode pairs) to obtain a single bulk rock resistance measurement, which was achieved by averaging the 12 wide electrode resistances and the 12 narrow electrode resistances respectively on the assumption of homogeneous samples.

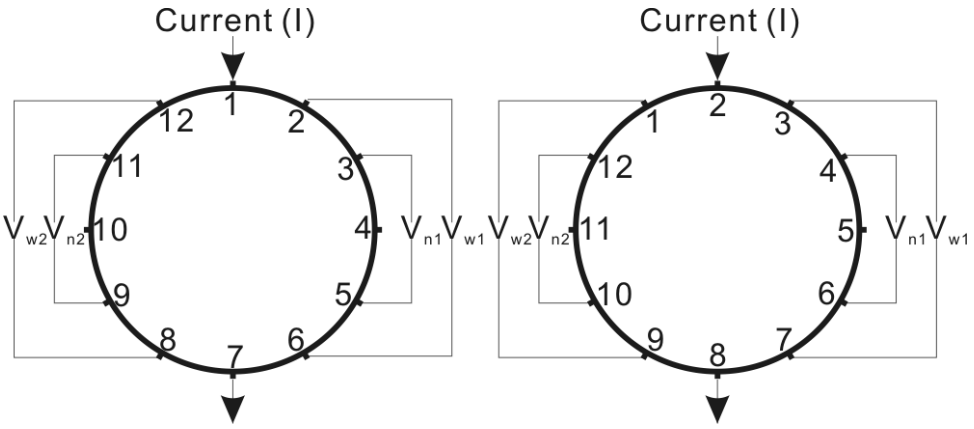

Figure 3.4. Circumference resistivity measurement procedure. Voltages are measured at adjacent wide (V_{w1} and V_{w2}) and narrow (V_{n1} and V_{n2}) electrode pairs with respect to the current (I) electrodes. The process of rotating the current and voltage electrode positions was continued through 360° (after Ellis, 2008).

3.2.3. Electrode polarisation

The 12 electrodes used in electrical resistivity measurements were made from stainless steel. Ionic charges may accumulate on the electrode surfaces and form electrical double layers upon contact with the sample resulting in electrode polarisation (Feldman *et al*., 2001). To test whether the stainless steel electrodes have low electrode polarisation, a separate experiment was designed and performed together with Dr. Laurence North by comparing the electrode polarisation of the stainless steel electrodes with that of non-polarising, silver chloride (AgCl) electrodes.

An electrode polarisation test cell (Figure 3.5) was made to be exactly the same geometry as the sandstone samples (5 cm in diameter and 2 cm depth); 4 stainless steel electrodes and 4 silver chloride electrodes (disk electrodes from A-M systems, inc.), all with diameters of 4 mm, were then embedded into the base of the test cell with positions relative to the centre of the cell given in Table 3.1 and illustrated in Figure 3.5.

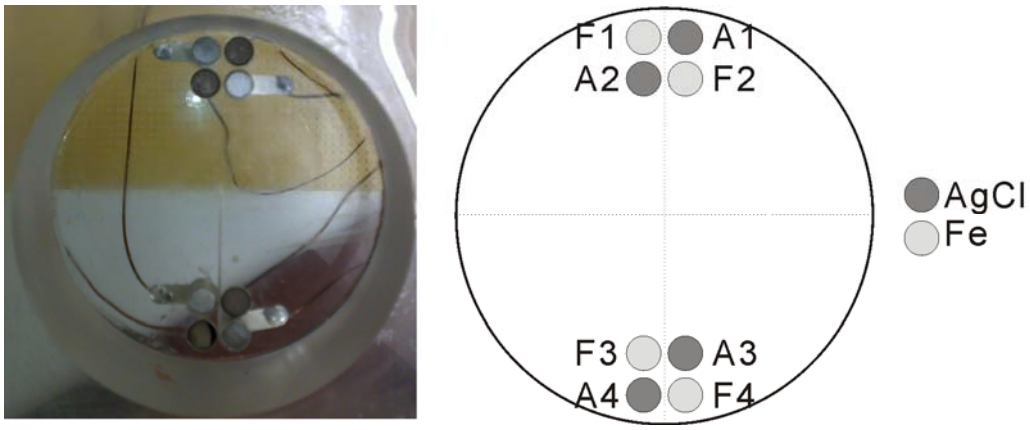

Figure 3.5. Electrode polarisation test cell.

Table 3.1. Electrodes position in the electrode polarisation test cell relative to the centre of the cell.

Electrode	X position (mm)	Y position (mm)
F1	-2.5	21.5
A1	2.5	21.5
F2	2.5	16.5
A2	-2.5	16.5
F3	-2.5	-16.5
A3	2.5	-16.5
F4	2.5	-21.5
A4	-2.5	-21.5

The electrical resistance of the brine filling the test cell was measured using the same types of electrode, that is, stainless steel electrodes and silver chloride electrodes respectively. For each type of the electrode, the resistance was measured by applying a constant alternating current to the large-spaced electrodes (e.g., F1 and F4 for the

stainless steel electrodes and A1 and A4 for the silver chloride electrodes) and the voltage was recorded over the small-spaced electrodes (e.g., F2 and F3 & A2 and A3 for the stainless steel electrodes and the silver chloride electrodes respectively). A finite element model (Adler and Lionheart, 2006) was utilized to calculate the electrical resistivity from the measured resistance and the geometry of the test cell.

Figure 3.6 compares the brine resistivity when measured using the 2 types of electrodes at A/C frequency from 1 Hz to 50 kHz. The almost flat response of resistivity with frequency for both types of electrode shows that both stainless steel and silver chloride electrodes have negligible electrode polarisation. If there were significant electrode polarisation effects, then the resistivity would be expected to decrease with increasing frequency (e.g., Feldman *et al*., 2001).

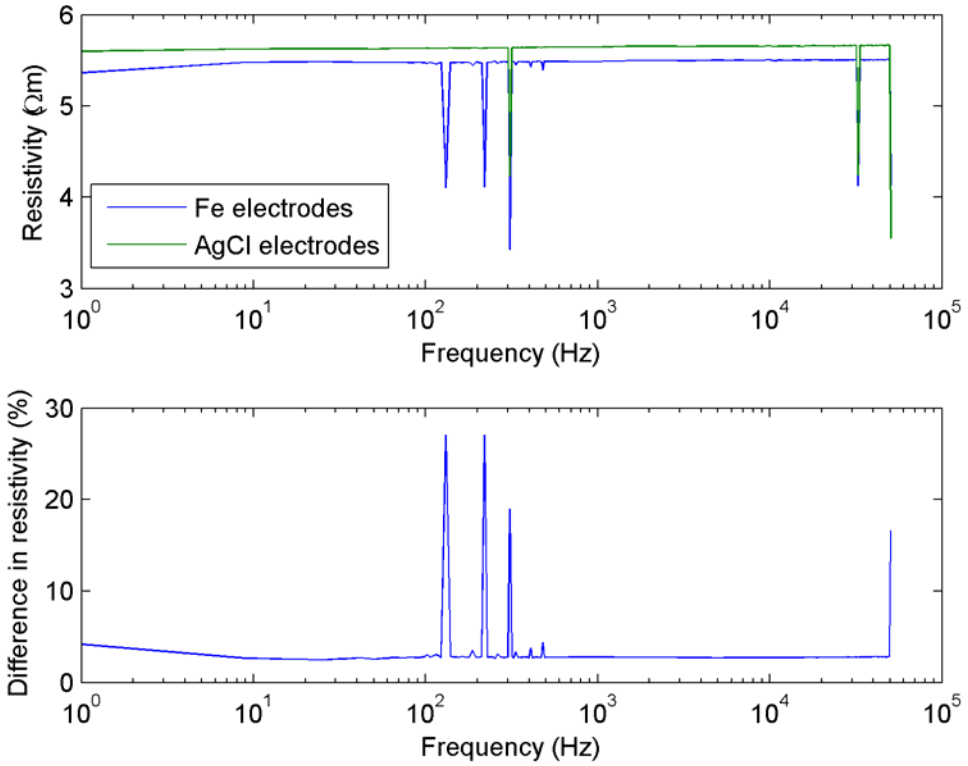

Figure 3.6. Comparison and the difference between the electrical resistivity of a brine measured using stainless steel electrodes and silver chloride electrodes respectively at frequencies from 1 Hz to 50 kHz.

The difference between the resistivities measured with stainless steel and silver chloride electrode is approximate 3%. This is possibly a result of the difference in thickness of the electrodes. Since the stainless steel electrodes were a little thinner than the silver chloride electrodes, there was a larger gap between the stainless steel

electrodes and the base surface of the test cell. As this cavity was filled with conductive brine, it led to a lower resistivity.

Also, other researchers have reported that a four-electrode geometry can minimize electrode polarisation effects (e.g., Schwan, 1968; Olhoeft, 1985; Mazzeo, 2009).

3.3. Sandstone samples

Sandstones are the major hydrocarbon reservoir rocks in the Earth (see Section 1.1.4). It is therefore of vital importance to understand the joint elastic-electrical behaviour of sandstones for the joint seismic-CSEM inversion purposes in case of sandstone reservoirs.

3.3.1. Sample collection

Samples should be selected to represent as wide a range of porosity, permeability and clay content as possible. To meet this requirement 67 sandstone samples were collected from both borehole cores and quarry blocks from all over the world.

One Berea sandstone sample, a lithology much referred to in rock physics literature, was already available in the Rock Physics laboratory of NOCS, as well as 3 orthogonal sandstone samples from the Andrew Field of the North Sea (from a depth of approximately 2500 m) provided by British Petroleum (referred to here as BP AX, BP AY and BP AZ1 respectively) for another project.

Ten samples originating from Borehole No. 2 of the Whitchester test site (see Sams *et al*., 1993 for details of the borehole test site) were then obtained from the University of Oxford in 2007. These samples are here identified by the letter ‘W’ followed by the depth at which they are from. When the sample identification number ends with ‘H’, this means the sample was drilled horizontally (i.e., perpendicular to the borehole axis assuming a vertical borehole) otherwise the sample was cut vertically to the borehole axis. For example, sample No. W165.6 is a sample cut vertically from a depth of 165.5 m at the Whitchester test site, while sample No. W165.6H is from the same depth but cut horizontally.

Six samples from various quarries in the UK were obtained from RealStone Ltd. in 2008 (Figure 3.7).

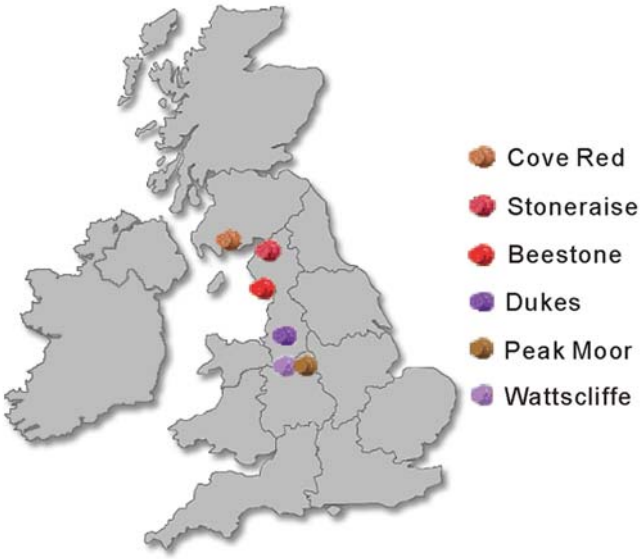

Figure 3.7. Locations of the quarries from where Realstone supplied samples (adapted from http://www.blockstone.co.uk/quarries.html).

Fifteen sandstones were inherited that originated from other quarries in the UK, but with unknown locations. Of these samples, 7 had been studied by Simon M. Jones at the University of Reading (Jones, 1996).

Due to the extreme difficulty of getting sufficient samples for this project, I collected 11 sandstones form Shanxi province (SX) and 4 blocks from Shandong province (SD) of China in 2009. Prof. Jinliang Zhang of the Ocean University of China provided 14 borehole sandstones (CZ) from production wells of different oil companies in China, and Prof. Cheng Xu of Peking University, China contributed another 4 borehole samples from China (CX).

3.3.2. Sample preparation

The selected sandstone samples were cut into 2 cm long cylinders with a diameter of 5 cm. The end faces of each sample were ground flat and parallel to within ± 0.01 mm to make sure the sample would be tightly contacted with the buffer rods in the high pressure rig. The samples were then dried in an oven for three days at 40 ºC, a temperature low enough to avoid damaging clay minerals. For some of the CZ samples that contained oil from production wells, the samples were completely

washed (Figure 3.8) using a mixture of 75% dichloromethane (CH_2Cl_2) and 25% methanol (CH_3OH) in a Soxhlet reflux apparatus before they were dried.

Figure 3.8. A picture showing samples that contain oil being washed in a Soxhlet reflux apparatus.

3.3.3. Sample characterisation

The cleaned and dried samples were weighed and their dimensions were measured. The porosity and permeability (in millidarcies; 1 mD = 9.869233×10^{-16} m^2) were then determined on each dry sample using a helium porosimeter and nitrogen gas permeameter to an accuracy of ± 0.1 % and ± 2% respectively. Clay weight percentage was measured using whole rock X-ray diffraction (XRD) on the off-cut of each sample and transformed to volumetric clay content (a percentage of clay mineral volume without microporosity to the bulk volume of the rock sample) to an accuracy of ± 5% (other mineralogical properties were measured and calculated in the same way). Thin sections and a scanning electron microscope (SEM) were used to study rock fabric and mineralogy. It turned out that the 67 samples used in this study cover a porosity range from 1.99% to 28.99%, permeability from 0.0001 mD to 997.49 mD and volumetric clay content from 0 to 27.63%, thus achieving the desired, wide spread of reservoir parameters. The petrophysical and mineralogical properties of the 67 sandstone samples are given in Appendix A.

3.4. Experimental procedure

The sandstone sample was put into the high pressure rig and evacuated to 10^{-2} Pa through the pore pressure port, a 35 g/l brine (made from sodium chloride and distilled, deionized and deaired water) was used to saturate the sample under a pore pressure of 5 MPa. The pore pressure was maintained for a minimum of 16 hours to make sure the sample was fully saturated. For samples with very low permeability (lower than 1 mD), the evacuation and saturation in the rig would take many days. To avoid wasting time, a saturation rig (Figure 3.9) was used to do this job. Several samples were put together in the saturation rig, evacuated to a pressure of 10^{-4} Pa and saturated under pore pressure of 7 MPa. The fully saturated samples were then put in a tank filled with the same brine and were quickly moved into the higher pressure rig for ultrasonic and electrical measurements.

Figure 3.9. A picture showing samples being evacuated in the saturation rig.

Once the sample was fully saturated the confining pressure was first loaded to 65 MPa and elastic and electrical measurements were made almost simultaneously at unloading steps of 65, 45, 31, 25, 20 and 13 MPa while the pore pressure was kept at 5 MPa. The sample was left to equilibrate for at least 1 hour before measurements between each pressure step. The first 4 samples (Berea, BP AX, BP AY and BP AZ1)

were measured at 31, 25, 20 and 13 MPa confining pressure only. Figure 3.10 shows the equipment during one of the measurement runs.

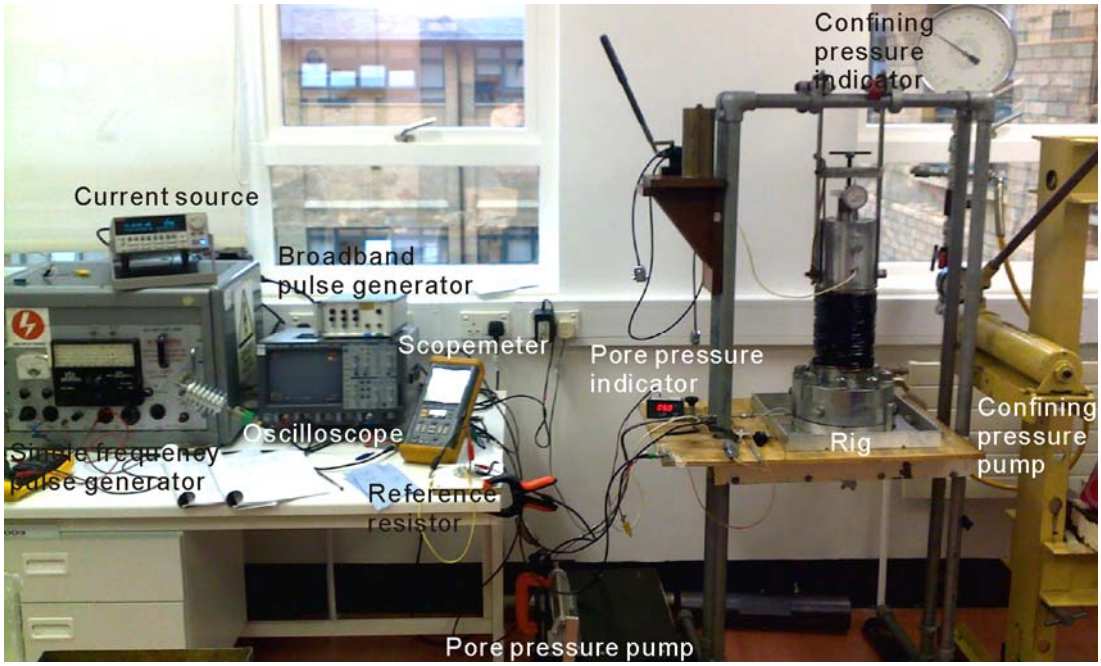

Figure 3.10. A picture showing the joint elastic-electrical measurement equipment.

Ultrasonic compressional and shear wave velocity and attenuation were measured at the frequency of 1.0 MHz and 0.7 MHz respectively while broadband (0.4 – 1.0 MHz) pulses were also recorded for both P- and S-waves. The ultrasonic signals were displayed and saved by a digital storage oscilloscope (DSO, LeCroy 9314AM). The travel times and amplitudes of the equivalent cycles of the single frequency reflection arrivals were recorded by hand on the DSO for future data processing.

A Keithley 6221 current source generated and applied a constant alternating current to the sample (RMS value of 1.0 mA but some cases 0.5 mA was used for the Chinese samples), and voltages were measured by a Fluke 92 scopemeter. A frequency of 2 Hz was used in the experiments to simulate the low frequencies used in marine CSEM, but data were also collected at 440 Hz and 50 kHz in an attempt to scope any frequency dependent effects between CSEM and well logging frequencies. The ability of the constant current source to deliver a constant current under different load impedances was monitored by recording the current through a reference resistor (R_f = 100 Ω) connected in series to the sample. It showed that there was a negligible effect at 2 Hz and 440 Hz, but there was a significant deviation from a constant current at 50 kHz for high impedance samples. Also the measurement results at 50 kHz were

strongly dependent on the sample impedance (see Appendix B) making the data lack accuracy.

The experiments were carried out in a temperature-controlled laboratory (19 ± 1 ºC) to minimize the effect of temperature change on the results.

3.5. Data processing

The raw data acquired from the experiments were in the form of arrival times and amplitudes for the ultrasonic single frequency measurements, and voltages for the electrical measurements, respectively. It was therefore necessary to process the raw data to arrive at the values of elastic velocity and quality factor and electrical resistivity needed for the following analyses.

3.5.1. Elastic velocity and attenuation

Although both single frequency and broadband signals were recorded, I chose to analyse the single frequency data only. The single frequency method was shown to give very accurate and repeatable velocity and attenuation measurements by McCann and Sothcott (1992).

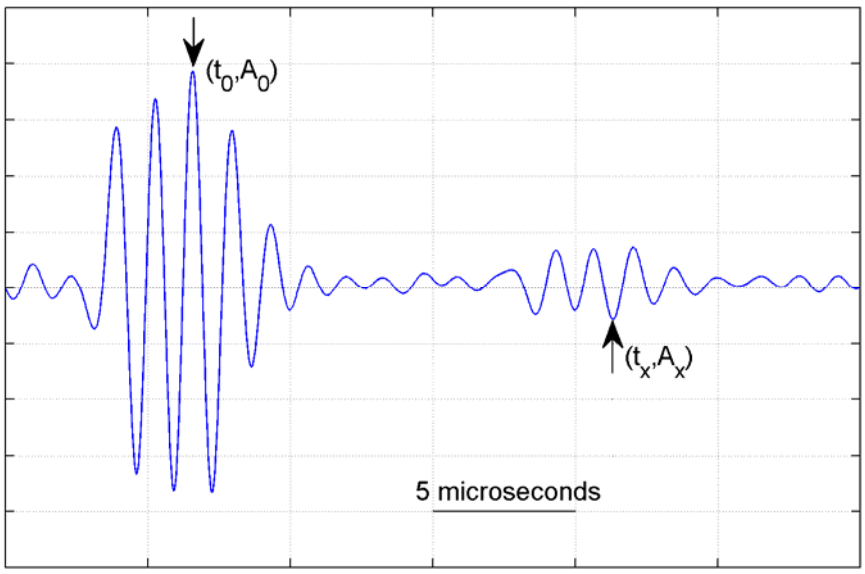

Figure 3.11. An example of a single frequency tone burst signal showing the reflections from the top (A) and base (B) of the sample in Figure 3.3.

The recorded arrival times and amplitudes of the equivalent cycles of the reflections from the top and base of the samples were t_0, A_0 and t_x, A_x (Figure 3.11). The elastic velocity of the rock sample V_r (in m/s) was calculated from the time difference (in μs) between the two reflected arrivals and the sample thickness x (in cm; measured at 7 different points to ensure that it was the same thickness within the required accuracy of ± 5 μm):

$$V_r = \frac{2x}{t_x - t_0 + \Delta t} \times 10^4, \tag{3.1}$$

where Δt was the diffraction correction (Best, 1992) for the difference in travel time between the top and base reflections.

Attenuation coefficient $\alpha(\omega)$ (in dB/cm) at the angular frequency ω (in radians/s) was calculated by comparing the amplitudes of the two reflected pulses (Klimentos and McCann, 1990; Best *et al.*, 1994):

$$\alpha(\omega) = \frac{8.686}{x} \cdot \ln[\frac{A_0(\omega)}{A_x(\omega)} \cdot (1 - R^2(\omega))], \tag{3.2}$$

where $R(\omega)$ was the reflection coefficient (perplex buffer rod to rock sample) at this frequency:

$$R(\omega) = \frac{d_r V_r(\omega) - d_p V_p(\omega)}{d_r V_r(\omega) + d_p V_p(\omega)}, \tag{3.3}$$

where d_r and d_p were the density of the rock sample and perplex buffer rod (both in kg/m^3) respectively, and $\omega = 2\pi f$, where f was the temporal frequency in Hz.

The quality factor $Q(\omega)$ of the sample was then determined by

$$Q(\omega) = \frac{\omega}{2\alpha(\omega)V_r(\omega)}. \tag{3.4}$$

The accuracy of the elastic velocity and attenuation coefficient measurements for the dual P/S transducer that was used are ± 0.3% and ± 0.2 dB/cm, respectively (McCann and Sothcott, 1992; Best, 1992).

3.5.2. Electrical resistivity

The wide electrode resistance of the samples was obtained through Ohm's law, given by

$$R_w = \frac{U_w}{U_r / R_r}, \tag{3.5}$$

where U_w was the wide electrode voltage, and U_r and R_r were the voltage and resistance of the reference resistor respectively. The narrow electrode resistance R_n was similarly calculated by replacing U_w with the narrow electrode voltage U_n in equation 3.5. The 12 wide and narrow electrode resistances were averaged respectively on the assumption of a homogeneous sample to get the final resistances of the wide and narrow electrodes respectively.

Figure 3.12. Brine calibration cell showing the configuration of the electrodes with exactly the same geometry as in the high pressure rig.

The calculation of electrical resistivity from the resistance required knowledge of the geometric factors associated with the wide and narrow electrode pairs. The complicated shape of the configuration meant that it was easiest to obtain the geometric factors through the use of a calibration cell on a range of brine solutions of known resistivities. Hence, a brine calibration cell (Figure 3.12) was made using identical electrodes and geometrical layout (diameter and length) to the high pressure cell for the sandstone samples. The cell was filled with brines of known salinity (the electrical resistivity of which was measured using a Wenner array setup by Ellis, 2008); the brine cell resistance was measured in the manner described in the above

section at the same temperature (19 ± 1 °C) as in the high pressure rig. The calibration results on the series of brines are given in Table 3.2.

Table 3.2. Sample numbers, salt content and resistance of the brine samples measured in the resistivity calibration cell (between two sets of electrodes) and known resistivity at 19 °C. Values given for the resistance are averaged over orientations around the cell as seen in Figure 3.12. The electrical resistance was measured at 2 Hz.

Brine sample number	Salt content (g/l)	Wide electrode resistance (Ω)	Narrow electrode resistance (Ω)	Resistivity (Ωm)
1	20.00	14.13	5.85	0.385
2	8.00	32.90	13.45	0.825
3	6.00	43.20	17.75	1.079
4	4.00	61.85	25.30	1.497
5	2.00	120.20	49.10	2.922
6	1.00	231.58	94.78	5.515

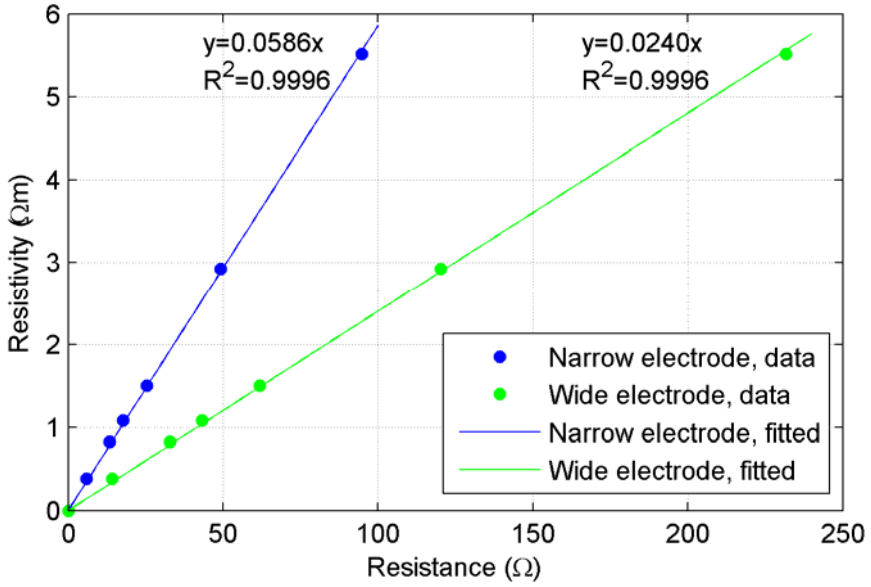

Figure 3.13. Resistivity calibration curves and geometric factors for 2 Hz frequency (after Ellis, 2008).

The geometric factors for the wide and narrow electrodes were then determined by cross-plotting the known resistivity for each brine concentration with the measured resistance for the electrode pairs in the brine cell (Figure 3.13). Geometric factors are

$$\rho = 0.0586 R_n, R^2 = 0.9996, \tag{3.6}$$

$$\rho = 0.0240 R_w, R^2 = 0.9996, \tag{3.7}$$

for the narrow and wide electrode pairs of the 2 Hz frequency respectively.

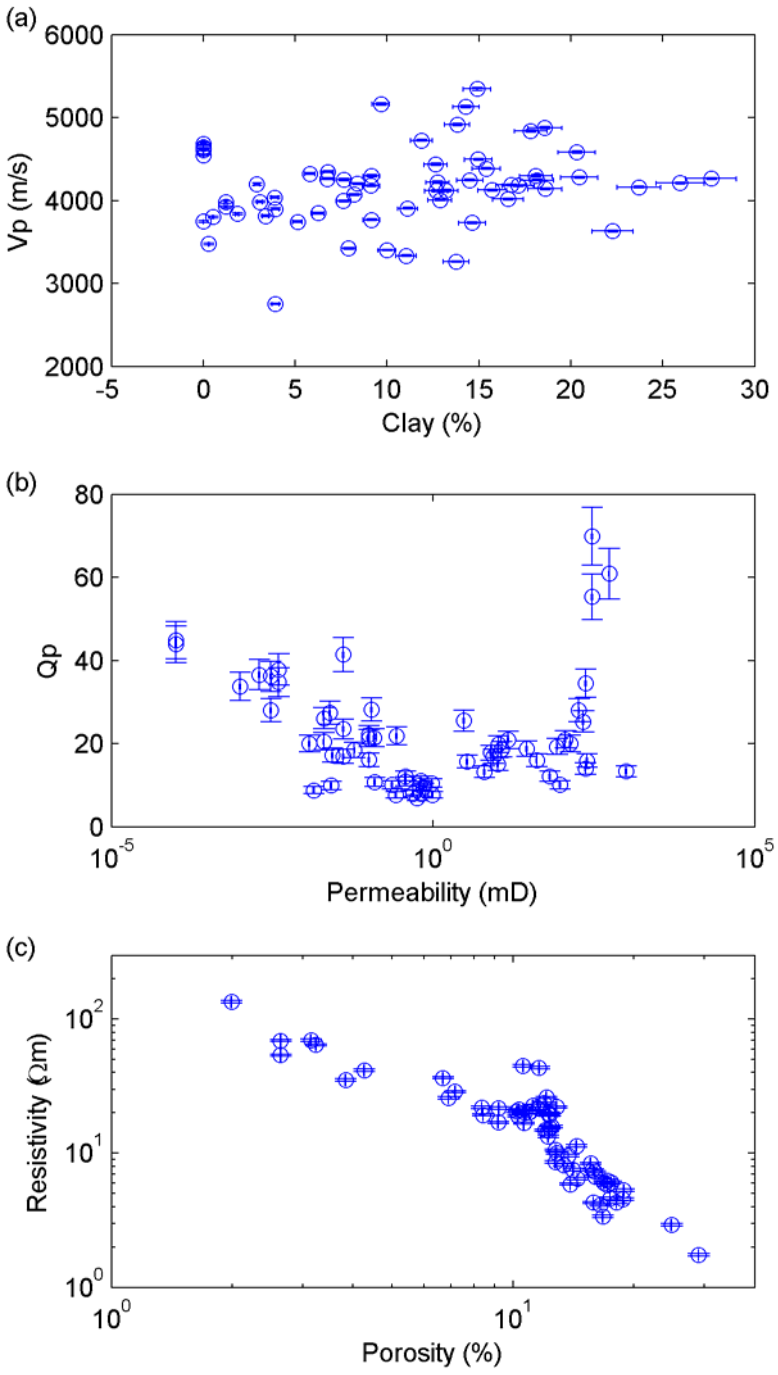

Figure 3.14. Relationships between (a) P-wave velocity and volumetric clay content, (b) P-wave quality factor and permeability and (c) resistivity and porosity with error bars given in the main text.

Rock resistivity was then calculated from the measured resistance through these two geometric factors for each frequency and the result averaged. The error of the final resistivity came from the errors of the measured resistance and the resistivity-resistance calibration correlations, whereas the resistance measurement error was a function of the errors of the voltage (± 1.25%) and current (± 0.05%) measurements. By using the error transmission equation

$$\Delta y = \sqrt{(\frac{\partial f}{\partial x_1})^2 \Delta x_1{}^2 + (\frac{\partial f}{\partial x_2})^2 \Delta x_2{}^2 + ... + (\frac{\partial f}{\partial x_n})^2 \Delta x_n{}^2} \qquad (3.8)$$

where $y = f(x_1, x_2, ..., x_n)$, and Δ represents the absolute error of each variant, the accuracy of the circumference resistivity measurement method was estimated to be better than ± 2%. Figure 3.14 gives an example of the cross plot between key parameters with error bars.

3.6. Summary of datasets collected

A large joint elastic-electrical dataset was successfully collected on 67 reservoir sandstone samples showing a wide range of petrophysical properties at differential pressure form 8 MPa to 60 MPa. Elastic velocity and attenuation were measured using the ultrasonic reflection system to accuracy of ± 0.3% and ± 0.2 dB/cm, respectively. Electrical resistivity was measured using a four-electrode circumference resistivity system at frequency of 2 Hz to an accuracy of ± 2%, where stainless steel electrodes showed negligible polarisation effects and the current source exhibited a good ability to transmit a constant current.

This novel, large, accurately determined dataset enables the relationships among low frequency (2 Hz) electrical resistivity (as well as ultrasonic velocity and attenuation), sandstone porosity, clay content and permeability to be investigated. It also allows the pressure effects on the joint elastic-electrical properties of reservoir sandstones and the joint elastic-electrical properties of reservoir sandstones and their relationships with petrophysical parameters to be studied. It also forms the basis of checking the validity and reliability of a 3-phase effective medium model developed for this project. The specific analyses of the data are presented in Chapters 4, 5, 6 and 7 respectively.

Chapter 4

Relationships among low frequency (2 Hz) electrical resistivity, porosity, clay content and permeability in reservoir sandstones

This chapter forms a paper submitted for publication to *Geophysics*, Han T., Best A.I., Sothcott J., North L.J. and MacGregor L.M. 2010. Relationships among low frequency (2 Hz) electrical resistivity, porosity, clay content and permeability in reservoir sandstones.

Abstract: The improved interpretation of marine controlled source electromagnetic (CSEM) data requires knowledge of the inter-relationships between reservoir parameters and low frequency electrical resistivity. Hence, the electrical resistivities of 67 brine (35 g/l) saturated sandstone samples with a range of petrophysical properties (porosity from 2% – 29%, permeability from 0.0001 mD – 997.49 mD and volumetric clay content from 0 – 28%) were measured in the laboratory at a frequency of 2 Hz using a four-electrode circumference resistivity method with an accuracy of ± 2%. The results show that sandstones with porosity higher than 9% and volumetric clay content up to 22% behave like clean sandstones and follow Archie's law for a brine concentration of 35 g/l. By contrast, at this brine salinity, sandstones with porosity less than 9% and volumetric clay content above 10% behave like shaly sandstones with non-negligible grain surface conductivity. A negative, linear correlation was found between electrical resistivity and hydraulic permeability on a logarithmic scale. We also found good agreement between our experimental results and a clay pore blocking model based on pore-filling and load-bearing clay in a sand/clay mixture, variable (non-clay) cement fraction and a shaly sandstone resistivity model. The model results indicate a general transition in shaly sandstones from clay-controlled resistivity to sand-controlled resistivity at about 9% porosity. At such high brine concentrations, no discernible clay conduction effect was observed above 9% porosity.

4.1. Introduction

Electrical resistivity prospecting is an important and long-established geophysical survey method. Borehole electrical resistivity logging has been widely used with great success in the hydrocarbon industry for decades. In recent years, the rapid development of marine controlled source electromagnetic survey methods (Young and Cox, 1981; Sinha *et al*., 1990; MacGregor and Sinha, 2000; Constable and Srnka, 2007) has renewed interest in the low frequency (< 10 Hz) resistivity of reservoir rocks for improved data inversion and interpretation.

The empirical equation of Archie (1942) (equation 2.26) is well known for relating the conductivity (the reciprocal of resistivity) of the bulk rock to that of the electrolyte

(fluid) within the rock pores and to the rock porosity by $\frac{\sigma_w}{\sigma_0} = \varphi^{-m}$ for clean sandstones, where: σ_0 is the conductivity of the rock fully saturated with an electrolyte of conductivity σ_w; φ is the rock porosity and m is the cementation coefficient. The latter is related to lithology, grain shape and size and the degree of connectedness of the pore network (Jackson *et al*., 1978; Salem and Chilingarian, 1999; Glover, 2009) and has various values for different lithologies.

Archie's equation (equation 2.26) is known to give good predictions of the resistivity of clean sandstones but gives poor results for shaly sandstones which contain significant amounts of clay minerals (Cohen, 1981). Several models have been proposed to account for the surface conductivity associated with clay minerals (e.g., Simandoux, 1963; Waxman and Smits, 1968; Clavier *et al*., 1984; Sen and Goode, 1988; de Lima and Sharma, 1990; Glover *et al*., 1994; Tenchov, 1998; Revil *et al*., 1998; Revil and Leroy, 2001; Rabaute *et al*., 2003). However most of these models relate to high frequency (~ 50 kHz) well logging data analysis. There is a need for a systematic experimental study of resistivity at low frequency (< 10 Hz) and high brine salinity ($\sigma_0 >> \sigma_w$) to verify these models for use in CSEM surveying. Although some theoretical models account for frequency-dependent electrical properties of shaly sandstones (e.g., de Lima and Sharma, 1992; Leroy *et al*., 2008; Leroy and Revil, 2009), there is still a need for new experimental data to test such models. In addition to clay surface conductivity issues, clay minerals in sandstones also affect porosity in a systematic manner (Marion *et al*., 1992; Sams and Andrea, 2001; Rabaute *et al*., 2003), and hence affect electrical resistivity as porosity is the first order parameter in controlling electrical resistivity when other parameters are kept the same. This combined clay-porosity influence makes the interpretation of resistivity data complicated.

This chapter focuses on the effects of some reservoir parameters (i.e., pressure, porosity, clay content and permeability) on the low frequency (2 Hz) electrical resistivity behaviour of 67 typical sandstones saturated with a relatively high salinity brine (35g/l NaCl). We compared the data to existing theoretical models for shaly sandstones, and found it necessary to develop a clay-blocking resistivity model to explain the experimental observations.

4.2. Experimental results

4.2.1. Pressure dependence

All rocks showed a general trend of increasing resistivity with increasing differential pressure. The example in Figure 4.1 shows the measured change in resistivity with differential pressure normalized to the resistivity at 8 MPa. This has been noted by other researchers (e.g., Fatt, 1957; Glanville, 1959; Brace *et al*., 1965; Brace and Orange, 1968; Timur *et al*., 1972; Jing, 1990; Mahmood *et al*., 1991).

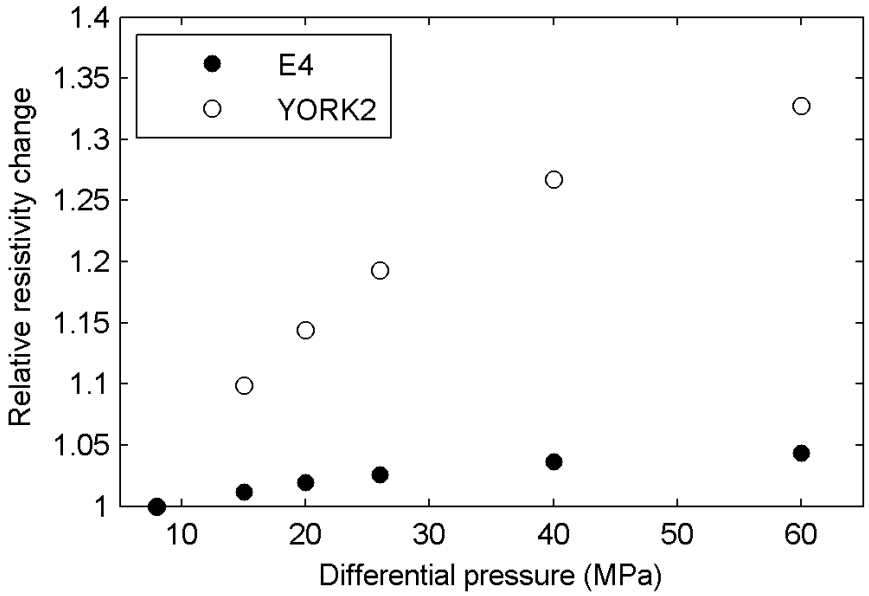

Figure 4.1. Relative electrical resistivity change with differential pressure. Example plots for samples E4 (a clean sandstone) and YORK2 (a clay-rich sandstone). Relative resistivity change corresponds to the normalized resistivity at each differential pressure by the resistivity measured at 8 MPa.

In general, the clay-rich sandstones (microstructural images of a typical sample given in Figure 4.2) show greater pressure sensitivity than the clean sandstones (microstructural images of a typical sample given in Figure 4.3) and this is thought to be caused by the closure of low aspect ratio pores (e.g., Glover *et al*., 2000) located at grain contacts and associated with clay minerals, with increasing pressure. The closure of these low aspect ratio conduits connecting open pores leads to a reduction in the number of conductive pathways through the framework of solid mineral grains saturated by electrolyte.

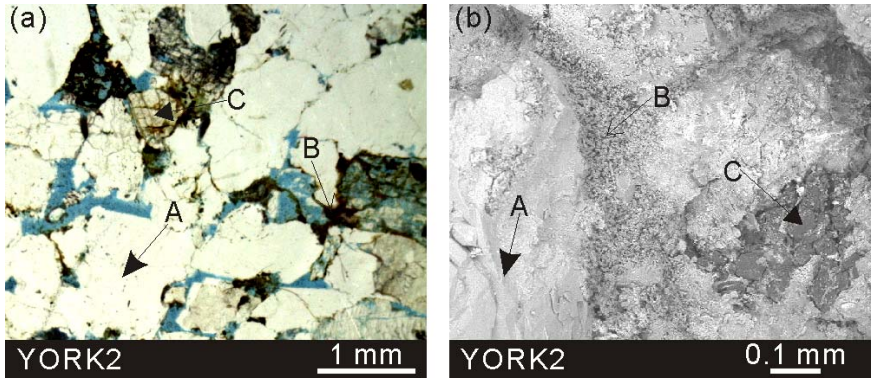

Figure 4.2. Example images of a typical clay-rich sandstone (sample YORK2) showing quartz (A) and feldspar (C) grains with pore-filling clay (B). (a) thin section, (b) SEM image.

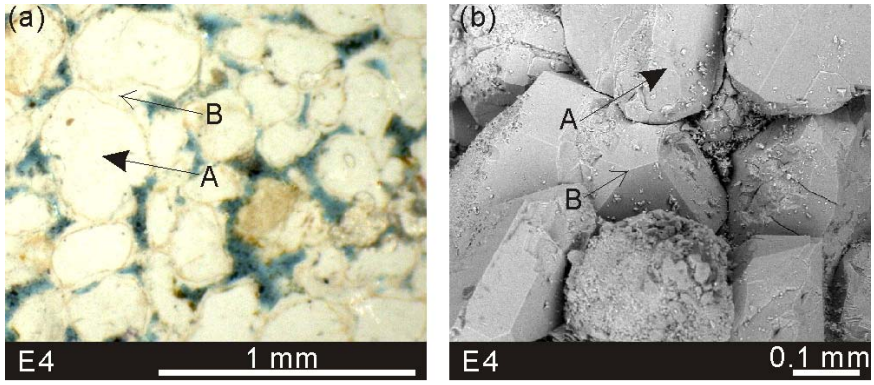

Figure 4.3. Example images of a typical clean sandstone (sample E4) showing quartz grains (A) and cement in terms of quartz overgrowth (B). (a) thin section, (b) SEM image.

Having noted similar trends for electrical resistivity with differential pressure, we will restrict further discussion of our results to a differential pressure of 26 MPa (as the Berea and the three BP samples were measured only to a differential pressure of 26 MPa, this gives the maximum number samples and also 26 MPa is a representative pressure of shallow reservoirs); these values are given in Appendix D. Further analysis of pressure effects is the subject of Chapter 5.

4.2.2. Resistivity and porosity

Figure 4.4 shows a cross-plot of the apparent formation factor F^* (defined as ρ_0/ρ_w, where ρ_w = 0.213 Ωm for 35 g/l brine at a temperature of 19 °C) and porosity φ by colour-coding volumetric clay content on a log-log scale for all 67 sandstones at 26 MPa and frequency of 2 Hz. It is striking that two major, adjoining, approximately linear trends can be seen with an inflexion point at a porosity of about 0.09. Samples in Group 1 (solid circles) have porosities higher than about 0.09; samples in Group 2

(solid squares) have porosities lower than about 0.09. A third, minor, linear trend is also seen that partially coincides with Group 1, shown by the open circles; these samples have a porosity from about 0.11 to 0.13. These Group 3 samples were chosen because they all contain kaolinite unlike any of the other samples (see below).

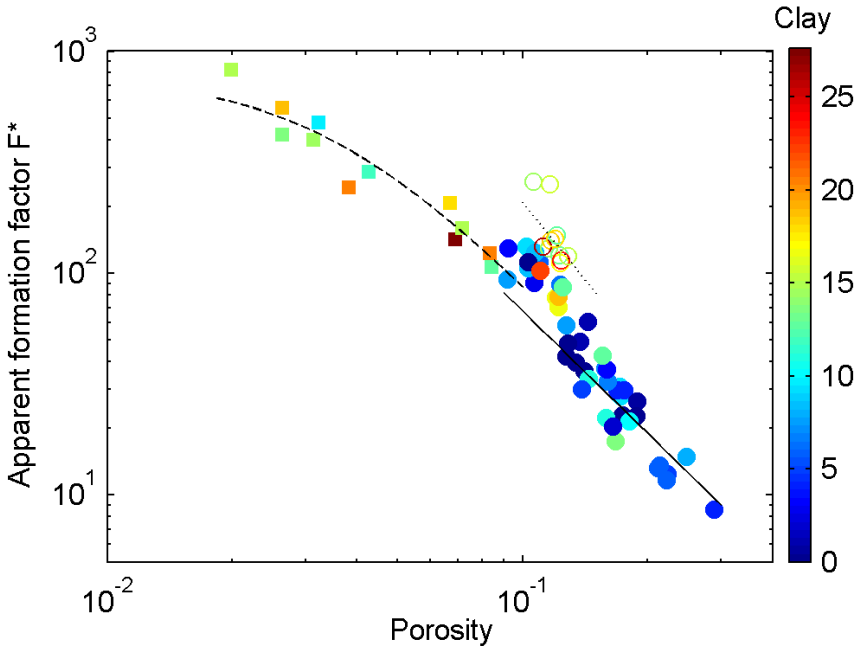

Figure 4.4. Apparent formation factor (AC 2 Hz) against porosity at 26 MPa differential pressure for the 67 brine-saturated sandstone samples by colour-coding volumetric clay content on a log-log scale. Samples are divided into three groups (solid circles for Group 1, solid squares for Group 2 and open circles for Group 3) with best fitted curves form the model of Archie (1942) for Groups 1 and 3 (solid and dotted lines respectively) and de Lima and Sharma (1990) for Group 2 (dashed curve).

It turns out that very good correlation coefficients ($R^2 > 0.9$) result from linear least-squares regression of the Groups 1 and 2 samples in Figure 4.4 using an equation of the form $y = A \cdot x^{-B}$, where A and B are arbitrary constants and x, y represent porosity and apparent formation factor, respectively. However, this form of equation is at odds with current theoretical thinking on modelling resistivity in shaly sandstones (e.g., Glover, 2009). In any case, we provide all the data in Appendix D for the purpose of developing and testing rock physics models by the wider scientific community.

Hence, to interpret the experimental data in terms of the three groups and remain consistent with current theoretical knowledge, we chose to implement the shaly sandstone conductivity model of de Lima and Sharma (1990) for high salinity limit, given by

$$\sigma_0 = \frac{1}{F}[\sigma_w + m(F-1)\sigma_s], \tag{4.1}$$

where $F = \varphi^{-m}$ is the intrinsic formation factor (de Lima and Sharma, 1990; Revil *et al*., 1998; Revil and Cathles III, 1999; Rabaute *et al*., 2003; Lee and Collett, 2006) of a rock, m is Archie's cementation coefficient and σ_s is the surface conductivity. Integrating $F = \varphi^{-m}$ into equation 4.1 it can be expressed more explicitly as

$$\sigma_0 = \varphi^m[\sigma_w + m(\varphi^{-m} - 1)\sigma_s]. \tag{4.2}$$

The parameters m and σ_s are solved by best fitting equation 4.2 to each group defined in Figure 4.4 using least-squares regression assuming samples in each group have similar cementation coefficients:

$$\text{Group 1: } m = 1.639,\ \sigma_s = -0.046 \text{ S/m, with } R^2 = 0.904, \tag{4.3}$$

$$\text{Group 2: } m = 1.989,\ \sigma_s = 0.003 \text{ S/m, with } R^2 = 0.937, \tag{4.4}$$

$$\text{Group 3: } m = 2.105,\ \sigma_s = -0.009 \text{ S/m, with } R^2 = 0.492. \tag{4.5}$$

The negative values of surface conductivity σ_s in Groups 1 and 3 are not physically realizable and we take this to indicate negligible grain surface conductivity ($\sigma_s = 0$) in these samples. Setting $\sigma_s = 0$ reduces equation 4.2 to Archie's equation (equation 2.26). The best fit of Archie's equation (solid and dotted lines for Groups 1 and 3 respectively in Figure 4.4) to these two groups is therefore performed where the cementation coefficient is the only variable:

$$\text{Group 1: } m_1 = 1.828, \text{ with } R^2 = 0.860, \tag{4.6}$$

$$\text{Group 3: } m_3 = 2.319, \text{ with } R^2 = 0.445. \tag{4.7}$$

The lower correlation coefficients for the 11 samples in Group 3 are possibly due to the smaller porosity range covered by these samples. Hence, we will focus on the samples in Group 1 and Group 2 in the following analysis.

Although small ($\sigma_s = 0.003$ S/m), the positive surface conductivity value for samples in Group 2 indicates that surface conductivity does make contributions to the bulk conductivity in addition to the electrolyte conductivity in these samples. In Figure 4.5 we plot the expected bulk conductivity change with varying pore fluid conductivity for porosities of 0.1 and 0.02 (which bracket the porosities of all Group 2 samples) using the parameters defined in equation 4.4. We see in both cases that the bulk

conductivity for a 35 g/l brine electrolyte (σ_w = 4.6948 S/m, indicated by the open circle and open square respectively) deviates from Archie's trend (dotted lines) and thus confirms that surface conductivity is significant in these samples. Therefore using equation 4.2 with parameters m_2 = 1.989 and σ_{s2} = 0.003 S/m (the dashed curve in Figure 4.4) gives the best fit to samples in Group 2.

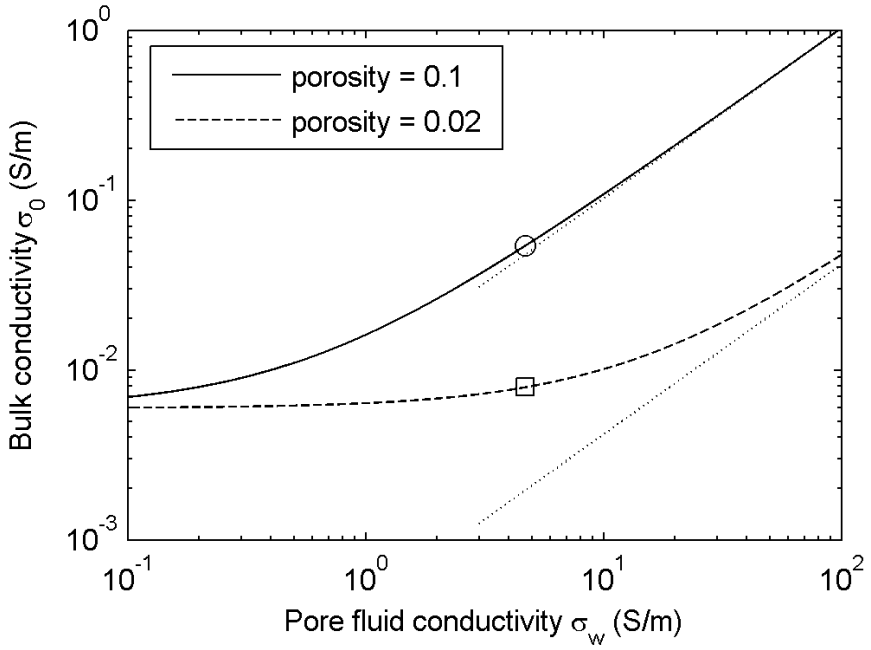

Figure 4.5. Expected bulk conductivity change with varying pore fluid conductivity from the shaly sandstone model of de Lima and Sharma (1990) for a sample with porosity of 0.1 (solid curve) and 0.02 (dashed curve) respectively using best fitted parameters to samples in Group 2, m_2 = 1.989, σ_{s2} = 0.003 S/m. The bulk conductivity using 35 g/l brine (open circle and square) deviates from Archie's trend (dotted lines) for both cases.

4.2.3. Salinity effects

According to Worthington (1982), 'during the course of electrical measurement under conditions of full electrolyte saturation, any given lithology can exhibit both negligible and highly significant shale effects depending upon the resistivity of the interstitial aqueous electrolyte'. The dependence of this so-called clay effect on brine salinity (and so brine resistivity) has been studied by Patnode and Wyllie (1950), Wyllie and Southwick (1954), Waxman and Smits (1968), Rink and Schopper (1974) and Worthington (1982). The last author nominated a critical value of brine resistivity below which the particular clay content used in each of the above studies shows a

negligible conductive effect. By contrast, our results suggest a critical clay content (we call it critical clay conductive content below), above which the sandstones saturated with a particular salinity brine show a significant conductive effect. This is a similar concept to that of Worthington (1982) but expressed from the perspective of clay content as opposed to electrolyte salinity. Brines in a specific sandstone reservoir will tend to keep the same salinity on exploration timescales, so whether clay exhibits a non-negligible conductive effect or not will depend on whether sandstone clay content is below or above the critical clay conductive content for that particular brine concentration, providing other reservoir parameters stay the same (e.g., differential pressure and temperature).

It appears that for the 44 sandstones in Group 1 saturated with 35 g/l brine at a differential pressure of 26 MPa and a temperature of 19 °C, the clay content does not reach the critical clay conductive content value as samples in this group still follow Archie's trend. In other words, in our experiments, the critical clay conductive content for the clay conduction effect is above the highest clay content of about 22% for Group 1 samples with porosity higher than 0.09. However, for the 12 sandstone samples in Group 2 with porosity less than about 0.09, even the lowest volumetric clay content (about 10%) shows a non-negligible conductive effect indicating that the critical clay conductive content for these samples is lower than 10%. These observations suggest that porosity is the first order parameter that affects resistivity while clay has a secondary effect that also depends on porosity.

It is interesting to note that for most Group 1 samples, clay content is less than the percentage porosity, while the opposite is true for all samples in Group 2 as shown in Figure 4.6 by normalizing clay content with porosity percentage for the samples that contain some clay. This suggests a possible way to connect electrical properties to elastic wave velocity relationships according to pore-filling or load-bearing clay in clay/sand mixtures (Marion *et al*., 1992). Figure 4.6 also shows that samples in all 3 groups fall along the same trend of apparent formation factor versus clay content/porosity ratio (although with some scatter, especially in Group 1); this indicates a broadly similar clay effect on electrical resistivity per unit porosity (the trend line) for the 3 groups. This differs from the shaly sandstone model of Revil *et al*. (1998) that shows a decrease in resistivity with clay/porosity ratio. While Revil *et al*. (1998) used a single cementation coefficient of 2 in their model; we have already

shown for our dataset that sandstones can be grouped according to different cementation coefficients. Hence, in addition to clay grain surface conductivity effects (Revil *et al*., 1998; Glover, 2009), the presence of clay minerals also affects the cementation coefficient (related to the connectivity of pore spaces; Glover, 2009) which in turn influences resistivity.

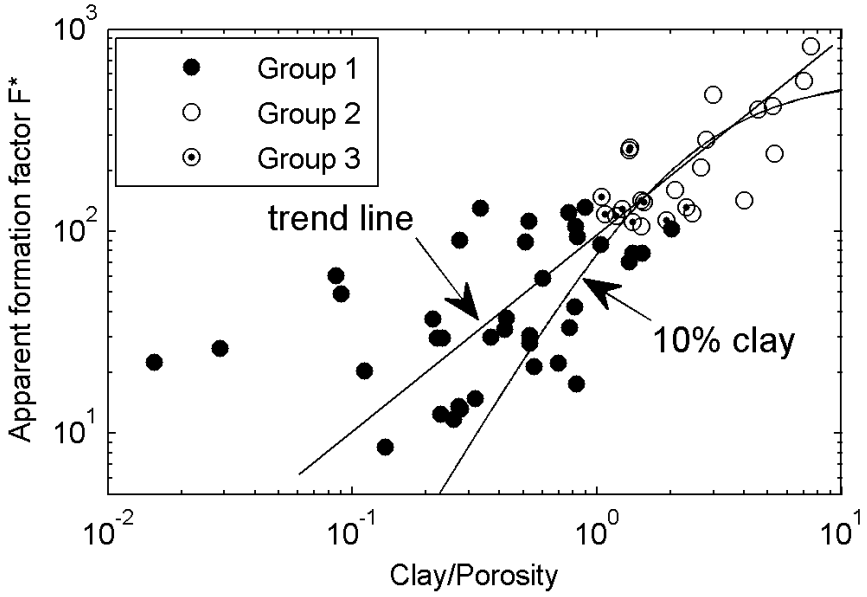

Figure 4.6. Electrical resistivity formation factor against the ratio of volumetric clay content to the porosity percentage for the 67 brine-saturated sandstone samples in the 3 groups defined in Figure 4.4 at 26 MPa differential pressure. The shaly sandstone model of Revil *et al*. (1998) for 10% illite is compared to our data.

The fact that porosity percentage is higher than clay content in Group 1 samples (i.e., pore filling clays do not occupy all the available cemented sand grain framework porosity) indicates that the overall connected porosity in Group 1 sandstones is dominated by the geometry of the cemented sand grain framework. By contrast, the opposite is true for Group 2 sandstones where porosity percentage is lower than the clay content (hence, all cemented sand grain framework porosity is filled by clay minerals assemblages with their associated connected microporosity). This means that the connected porosity in Group 2 samples is dominated by the geometry of clay mineral assemblages. The wider scatter about the trend for Group 1 samples in Figure 4.6 might be related to different amounts of sand grain overgrowth cement (non-clay, e.g., silica or calcite), while the dominance of clay porosity gives less scatter about the trend for Group 2 samples (i.e., the trend is independent of sand grain overgrowth cement).

The above observations provide evidence for the dominance of purely geometric effects on pore connectivity and hence resistivity of high salinity reservoir sandstones.

4.2.4. Resistivity and clay content

Apparent formation factor F^* measured at 2 Hz versus volumetric clay content for all 67 samples is shown in Figure 4.7a on a log-log scale. Apparent formation factor F^* shows a general decreasing trend with increasing clay content for samples in Group 2, but shows an increasing trend with clay content for most samples in Group 1, although with a larger scatter. The increase in resistivity with clay content for Group 1 samples contradicts conventional knowledge about the clay conductive effect in terms of surface conductivity (e.g., Simandoux, 1963; Waxman and Smits, 1968; Clavier *et al*., 1984; de Lima and Sharma, 1990; Revil and Leroy, 2001), but could be a result of the geometry of clay mineral assemblages controlling the Archie cementation coefficient (e.g., Revil *et al*., 1998). However, the correlation between resistivity and clay content observed in our samples is strongly related to the relationship between porosity and clay content shown in Figure 4.7b. Here, porosity (the first order parameter that affects resistivity) appears to decrease with clay content for samples in Group 1 but increase with clay content for samples in Group 2.

The opposite effects of clay content on porosity for samples in different groups can be interpreted using Yin's critical porosity concept (Yin, 1993), which states the inclusion of clay minerals into sand will initially lead to a decrease in porosity as clay minerals fill the pores between sand grains (pore-filling) and the porosity decreases to its minimum value (known as the critical porosity value) when volume clay fraction reaches the 'critical clay concentration' (we will call it critical clay blocking concentration from now on to avoid confusion with the critical clay conductive content mentioned earlier) that equals the porosity of the cemented sand grain framework. Note the difference between this volume clay fraction C and the volumetric clay content V_{clay} definition used in the context. The volumetric clay content is the percentage volume clay fraction without any clay porosity φ_{clay} associated with clay mineral assemblages, where $V_{clay} = C(1 - \varphi_{clay})$. After the critical clay blocking concentration is reached, any increase in clay with cause the clay mineral assemblages to become load-bearing (in terms of elasticity) while the sand

grains become dispersed in the framework of clay minerals, and will cause a continuous increase in porosity related to the clay mineral assemblage porosity. A diagram of the geometry of a sand-clay mixture with varying clay content used in the model is given in Figure 4 of Marion *et al*. (1992).

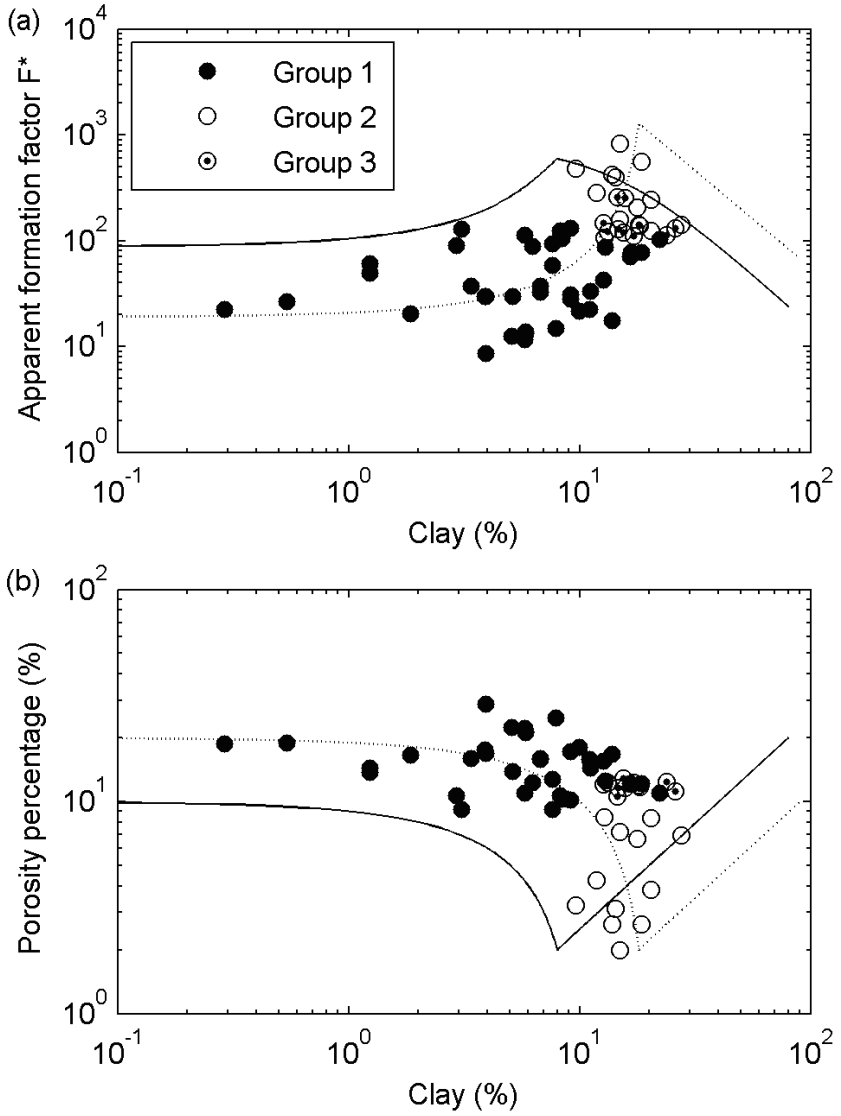

Figure 4.7. (a) Apparent formation factor (AC 2Hz) against volumetric clay content and (b) porosity percentage against volumetric clay content for the 67 brine-saturated sandstone samples in the 3 groups defined in Figure 4.4 at 26 MPa differential pressure. The porosity curves in (b) are calculated from Marion's (Marion *et al*., 1992) porosity model (equations 4.8 to 4.10), and the resistivity curves in (a) are the models integrating the porosity model (equations 4.8 to 4.10) and Archie's (Archie, 1942) equation and the model of de Lima and Sharma (1990) using initial sand porosity 0.4, cementation 0.2, clay porosity 0.1 and m_1 = 1.828 for the dotted curve to model Group 1; and initial sand porosity 0.4, cementation 0.3, clay porosity 0.2 and m_2 = 1.989, σ_{s2} = 0.003 S/m for the solid curve to model Group 2.

Here, we choose to integrate Marion's (Marion *et al*., 1992) clay-porosity model with Archie's (1942) equation and the model of de Lima and Sharma (1990) in an effort to explain the change of resistivity of our sandstones with porosity in Figure 4.4 and with clay content in Figure 4.7a. Since our sandstones comprise cemented sand grains rather than the unconsolidated sand pack of the original model, we assume the volume fraction of cement to be φ_m which reduces the initial porosity of the uncemented sand grain pack φ_{sand}. The expressions for (total) porosity φ based on the initial porosity of the sandstone φ_{sand}, the volume fraction of cement φ_m, the clay porosity φ_{clay}, and the volume fraction of clay C are given as follows.

$$\varphi = (\varphi_{sand} - \varphi_m) - C(1 - \varphi_{clay}) \text{ for } C < \varphi_{sand} - \varphi_m \tag{4.8}$$

$$\varphi = (\varphi_{sand} - \varphi_m)\varphi_{clay} \text{ for } C = \varphi_{sand} - \varphi_m \tag{4.9}$$

$$\varphi = C\varphi_{clay} \text{ for } C > \varphi_{sand} - \varphi_{m.} \tag{4.10}$$

A similar approach was used by Rabaute *et al*. (2003) to predict the porosity of chlorite-bearing sandstones; they then used the effective medium model of Revil *et al*. (1998) to calculate the resistivity. However, the fact that most of our samples are cemented with quartz (or calcite) overgrowths rather than by clay minerals justifies our addition of cement fraction in our model, which distinguishes it from Rabaute's approach (Rabaute *et al*., 2003).

Whereas the clay effect on porosity (clay blocking effect) is accounted for by the model of Marion *et al*. (1992), we use the parameters listed in equations 4.6 and 4.4 for Groups 1 and 2 respectively to plot the expected trends of resistivity versus clay content via porosity caused by the clay-blocking effect. By adjusting the cement fraction φ_m and clay porosity φ_{clay}, it was possible to get a reasonable fit to the data. Note that we are attempting to fit the general observed trends for sandstones with a range of cement fractions when $C < \varphi_{sand} - \varphi_m$ and for sandstones with a range of clay porosities when $C > \varphi_{sand} - \varphi_m$. Each curve is valid strictly only for a constant cement fraction and clay porosity.

In Figure 4.7, $\varphi_{sand} = 0.4$, $\varphi_m = 0.2$ and $\varphi_{clay} = 0.1$ for Group 1 (dotted curve) and $\varphi_{sand} = 0.4$, $\varphi_m = 0.3$ and $\varphi_{clay} = 0.2$ for Group 2 (solid curve). Figure 4.7b also shows that most samples in Group 1 have porosity (%) higher than their volumetric clay content (%) and all samples in Groups 2 and 3 have porosity (%) lower than their volumetric

clay content (%). This is consistent with the results in Figure 4.6 and the concept of pore-filling versus load-bearing clay for clay fraction lower and higher than the critical clay concentration respectively (Marion *et al*., 1992).

In Figure 4.7b, the decreasing trend of porosity (increasing apparent formation factor and resistivity) with volumetric clay content for Group 1 samples suggests that the average volumetric clay content is lower than the average critical clay blocking concentration. By contrast, the increasing porosity (hence decreasing apparent formation factor and resistivity) with clay content for Group 2 samples indicates that the average volumetric clay content is above the average critical clay blocking concentration. Again, we are seeking an explanation for the general observed trends.

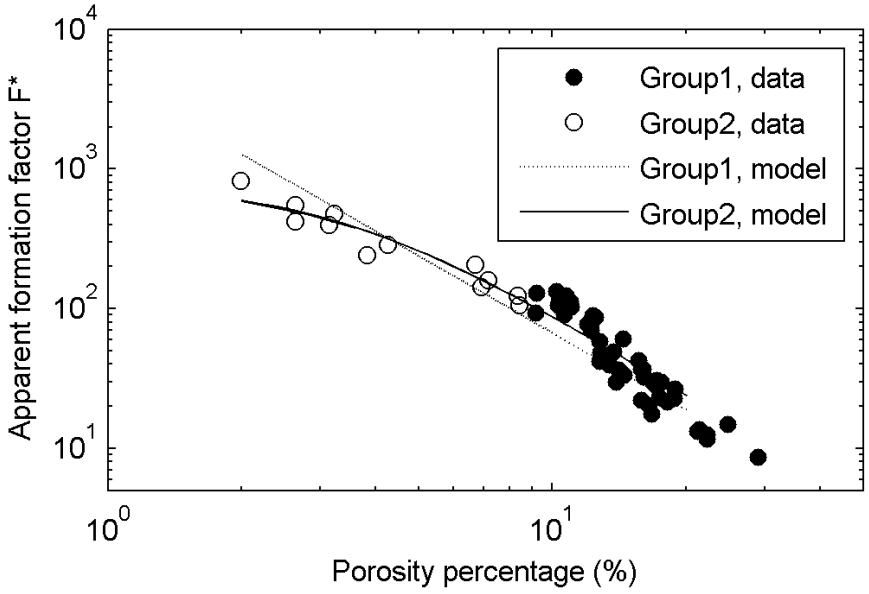

Figure 4.8. Comparison of integrated porosity (Marion *et al*., 1992) and Archie (1942) model and model of de Lima and Sharma (1990) with experimental data for the relationship between apparent formational factor *F** (AC 2 Hz at 26 MPa differential pressure) and porosity percentage. Parameters are the same as used in Figure 4.7.

Figure 4.8 shows the model (using the same parameters as in Figure 4.7) predicted apparent formation factor *F** against porosity for Group 1 and Group 2. According to our clay blocking model trends shown in Figure 4.8 for Group 1 (dotted line) and Group 2 (solid curve), it is theoretically possible for samples with porosity less than 9% to fall along the Group 1 trend and for samples with porosity greater than 9% to fall along the Group 2 trend. In fact, it is possible to adjust the model input parameters (sand porosity, cement fraction, clay porosity) to provide any reasonable range of porosities along each *F** - porosity trend. The key information that was not modelled

is the link between porosity and resistivity (or apparent formation factor F^*); we simply used Archie's law (1942) and de Lima and Sharma (1990) model curve fits to the observations. However, our observations in Figure 4.4 indicate that a 9% porosity cross-over is significant for a wide range of shaly sandstones and most probably marks the transition from a predominantly clay-controlled to a sand-controlled resistivity regime in terms of pore geometry and connectivity.

4.2.5. Resistivity and permeability

Figure 4.9 shows the relationship between apparent formation factor F^* measured at 2 Hz and the permeability (in millidarcies) on a log-log scale. Although there is some scatter, the 67 sandstone samples show a general linear trend (solid line) of decreasing resistivity with increasing permeability K. The least-squares regression equation is

$$\log(F^*) = -0.2100 \cdot \log(K) + 1.8554 \,,\; R^2 = 0.7371. \qquad (4.11)$$

This negatively correlated resistivity-permeability relationship can be interpreted intuitively in terms of the connectivity of pores (and hence of pore fluids for resistivity under fully saturated conditions), i.e., the better the connectivity of the pores, the higher the permeability but the lower the resistivity. The literature shows both a negative (e.g., Wong *et al*., 1984; Frohlich *et al*., 1996) and positive (e.g., Urish *et al*., 1981; Ponzini *et al*., 1983) relationship between resistivity and permeability based on high frequency well logging data. We applied a model from Glover *et al*. (2006) relating permeability to formation factor by $k = \frac{d^2}{4am^2F^3}$, based on a possible electrokinetic approach (see also Revil and Cathles III, 1999 and discussion in Revil, 2007), where d is the grain diameter in meters; a is a constant in the range 2-12 depending upon the topology of the pore space, and is equal to 8/3 for three-dimensional arrangements of quasi-spherical grains; m is cementation coefficient; and F corresponds to intrinsic formation factor. The model result for m = 1.5 and d = 100 μm (dashed line in Figure 4.9) gives a reasonable fit to the experimental data.

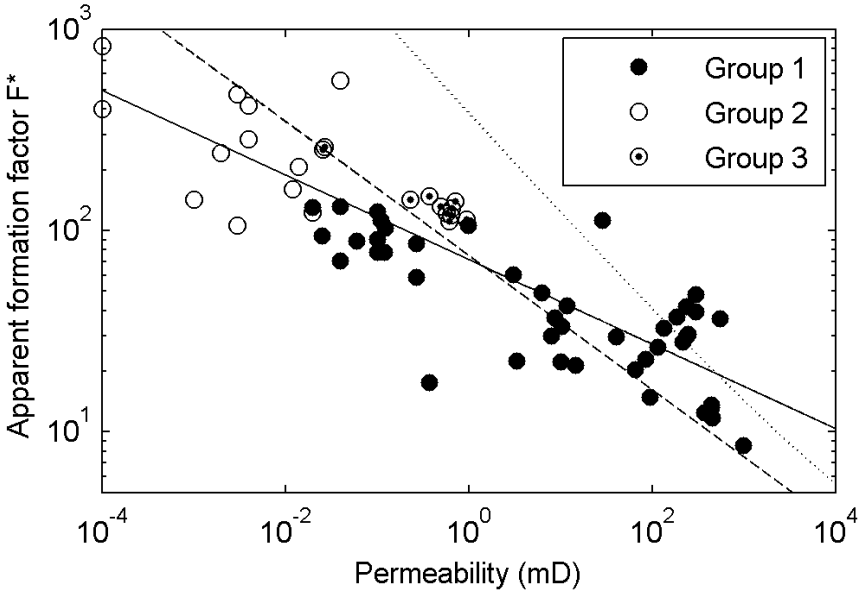

Figure 4.9. Apparent formation factor F^* against permeability for the 67 brine-saturated sandstone samples. Electrical resistivity measured at an AC frequency of 2 Hz and a differential pressure of 26 MPa. The least-squares regression trend (solid) line is: $\log(F) = -0.2100 \cdot \log(K) + 1.8554$, R^2 = 0.7371. Glover's model (Glover *et al*., 2006) is shown by the dashed line.

The apparent formation factor - permeability relationship can also be explained in terms of the Kozeny-Carmen (Kozeny, 1927; Carman, 1937) equation that relates porosity and tortuosity to permeability. Resistivity is some measure of tortuosity for a given porosity, so we might expect resistivity to be closely related to permeability for purely electrolytic conduction of ions. The combination of Archie's equation and the Kozeny-Carmen equation using the same parameters as that used in the model from Glover *et al*. (2006) is shown in Figure 4.9 by the dotted line; however the fit to the experimental data is unsatisfactory.

The relationship between porosity and permeability for all 67 samples is shown in Figure 4.10a together with the Kozeny-Carmen equation using constant hydraulic tortuosity $\tau = 2.5^{1/2}$ (Revil and Cathles III, 1999; Gomez, 2009) with grain diameter d varying from 100 μm to 1 μm. These equations can be used to give a rough estimation of the grain size when no grain size data exist. Figure 4.10b shows a comparison of our data to the permeability model from Glover *et al*. (2006) by using electrical parameters that separate pore throat from total porosity and hydraulic radius. The model predictions bracket the data and indicate likely variations in grain size and their influence on the transport properties of reservoir sandstones.

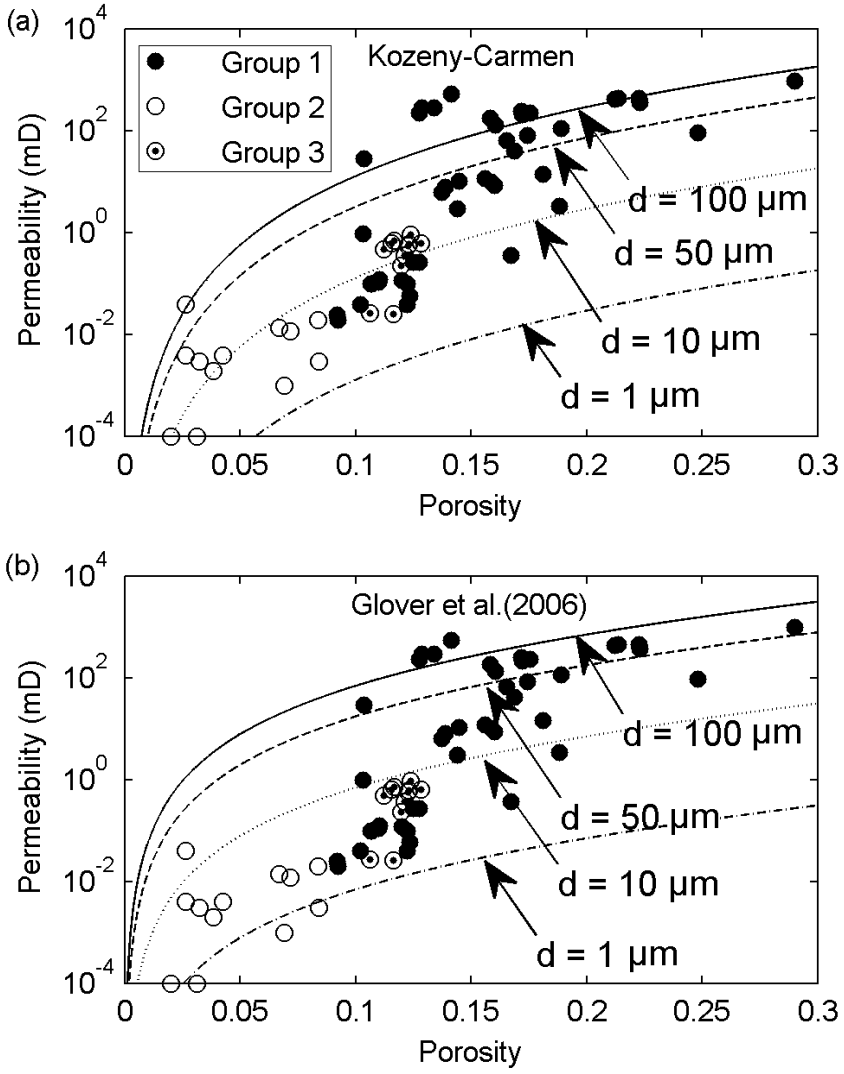

Figure 4.10. Permeability against porosity for the 67 sandstone samples together with (a) Kozeny-Carmen equation and (b) Glover's model with varying grain diameter from 1 μm to 100 μm. The data indicate that sandstones with higher porosities tend to have higher permeabilities.

4.3. Discussion

The root of the so-called shaly-sand problem in hydrocarbon evaluation can be traced to the presence of excess electrical conductivity associated with fine-grained clay minerals (Worthington, 1982). The clay effect is one of the main obstacles to overcome when interpreting resistivity measurements from both conventional well logging and newly developed CSEM methods. Consequently, it is extremely important to understand clay effects when inverting CSEM data with constraints from well logging data.

It is known that there are excess ions associated with clay minerals (e.g., Revil and Glover, 1998) that form thicker fluid double layers than in the case of non-clay minerals (e.g., Revil and Glover, 1997). In theory, this implies that clay-rich sandstones should have lower resistivities than clean sandstones depending on the resistivity of the electrolyte saturating the sandstones; this is the so called clay conductive effect, and several clay conductivity models (e.g., Simandoux, 1963; Waxman and Smits, 1968; Clavier *et al*., 1984; Sen and Goode, 1988; de Lima and Sharma, 1990; Tenchov, 1998; Revil *et al*., 1998; Rabaute *et al*., 2003) have tried to account for it. However, Yin's work (Yin, 1993) indicates that the location and geometry of clay mineral assemblages within a sand/clay mixture also has a profound effect on porosity which in turn affects resistivity (see Figure 4.7); we call this the clay blocking effect. Therefore, the clay effect on electrical resistivity can work in two ways: on the one hand the surface conduction associated with clay minerals provides extra conductive paths, in addition to the normal pore electrolyte conductivity, which leads to a decrease in electrical resistivity (clay conductive effect). On the other hand there is a strong correlation between clay content and porosity; clay minerals in sandstones make the porosity either decrease or increase depending whether clay content is lower or higher than the critical clay blocking concentration (Marion *et al*., 1992), which in turn causes an increase or decrease in resistivity (clay blocking effect).

The clay conductive effect and clay blocking effect operate simultaneously and the final resistivity of a sandstone that contains clay minerals will depend on whether the clay conductive or the clay blocking effect prevails.

If the porosity of clay-rich sandstones is high enough when saturated with low resistivity electrolyte, then the conduction of electrical current takes place through the more conductive electrolyte rather than via the clay double layer; in this case the clay minerals can be treated as insulators similar to quartz grains and they show a negligible conductive effect. When the differential pressure increases, the electrolyte is expelled from shrinking low aspect ratio pores and microcracks; this reduces ionic conduction through the electrolyte and increases the proportion of clay surface conduction. As pressure increases, or as porosity reduces due to cementation, or as the salinity of the electrolyte decreases, the clay conductive effect may overtake the clay

blocking effect and lead to resistivity deviations from Archie's equation (equation 2.26).

On the other hand, for samples with increasing clay content, the clay effect depends largely on the electrolyte resistivity. One limit of behaviour, for example, would be a sample saturated with electrolyte of low enough resistivity (e.g., a very high salinity brine) when clay for all porosities can be regarded as an insulator with negligible surface conduction taking place through the clay double layer compared to the bulk pore fluid conduction; here, the addition of clay shows a purely blocking effect. The resistivity change of the sandstone therefore follows the clay-porosity trend (Yin, 1993) but in an inverse manner; that is, the resistivity increases first with increasing clay content and reaches its peak value when clay content arrives at a critical clay blocking concentration. Afterwards, the resistivity reduces with increasing clay content. This behaviour is shown by the dotted curves in Figure 4.7. The other limit of behaviour would be a sample saturated with very high resistivity electrolyte (for example gas or oil). Here, clay mineral surface conductivity effects dominate and clay shows the conductive effect only. This time an increase in clay content leads to a consistent decrease in resistivity, indicating that resistivity reaches its maximum value for a clay content equal to zero.

The XRD results show that clay minerals in the 11 samples of Group 3 are kaolinite, whereas clay in other samples is dominantly illite. Figure 4.7b shows that for clay content higher than 13%, samples in Group 1 and Group 3 have similar porosity (about 0.12) indicating kaolinite and illite have an approximately equivalent blocking effect in reducing porosity at this clay content range. Comparison of resistivities of these samples with similar clay content in Figure 4.7a shows that samples where clay minerals are dominantly illite in Group 1 have slightly lower resistivity than samples containing kaolinite in Group 3. This confirms the results of Thomas (1976), Johnson and Linke (1978), Ridge (1983) and Ellis (1987) that kaolinite does not play an important role in reducing the resistivity of shaly sand. It also explains the observation in Figure 4.4 that the highest resistivity dependence on porosity is seen for samples in Group 3. Our ability to study in detail the types and modes of occurrence of the clays and their effect on the signature of electrical resistivity is currently limited by the single high salinity brine (35 g/l) used in our experimental dataset.

Our sandstone samples were selected to represent as wide a range of porosity, permeability and clay content as possible. Nevertheless, they represent a somewhat eclectic mix of geological provenance including a range of Carboniferous, Permian and Triassic sandstones from quarries and boreholes in the United Kingdom, a selection of borehole samples from Chinese petroleum wells, as well as Berea sandstone, much referred to in rock physics literature. It is usually the case that empirical physical property relationships will be specific to a particular geographic location or geological sequence. However, comparison of Figure 4.11 to Figure 4.7a shows that the geological grouping of samples has no apparent influence on the deductions made from the overall dataset. For example, the China borehole samples straddle both groups, both above and below a critical clay blocking concentration, and seem to follow a general clay-blocking model trend. We take this as a further affirmation of the generality of our clay-blocking model.

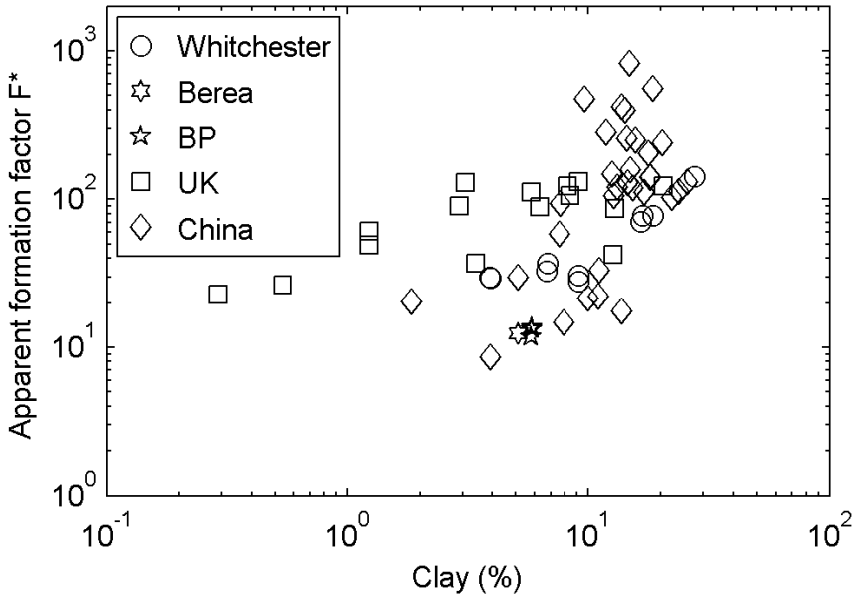

Figure 4.11. Apparent formation factor against volumetric clay content by grouping the samples with the geological information of where they are cored from.

We were interested in the low frequency electrical resistivity (2 Hz) behaviour relevant to CSEM surveys. The results presented above are expected to be different from those derived from well logging and measurements while drilling at around 50 kHz as polarisations (e.g., Maxwell-Wagner polarisation, the polarisation of Stern layer and membrane polarisation) take place at different frequencies affecting the frequency dependence of electrical resistivity (e.g., de Lima and Sharma, 1992; Leroy *et al*., 2008; Leroy and Revil, 2009). We tried to trace this resistivity change with

frequency by also measuring electrical resistivity at 440 Hz and 50 kHz. The 440 Hz data showed negligible variation with the 2 Hz data but the 50 kHz data unfortunately lacked the necessary accuracy which degrades with frequency in our measurement system (a function of sample impedance, see Appendix B). This will be addressed in further studies.

4.4. Conclusions

There are important conclusions to be drawn from the experimental data presented in this chapter.

(1) We have confirmed the feasibility of Archie's equation (Archie, 1942) to model the resistivity of effectively clean sandstones and the model of de Lima and Sharma (1990) to model that of shaly sandstones at 2 Hz. Saturated with 35 g/l brine (σ_w = 4.6948 S/m at 19 °C), our sandstone samples show a very good correlation with Archie's equation (Archie, 1942) and the model of de Lima and Sharma (1990) for clean and shaly sandstones respectively at 2 Hz.

(2) Porosity is the first order parameter that affects resistivity and clay shows a secondary effect on resistivity that depends on porosity. Under our experimental conditions (full saturation with 35 g/l brine at a differential pressure of 26 MPa and temperature of 19 °C), sandstone samples with volumetric clay contents as high as 22% were found to behave like Archie's clean sandstones when porosity is higher than 9% while samples with volumetric clay content as low as 10% behave like shaly sandstones when porosity is less than 9%. The integration of Marion's (Marion *et al*., 1992) porosity model with the resistivity models of Archie (1942) and de Lima and Sharma (1990) gives a reasonable fit to the resistivity-clay trends of effectively clean and shaly sandstones respectively.

(3) We observed a negative correlation between electrical resistivity and hydraulic permeability. Two possible causes of this relationship are proposed: firstly, low permeabilities result from low porosities and increased tortuosity of connected pores due to dispersed clay minerals, which leads to high resistivities according to Archie's equation (Archie, 1942); secondly, low

permeability means there is a lack of connected pores and so the electrolyte is not so well connected, again leading to higher resistivities.

(4) The clay effect on resistivity is complicated since it depends not only on the amount of clay (clay content), porosity and electrolyte resistivity but also on the differential pressure; differences in clay type (kaolinite and illite in this study) may have different effects on electrical resistivity which however needs further investigation.

Overall, the results provide insight into electrical resistivity phenomena likely to be seen in reservoir rocks *in situ*. Our results for the first time provide quantitative empirical relations among resistivity, porosity, clay content and permeability for typical reservoir sandstones at low frequency (2 Hz) likely to be employed by CSEM surveys. Of course, these empirical relations should be used with caution when applied to new geological provinces, but nevertheless they serve to illustrate the likely behaviour of typical reservoir sandstones given the wide range of lithological parameters in our dataset. Nevertheless, a new clay-blocking model (based on pore filling and load-bearing clay with variable cement content and Archie's Law) provides a good description of the general trends seen in our data where no clay conduction effect is expected. The results indicate a general transition from clay-controlled to sand-controlled resistivity at about 9% porosity for shaly sandstones. Further theoretical developments are needed to model the clay conduction effect in competition with the clay-blocking effects observed here, together with new experimental data at low pore fluid salinities and different measurement frequencies.

Chapter 5

Pressure effects on the joint elastic-electrical properties of reservoir sandstones

This chapter forms a paper submitted for publication to *Geophysical Prospecting*, Han T., Best A.I., Sothcott J. and MacGregor L.M. 2010. Pressure effects on the joint elastic-electrical properties of reservoir sandstones.

Abstract: The joint elastic-electrical properties of 63 sandstone samples were studied in the laboratory. Sample porosities ranged from 1.99% to 28.99%, permeabilities from 0.0001 mD to 997.49 mD and volumetric clay contents from 0 to 27.63%. Ultrasonic (0.7 – 1.0 MHz) compressional- and shear-wave velocity (V_p, V_s) and attenuation ($1000/Q_p$, $1000/Q_s$) and electrical resistivity (A/C 2 Hz, ρ) were measured simultaneously at differential pressures (difference between confining and pore pressures) from 60 MPa down to 8 MPa on 5 cm diameter plugs fully saturated with 35 g/l brine. We found that a regression equation of the form $Z = A - Be^{-CP_{diff}}$ (where: Z represents each of the 5 measured geophysical parameters V_p, V_s, $1000/Q_p$, $1000/Q_s$ and ρ; A, B, C are constants fitted to the data; and P_{diff} is differential pressure) gave a good fit to the results for all 5 geophysical parameters. Electrical resistivity ρ was more pressure-sensitive in clay-rich sandstones with higher concentrations of low aspect ratio pores and micropores than in clean sandstones. Ultrasonic wave attenuation ($1000/Q_p$ and $1000/Q_s$) was more pressure-sensitive in clean sandstones with large open pores (macropores) than in clay-rich sandstones. Pore type did not show any influence on the pressure sensitivity of elastic velocity (V_p and V_s). As differential pressure increases, the effect of the low aspect pores and micropores on electrical resistivity gets higher than that of the macropores on attenuation. Further analysis of correlations among the 5 parameters as a function of pressure revealed potentially diagnostic relationships for geopressure prediction in reservoir sandstones.

5.1. Introduction

Marine controlled source electromagnetic techniques are growing in importance for hydrocarbon exploration, reservoir characterisation and monitoring. They provide sub-seabed electrical resistivity as a complementary parameter to elastic wave velocity and attenuation derived from co-located seismic surveys (Harris *et al*., 2009). This extra information can improve geophysical inversion schemes for pore fluid type and saturation given sufficient knowledge about rock properties. Lithology (mineralogy, porosity, permeability, etc.) also influences electrical and elastic properties in addition to pore fluid effects, all of which can be affected by changes in effective stress in the subsurface. In particular, effective stress controls the dilation of fractures and microcracks in reservoir rocks which in turn affect reservoir

permeability, mechanical strength and anisotropy (Nur and Simmons, 1969). The remote geophysical characterisation and monitoring of geopressure and associated geomechanical changes is immensely important for hydrocarbon reservoir production, and not least for detecting leakage pathways from future CO_2 storage reservoirs. The addition of electrical resistivity information to elastic velocity and attenuation may give better insight into reservoir pressure conditions and is therefore worthy of further investigation.

The effect of differential pressure (here defined as the difference between the confining and pore fluid pressures) on elastic velocity and attenuation has been reported in the literature by various authors, e.g., Gardner *et al*. (1964), Gordon and Davis (1968), Nur and Simmons (1969), Toksöz *et al*. (1979), Johnston and Toksöz (1980), Jones (1995), Best and Sams (1997) and Khaksar *et al*. (1999); they found that increasing pressure generally increases elastic velocity and decreases attenuation in rocks due to the closure of microcracks. Similarly, increasing differential pressure was found to increase electrical resistivity (e.g., Fatt, 1957; Glanville, 1959; Brace *et al*., 1965; Brace and Orange, 1968; Timur *et al*., 1972; Jing, 1990; Jing *et al*., 1990; and Mahmood *et al*., 1991). Jing *et al*. (1992) observed a more rapid increase in resistivity with pressure at lower pressures (< 10 MPa) than at higher pressures where resistivity approaches a constant value, and also attributed this to the higher compressibility of pores at lower pressures. A logical extension of these studies is to investigate the effect of pressure on all five geophysical parameters of interest (i.e., P- and S-wave velocity and attenuation, and electrical resistivity) to see what might be gained from joint elastic and electrical parameter inversions over single elastic or electrical parameters. Despite the extensive use of both seismic and electrical methods in borehole wireline logging and surface geophysics for many decades, there does not appear to be any systematic study of joint elastic and electrical properties of reservoir rocks reported in the open literature.

This chapter presents the results of a laboratory study into the effect of differential pressure on the joint elastic-electrical properties of typical reservoir sandstones. Five parameters were measured on a set of 63 sandstones samples taken from quarries and boreholes with a wide range of reservoir properties. All 5 measured parameters (P- and S-wave velocity, V_p and V_s respectively; P- and S-wave attenuation, $1000/Q_p$ and $1000/Q_s$ respectively, where Q is the quality factor; and electrical resistivity, ρ) were

found to follow pressure trends defined by the equation $Z = A - Be^{-CP_{diff}}$ (see below for definitions). Significantly, the pressure sensitivity of electrical resistivity was found to increase with higher proportions of low aspect ratio pores and micropores, while that attenuation increased with increasing content of large open pore (macropores), and elastic velocity showed no dependence on the different pore types. When cross-plotted for different pressures, all trends were approximately linear (e.g., ρ-V_p), the gradient of which varied between samples and was found to have a correlation with the proportions of low aspect ratio pores and micropores. Interestingly, the resistivity-velocity and resistivity-attenuation slopes showed a high correlation with electrical resistivity measured at 8 MPa differential pressure. The results show that joint elastic-electrical properties have the potential to reveal subtle rock responses to pressure that are not discernible from elastic or electrical properties alone.

5.2. Experimental results

5.2.1. The effect of differential pressure on velocity, attenuation and resistivity

Least-squares regression analysis was performed on the data to quantify the effect of differential pressure on elastic wave velocity and attenuation and electrical resistivity for each sample. Based on work of Eberhart-Phillips *et al*. (1989), Jones (1995), Khaksar *et al*. (1999), Brace *et al*. (1965) and Kaselow and Shapiro (2004), it was found that a regression equation of the form

$$Z = A - Be^{-CP_{diff}}, \tag{5.1}$$

gave the best fit to all 5 parameters, i.e., P- & S-wave velocity and attenuation and electrical resistivity, where Z corresponds to the parameter of interest; P_{diff} is the differential pressure, and A, B and C are the best-fit coefficients.

Figure 5.1 shows results for Sample No. 1SU as a typical example of the experimental data and pressure-dependent regression curves for P-wave velocity and attenuation (S-wave velocity and attenuation give similar results) and electrical resistivity. The best fit regression coefficients for equation 5.1 for all 63 samples are given in Appendix C. Note that all correlation coefficients were better than $R^2 = 0.9$.

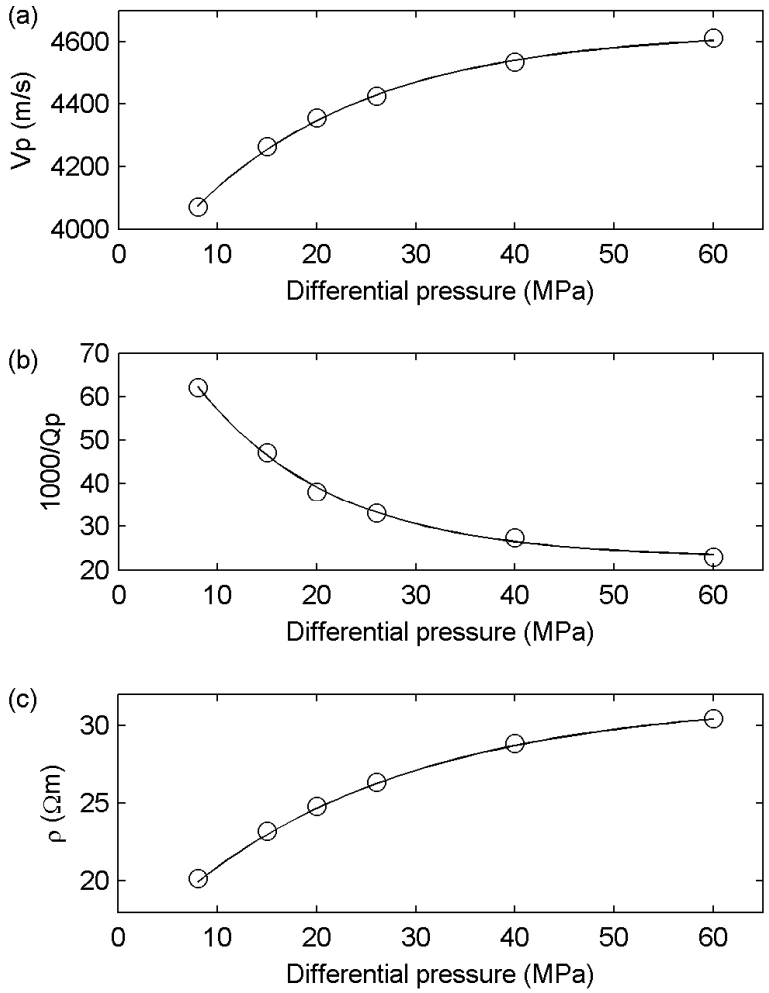

Figure 5.1. Experimental data and regression curves for sample 1SU showing the variation of (a) P-wave velocity, (b) P-wave attenuation and (c) electrical resistivity with differential pressure. S-wave velocity and attenuation show similar trends to those for P-waves.

As expected, V_p and ρ increase, and $1000/Q_p$ decreases, smoothly and with the rate of change diminishing with pressure converging on a constant value at higher pressures. The closure of low aspect ratio pores in the rock is the most plausible explanation for this pressure-dependent behaviour (e.g., Glover *et al*., 2000). Low aspect ratio pores could be present as cracks either within mineral grains, or more probably at grain contacts, or could be associated with clay minerals with their platy grains and related porosity (note range of clay contents up to 27.63% in Appendix A). Hence, increasing velocities can be explained by the increasing stiffness of the rock frame relative to the negligible increase in rock density as the reduction in porosity due to closure of microcracks in sandstones is very small, generally less than 1% (Mavko and Jizba, 1991; Mavko *et al*., 1998). The decrease in attenuation is most probably explained by a reduction in microcrack squirt flow as cracks close according to mechanisms

described by, for example, Murphy *et al*. (1986), Dvorkin *et al*. (1995). The finite attenuation at high pressure could indicate background Biot type losses (Biot, 1956a, b) or even those due to clay-squirt flow (e.g., Best and McCann, 1995; Marketos and Best, 2010). The increase in electrical resistivity with pressure indicates the importance of low aspect ratio pores in controlling electrical properties. If ionic conduction in the pore fluid is taken to be the dominant mechanism of electrical current flow, then the pressure dependence could be explained by the closure of narrow conductive pathways at grain contacts with increasing pressure.

The pressure sensitivity of each of the 5 geophysical parameters can be expressed by the differential of each geophysical parameter Z to the differential pressure P_{diff}

$$S(Z) = \frac{dZ}{dP_{diff}} = \frac{d(A - Be^{-CP_{diff}})}{dP_{diff}} = BCe^{-CP_{diff}}, \qquad (5.2)$$

where the pressure sensitivity $S(Z)$ decreases with differential pressure. To estimate the overall pressure sensitivity of each of the geophysical parameter we average $S(Z)$ at the 6 differential pressures (60, 40, 26, 20, 15 and 8 MPa respectively) employed in the measurements.

Figure 5.2 shows the averaged pressure sensitivities of V_p, $1000/Q_p$ and ρ between 8 and 60 MPa plotted against sample porosity (although not shown, the S-wave results show similar trends to the P-wave results). It is worth pointing out that the magnitude of the pressure sensitivity of each parameter depends on the B coefficient which in turn is determined by the unit of that parameter (e.g., velocity in m/s will give a B coefficient different from in km/s and hence a different magnitude of the pressure sensitivity, and it is the same case for attenuation in terms of $1000/Q$ or $1/Q$). We therefore study the individual behaviour of the pressure sensitivity of one parameter rather than comparing the magnitude of two.

Figure 5.2 shows that electrical resistivity ρ is much more sensitive to pressure at lower porosities and there appears to be a systematic trend of decreasing sensitivity with porosity, although with some scatter. In an inverse manner to the pressure sensitivity of resistivity with porosity, P-wave attenuation shows a dominant trend of higher pressure sensitivities (higher absolute sensitivity values) at greater porosities and the sensitivity decreases with decreasing porosity. There is also a curious grouping of data points at around 10% porosity which show a wide range of $1000/Q_p$

pressure sensitivity for a small range of porosity. The pressure sensitivity of P-wave velocity however shows no discernible change with porosity.

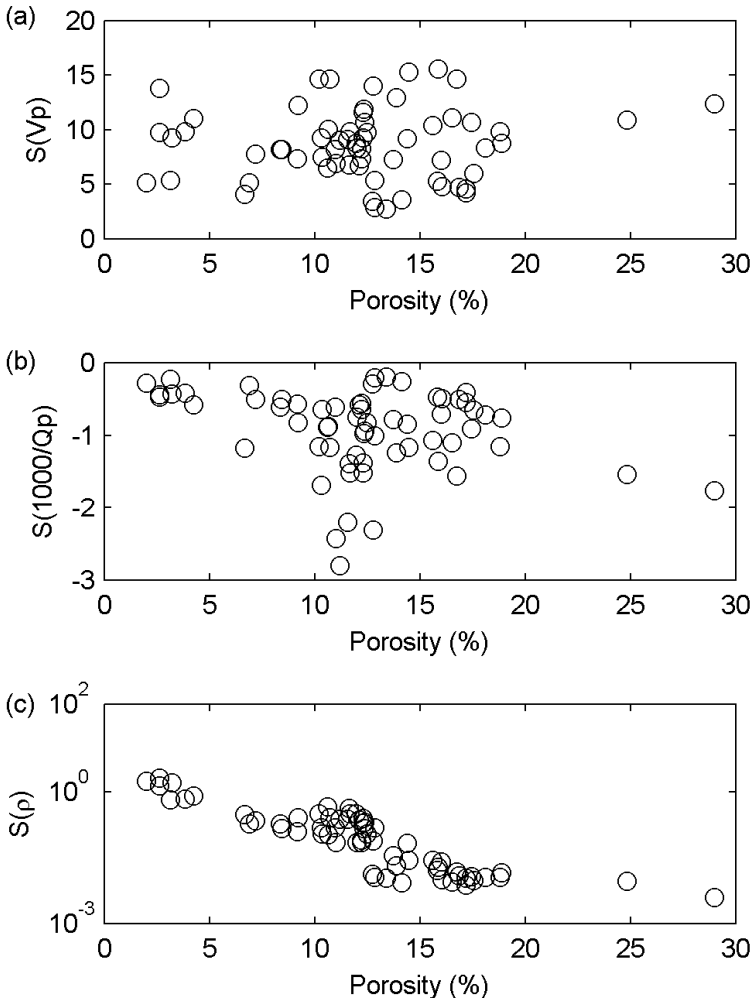

Figure 5.2. Experimental data for all samples showing pressure sensitivity (*S*) of (a) P-wave velocity (b) P-wave attenuation and (c) electrical resistivity, plotted against porosity. S-wave velocity and attenuation show similar behaviour to the P-waves.

Thin sections and SEM observations (Figures 5.3 and 5.4) confirm that the dominant pore type shifts from i) macropores (intergranular and generally high aspect ratio pores, Figure 5.3) in the higher porosity samples to a combination of ii) connective pores (low aspect ratio pores at grain contacts, Figure 5.4a) and iii) micropores (small pores within clay mineral aggregates and altered rock fragments, Figure 5.4b) in the lower porosity samples; these pore type definitions were taken from Khaksar *et al*. (1999). This confirms the observations made by Xu *et al*. (1990) who discussed the relative importance of high and low aspect ratio pores on electrical and hydraulic rock properties.

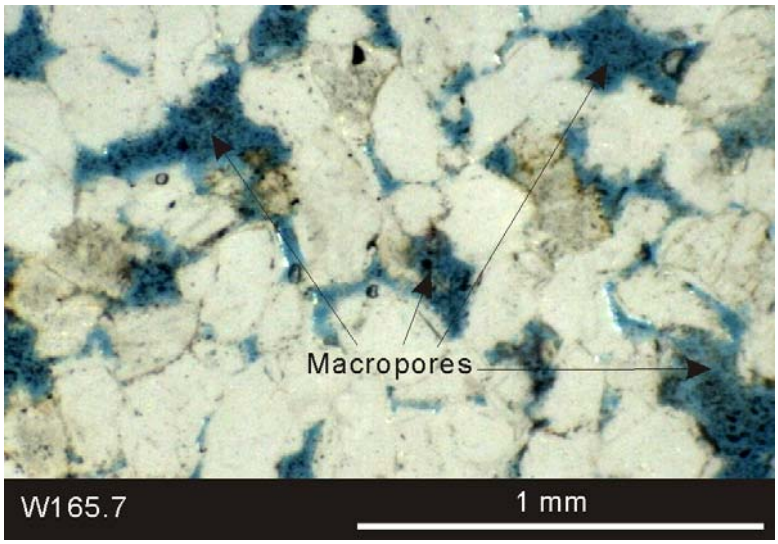

Figure 5.3. Thin section image of sample No. W165.7 with porosity of 16.87% showing dominant pore type of macropores in this sample. Scale bar = 1 mm.

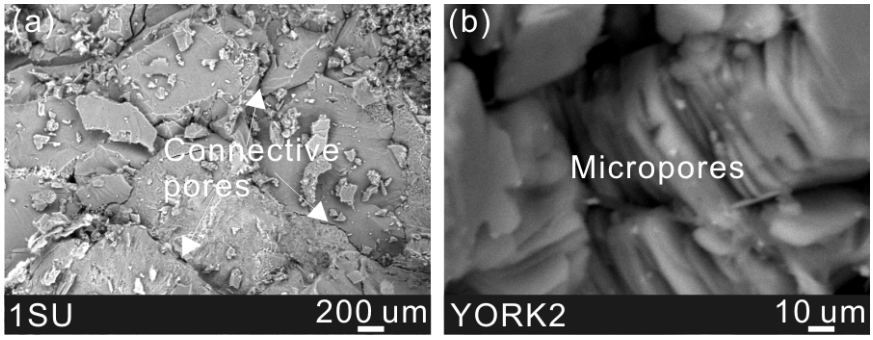

Figure 5.4. SEM images showing different pore types. (a) Connective pores in sample No. 1SU with porosity of 10.71%, scale bar = 0.2 mm; (b) Micropores associated with clay minerals for sample No. YORK2 with porosity of 10.31%, scale bar = 0.01 mm.

To quantify our observations the porosity is plotted against Archie's (Archie, 1942) cementation coefficient *m*, which according to Salem and Chilingarian (1999) contains information of the shape of the pores. That is, low aspect ratio pores usually have higher surface areas which give higher Archie cementation coefficients; the term cementation coefficient is misleading as it is primarily controlled by pore surface area, not cementation itself. The result is shown in Figure 5.5, where the cementation coefficient *m* is calculated using the method proposed by Olsen *et al*. (2008). Although scattered there seems a trend of decreasing cementation coefficient *m* with porosity, indicating higher proportions of low aspect ratio pores in the lower porosity samples.

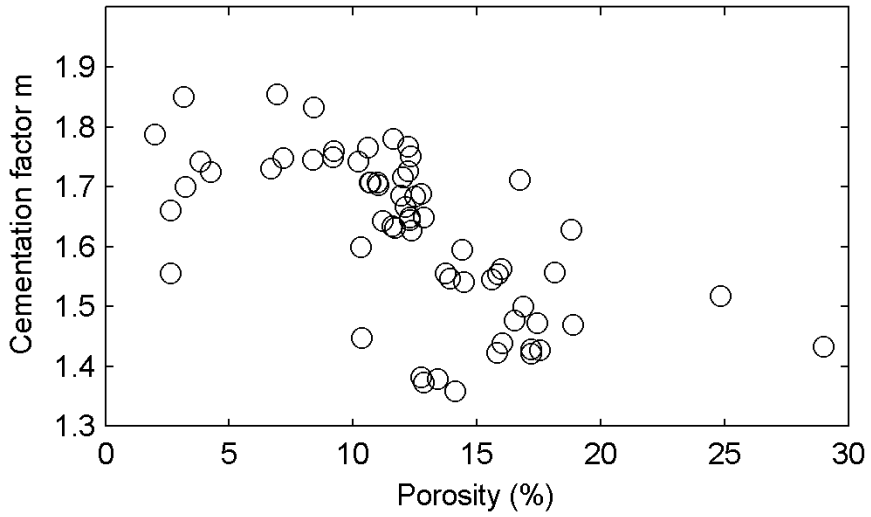

Figure 5.5. Experimental data showing the relationships between cementation coefficient *m* and porosity of all 63 samples.

With this observation it is possible to explain the pressure sensitivity of the geophysical parameter with porosity. That is, the greater sensitivity of electrical resistivity to pressure in the less porous samples is due to their higher proportions of connective pores and micropores. This explanation resembles that of Glanville (1959) for the higher formation factor (F) sensitivity to pressure seen in less porous, less permeable rocks. The higher pressure sensitivity of attenuation in the higher porosity samples seems to be related to the greater proportion of macropores.

As discussed above, the decreasing attenuation with pressure is probably caused by a reduction in microcrack squirt flow with increasing differential pressure. However our data show that attenuation is more sensitive to pressure in more porous samples where there are higher proportions of large open pores (macropores). This possibly implies that although microcrack squirt flow decreases with differential pressure, and although macropores show finite change with differential pressure, it is the loss via the finite shrinking macropores (Biot type losses, Biot, 1956a, b) that determines the pressure sensitivity of attenuation.

The decreasing pressure sensitivity of electrical resistivity with porosity is explained by the relative importance of ionic charge conduction in the fluid versus surface charge conduction on mineral grains. Ionic conduction might be expected to dominate in large open pores, but may compete with surface charge conduction in narrow pores.

The lack of any correlation of pressure sensitivity of elastic velocity to porosity suggests that changes in rock frame elastic moduli due to pressure are equally determined by micropores or macropores. The reason why porosity shows an opposite effect on the pressure sensitivity of attenuation and electrical resistivity needs further investigation. However, our observation could prove to be a useful diagnostic feature of reservoir rock properties from joint elastic-CSEM surveys.

5.2.2. The effect of pressure on the relationship between resistivity and velocity

Electrical resistivity is cross-plotted against V_p and V_s as a function of differential pressure for Sample No. 1SU in Figure 5.6. Also shown are the curves derived from the least-squares regressions according to equation 5.1 (see above).

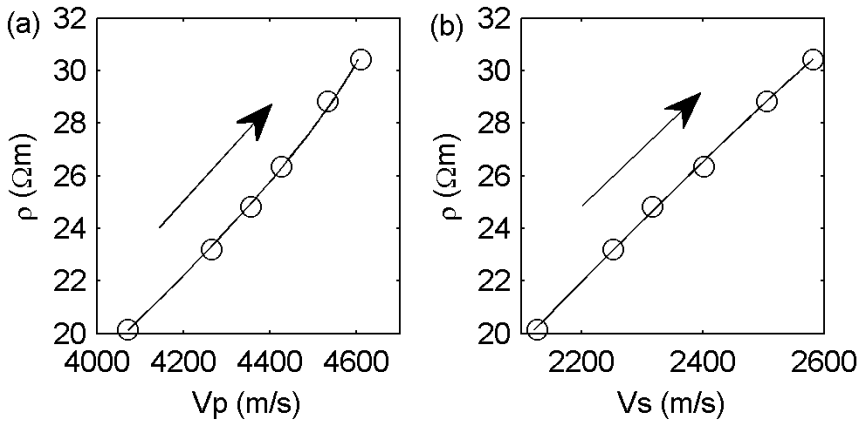

Figure 5.6. Experimental data and regression curves for sample 1SU showing the relationships between electrical resistivity and (a) P-wave velocity and (b) S-wave velocity with differential pressure. Arrows show direction of increasing differential pressure.

Electrical resistivity increases in an approximately linear fashion with elastic velocity with differential pressure changing from 8 to 60 MPa. The relative change of electrical resistivity ρ with V_p as a function of differential pressure can be expressed as

$$G_1 = \frac{\dfrac{d\rho}{dP_{diff}}}{\dfrac{dV_p}{dP_{diff}}} = \frac{B_\rho C_\rho e^{-C_\rho P_{diff}}}{B_{Vp} C_{Vp} e^{-C_{Vp} P_{diff}}} = \frac{B_\rho}{B_{Vp}} \frac{C_\rho}{C_{Vp}} e^{(C_{Vp} - C_\rho) P_{diff}}, \qquad (5.3)$$

where G_1 corresponds to the gradient of the resistivity-velocity curve at each differential pressure P_{diff}. The linearity of the resistivity-velocity trend is determined

by the difference between the C coefficients of electrical resistivity and elastic velocity in equation 5.1; i.e., the smaller the difference, the more linear the resistivity-velocity trend. The fact that the difference in the C coefficient for all 63 sandstones studied varies on average between 20.56% and 23.69% for the ρ-V_p and ρ-V_s relations respectively allows us to approximate $C_\rho = C_{Vp}$, leading equation 5.3 to become

$$G_1 \approx \frac{B_\rho}{B_{Vp}}. \tag{5.4}$$

Hence, the change of electrical resistivity with elastic velocity as a function of differential pressure can be approximated by a linear function for each of the sandstone samples, and G_1 can be used to represent the slope of the ρ-V_p relationships.

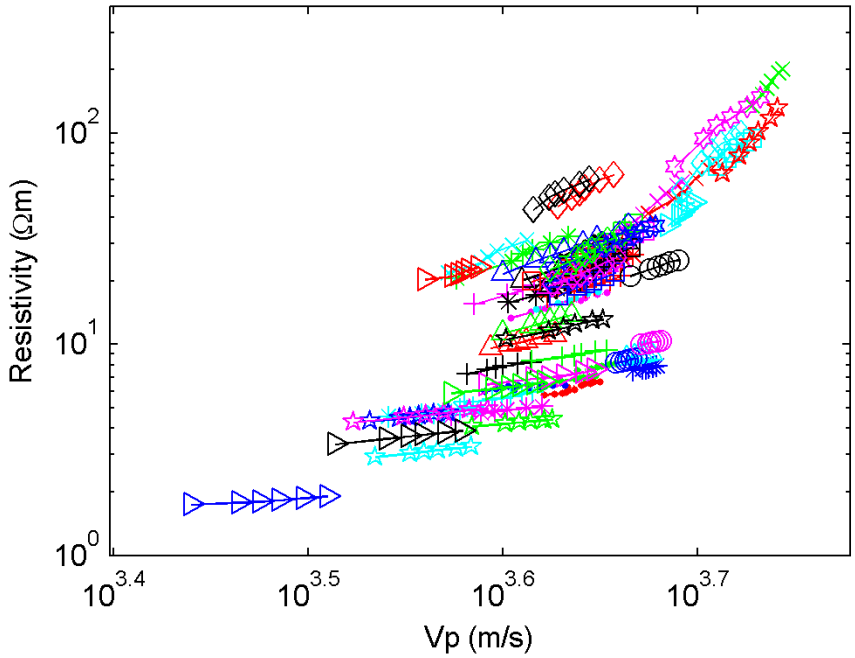

Figure 5.7. Experimental data for all 63 samples showing the relationships between electrical resistivity and P-wave velocity with differential pressures on a logarithmic scale. Resistivity-V_s relationships are similar.

Figure 5.7 shows the ρ-V_p relationships as a function of differential pressures for all 63 samples (ρ-V_s relationships are similar) on a log-log scale. We choose to plot Figure 5.7 on a logarithmic scale because, as the resistivity data cover more than 2 orders of magnitude, it makes the distribution of the curves much clearer. As expected all samples show approximately linear curves but the slope varies between samples. It is interesting that samples with a larger slope (e.g. sample SD1, green x-marks) usually have a higher initial elastic velocity and electrical resistivity (the values at 8

MPa differential pressure respectively) while samples with smaller slopes (e.g. sample CZ5, blue right triangles) generally start from a lower elastic velocity and electrical resistivity.

In order to analyze the variation of the ρ-V_p slopes between samples we first plot G_1 for all 63 samples against porosity in Figure 5.8. A systematic decrease in slope is seen with increasing porosity which again suggests the relative importance of low to high aspect ratio pores at low and high porosities in affecting electrical resistivity rather than elastic velocity as discussed in the previous section.

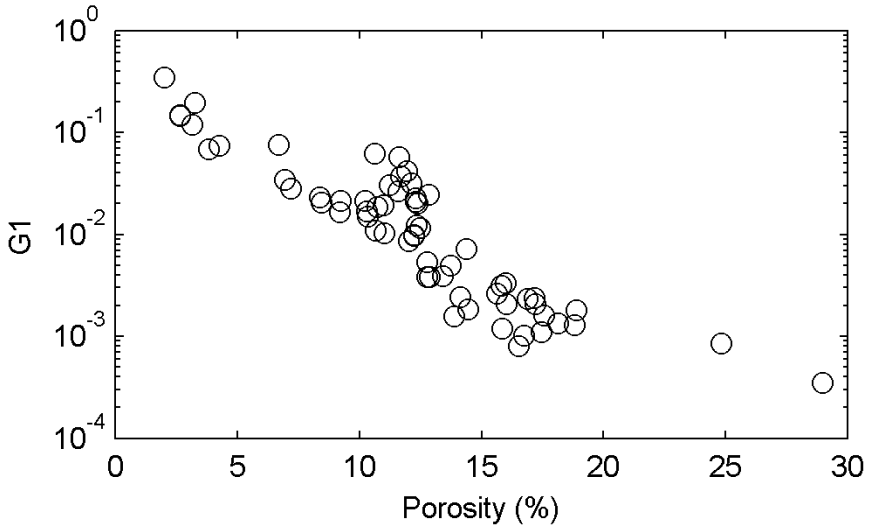

Figure 5.8. Relationship between the slope G_1 of the resistivity-V_p curves (linear approximation) and porosity. Slopes for resistivity-V_s against porosity show a similar trend.

Figure 5.9 shows the ρ-V_p slope G_1 against P-wave velocity measured at 8 MPa differential pressure (the initial values mentioned above). Two groups appear in Figure 5.9 with samples in both groups showing increasing ρ-V_p slope with P-wave velocity. The increasing slope G_1 with velocity can be explained by combining the relationships between G_1 and porosity and between velocity and porosity. That is, the slope G_1 increases with decreasing porosity where there are higher proportions of low aspect ratio pores to which electrical resistivity is more sensitive than the elastic velocity; at the same time with decreasing porosity the rock frame gets stiffer giving higher elastic velocity. However the two groups in Figure 5.9 indicate some other controlling parameter apart from porosity, which after investigation is found to be clay content. The lower group in Figure 5.9 consists of clean sandstones (volumetric clay content less than about 10%), while samples in the upper group of Figure 5.9 are all clay-rich sandstones. Since there are more micropores associated with clay

minerals in the clay-rich samples, it is this higher proportion of clay micropores that makes the ρ-V_p slope greater than in the clean sandstones where the majority of the pores are relatively pressure-insensitive macropores.

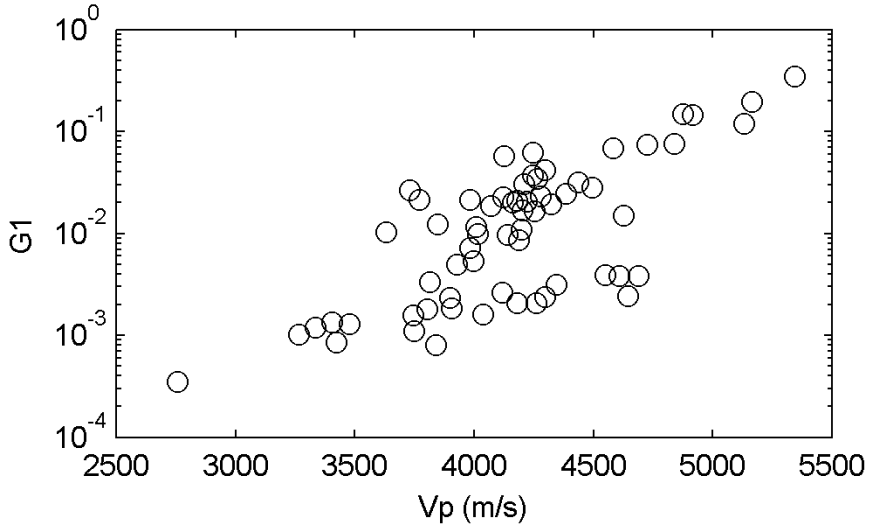

Figure 5.9. Relationship between the slope G_1 of the resistivity-V_p curves (linear approximation) and P-wave velocity measured at 8 MPa differential pressure. Slopes for resistivity-V_s against S-wave velocity show a similar trend.

The ρ-V_p slope G_1 against electrical resistivity measured at 8 MPa differential pressure is shown in Figure 5.10, where the slope G_1 increases linearly with electrical resistivity on a logarithmic scale:

$$\log(G_1) = 1.7766\log(\rho) - 4.0470 \text{ with } R^2 = 0.9769. \quad (5.5)$$

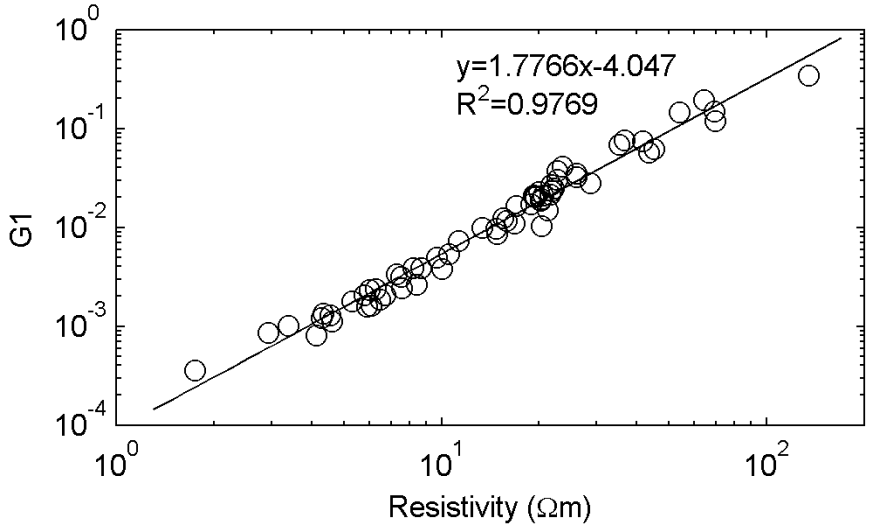

Figure 5.10. Relationship between the slope G_1 of the resistivity-V_p curves (linear approximation) and electrical resistivity measured at 8 MPa differential pressure. Slopes for resistivity-V_s against electrical resistivity show a similar trend.

Different from the correlation between the ρ-V_p slope G_1 and elastic velocity where clay content shows a systematic effect, the relationship between G_1 and electrical resistivity is no longer influenced by clay content. This indicates the presence of a more fundamental relationship between G_1 and electrical resistivity than that between G_1 and elastic velocity, which needs further investigation. However the two relationships are complementary and together reveal the importance of clay content on the pressure dependence of joint elastic-electrical properties of reservoir sandstones.

The above analysis gives a possible way to discriminate between different porosity and clay content rocks from the resistivity-velocity pressure sensitivity. Using empirical velocity-porosity and resistivity-porosity regression equations (see Chapter 4), it is then possible to construct the exact behaviour for any given pressure range in combination with equation 5.1 regression curves (see Appendix C). Possible explanations for different pressure sensitivities of the 5 geophysical parameters were discussed above.

5.2.3. The effect of pressure on the relationship between resistivity and attenuation

The resistivity-attenuation relationships are presented in a similar format to that used for resistivity-velocity above. Approximately linear relations are seen between resistivity and P-wave attenuation ($1000/Q_p$), and similarly for S-wave attenuation, in Figure 5.11 for Sample No. 1SU, which is typical of all samples shown in Figure 5.12 on a logarithmic scale.

As expected, electrical resistivity increases while elastic wave attenuation decreases with increasing differential pressure, and the slopes of the ρ-$1000/Q_p$ curves, approximated by $G_2 \approx \frac{B_\rho}{B_{1000/Qp}}$, vary between samples. The attenuation data for both compressional- and shear-waves confirm the results of Jones (1995) and Best and Sams (1997).

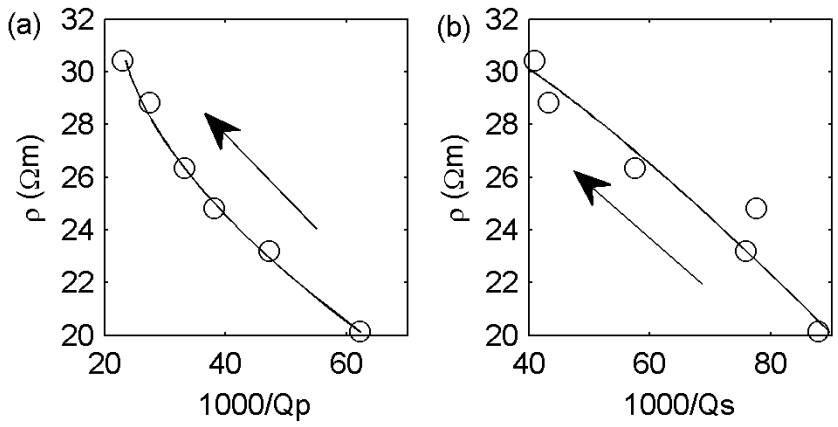

Figure 5.11. Experimental data and regression curves for sample 1SU showing the relationships between electrical resistivity and (a) P-wave attenuation and (b) S-wave attenuation with differential pressure. Arrows show the direction of increasing differential pressure.

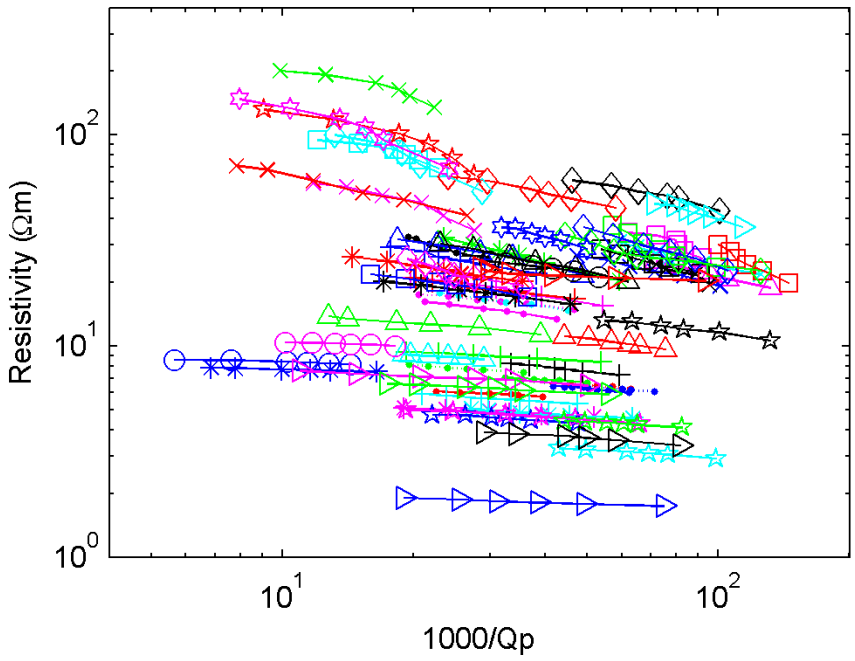

Figure 5.12. Experimental data for all 63 samples showing the relationships between electrical resistivity and P-wave attenuation with differential pressures on a logarithmic scale. Relationships between resistivity and S-wave attenuation show similar trends but with more scatter.

Figure 5.13 shows the variation of G_2 with porosity for all 63 samples. The decreasing absolute values of G_2 with increasing porosity indicates that the ρ-1000/Q_p curves for the less porous samples change more steeply with differential pressure than the higher porosity samples. This is similar to the observation between the ρ-V_p slopes G_1 against porosity, but suggests differences in the ways in which electrical resistivity and elastic

velocity and attenuation are linked by differential pressure. As we established above, electrical resistivity is more sensitive to low aspect ratio pores with changing pressure, attenuation is more subject to the large open pores (macropores), while elastic velocity seems to be independent of pore type. The decreasing magnitude of ρ-1000/Q_p slope G_2 with porosity therefore implies that the micropores have a more profound effect on electrical resistivity than on elastic wave attenuation with changing differential pressures.

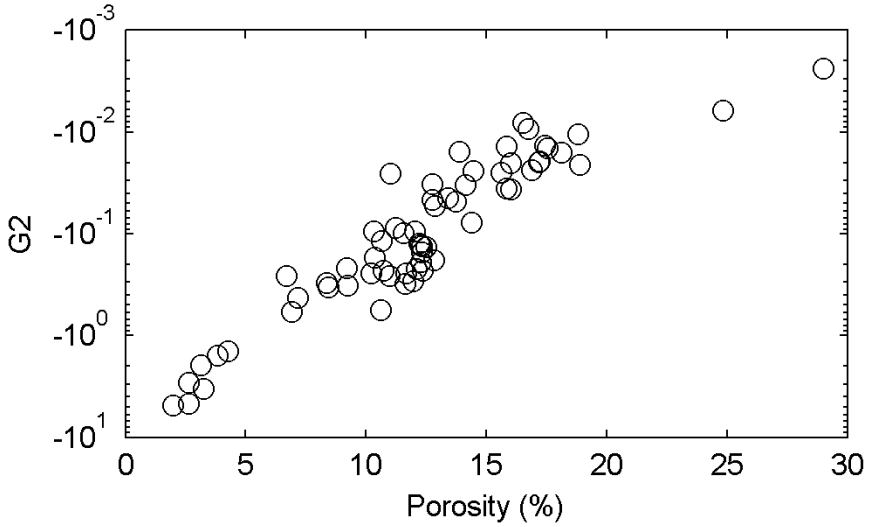

Figure 5.13. Relationship between the slope G_2 of the ρ-1000/Q_p curves (linear approximation) and porosity. Slopes for ρ-1000/Q_s against porosity show a similar trend.

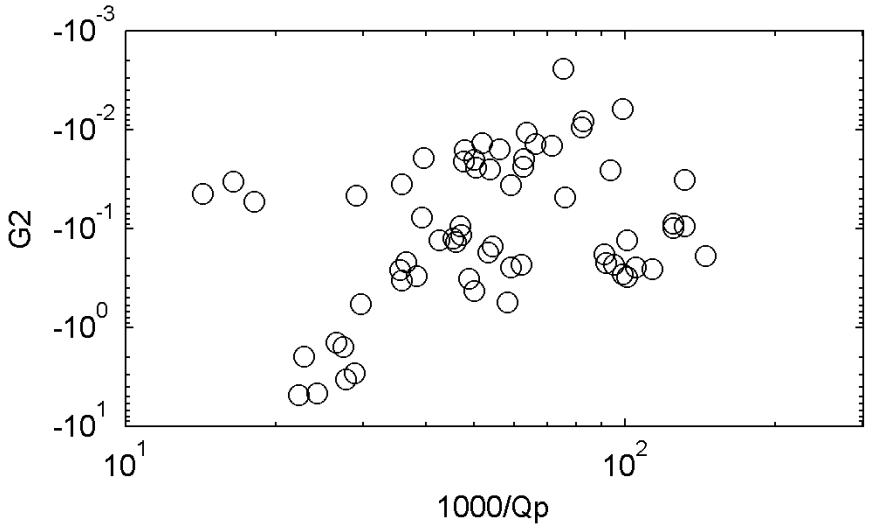

Figure 5.14. Relationship between the slope G_2 of the ρ-1000/Q_p curves (linear approximation) and P-wave attenuation measured at 8 MPa differential pressure. Slopes for ρ-1000/Q_s against S-wave attenuation show a similar trend.

The relationship between ρ-1000/Q_p slopes G_2 and the P-wave attenuation measured at 8 MPa differential pressure is shown in Figure 5.14; the data however are too scattered to get a systematic correlation for the whole dataset, although there is a suggestion of two separate groups with higher and lower G_2 values. Figure 5.15 shows the plot of the ρ-1000/Q_p slopes G_2 against the electrical resistivity measured at 8 MPa differential pressure.

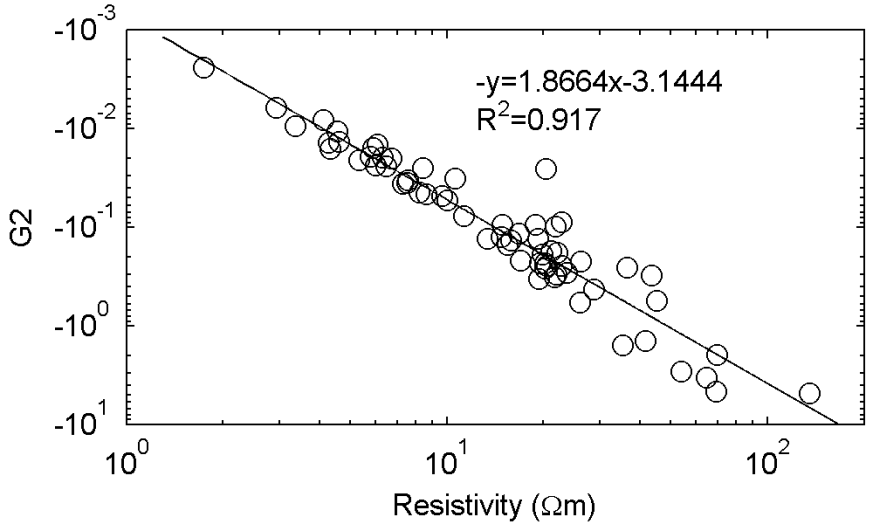

Figure 5.15. Relationship between the slope G_2 of the ρ-1000/Q_p curves (linear approximation) and electrical resistivity measured at 8 MPa differential pressure. Slopes for ρ-1000/Q_s against electrical resistivity show a similar trend.

Again a strong linear correlation between the two parameters appears on a logarithmic scale

$$\log(-G_2) = 1.8664\log(\rho) - 3.1444 \text{ with } R^2 = 0.9170. \qquad (5.6)$$

This is another important observation. Since electrical resistivity is easier to measure than attenuation, once we measure electrical resistivity at two end differential pressures (e.g., differential pressures before and after hydrocarbon production) and elastic attenuation at one of the differential pressure, we can predict the behaviours of both electrical resistivity and elastic attenuation at any differential pressure in between using equation 5.6 provided that the change in either electrical resistivity or elastic attenuation with differential pressure is known.

5.2.4. The effect of pressure on the relationship between velocity and attenuation

As established above, both resistivity-velocity and resistivity-attenuation relationships are approximately linear; this leads to the deduction that the velocity and attenuation relation should also be approximately linear with pressure. Figures 5.16 and 5.17 confirm this deduction. Figure 5.17 also shows that the slope of the velocity-attenuation approximation, given by $G_3 \approx \frac{B_{Vp}}{B_{1000/Qp}}$, varies between samples but is visually much smaller than for resistivity-velocity and resistivity-attenuation in Figures 5.7 and 5.12 respectively.

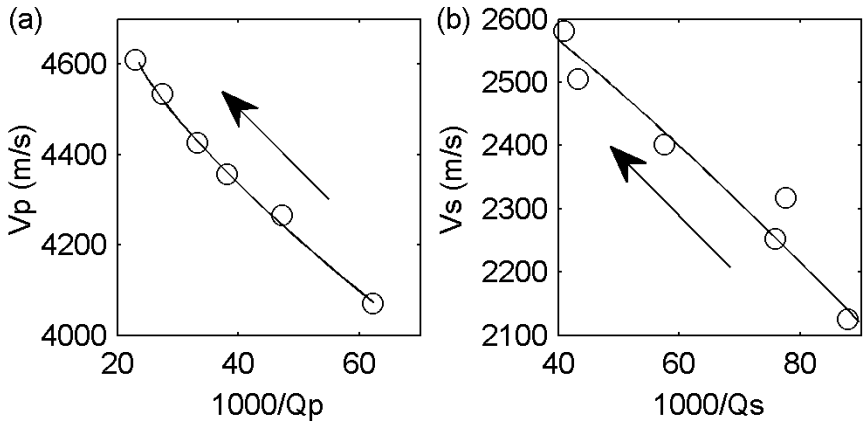

Figure 5.16. Experimental data and regression curves for sample 1SU showing the relationships between (a) P-wave velocity and attenuation and (b) S-wave velocity and attenuation with differential pressure. Arrows show the direction of increasing differential pressure.

Figure 5.18 shows there is a general decreasing trend of the absolute slope G_3 values with increasing porosity as expected, with some outlier samples between 10 – 13% porosity. The relationship between the velocity-attenuation slope G_3 and porosity is entirely due to the elastic attenuation sensitivity to macropores with changing pressure since elastic velocity is not sensitive to different pore types. The velocity-attenuation slope G_3 in Figure 5.18 covers less than 2 orders of magnitude, much smaller than that of the resistivity-velocity slope G_1 and resistivity-attenuation slope G_2 which both cover about 4 orders of magnitude. Again, this confirms that the change of elastic attenuation with increasing differential pressure due to shrinkage of macropores is less than the resistivity change due to shrinkage of micropores.

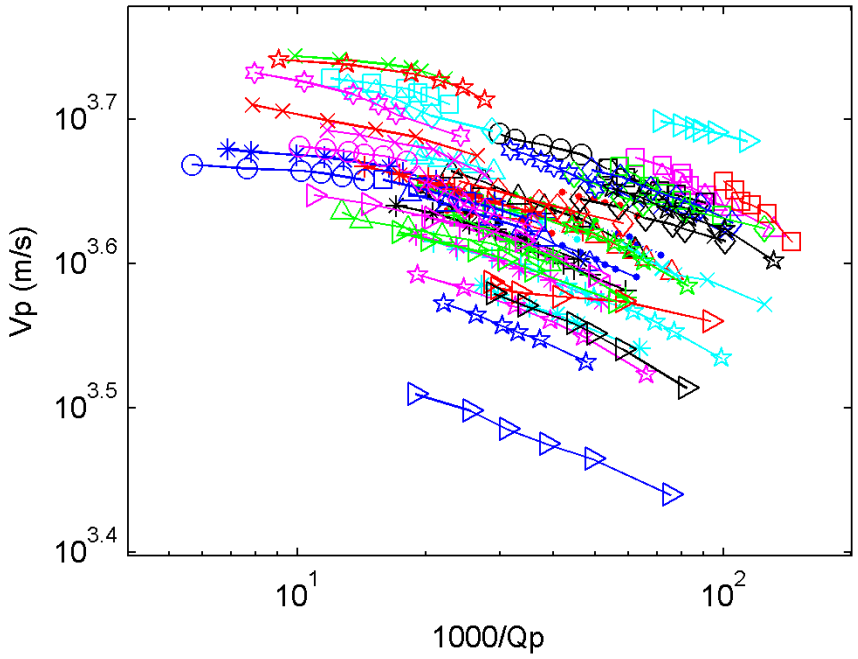

Figure 5.17. Experimental data for all 63 samples showing the relationships between P-wave velocity and P-wave attenuation with differential pressures on a logarithmic scale. S-wave results show similar trends but with more scatter.

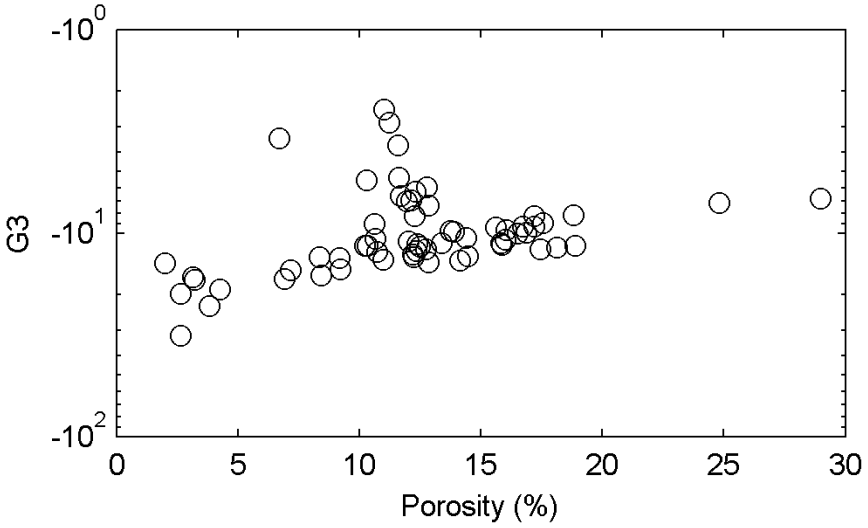

Figure 5.18. Relationship between the slope G_3 of P-wave velocity to P-wave attenuation (linear approximation) versus porosity. S-wave results show a similar trend.

Figures 5.19 and 5.20 show the relationships between the velocity-attenuation slope G_3 and the elastic velocity and attenuation measured at 8 MPa differential pressure respectively. They show that generally the higher the initial elastic velocity and the lower the initial elastic attenuation the steeper is the velocity-attenuation curves with changing differential pressures.

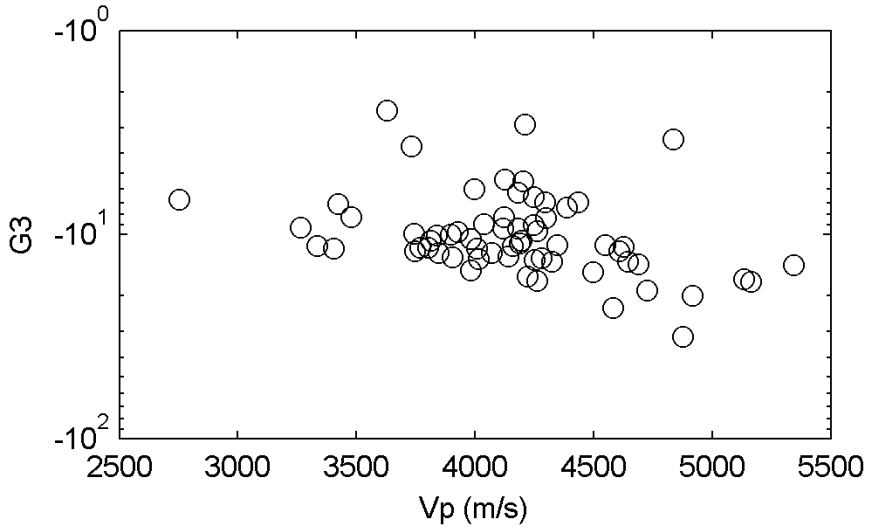

Figure 5.19. Relationship between the slope G_3 of P-wave velocity to P-wave attenuation (linear approximation) versus P-wave velocity measured at 8 MPa differential pressure. S-wave results show a similar trend.

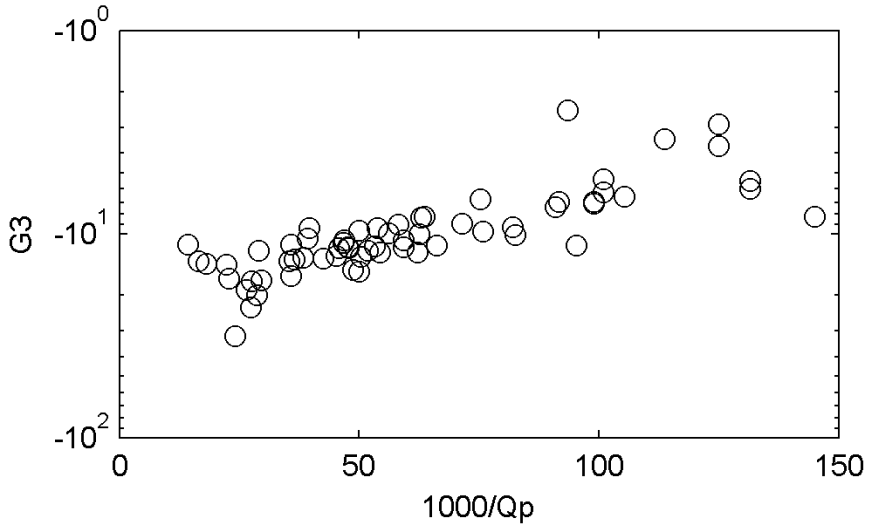

Figure 5.20. Relationship between the slope G_3 of P-wave velocity to P-wave attenuation (linear approximation) versus P-wave attenuation measured at 8 MPa differential pressure. S-wave results show a similar trend.

5.3. Discussion

Direct hydrocarbon detection, reservoir characterisation and monitoring are the main goals of not only exploration seismology (Khaksar *et al*., 1999) but also any other method of exploration geophysics (e.g., CSEM) and the joint use of those methods. Pressure is one of the key parameters that affects the accuracy of joint seismic-CSEM

interpretation and inversion and so must be taken into account. The pressure-dependent behaviours of electrical resistivity, elastic velocity and attenuation and joint elastic-electrical properties may influence the depth, porosity and hydrocarbon concentration values obtained from seismic and CSEM interpreted separately or jointly.

Khaksar *et al*. (1999) show that neglecting the pressure dependence of velocity by the conventional sonic-porosity methods during hydrocarbon depletion, which increases differential pressure by decreasing pore pressure, results in an underestimation of porosity by several porosity units. Similarly, without knowledge of pressure effects on resistivity using Archie's equation (Archie, 1942), depletion conditions lead to an underestimation of porosity or overestimation of hydrocarbon saturation and thus reduces the accuracy of joint seismic-CSEM interpretation in this case. This joint elastic-electrical dependence on the variation in differential pressure caused by depletion has a potential application to monitor the escape of CO_2 after its geological storage in an offshore reservoir by the joint seismic-CSEM method, as injection and escape of CO_2 has a profound effect on the differential pressure (Baines and Worden, 2004), which in turn influences the joint-electrical properties of reservoir rocks that CO_2 resides in.

5.4. Conclusions

A laboratory experimental investigation was conducted into the joint elastic-electrical properties of 63 brine saturated sandstone samples as a function of differential pressures from 8 to 60 MPa. The results lead to the following conclusions:

(1) Changes in P- and S-wave velocity and attenuation and electrical resistivity with differential pressures follow closely the relationship described by the expression $Z = A - Be^{-CP_{diff}}$, where Z is either seismic velocity, attenuation or electrical resistivity, P_{diff} is the differential pressure and A, B and C are the best-fit coefficients.

(2) The relationships between resistivity and velocity, resistivity and attenuation, and velocity and attenuation show approximately linear trends as a function of differential pressure.

(3) The slopes of the above trends decrease with increasing porosity. The slopes for velocity-attenuation trends show much smaller differences between samples than for resistivity-velocity and resistivity-attenuation. The resistivity-velocity slope G_1 and resistivity-attenuation slope G_2 are related to the electrical resistivity measured at 8 MPa differential pressure with high correlation coefficients.

(4) Electrical resistivity is more sensitive to low aspect ratio pores and micropores, elastic wave attenuation is more subject to large open pores (macropores), and different pore types do not have any impact on elastic velocity with changing differential pressure.

(5) Low aspect ratio pores and micropores have a more profound effect on electrical resistivity than macropores have on elastic wave attenuation. Therefore, the resistivity-attenuation slope G_2 decreases with higher proportions of low aspect ratio pores and micropores.

Chapter 6

Joint elastic-electrical properties of reservoir sandstones and their relationships with petrophysical parameters

This chapter forms a paper submitted for publication to *Geophysical Prospecting*, Han T., Best A.I., Sothcott J. and MacGregor L.M. 2010. Joint elastic-electrical properties of reservoir sandstones and their relationships with petrophysical parameters.

Abstract: We measured in the laboratory ultrasonic compressional and shear wave velocity and attenuation (frequency 0.7 – 1.0 MHz) and low frequency electrical resistivity (2 Hz) on 63 sandstone samples with porosity ranging from 1.99% – 28.99%, permeability from 0.0001 mD – 997.49 mD and volumetric clay content from 0 – 27.63%. The 5 cm diameter core plugs were fully saturated with 35 g/l brine and subjected to differential pressures (confining pressure minus pore pressure of 5 MPa) from 60 MPa down to 8 MPa. P- and S-wave velocities were found to be linearly correlated with apparent electrical formation factor on a semi-logarithmic scale for both clean and clay-rich sandstones; the slope of the linear best fit to the clay-rich sandstones is higher than that of the clean sandstones. P- and S-wave attenuations showed a bell-shaped correlation (partial for S-waves) with apparent electrical formation factor. We found that although all the petrophysical parameters had some effect on elastic and electrical properties, it was the volumetric clay content that best determined the joint elastic-electrical properties for this set of sandstones. Hence, joint elastic-electrical properties provide a way to discriminate between sandstones with similar porosities but with different clay contents. The strong correlation between permeability and clay content suggests that crossplots of joint elastic-electrical properties (especially elastic velocity and apparent formation factor) can give good estimates of sandstone permeability.

6.1. Introduction

Marine controlled source electromagnetic sub-seabed imaging has developed over the last decade to a state where routine resistivity mapping of hydrocarbon reservoirs is now possible. Co-located marine seismic and resistivity survey data could provide the engineering parameters needed to better assess the economic potential of hydrocarbon reservoirs away from boreholes, and could provide additional reservoir monitoring capabilities in the future. However, proper exploitation of joint seismic-CSEM datasets will require a much better understanding of the inter-relationships among geophysical (elastic and electrical) and reservoir petrophysical properties (e.g., porosity, permeability and clay content).

Elastic and electrical resistivity properties of reservoir sandstones have been investigated by different authors separately (e.g., Han *et al*., 1986; Klimentos and

McCann, 1990; Klimentos, 1991; Best *et al*., 1994; Worthington, 1982; Bussian, 1983; Jing *et al*., 1992; Daily and Lin, 1985; Revil and Glover, 1998; Kaselow and Shapiro, 2004), but there are relatively few studies of the joint properties. The earliest reported example of laboratory joint velocity and resistivity measurements on sandstones were performed by Carrara *et al*. (1999). They measured compressional wave velocity and electrical resistivity on 11 clean sandstones with different brine saturations at atmospheric pressures only. Carrara *et al*. (1999) did not give an explicit relationship between seismic velocity and electrical resistivity for samples under the same saturation conditions because their aim was to test and implement an electro-seismic model proposed by Carrara *et al*. (1994) for the evaluation of rock porosity and the degree of fluid saturation. Gomez (2009) measured electrical resistivity on 9 partially saturated clean sandstone samples. She used Archie's equation (Archie, 1942) and a pressure power law (Schön, 1996) to get the formation resistivity factor F of fully saturated rocks at different pressures. She gave the following linear relationship between the logarithm of F and the compressional wave velocity V_p in fully saturated rocks (V_p was measured under the same pressure conditions as the calculated F):

$$\log(F) = 0.782 \cdot V_p(km/s) - 1.954 .$$

Some disadvantages of Gomez's study are that the empirical equations (Archie, 1942; Schön, 1996) used to estimate the formation resistivity factor are untested and the electrical resistivity measured at the frequency of 1 kHz might be different from that experienced at the low frequencies employed in marine CSEM (Denicol and Jing, 1998). Apart from the apparently limited availability of laboratory measurement studies, joint elastic-electrical properties have also been investigated using well logging data (e.g., Sheng and Callegari, 1984; Salem, 2001; Hacikoylu *et al*., 2006). Unfortunately, the latter studies suffer from lack of precision with regard to rock properties, unlike laboratory studies where all parameters can be quantified with higher certainty.

In addition to getting the joint elastic-electrical relationships from measurements, theoretical approaches have been tried. Carcione *et al*. (2007) obtained cross-property relations between electrical conductivity (the reciprocal of resistivity) and elastic velocity using different combinations of electromagnetic and elastic models. Similar

work includes Brito Dos Santos *et al*. (1988) and Mukerji *et al*. (2009). However, the different theoretical relations have to be tested against observations, such as laboratory experiments on synthetic or real rocks, before they can be applied to practical work (Carcione *et al*., 2007).

We collected such a dataset for the purpose of gaining new insights into joint elastic-electrical rock properties and for rock physics model validation. We discovered novel joint relationships between electrical resistivity and the elastic velocity and attenuation of both compressional and shear waves (here called joint elastic-electrical relations for short) for the 63 samples at a differential pressure of 60 MPa corresponding to high pressure trends (equivalent to about 4 - 5 km burial depth in the Earth) given the similar joint elastic-electrical behaviours at other pressures, although the empirical equations vary slightly between pressures; a detailed discussion of pressure effects for this dataset is given in Chapter 5. Also, we were able to quantify the relationships among reservoir petrophysical parameters (porosity, permeability and clay content) and the joint elastic-electrical properties. These results show for the first time the potential for estimating *in situ* sandstone permeability using joint velocity-apparent formation factor crossplots from co-located seismic and CSEM surveys.

6.2. Experimental results and discussion

6.2.1. Joint elastic-electrical properties

Joint elastic-electrical properties in this chapter refer to cross-property relations between apparent electrical formation factor F^* (defined as ρ_0/ρ_w, where ρ_0 is the resistivity of a sample fully saturated with an electrolyte of resistivity ρ_w) and elastic velocity (V_p, V_s for P- and S-wave respectively) and attenuation (Q_p^{-1} and Q_s^{-1} for P- and S-wave respectively, where Q is the quality factor). These relations are useful when some rock properties can be measured more easily than other properties (Carcione *et al*., 2007), and are particularly important for joint seismic-CSEM data interpretation.

Figures 6.1a and b show the cross-property relations between the logarithm of F^* (ρ_w = 0.213 Ωm for 35 g/l brine at 19 °C) and V_p and V_s for all 63 samples. Apparent formation factor increases with increasing velocity, and two approximately linear

trends appear. Samples in one group (solid circles) have relatively high velocities (both P- and S-waves for the same F^* values) and low apparent formation factors (for the same velocity; Group A, fitted by the solid lines in Figure 6.1); samples in the other group (open circles) have relatively low velocities and high resistivities (Group B, trend given by the dashed lines in Figure 6.1) with a larger scatter. The most apparent outlier in Figure 6.1b which shows V_s of about 2000 m/s and F^* of around 100 is the sample CZ6. This is possibly because CZ6 contains about 6.7% smectite clay minerals which expand on saturation resulting in different resistivity-velocity dependence from the other sandstones without smectite. The deviation from the Group B trend is less apparent in Figure 6.1a for V_p, suggesting that the smectite primarily affects the shear modulus of the rock, and less so the resistivity and bulk modulus, compared to rocks without smectite.

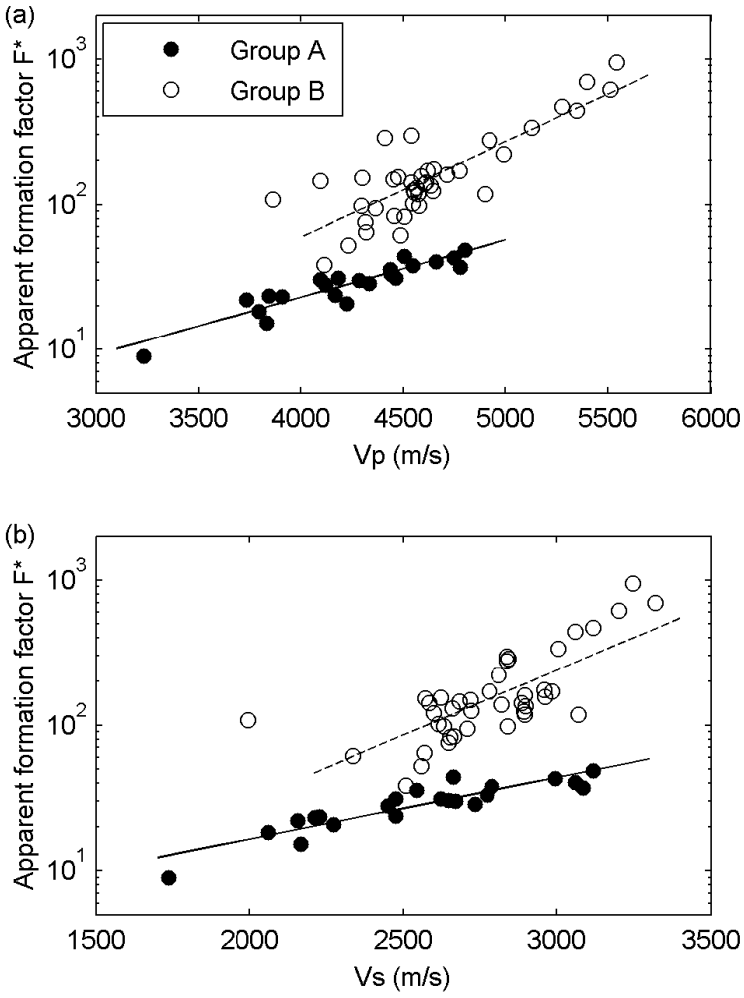

Figure 6.1. Scatter diagrams showing the relationship between apparent formation factor F^* and velocity for (a) P-waves and (b) S-waves.

The following least-squares linear regression equations were obtained for the two groups, where V_p and V_s are in km/s and R^2 is the correlation coefficient.

P-waves and electrical resistivity:

$$\log(F^*) = 0.396 \cdot V_p - 0.223 \text{ with } R^2 = 0.849, \text{ Group A} \quad (6.1)$$

$$\log(F^*) = 0.657 \cdot V_p - 0.853 \text{ with } R^2 = 0.685, \text{ Group B} \quad (6.2)$$

S-waves and electrical resistivity:

$$\log(F^*) = 0.423 \cdot V_s + 0.372 \text{ with } R^2 = 0.819, \text{ Group A} \quad (6.3)$$

$$\log(F^*) = 0.895 \cdot V_s - 0.304 \text{ with } R^2 = 0.550, \text{ Group B.} \quad (6.4)$$

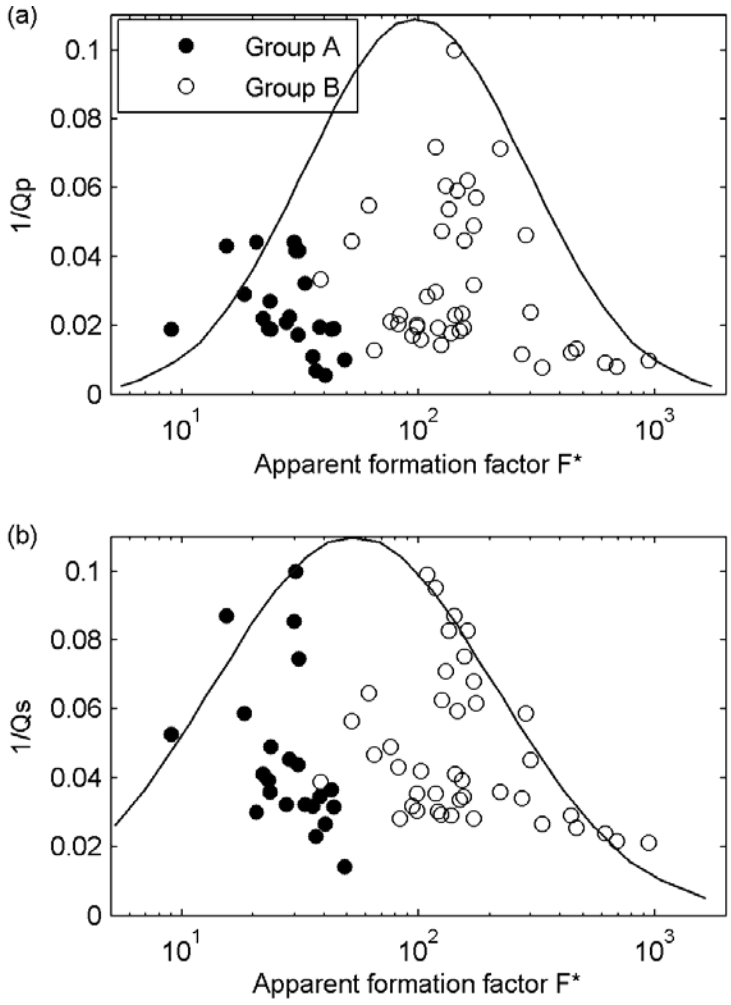

Figure 6.2. Scatter diagrams showing the relationship between apparent formation factor F^* and attenuation for (a) P-waves and (b) S-waves.

The cross-property relations between F^* and Q_p^{-1} and Q_s^{-1} are shown in Figures 6.2a and b respectively. In general, the joint resistivity-attenuation relations are more

complicated and scattered than the resistivity-velocity relations. However, a tentative interpretation can be offered as follows. The P-wave data in Figure 6.2a suggest Q_p^{-1} increases initially with F^* up to about $F^* = 100$ where Q_p^{-1} reaches a maximum, then Q_p^{-1} decreases with F^* above 100, forming a bell-shaped correlation Q_p^{-1} and F^* as outlined by the curve. The S-wave data in Figure 6.2b show a similar trend to the P-wave data, however there appears to be larger scatter and Q_s^{-1} arrives at its maximum value at $F^* < 100$. The P-wave trends could be justified on the basis that apparent formation factor is behaving in an analogous fashion to mean grain size in McCann and McCann (1969) and Hamilton (1972a) or sorting in Best *et al*. (2001). It is interesting to note that Groups A and B from Figure 6.1 broadly correspond to the increasing and decreasing attenuation limbs respectively of the proposed trend in Figure 6.2 (the location of the proposed attenuation peak is arbitrary and based on one data point only).

Understanding to the underlying causes of the observed trends in Figures 6.1 and 6.2 would clearly aid the interpretation of reservoir rock properties from joint seismic-CSEM surveys. We will investigate possible causes of these inter-relationships in the next sections.

6.2.2. Porosity and the joint properties

Porosity is one of the most important parameters that affect both elastic and electrical properties of reservoir rocks (Han *et al*., 1986; Klimentos and McCann, 1990; Klimentos, 1991; Best *et al*., 1994; Archie, 1942). Specifically, porosity reduces the velocity of both compressional and shear waves by reducing the bulk and shear moduli of the solid framework; this frame moduli effect usually overrides the opposite effect on velocity of reduced rock density caused by increasing porosity. Increased porosity generally increases the elastic attenuation of saturated rocks by providing more opportunity for viscous interaction between the pore fluids and the solid framework (Biot, 1956a,b; Murphy *et al*., 1986) by which process rocks convert compressional and shear wave energy into heat (Klimentos and McCann, 1990). Increasing porosity decreases the electrical resistivity of rocks saturated with ionic fluids because diffusion of free ions through the electrolyte is the main contribution to current flow in clean rocks.

The effects of porosity on the joint resistivity-velocity properties are shown in Figures 6.3a and b by colour-coding porosity. As expected both resistivity and velocity decrease with increasing porosity for samples in both groups illustrated in Figure 6.1, and the two groups converge at porosities around 17%. Samples with similar porosities in the range 11% – 14% fall in both groups. This leads to the conclusion that although porosity has a strong effect in determining both elastic and electrical properties separately, it does not control the resistivity-velocity groups. Hence, the cross-properties are controlled by lithological properties other than porosity and could provide a way of discriminating between rock types.

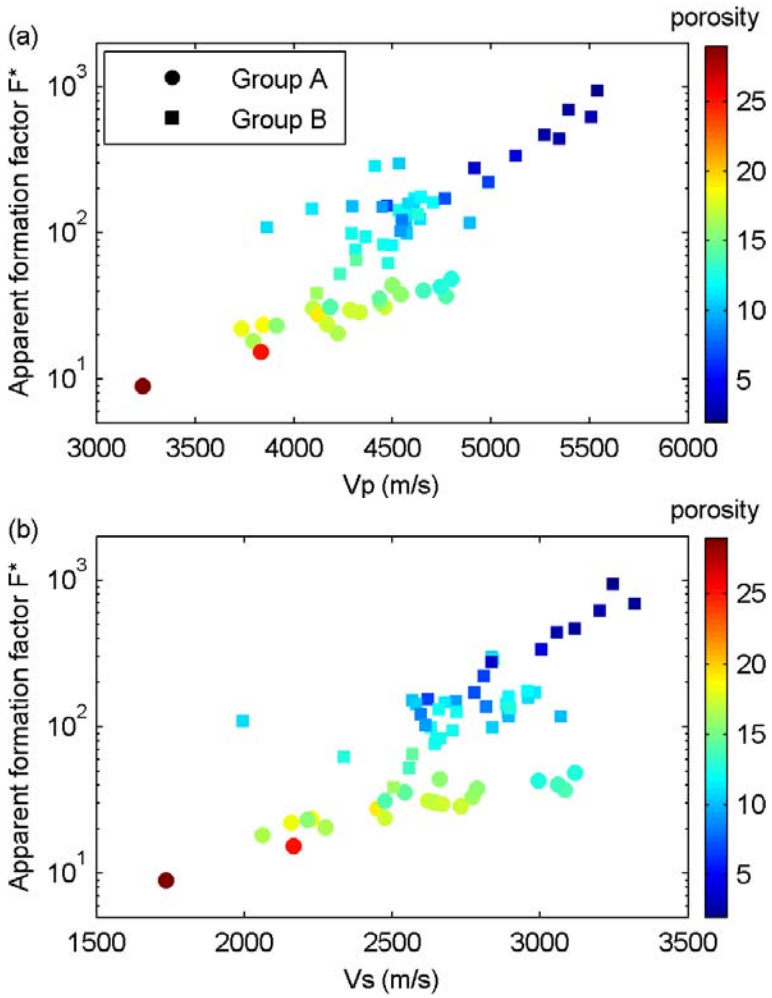

Figure 6.3. Scatter diagrams showing the relationship between apparent formation factor F^* and P-wave (a) and S-wave (b) velocity colour-coded by porosity (in percentage).

Figures 6.4a and b show the effects of porosity on the joint properties between apparent formation factor and attenuation of compressional and shear waves respectively. The results are consistent with our tentative explanation that apparent formation factor is behaving in a similar fashion to mean grain size or sorting in its

effect on P-wave attenuation (i.e., it gives rise to the "bell-shaped" curve); in this case, intermediate porosities of 10% – 15% (F^* values of 100 ± 50) show the highest attenuations. Such a clear pattern is not seen for S-waves in Figure 6.4b, although we could say that the attenuation maximum occurs over a much broader range of F^* values below about 100 (and hence a broader range of porosity) than for P-waves in Figure 6.4a.

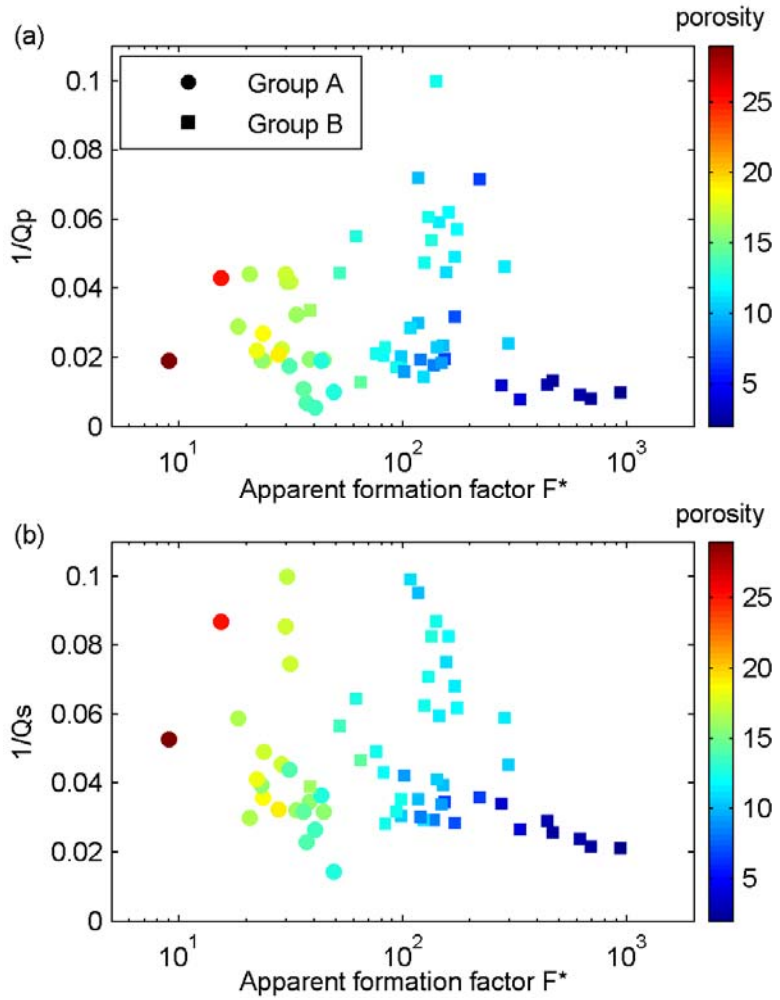

Figure 6.4. Scatter diagrams showing the relationship between apparent formation factor F^* and P-wave (a) and S-wave (b) attenuation colour-coded by porosity (in percentage).

6.2.3. Permeability and the joint properties

The relationships between the logarithm of permeability and the joint apparent formation factor - elastic velocity properties are shown in Figures 6.5a and b. For all samples taken together, F^* decreases strongly with increasing permeability while V_p and V_s seem to be independent of permeability in agreement with the velocity-

permeability data of Klimentos and McCann (1990) and Best *et al*. (1994). For example, permeabilities range between < 1 mD to 100 mD for a V_p of 4500 m/s. However, Figure 6.5 also shows that most samples in Group A have permeabilities higher than approximately 1 mD, whereas samples in Group B have permeabilities less than 1 mD. There is also evidence for a weak, but systematic, increase in both apparent formation factor and elastic velocity with increasing permeability in Group A samples (and with decreasing permeability in Group B samples). This correlation between permeability and resistivity confirms the results of Huntley (1986) for clean sandstones (see Figure 4.9).

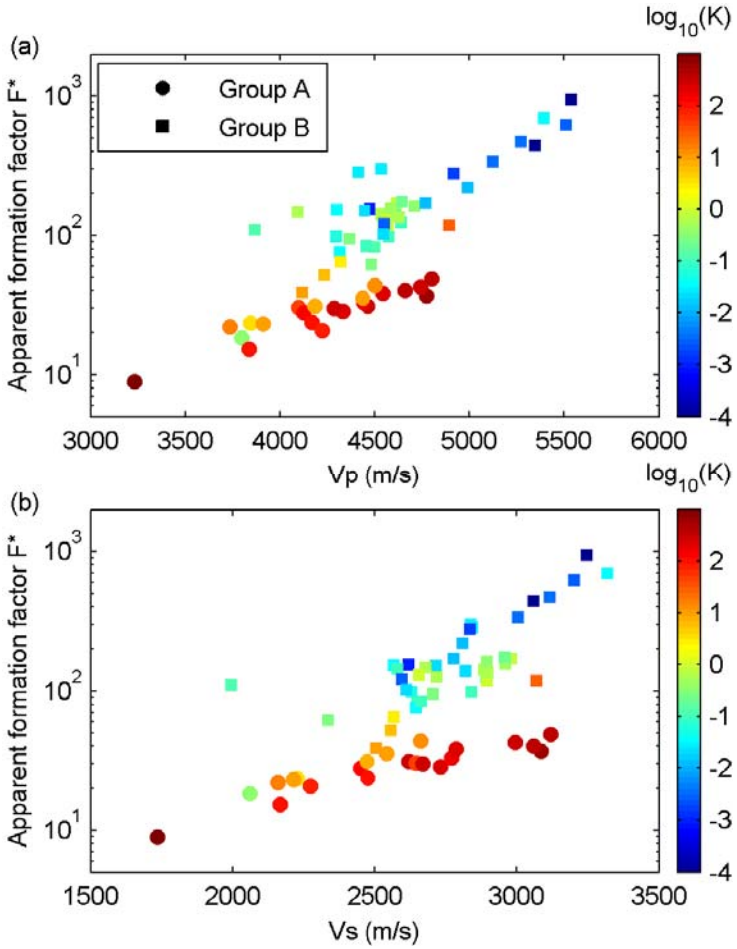

Figure 6.5. Scatter diagrams showing the relationship between apparent formation factor F^* and P-wave (a) and S-wave (b) velocity colour-coded by logarithmic permeability (permeability in mD).

Figures 6.6a and b show the relationships between permeability and the joint resistivity-attenuation properties. Again, the P-wave observations support F^* behaviour analogous to mean grain size or sorting where the intermediate F^* values correspond to intermediate permeabilities around the Q_p^{-1} maximum.

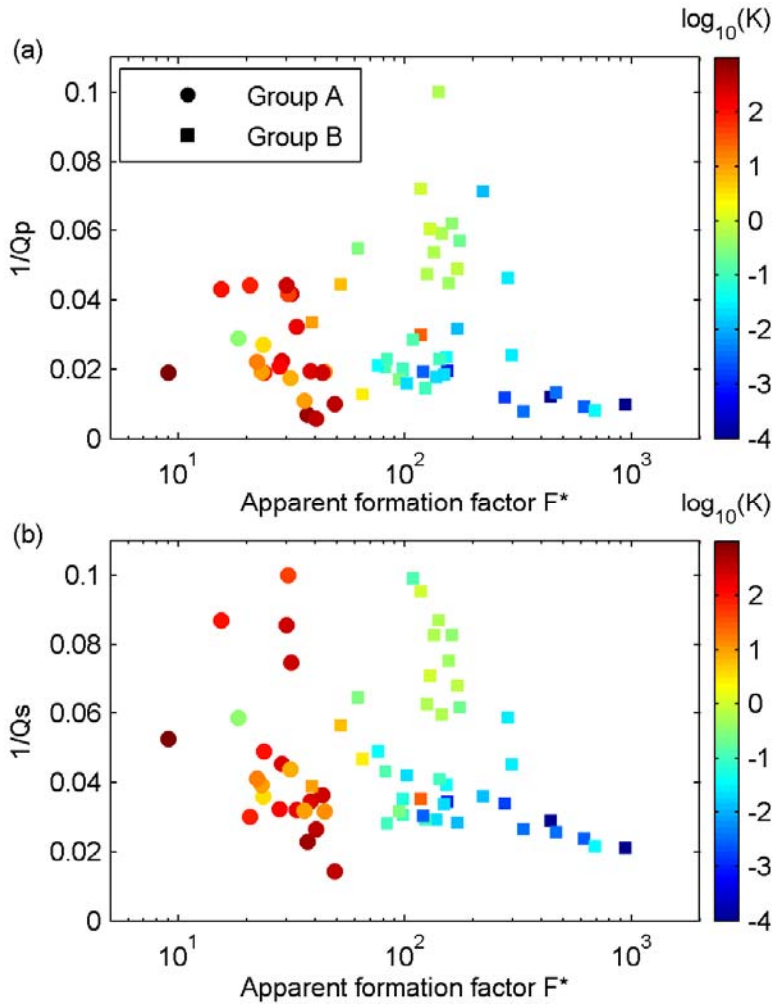

Figure 6.6. Scatter diagrams showing the relationship between apparent formation factor F^* and P-wave (a) and S-wave (b) attenuation colour-coded by logarithmic permeability (permeability in mD).

The experimental results of Klimentos and McCann (1990) and Best *et al*. (1994) showed that sandstone samples with permeabilities higher than about 100 mD tend to have low attenuations. This is consistent with our observations for P-waves if we consider the previous authors' results to coincide with the lower limb of the proposed bell-shaped Q_p^{-1} - F^* curve. That is Q_p^{-1} increases initially with permeability (and F^*) and then decreases above some critical value of permeability (and F^*). In the case of S-waves, the range of permeabilities (and F^*) giving high attenuations is much broader. The P-wave observations are qualitatively similar to predictions from the BISQ model (unified Biot and squirt flow) given in Figure 6 of Dvorkin and Nur (1993) if one considers F^* to be correlated with permeability.

Permeability looks to account for the grouping of both joint resistivity-velocity and joint resistivity-attenuation properties of the sandstone samples; however permeability itself depends on other petrophysical properties (e.g., porosity, grain size and shape, sorting, cementation and clay content as alluded to above). Although permeability can be used to discriminate between samples in the two groups in Figure 6.1 and to explain a possible bell-shaped curve in Figure 6.2, we will investigate whether there are other petrophysical parameters that can explain these observations.

6.2.4. Clay content and the joint properties

Clay minerals have a large impact on both elastic and electrical properties of reservoir sandstones. Small amounts of clay situated between grain boundaries in sandstones tend to soften grain contacts, leading to a dramatic decrease in both compressional and shear wave velocities (Han *et al*., 1986; Sams and Andrea, 2001). Enhanced viscous interaction between pore fluids and the large surface area and microporosity associated with clay minerals gives rise to higher attenuation (Klimentos and McCann, 1990). The clay effect on electrical resistivity can work in two ways: on the one hand the excess ions carried by clay minerals provide extra conductive paths in addition to the pore electrolyte conductivity leading to a decrease in electrical resistivity; and on the other hand clay minerals in the pores block the connectivity of the pore fluids, which in turn causes an increase in resistivity. The detailed clay effects on electrical resistivity are discussed in Chapter 4.

Figures 6.7a and b show the influence of volumetric clay content on the joint resistivity-velocity properties of the sandstone samples. A correlation is found between clay content and the joint resistivity-velocity properties, i.e., most of samples in Group A defined in Figure 6.1 have volumetric clay content less than about 10%, whereas samples in Group B have clay content higher than about 10% with a few exceptions. This correlation is similar for the relationships between clay content and the joint resistivity-attenuation properties shown in Figures 6.8a and b, although with more scatter.

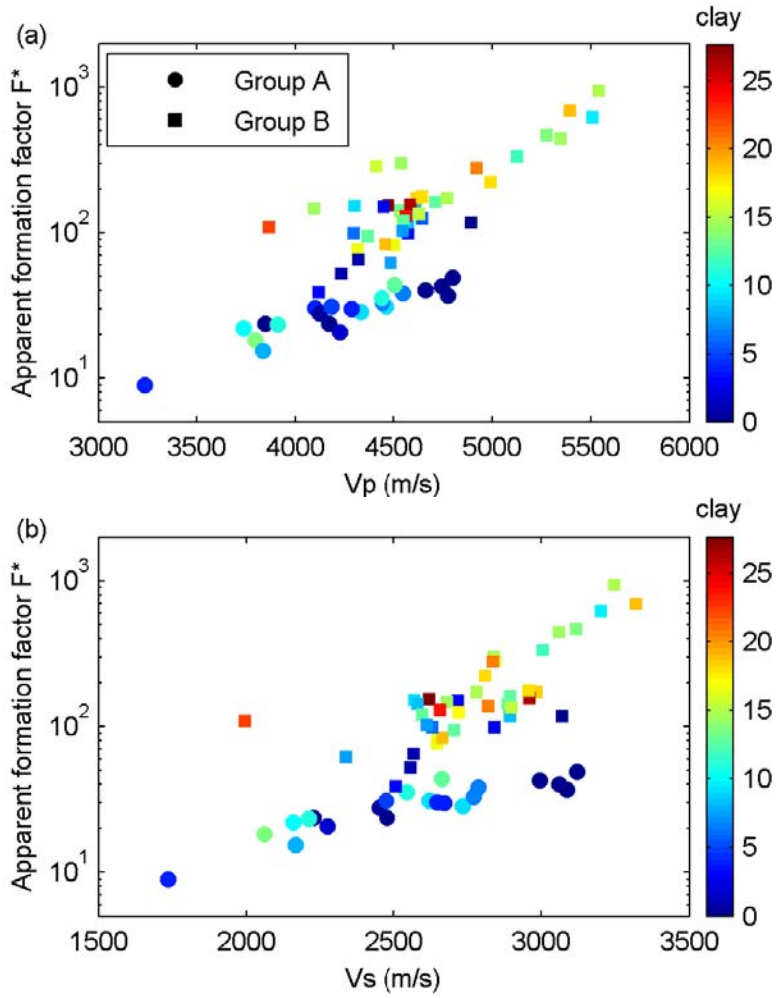

Figure 6.7. Scatter diagrams showing the relationship between apparent formation factor *F** and P-wave (a) and S-wave (b) velocity colour-coded by volume clay content (in percentage).

The existence of pore-filling clay minerals contributes little to the bulk and shear moduli of the rocks, but it increases the density slightly and therefore causes a small reduction in both compressional and shear wave velocities. On the other hand for resistivity, the initial increase in pore-filling clay minerals tends to reduce the mean pore size and the overall porosity, as well as to block the connectivity between pores (and hence of electrolyte in the case of brine saturation). This reduction in porosity and pore fluid connectivity leads directly to a significant increase in electrical resistivity. This explains why 'clean' samples with few clay minerals have relatively lower resistivities (Group A) for a given velocity, and why clay-rich sandstones show higher resistivities (Group B) for the same velocity. This is an explanation that takes into account the effects of both clay content and porosity, because porosity and clay content are highly negatively correlated for most of our samples as shown in Figure 4.7.

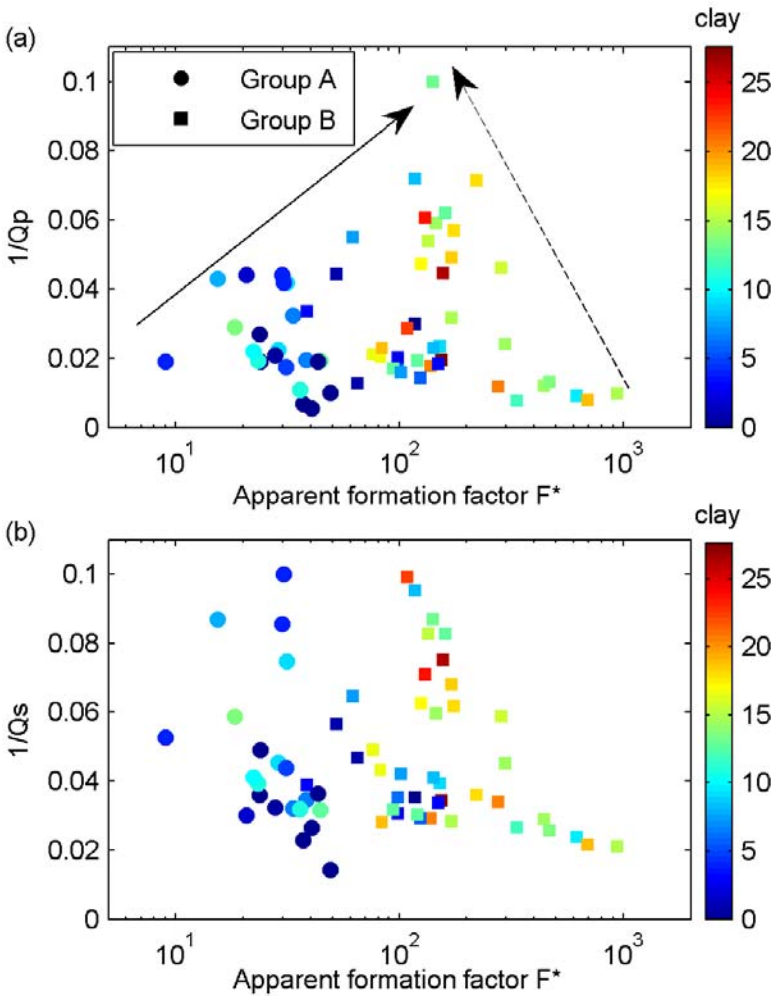

Figure 6.8. Scatter diagrams showing the relationship between apparent formation factor F^* and P-wave (a) and S-wave (b) attenuation colour-coded by volume clay content (in percentage).

Least-squares linear regression equations between F^* and V_p and V_s were obtained with better correlation coefficients for Groups A and B by introducing porosity and clay content.

P-waves and electrical resistivity:

$$\log(F^*) = 0.274 \cdot V_p - 1.669 \cdot \varphi + 0.181 \cdot C + 0.559 \quad (6.5)$$

with $R^2 = 0.903$, Group A

$$\log(F^*) = 0.343 \cdot V_p - 3.749 \cdot \varphi + 0.765 \cdot C + 0.864 \quad (6.6)$$

with $R^2 = 0.801$, Group B.

S-waves and electrical resistivity:

$$\log(F^*) = 0.303 \cdot V_s - 1.834 \cdot \varphi + 0.445 \cdot C + 0.964 \quad \text{with } R^2 = 0.909, \text{ Group A} \tag{6.7}$$

$$\log(F^*) = 0.459 \cdot V_s - 4.928 \cdot \varphi + 0.690 \cdot C + 1.301 \quad \text{with } R^2 = 0.841, \text{ Group B.} \tag{6.8}$$

Parameters V_p and V_s are in km/s, and φ and C represent fractional porosity and volumetric clay content respectively in equations 6.5 – 6.8, which indicate a much higher (more than 3.8 times) porosity effect than the clay effect in controlling the joint resistivity-velocity relations for samples in both groups.

Similarly to the explanation for the joint resistivity-velocity properties, the joint resistivity-attenuation relations can also be explained by combining the effect of porosity and clay content. Like for porosity and permeability, there also appears to be a strong correlation between F^* and clay content and their effects on Q_p^{-1} if a bell-shaped curve is considered. The highest Q_p^{-1} values in Figure 6.8a occur at intermediate volumetric clay contents of about 15% (corresponding to intermediate porosities and permeabilities).

In Chapter 4 we suggest a possible link between electrical resistivity, porosity and clay content based on the concept of a critical porosity dividing regimes of pore-filling versus load-bearing clay minerals (Marion *et al*., 1992). A similar qualitative explanation could be offered here for the two limbs of the F^* - Q_p^{-1} bell-shaped curve. However, it is interesting to note that while the critical clay blocking concentration (Marion *et al*., 1992) for this dataset was about 10% (see Chapter 4), there seems to be no sharp transition in Q_p^{-1} at volumetric clay content = 10%, but instead a fairly broad range of clay contents corresponding to the Q_p^{-1} maximum at $F^* = 100 \pm 50$. This may be partly due to the difficulty of estimating clay content to any degree of accuracy (± 5% from XRD analysis is considered a good estimate) making it difficult to resolve exactly the transition from pore-filling to load-bearing clay (a similar transition zone of porosity and clay content was noted for apparent formation factor in Chapter 4). However, it could also indicate a genuine range of clay contents over which high P-wave attenuations can be expected. Such a transition range could be caused by an imperfect distribution of clay minerals between pore-filling and load-bearing as would happen with some detrital clay grains in a sandstone otherwise

dominated by pore-filling clay, or diagenetic alteration of feldspars into load-bearing clay grains. Despite this, Figure 6.8a seems to support this critical porosity model concept with highest attenuations when clay content is about equal to the initial cemented sand porosity. This observation needs further investigation.

Similar arguments hold for S-wave attenuation in Figure 6.8b, but with a much broader Q_s^{-1} peak than for Q_p^{-1}. This is consistent with the idea that pore-filling clay does not affect the sandstone frame stiffness while load-bearing clay does, and presumably this has some influence on S-wave attenuation. By contrast, both pore-filling and load-bearing clay affect the saturated rock bulk modulus (and thus P-wave attenuation), hence two limbs of the bell-shaped curve are seen in Figure 6.8a.

In Chapter 4 we conclude that for the samples with porosity less than 9% (corresponding to $F^* = 100$), clay contents higher than about 10% are above their critical clay blocking concentration and show an effect of increasing porosity, and therefore decreasing F^*, no matter whether clay shows a conductive effect or not. For samples with porosity greater than 9%, most of their clay contents are less than 10% which is below the critical clay blocking concentration. In this case increasing clay content tends to decrease the porosity, and hence increase apparent formation factor, as the clay conductive effect (if present) is not strong enough to lower resistivity in this porosity range.

Combining this finding with the observations in Figure 6.8a, it is reasonable to conclude that for clay contents lower than the critical clay blocking concentration, increasing clay content tends to reduce porosity and hence increase F^*. Also, because clay minerals provide a higher proportion of microporosity for a given total porosity (although total porosity reduces overall), this leads to a greater interaction between pore fluid and rock framework giving rise to heightened elastic wave attenuation; this process is shown by the solid arrow in Figure 6.8a. On the other hand, for clay contents higher than the critical clay blocking concentration, the increase in clay content will increase porosity and therefore reduce F^*. Due to the joint effect of higher porosity and higher microporosity associated with the clay minerals, elastic wave attenuation increases more rapidly, shown by the dashed arrow in Figure 6.8a.

As suggested above, the parameter that explains the joint elastic-electrical properties should correlate with permeability. Figure 6.9 shows the relationship between

permeability and the volumetric clay content for all 63 samples by colour-coding porosity. For these samples, permeability and porosity decrease with increasing clay content. This is expected because with more clay mineral assemblages inside the pores, the pore size reduces and the connection between pores is affected and accordingly the porosity and permeability decrease. With this explanation, the observed relationships among permeability, porosity, clay content and the joint elastic-electrical properties become much clearer.

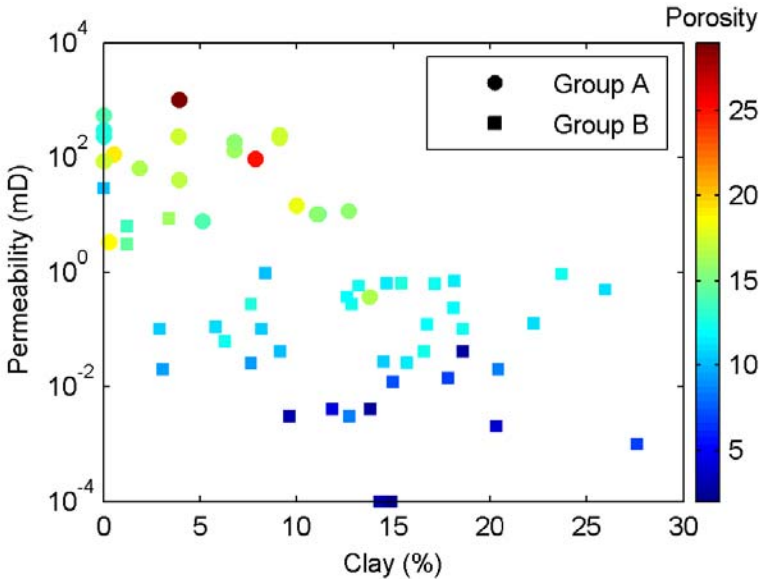

Figure 6.9. Scatter diagram showing the relationship between the logarithm of permeability and volumetric clay content by colour-coding porosity (in percentage).

6.3. Conclusions

Laboratory joint elastic-electrical measurements were successfully performed on 63 sandstone samples with a wide range of petrophysical properties. The joint resistivity-velocity and resistivity-attenuation of both compressional and shear waves and the effects of primary petrophysical parameters on the joint elastic-electrical properties were investigated. The following conclusions can be drawn from the results:

(1) Elastic velocity (both compressional and shear) is approximately positively linearly correlated with apparent formation factor F^* on a semi-logarithmic scale. The sandstones fall into two discernible groups (Group A and Group B) on the cross plot between elastic velocity and apparent formation factor. The slope for the clay-rich sandstones is higher than that of the clean sandstones.

(2) P-wave attenuation seems to follow a bell-shaped trend with apparent formation factor analogous to P-wave attenuation dependence on mean grain size and sorting reported in the literature for marine sediments. S-wave attenuation shows only part of this bell-shaped curve with high Q_s^{-1} values seen at lower F^* values.

(3) Although porosity is one of the most important parameters that affect both elastic and electrical properties of reservoir rocks, no direct correlation was seen between porosity and the distinct groups for both joint resistivity-velocity and resistivity-attenuation properties. Since sandstone samples with similar porosities exist in both groups, joint elastic and electrical data can be used to discriminate between samples of similar porosity but different lithological properties. The latter seem to be the main factor controlling the grouping of data points in joint property space.

(4) The combination of the clay-porosity effect divides the samples in the joint resistivity-velocity plots into two groups – clean sandstones and clay-rich sandstones. The clay content below or above critical clay concentration controls both porosity and the joint resistivity-attenuation properties.

(5) Since clay minerals and porosity have a determining effect on sandstone permeability, there is also a strong relationship between permeability and the joint elastic-electrical properties. Considering conclusion 3, the petrophysical properties that best discriminate between sandstones of similar porosities in joint elastic-electrical property space are either clay minerals or permeability.

The results show for the first time how joint elastic-electrical properties can give better discrimination between lithologies, for example between clean (high permeability) and clay-rich (low permeability) sandstones. While the electrical results are directly applicable to CSEM survey data, there is evidence that electrical resistivity changes with frequency and rock type so that different relationships are expected for electrical well logging frequencies. It remains to be seen how the ultrasonic properties will change with measurement frequency down to the sonic and seismic ranges used in exploration seismology; this is a topic of ongoing investigations. However, the clearly observed links between electrical resistivity at 2 Hz (in the form of apparent formation factor) and ultrasonic velocity (and to a lesser

extent with attenuation) are exciting developments. It is reasonable to expect the underlying mechanisms to be present at all measurement scales.

Most importantly, there appears to be a strong link between elastic wave velocity (for both P- and S-waves) and apparent formation factor (equations 6.1 – 6.8) that could be used to discriminate the permeability of reservoir rocks from inversion of joint seismic-CSEM survey data. What is required are better rock physics models to describe these phenomena and facilitate inversion of field data. The empirical relations given here could be used as a crude guide in the first instance.

Chapter 7

Effective medium models for the joint elastic-electrical properties of reservoir sandstones

This chapter forms a paper submitted for publication to *Geophysical Prospecting*, Han T., Best A.I., MacGregor L.M., Sothcott J. and Minshull T.A. 2010. Effective medium models for the joint elastic-electrical properties of reservoir sandstones.

Abstract: Improvements in the joint inversion of seismic and marine controlled source electromagnetic datasets will require better constrained models of the joint elastic-electrical properties of reservoir rocks. Various effective medium models were compared to a novel laboratory dataset of elastic velocity and electrical resistivity (obtained on 67 reservoir sandstone samples saturated with 35 g/l brine at a differential pressure of 8 MPa) with mixed results. Hence, we developed a new 3-phase effective medium model for sandstones with pore-filling clay minerals based on the combined self-consistent approximation and differential effective medium model. We found that using a critical porosity of 0.5 and an aspect ratio of 1 for all three components gave accurate model predictions of the observed magnitudes of P-wave velocity and electrical resistivity and the divergent trends of clean and clay-rich sandstones at higher porosities. Using only a few well-constrained input parameters, the new model offers a practical way to predict *in situ* porosity and clay content in brine saturated sandstones from co-located P-wave velocity and electrical resistivity datasets.

7.1. Introduction

Improved reservoir management and production optimisation demands require accurate characterisation of reservoir rock and fluid properties. Advances in seismic data acquisition and processing have led to dramatic improvements in remote imaging of earth structure. However when only a single data type is considered ambiguities in the interpretation of reservoir properties can remain. There is growing support for the application of an integrated approach to reservoir characterisation, in which both seismic and marine controlled source electromagnetic (CSEM) data are used so that strengths in one technology can be used to compensate for weaknesses in the other. However an integrated interpretation approach such as this is only possible within a consistent rock physics framework which describes both electrical and elastic parameters, linking them to the reservoir rock and fluid properties of interest (Du and MacGregor, 2009).

Effective medium models are a kind of rock-physics model usually employed by geophysicists to describe the macroscopic properties of a rock based on the physical properties, the relative fractions of its components and the geometric details of how

the components are arranged relative to each other. The geometric details of the components are essential to give accurate estimation of rock properties as without them effective medium models give only possible bounds (e.g., Reuss, 1929; Hashin and Shtrikman, 1962, 1963; Milton, 1981). Gelius and Wang (2008) reviewed various effective medium models for electrical conductivity (the reciprocal of electrical resistivity) and proposed an extended effective medium scheme for electrical conductivity that potentially takes into account the effect of important parameters like grain-shape distribution, grain alignment, shalyness, salinity, saturation, temperature and stress to model reservoir production effects. Carcione *et al*. (2007) introduced a range of effective medium models for both electrical conductivity and elastic velocity and the relations between them. They also combined these models to get the cross-property relations between the electrical conductivity and seismic velocity of rocks. However the different theoretical joint relations have to be tested against observations, such as laboratory experiments on synthetic or real rocks, before they can be applied to practical work (Carcione *et al*., 2007).

Carrara *et al*. (1994) proposed an electro-seismic model by assuming all phases (matrix, clay, water and air) in the rock are contiguous, i.e., in parallel for the case of electrical conductivity and in series with regard to the propagation of elastic waves for the purpose of evaluating porosity and saturation; the validity of this model was confirmed experimentally by Carrara *et al*. (1999).

We collected a joint elastic-electrical dataset on 67 typical reservoir sandstones showing a wide range of petrophysical properties under full brine saturation conditions at a differential pressure of 8 MPa; measurement frequencies were 2 Hz for electrical resistivity (relevant to low frequencies used in marine CSEM) and 1.0 MHz for P-wave velocity. Detailed sample characterisation and measurement procedures are presented in Chapter 3. Various effective medium models for the joint elastic-electrical properties of reservoir sandstones were implemented and compared to this novel dataset. Carcione's cross relations (Carcione *et al*., 2007) did not adequately describe our clay-rich sandstone observations. Also, Carrara's electro-seismic model (Carrara *et al*., 1994) did not match our clean sandstone results although it showed the observed clay effect on the joint elastic-electrical properties of our sandstones. Therefore, we developed a new 3-phase effective medium model based on the combined self-consistent approximation and differential effective medium model for

quartz, brine and pore-filling clay minerals. The results show that the model gives reasonable agreement with our observations for both clean and clay-rich sandstones when a critical porosity of 0.5 and an aspect ratio of 1 are used for all three phases.

7.2. Effective medium models

This section first implements and compares existing effective medium models to our joint elastic-electrical dataset in sequence for clean and clay-rich sandstones; it then develops a 2-phase model for inclusions with arbitrary aspect ratio; a 3-phase model for quartz, brine and pore-filling clay minerals is finally developed and compared well to the joint dataset.

7.2.1. Carcione's method

Carcione *et al*. (2007) conducted a theoretical study of the joint elastic-electrical behaviour of reservoir rocks by combining elastic velocity calculated from Gassmann's equation (Gassmann, 1951) with electrical conductivity obtained from Archie's equation (Archie, 1942), Hermance's model (Hermance, 1979), the CRIM model (Schön, 1996) and the self-similar model (Sen *et al*., 1981). They found a reasonable fit to well logging data by using the Gassmann/CRIM and Gassmann/self-similar effective medium relations.

Table 7.1. Physical properties of the components used in the effective medium models.

Medium	Bulk modulus K (GPa)	Shear modulus G (GPa)	Resistivity ρ (Ωm)	Density d (g/cm^3)
Quartz	36.6	45	10^5	2.65
Clay	20.9	6.85	50	2.58
Brine	2.29	0	0.213	1.025

Figure 7.1 shows a comparison of the above models with the experimental data collected on the 67 reservoir sandstones with porosity from 2% to 29% at differential pressure of 8 MPa. The models are calculated for clean sandstones fully saturated with brine using the medium properties given in Table 7.1, where the brine properties are for the 35 g/l brine used in our experiments. Also shown are the Gassmann/HS bounds (Hashin and Shtrikman, 1962).

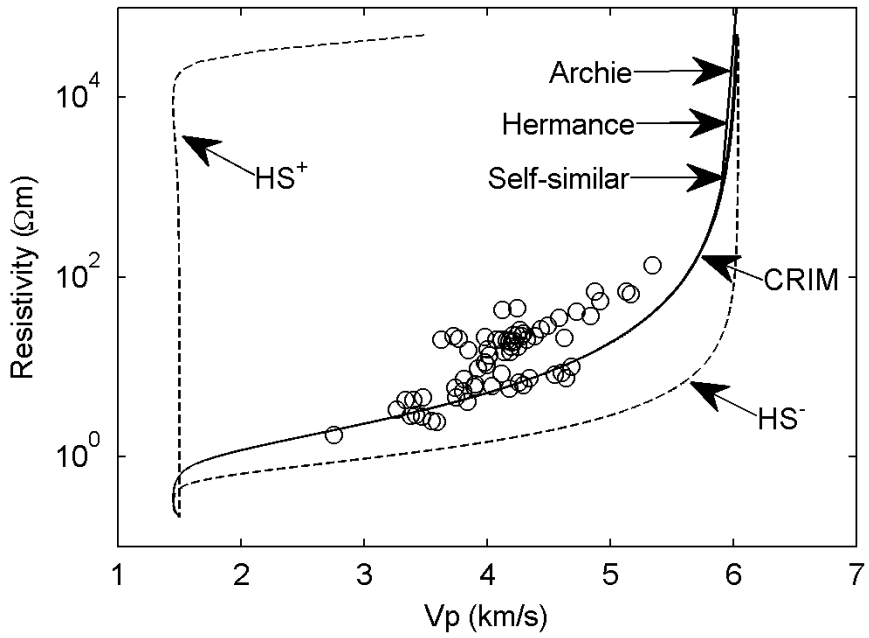

Figure 7.1. Comparison of Carcione's cross relations (Carcione *et al*., 2007) between elastic velocity and electrical resistivity with experimental data. Elastic velocity is calculated from Gassmann's equation, and electrical resistivity is obtained using Archie, Hermance, self-similar, CRIM and HS electrical models respectively.

All the 4 models fall within the HS bounds confirming their validity. In spite of the limited input information (physical properties and volume fractions of components) all models show a good fit to the general trend of the lower grouping of laboratory data. According to Chapter 6, these datapoints correspond to clean sandstones with porosity consisting of mainly large open pores. However the 4 models are too close to each other to distinguish between them; they also lack any clay component and grain shape information that are needed to simulate the clay-rich sandstones in the upper grouping of datapoints. The latter might have lower aspect ratio pores associated with clay minerals.

7.2.2. Carrara's model

The electro-seismic model proposed by Carrara *et al*. (1994) takes into account the effect of clay on both elastic velocity and electrical resistivity. The model assumes contiguous rock phases, specifically in parallel for the case of electrical conductivity and in series for the case of elastic wave propagation, and gives

$$\frac{1}{\rho} = \frac{(1-\varphi)(1-P_{cl})}{\rho_m} + \frac{(1-\varphi)P_{cl}}{\rho_{cl}} + \frac{\varphi S_w}{\rho_w} + \frac{\varphi(1-S_w)}{\rho_a}, \tag{7.1}$$

$$\frac{1}{V} = \frac{(1-\varphi)(1-P_{cl})}{V_m} + \frac{(1-\varphi)P_{cl}}{V_{cl}} + \frac{\varphi S_w}{V_w} + \frac{\varphi(1-S_w)}{V_a}, \tag{7.2}$$

where ρ and V, ρ_m and V_m, ρ_{cl} and V_{cl}, ρ_w and V_w and ρ_a and V_a are the resistivity and velocity of the effective medium, the matrix, the clay mineral, the water and the air respectively, S_w is the water saturation fraction in the porosity φ, and P_{cl} corresponds to the volume clay fraction in the solid matrix. In order to adjust P_{cl} to the conventionally used concept of volumetric clay content of the whole rock and to simulate our full brine saturation condition (S_w = 1), equations 7.1 and 7.2 can be transformed into

$$\frac{1}{\rho} = \frac{1-\varphi-C}{\rho_m} + \frac{C}{\rho_{cl}} + \frac{\varphi}{\rho_w}, \tag{7.3}$$

$$\frac{1}{V} = \frac{1-\varphi-C}{V_m} + \frac{C}{V_{cl}} + \frac{\varphi}{V_w}, \tag{7.4}$$

where C represents the volumetric clay content over the whole rock.

Figure 7.2 shows the model results compared to the experimental data by colour-coding volumetric clay content. The matrix is assumed to be quartz; electrical resistivities and elastic moduli of each component are listed in Table 7.1, and P-wave velocities are calculated by $V = \sqrt{\frac{1}{d}(K + \frac{4}{3}G)}$. The model shows a profound clay effect on the joint elastic-electrical properties of reservoir sandstones, that is, with increasing volumetric clay content both electrical resistivity and elastic velocity decrease provided porosity keeps constant. However this cannot be explained by the clay softening effect at grain boundaries for reducing elastic velocity (e.g., Sams and Andrea, 2001) or excess ions associated with clay minerals in reducing electrical resistivity (e.g., Waxman and Smits, 1968) since the model assumes contiguous connections of each component. Instead, it is purely because of the lower electrical resistivity and elastic velocity of the clay minerals compared to the quartz matrix.

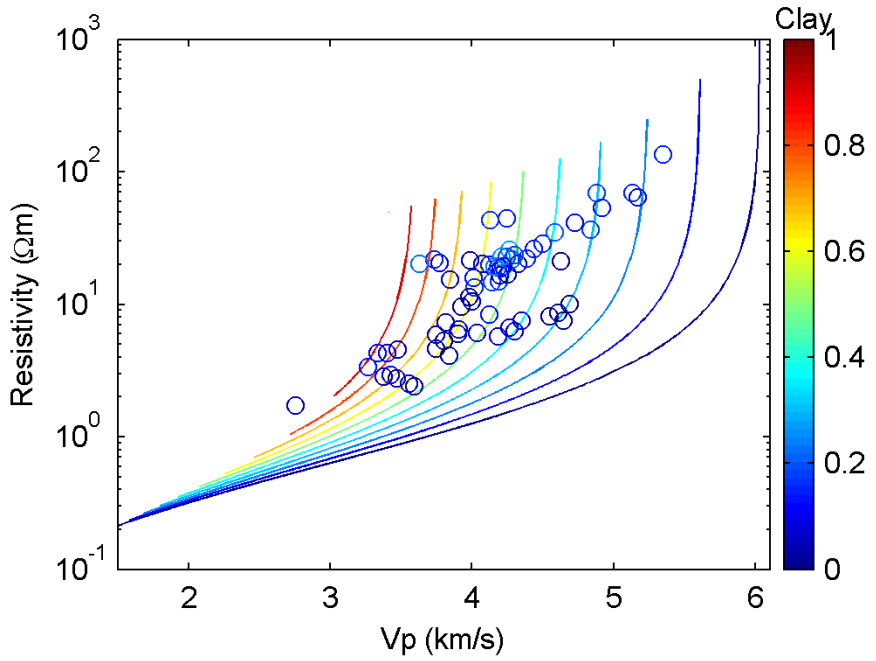

Figure 7.2. Comparison of Carrara's electro-seismic model (Carrara *et al*., 1994) for quartz matrix, brine and clay with experimental data by colour-coding volumetric clay content.

The clay effect on the joint elastic-electrical properties of sandstones shown by the model generally matches the manner of the two groups of the experimental data caused by clay content (Chapter 6); however the actual values predicted by the model fail to fit the data. In fact the model predicts electrical resistivity that is too low and elastic velocity that is too high which can be traced back to the assumptions in the model. The assumption of in series phases for the elastic velocity and in parallel phases for electrical resistivity overestimates the high velocity value phase (e.g., quartz matrix) and the low resistivity value phase (e.g., brine). Equations 7.1 and 7.2 are the well-known equations which perform poorly at high porosities (e.g., Berryman, 1995).

7.2.3. Combined self consistent approximation (SCA) and differential effective medium (DEM) model

7.2.3.1. Elastic velocity

The combined self consistent approximation (Hill, 1965; Wu, 1966; Berryman, 1980a, b) and differential effective medium (Cleary *et al*., 1980; Berryman, 1992) model (combined SCA/DEM) is a more advanced model than those discussed above because it specifies the grain shapes. It has been used to estimate elastic velocity of both

unconsolidated sediments and consolidated sandstones with great success (e.g., Sheng, 1990; Hornby *et al*., 1994; Jakobsen *et al*., 2000; Chand *et al*., 2004; Ellis, 2008). The combined SCA/DEM model starts by calculating the effective bulk and shear moduli for a two phase medium at a specific porosity (known as the critical porosity φ_c, note the difference in meaning between this critical porosity and that defined by Marion *et al*., 1992) using the SCA model, which are then entered into the DEM model as the holding matrix component. The final effective moduli are then calculated using DEM by adding brine and quartz (for sandstones) as the inclusion components into the matrix for porosity higher and lower than the critical porosity φ_c respectively. The procedure of the combined SCA/DEM model is schematically shown in Figure 7.3. Ellis (2008) gives a detailed description of the advantages of the combined SCA/DEM model over each method applied alone.

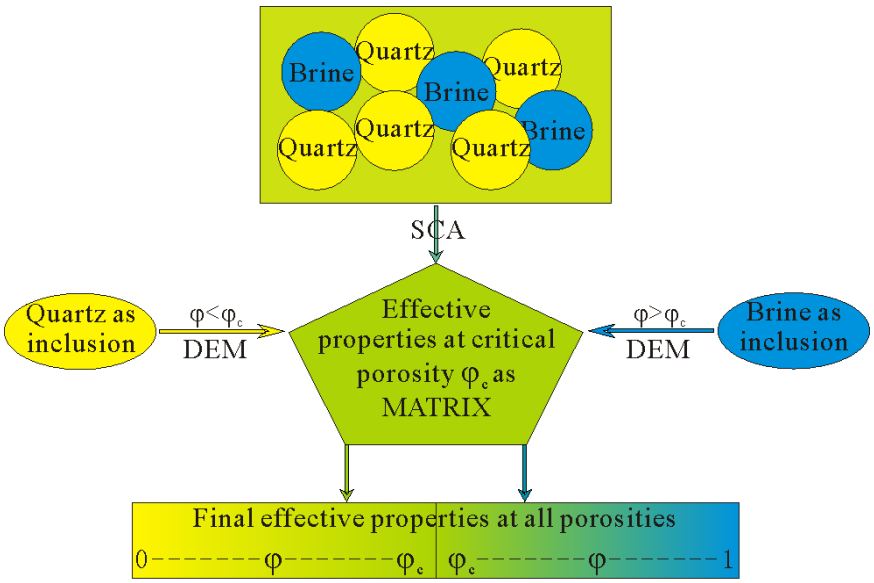

Figure 7.3. Schematic diagram showing the implementation procedure of 2-phase (both elastic and electrical) combined SCA/DEM model for clean sandstones.

Figure 7.4 shows the comparison of the combined SCA/DEM model for spherical shaped medium components to the experimental velocity data; also shown are the elastic HS bounds. The choice of the starting porosity (critical porosity φ_c) for the DEM model has a great influence on the final results. Similarly to the critical porosity value suggested by Sheng (1990), our data show that the combined SCA/DEM gives a good fit to the brine saturated sandstones when a critical porosity of $\varphi_c = 0.5$ is used.

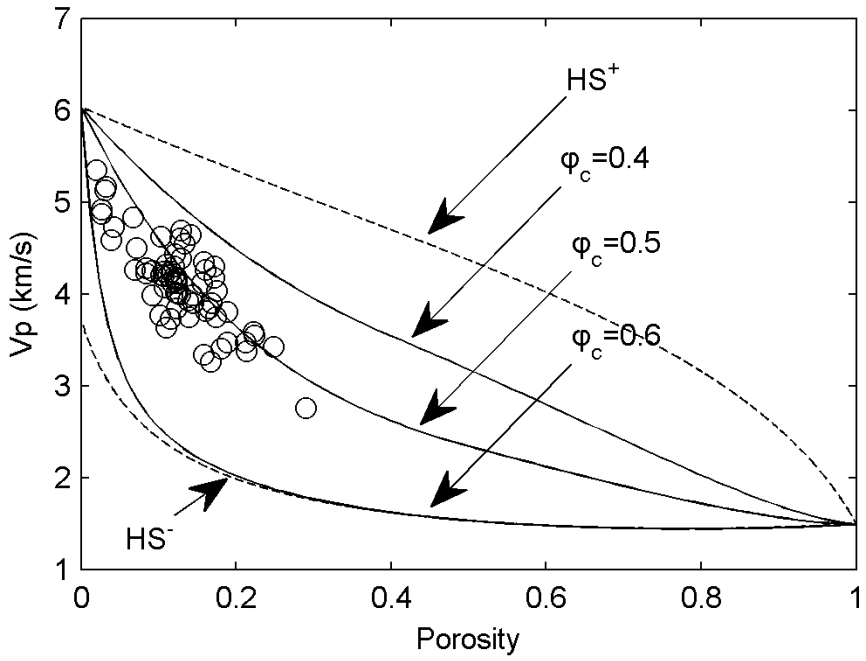

Figure 7.4. Elastic velocity calculated using the 2-phase (elastic) combined SCA/DEM model with varying critical porosities showing that the model with critical porosity of 0.5 gives the best fit to the samples.

7.2.3.2. Electrical resistivity

SCA and DEM models have also been employed to model the electrical properties of rocks (Bruggeman, 1935; Landauer, 1952; Sen *et al*., 1981; Berryman, 1995). In a similar format to the combined SCA/DEM for elastic velocity, we propose a combined SCA/DEM for electrical resistivity, where the SCA model is well described in the literature (e.g., Berryman, 1995), and DEM model for electrical conductivity is given by

$$(1-x_i)\frac{d}{dx_i}\left[\sigma^*(x_i)\right]=\left[\sigma_i-\sigma^*(x_i)\right]\cdot\left[3\sigma^*(x_i)\right]R^{*i}, \qquad (7.5)$$

where x_i and σ_i correspond to the volume fraction and conductivity of the inclusion respectively, σ^* is the conductivity of the effective medium and R^* is a function of the depolarisation factors L_a, L_b and L_c (Berryman, 1995; Mavko *et al*., 1998):

$$R^{*i}=\frac{1}{9}\sum_{j=a,b,c}\frac{1}{L_j\sigma_i+(1-L_j)\sigma^*}, \qquad (7.6)$$

The depolarisation factors L_a, L_b and L_c for prolate spheroid are calculated according to Osborn (1945):

$$L_a = \frac{1}{m^2-1}\left[\frac{m}{2(m^2-1)^{1/2}} \times \ln\left(\frac{m+(m^2-1)^{1/2}}{m-(m^2-1)^{1/2}}\right)-1\right], \tag{7.7}$$

$$L_b = L_c = \frac{m}{2(m^2-1)}\left[m - \frac{1}{2(m^2-1)^{1/2}} \times \ln\left(\frac{m+(m^2-1)^{1/2}}{m-(m^2-1)^{1/2}}\right)\right], \tag{7.8}$$

where $m = a/b$ equals the reciprocal of aspect ratio, and a, b and c are the ellipsoid semi-axes fulfilling $a \geq b = c$. Electrical resistivity ρ can be easily calculated by $\rho = 1/\sigma$.

Figure 7.5 shows the effect of critical porosity on the electrical resistivity of the models for medium components with spherical shapes. With varying critical porosity values from 0.4 to 0.6, the electrical resistivity calculated by the electrical combined SCA/DEM model is well within the electrical HS bounds indicating the validity of this model. Similarly to the critical porosity value used for the elastic combined SCA/DEM model, the critical porosity value of 0.5 for the electrical combined SCA/DEM model gives a good fit to most of our measured electrical resistivity data.

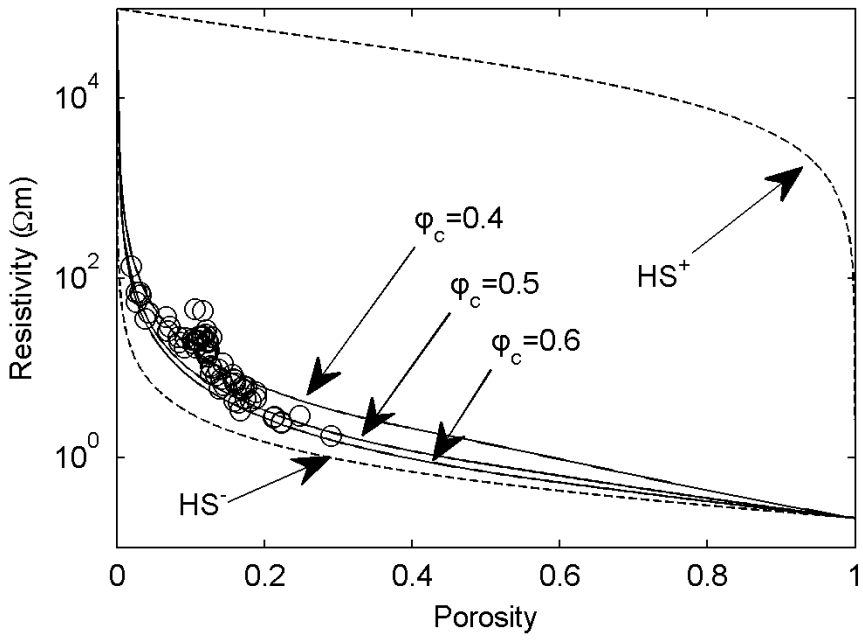

Figure 7.5. Electrical resistivity calculated using the 2-phase (electrical) combined SCA/DEM model with varying critical porosities showing that the model with critical porosity of 0.5 gives the best fit to the samples.

7.2.3.3. Joint elastic velocity-electrical resistivity

Both the elastic and electrical combined SCA/DEM models give good predictions of elastic velocity and electrical resistivity respectively for a critical porosity of 0.5. It is therefore reasonable to expect that the joint elastic-electrical combined SCA/DEM models with critical porosity 0.5 would also give good estimates of the joint elastic-electrical properties of our reservoir sandstones. This is confirmed by the results shown in Figure 7.6 where the same critical porosity value is employed by the electrical resistivity and elastic velocity models for each curve. However, the models using a critical porosity value of 0.5 for spherical shaped components only coincide with the clean sandstone data.

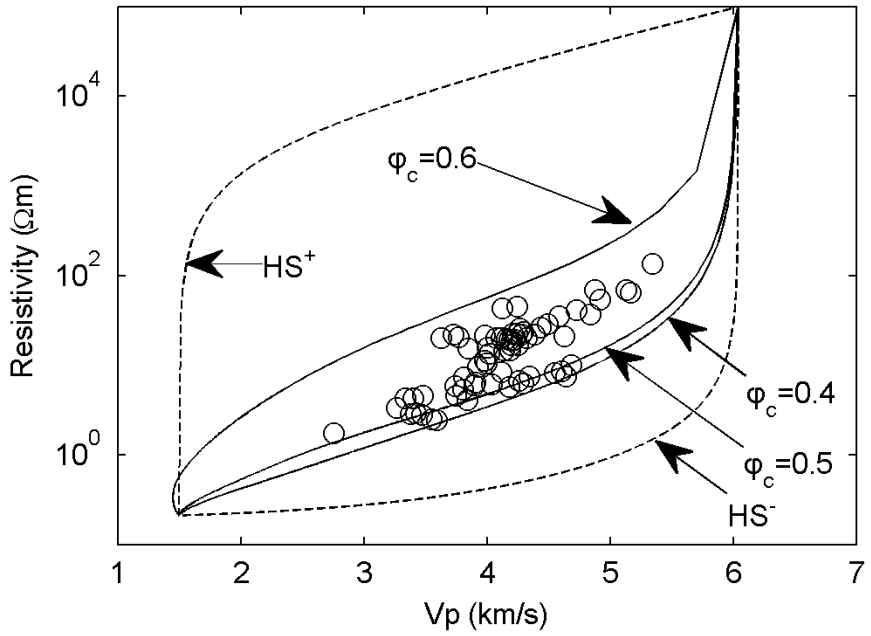

Figure 7.6. Joint elastic-electrical properties obtained from the 2-phase (joint elastic-electrical) combined SCA/DEM model with varying critical porosities showing that the model with critical porosity of 0.5 gives the best fit to the samples.

As mentioned above, the clay-rich sandstones in the upper group of our samples might have lower aspect ratio components due to the existence of clay minerals. To account for this, we varied the component aspect ratios for the joint models even though a third clay component is not included in these models. In the following discussions, a critical porosity of 0.5 is employed for the combined SCA/DEM models of both elastic velocity and electrical resistivity.

Figure 7.7 shows a comparison of the joint elastic-electrical combined SCA/DEM model with varying components aspect ratio from 1 to 0.1 with the experimental data. The same aspect ratio in the combined SCA/DEM model is assigned to the two components, which is determined by the assumption that the SCA model treats the two components symmetrically. As component aspect ratio decreases there is an upwards shift of the model indicating a decrease in elastic velocity while an increase in electrical resistivity. The decreasing elastic velocity is mainly caused by the pore fluid; with decreasing pore fluid aspect ratio the compressibility of the medium increases resulting in lower bulk and shear moduli and elastic velocity. By contrast the increase in electrical resistivity is highly sensitive to the random arrangement of the insulating grains; with decreasing grain aspect ratio, the grains block the connectivity of the conducting pore fluids and lead to an increase in electrical resistivity.

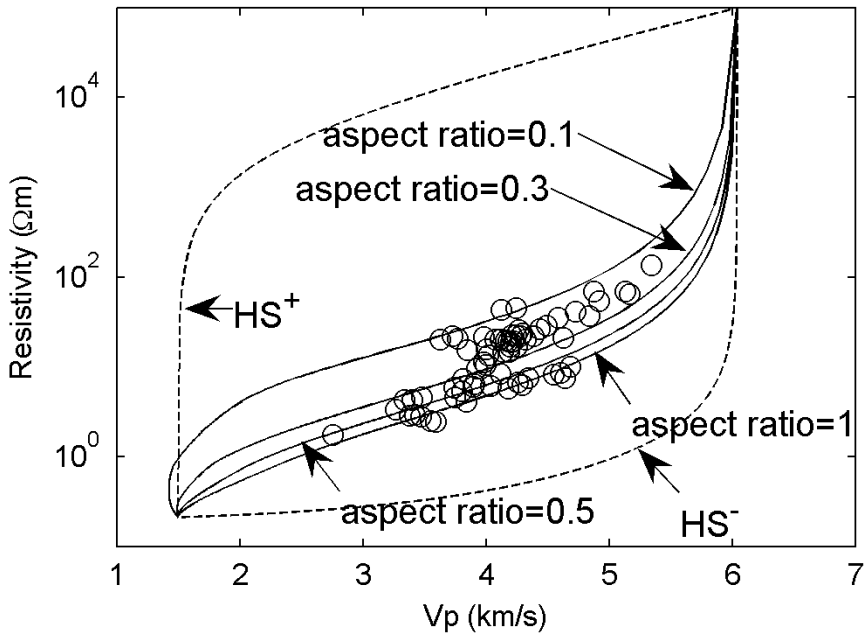

Figure 7.7. Joint elastic-electrical properties obtained from the 2-phase (joint elastic-electrical) combined SCA/DEM model showing the effect of varying aspect ratios on the joint properties of sandstones. The same aspect ratio is assigned to the two components.

With component aspect ratios ranging from 1 to 0.1, the models cover the whole range of the experimental data. However Figure 7.7 shows that the model curves are approximately parallel to each other in the possible sandstone velocity range (2.5 – 5.5 km/s). This implies that the effect of mineral and fluid shapes on the joint elastic-electrical properties of reservoir sandstones are due to velocity-resistivity relations

(defined by other parameters such as clay content or critical porosity) also modified in a parallel manner.

7.2.4. Three-phase combined self consistent approximation and differential effective medium model

In order to fit the upper group of our sandstone samples which according to Chapter 6 contain non-negligible clay content, we introduce a clay component into the 2-phase combined SCA/DEM model, thus giving a 3-phase effective medium model. There are a number of ways to include a third phase such as clay minerals and gas hydrate (e.g., Jakobsen *et al*., 2000; Ellis, 2008). Here, we choose to develop a 3-phase effective medium model specifically for sandstones with pore-filling clay minerals. This best resembles the distribution of clay minerals found in most of our samples.

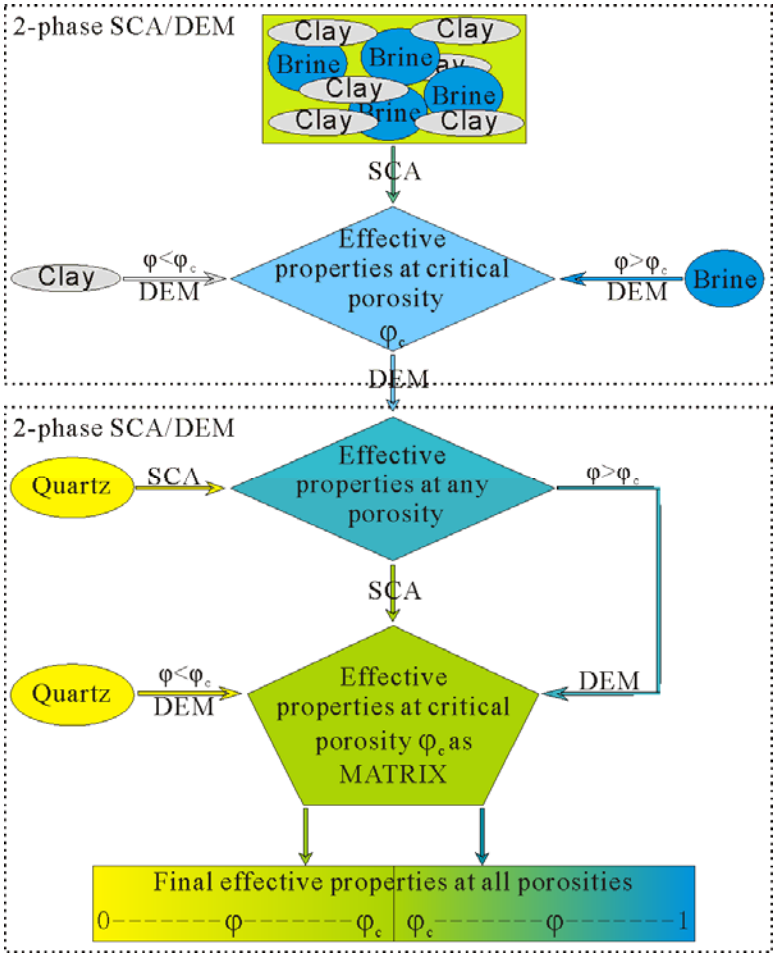

Figure 7.8. Schematic diagram showing the implementation procedure of 3-phase (both elastic and electrical) combined SCA/DEM model for sandstones with pore-filling clay minerals.

The 3-phase effective medium is modelled firstly by using the 2-phase combined SCA/DEM method described above for clay and brine with volume fractions of β_c and β_b respectively; the clay and brine mixture is then calculated with quartz (volume fraction of β_q) using the 2-phase combined SCA/DEM model for a second time to get the final effective properties of the medium. The porosity of the 3-phase medium corresponds to the final volume fraction of brine given by $\varphi = \beta_b(1-\beta_q)$, and volumetric clay content is given by $C = \beta_c(1-\beta_q)$. Figure 7.8 shows schematically the implementation of the 3-phase combined SCA/DEM model, where the critical porosity φ_c = 0.5 is used for both the two rounds of 2-phase models.

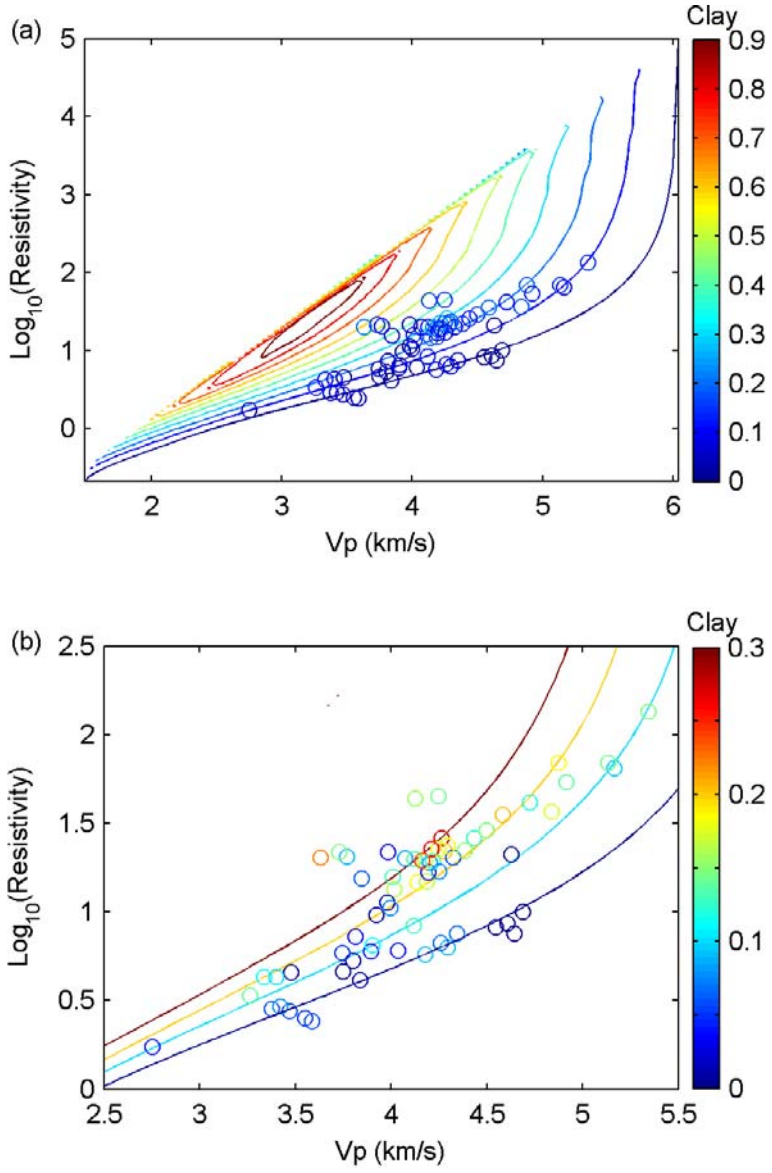

Figure 7.9. Comparison of the joint elastic-electrical properties obtained from the 3-phase (joint elastic-electrical) combined SCA/DEM model with varying volumetric clay contents to

the experimental data (a) general comparison and (b) detailed comparison. Both models and experimental data are colour-coded by volumetric clay content.

Figure 7.9a shows the results of the 3-phase joint elastic-electrical combined SCA/DEM model for components aspect ratio 1 with varying volumetric clay content from 0 to 0.9. Clay shows a similar effect to that of Carrara's electro-seismic model (Carrara *et al*., 1994) on the joint elastic-electrical properties of reservoir sandstones; that is with increasing clay content elastic velocity decreases while electrical resistivity increases. This is expected since we are modelling pore-filling clay minerals, the existence of which reduces the mean pore size and the overall porosity, as well as blocking the connectivity of the conducting brine between pores (in case of full brine saturation) resulting in increasing electrical resistivity. On the other hand for elastic velocity, the existence of pore-filling clay minerals contributes little to the bulk and shear moduli of the rocks, but increases the density and therefore causes a reduction in elastic velocity.

The model also shows the important role played by porosity in controlling the joint elastic-electrical properties of reservoir sandstones. With increasing porosity both elastic velocity and electrical resistivity decrease and clay content shows a diminishing effect enabling the model to fit the converging pattern of the two groups in the higher porosity range. Another interesting feature of the model is that it confirms the approximate linear correlation between electrical resistivity and elastic velocity on a semi-logarithmic scale observed for the laboratory data for both groups of clean and clay-rich samples.

Whereas Figure 7.9a shows generally the effects of clay content on the joint elastic-electrical properties of reservoir sandstones, Figure 7.9b shows the detailed comparison of the model with our experimental data, where both the model curves and the data are colour-coded by volumetric clay content from 0 to 0.3 covering the whole clay content range shown by our samples. Although calculated for spherical shaped components (aspect ratio = 1) the model fits the clay effects on the experimental data with an acceptable error since the accuracy of the clay measurement using whole rock X-ray diffraction (XRD) is ± 5%. As mentioned above, by lowering the aspect ratio of model components the model curves shift upwards without changing shape (i.e., parallel curves). Therefore, we would expect to get a better fit to the clay-rich samples using lower aspect ratios for the components.

However, this would add unnecessary complexity to the model because it uses the same aspect ratio for all phases and it is difficult to determine an 'effective' aspect ratio for the whole rock.

7.3. Discussion

A 3-phase joint elastic-electrical combined SCA/DEM effective medium model has been developed for isotropic and homogeneous sandstones. It requires that the constituents of the effective medium are linear and isotropic, the inclusion shapes are idealized and all inclusions have the same shape, and the size of all inclusions is much smaller than the wavelength of both elastic and electrical waves passing through the medium. This last condition implies that the medium is suitable for low frequencies and is frequency independent. The effective electrical resistivity can therefore be applied directly to the low frequencies employed by marine CSEM and the effective elastic velocity to low frequency surface seismic data.

The arrangement of the components determines whether the medium is isotropic or anisotropic when the aspect ratio differs from unity. Since we are modelling isotropic sandstones, all inclusions in the medium are required to be randomly arranged; this leads to reducing elastic velocity and increasing electrical resistivity with decreasing aspect ratio, as established above. However if all inclusions are arranged regularly (i.e., all inclusions are arranged along the same direction) the medium will be anisotropic. The arrangement of low aspect ratio inclusions has a particularly strong effect on electrical anisotropy (Ellis *et al*., 2010).

The model assumes the same aspect ratio for all inclusions (i.e., quartz, clay and brine). This is not the case for natural rocks and sediments where quartz and other minerals typically have sub-spherical grains (aspect ratio close to 1) while clay platelets have very low aspect ratios. However this complexity can be addressed by assigning an 'effective aspect ratio' to the phases if necessary when clay forms an important part of the sandstones. A possible way of calculating an effective aspect ratio is to average the aspect ratios of each inclusion by weighting their volume fractions using equation

$$\alpha = \varphi_1\alpha_1 + \varphi_2\alpha_2 + \varphi_3\alpha_3, \tag{7.9}$$

where α is the effective aspect ratio and φ_1 α_1, φ_2 α_2 and φ_3 α_3 are the volume fractions and aspect ratios of the three phases respectively.

Clay has a profound effect on electrical resistivity as well as on elastic velocity. Based on laboratory data (Patnode and Wyllie, 1950; Wyllie and Southwick, 1954; Waxman and Smits, 1968; Rink and Schopper, 1974) Worthington (1982) suggested a critical value of brine resistivity below which sandstones with a particular clay content can show a negligible conductive effect; similarly in Chapter 4, we proposed a critical value of clay content above which sandstones saturated with a particular salinity brine show a non-negligible conductive effect. We also discussed the two ways clay works on electrical resistivity, that is, a blocking effect at low clay concentrations and both blocking and conductive effects at higher clay concentrations. Unfortunately our model does not take into account the clay conductive effect due to limited knowledge about the critical clay content (if it does exist) for a particular brine and the clay conductive behaviours at concentrations higher than the critical clay content for that particular brine. A way to include the clay conductive effect is to assign a decreasing electrical resistivity value to clay minerals in case of saturation with increasing brine resistivity and/or clay content. Further experiments will be required to know the extent to which clay resistivity decreases although theoretical approaches (e.g., Revil and Glover, 1998; Revil *et al*., 1998; Rabaute *et al*., 2003) to account for clay surface conduction already exist.

Differential pressure is another parameter that affects both elastic and electrical properties and hence joint elastic-electrical properties of reservoir sandstones. In Chapter 5 we studied systematically the pressure effects on the joint elastic-electrical properties of reservoir sandstones. By combining the model developed in this chapter and the empirical joint relations established in Chapter 5 it is possible to construct the exact behaviours of the joint elastic-electrical properties for any given pressure.

The 3-phase effective medium model developed in this chapter for pore-filling clay minerals requires all clay minerals to reside in the pore spaces. By replacing the clay phase with hydrate (either CO_2 hydrate or methane hydrate) the model is potentially applicable to hydrate-bearing reservoir sandstones. However because the SCA and DEM models can not be used to predict the elastic properties of two fluid phases (e.g., gas or oil) due to the zero moduli, the clay phase in this 3-phase effective medium

model can not be replaced by a fluid phase to simulate hydrocarbon saturation effects on the joint elastic-electrical properties of reservoir sandstones.

7.4. Conclusions

A robust rock-physics model that links elastic and electrical properties of reservoir rocks is essential for joint seismic-CSEM interpretation and inversion. A number of effective medium models were implemented to fit the joint elastic-electrical experimental data collected on 67 brine saturated clean and clay-rich sandstones. Carcione's (Carcione *et al*., 2007) cross relations using Gassmann's equation for elastic velocity and the Archie, Hermance, self-consistent and CRIM models for electrical resistivity all predict the joint elastic-electrical behaviours of clean sandstones quite well but they fail to predict the correct behaviour for clay-rich samples. Although Carrara's electro-seismic model (Carrara *et al*., 1994) succeeds in showing the effect of clay on the joint elastic-electrical properties of sandstones, it underpredicts electrical resistivity and overpredicts elastic velocity compared to the experimental results.

We developed a new 3-phase effective medium model based on 2 rounds of a 2-phase, combined SCA/DEM model for quartz, brine and pore-filling clay minerals with the same aspect ratio and a critical porosity of 0.5 for both rounds. By using an aspect ratio of 1 for all three phases, the model gives accurate predictions of P-wave velocity and electrical resistivity and the observed trends for both clean and clay-rich sandstones. Using only a few, well constrained input parameters, this model offers a robust description of the joint elastic-electrical response of both clean and shaly sandstones. The model could be used to invert *in situ*, co-located, P-wave velocity and electrical resistivity datasets from boreholes and surface geophysical surveys in terms of the porosity and clay content of brine saturated reservoir sandstones.

Chapter 8

Conclusions

8.1. Overview and main conclusions

The aim of this project was to study the inter-relationships among the elastic and electrical properties of typical reservoir sandstones and to relate the joint elastic-electrical properties to reservoir sedimentological properties so that *in situ* reservoir parameters can be better predicted by joint seismic-CSEM measurements.

Chapter 1 gave a brief introduction to the marine CSEM method; it was shown that a successful joint seismic-CSEM inversion which can better characterise rock and fluid properties depends largely on the knowledge of the inter-relationships among elastic, electrical and reservoir petrophysical properties and the development of a robust rock physics model linking these parameters. This was the initial motivation for this laboratory rock physics study, which was considered to be the best way to obtain the required knowledge.

From the literature review of the current knowledge of some key reservoir parameters on the elastic and electrical properties of reservoir sandstones presented in Chapter 2, it was found that although tremendous work has been done there is still a lack of understanding in terms of clay and permeability on attenuation, frequency effects on elastic properties and the combined influence of petrophysical parameters on electrical resistivity. There seems to be a complete lack of studies of the joint elastic-electrical properties and petrophysical control on these properties for reservoir sandstones.

In Chapter 3 the principle of the joint elastic-electrical laboratory apparatus used in this project was described. The collection, characterisation and preparation of the sandstone samples, the experimental and data processing procedures were described therein. It concluded that the large joint elastic-electrical dataset collected on 67 typical sandstones showing a wide range of petrophysical properties was accurate and of high quality. This enabled the data to be analysed for subtle inter-relationships among the parameters and gave the basis for validating some existing mathematical models and for developing a new model as part of this study.

While most of the previous knowledge of electrical resistivity was obtained from well logging data at high frequency (~ 50 kHz), Chapter 4 reported for the first time quantitative empirical relations among electrical resistivity, porosity, clay content and permeability for typical reservoir sandstones at low frequency (2 Hz) likely to be

employed by CSEM surveys. It was found that at our particular experimental conditions sandstone samples with volumetric clay contents as high as 22% were found to behave like Archie's clean sandstones when porosity is higher than 9%, while samples with volumetric clay content as low as 10% behave like shaly sandstones when porosity is less than 9%. The clay effect on resistivity depended not only on clay content, porosity and electrolyte resistivity but also on the differential pressure and clay type; electrical resistivity was negatively correlated with hydraulic permeability.

Chapter 5 presented for the first time the pressure effects on the cross-property relations between electrical resistivity and elastic velocity, electrical resistivity and elastic attenuation and elastic velocity and elastic attenuation in reservoir sandstones. Elastic velocity, attenuation and electrical resistivity were found to follow similar trends with changing differential pressure which were described by empirical expressions of the form $Z = A - Be^{-CP_{diff}}$. The minor differences between C coefficients gave rise to almost linear correlations between parameters (elastic velocity, attenuation and electrical resistivity) as a function of differential pressure. The slopes of the linear correlations were defined by the ratios of B coefficients between parameters. It was shown that electrical resistivity was more sensitive to low aspect ratio pores and micropores while elastic attenuation was more subject to large open pores (macropores); different pore types did not have any impact on elastic velocity with changing differential pressure. Low aspect ratio pores and micropores had a more profound effect on electrical resistivity than that of the macropores on elastic attenuation.

Chapter 6 explored the joint elastic-electrical properties of reservoir sandstones and the petrophysical influence on the joint properties. It demonstrated that elastic velocity (both compressional and shear) was approximately positively linearly correlated with apparent formation factor F^* on a semi-logarithmic scale; the data fell into two converging groups, where the slope for the clay-rich sandstones was higher than that of the clean sandstones. P-wave attenuation seemed to follow a bell-shaped trend with apparent formation factor F^*, analogous to P-wave attenuation dependence on mean grain size and sorting reported in the literature for marine sediments; S-wave attenuation showed only part of this bell-shaped curve. The combination of the clay-porosity effect was found to best explain the joint elastic-electrical behaviour.

Chapter 7 described the implementation of some existing joint elastic-electrical models and compared them to the dataset. Also, a 3-phase combined SCA/DEM model for quartz brine and pore-filling clay minerals was developed. The existing models either did not fit any observations very well, or fitted only the group of clean sandstones. However, the newly developed model gave a reasonable fit to both clean and clay-rich sandstones.

Since different rationales and nomenclature were used for grouping various data points in Chapter 4 (Groups 1, 2 & 3) and Chapter 6 (Groups A & B), the correspondence between these five groups is explained here.

Firstly to reiterate the rationale for the various groupings. In Chapter 4, the three groups (1, 2 & 3) were chosen arbitrarily on the basis of the plot of apparent formation factor F^* against porosity φ (Figure 4.4). The data show an approximately linear trend of increasing F^* with decreasing φ until a porosity of about 0.09 where there is a reduction in slope. Hence, data above $\varphi = 0.09$ were assigned to Group 1 and those below $\varphi = 0.09$ to Group 2. Additionally, all samples with kaolinite clay minerals were assigned to Group 3; these have porosities greater than 0.09 but show higher F^* values for a given porosity than Group 1 samples. In Chapter 6, the two groups were assigned arbitrarily on the basis on the plot of F^* against P-wave velocity V_p (Figure 6.1). Here, two approximately linear trends F^* rising with V_p were seen with the Group A trend having a lower gradient and smaller values of F^* for a given V_p than the Group B trend. Both trends converge below $V_p = 3000$ m/s.

The exact correspondence between the samples in Groups 1, 2 & 3 and Groups A & B has not yet been established. However, some general observations are that, from an electrical properties point of view: i) only clean sandstones reside in Group A (i.e., little clay); ii) Group B comprises shaly sandstones only (i.e., all have some clay), a mixture of sandstones with clay contents that exceed, and are below respectively, the clay surface conductivity threshold for a salinity of 35 g/l; iii) Group 1 contains both clean sandstones and shaly sandstones, the latter with clay contents below the clay surface conductivity threshold; iv) Group 2 contains only shaly sandstones with clay contents that exceed the clay surface conductivity threshold; v) Group 3 contains sandstones with kaolinite clay minerals (all the other shaly sandstones have dominantly illite clay minerals). From the point of view of elasticity: vi) Group A only contains clean sandstones; vii) Group B contains shaly sandstones with both

pore-filling and load-bearing clay minerals; viii) Group 1 has both clean sandstones and shaly sandstones with pore-filling clay (i.e., with clay content partially filling the pores); ix) Group 2 has only shaly sandstones with load-bearing clay (in the sense that the clay content at which the pore space is totally filled with clay is exceeded); x) Group 3 has only shaly sandstones with partially pore-filling kaolinite clay.

8.2. Discussion

Work done in this thesis has provided fundamental new data and correlations, but how these new findings impact on hydrocarbon exploration and other suitable targets for joint seismic-CSEM surveying (e.g., gas hydrates and geological sequestration of CO_2) needs to be discussed.

8.2.1. Are the samples representative of reservoir sandstones?

As mentioned in Chapter 3, although some of the samples (e.g., CZ samples) are reservoir sandstones that contain oil, most of the rest are quarry and shallow borehole samples. This naturally raises the question: are these samples representative of real reservoir sandstones? Indeed quarry sandstones may differ from real reservoir sandstones in terms of rock properties (e.g., compaction, consolidation history and age) and environment (e.g., stress history and depositional environment) as seen in Table 2.1. However all these factors prove to have minor effects on the elastic properties of sandstones compared to other parameters such as porosity and pore shape (e.g., Wang, 2001), which might be exactly the same between quarry and reservoir sandstones. In fact, a lot of rock physics studies (e.g., Best 1992; Jones, 1995; Gomez, 2009) are performed (fully or partially) on quarry and shallow borehole rocks (e.g. Berea sandstone) since they can be obtained more easily and economically.

A comparison in Figure 8.1 of the elastic measurement results from this thesis with the data from Han *et al*. (1986), a classic rock physics study, shows a good coincidence in both the porosity range (although my dataset has few samples with porosity in the range from 0.2 to 0.3) and the measured velocity values. The samples in this study can be considered to be representative of typical reservoir sandstones as

the majority of samples in Han's (Han *et al*., 1986) study are from real reservoir cores.

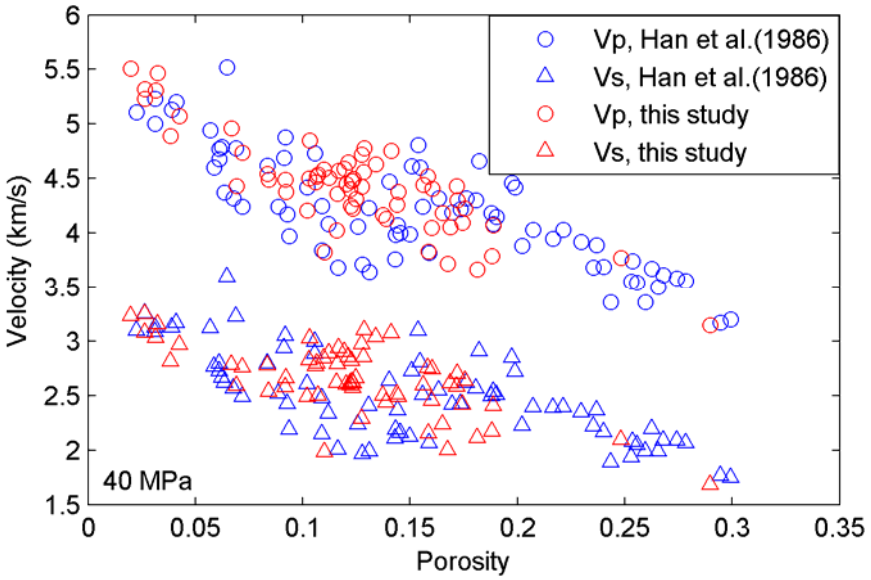

Figure 8.1. Comparison of velocity measured in this study (red) with that from Han *et al*. (1986, blue) as a function of porosity at 40 MPa differential pressure. Open circles and triangles represent P- and S-wave velocity respectively.

8.2.2. Frequency dependent effects

The change of electrical resistivity with measurement frequency has been observed both from laboratory experiments and theoretical calculations (e.g., Olhoeft, 1985, 1987; de Lima and Sharma, 1992; Denicol and Jing, 1998). At low frequencies (less than 1 Hz) chemical interactions such as adsorption and cation exchange at the solid-brine interface play an important role while at higher frequencies (10 Hz to 10 MHz) ionic double-layer polarisations at the solid-fluid interface become significant (Garrouch and Sharma, 1994) leading to lower resistivities. Therefore caution should be exercised when comparing CSEM inversion results at a frequency lower than 10 Hz to well logging and measurement while drilling results at a frequency around 50 kHz. Existing theoretical models, such as the one of de Lima and Sharma (1992), could be used to transform high frequency well logging data to lower frequencies for comparison to the joint elastic-electrical relationship discovered in Chapter 6.

The frequency dependent nature of elastic properties is one of the key problems faced by geophysicists in interpreting surface seismic data at frequencies 10 – 200 Hz, and

at borehole sonic logging frequencies of about 2 – 20 kHz, when using empirical relations obtained from laboratory ultrasonic measurements in the MHz frequency range. It is shown in Section 2.4.4 that the elastic velocity of reservoir sandstones tends to increase with frequency, and there are several theoretical formulas for predicting the frequency dependent elastic velocities and attenuations of reservoir rocks (e.g., Gassmann, 1951; Biot, 1956a, b; Geertsma and Smit, 1961; Dvorkin and, Nur 1993; Dvorkin *et al*., 1994; Ruiz and Dvorkin, 2010). The joint ultrasonic-CSEM relations (e.g., Figure 6.1 and Figure 6.2) established in Chapter 6 can then be transformed to joint sonic-CSEM or joint seismic-CSEM relations using these theoretical formulas (assuming the models are valid).

8.2.3. Reservoir conditions

Whereas the experiments in this study simulated reservoir pressures, no effort was made to simulate elevated reservoir temperatures (in fact temperature was kept at around 19 ºC to minimize its impact on the results). Temperature is known to influence both the elastic and electrical properties of reservoir sandstones. The relations observed in the laboratory therefore need further calibration to account for reservoir temperature before they can be applied to *in situ* reservoir characterisation.

The temperature dependencies of velocity and resistivity in sandstones are for the most part controlled by the properties of the fluid filling the pore space (Johnston, 1987). Increasing temperature will decrease the viscosity and increase the conductivity of the pore fluid so that velocity and attenuation decrease (e.g., Jones and Nur, 1983; Johnston, 1987) and resistivity also decreases (e.g., Johnston, 1987; Sen and Goode, 1992). However temperature may also affect the chemical interactions between the rock framework and the pore fluid resulting in a more complicated frequency dependence of both elastic (e.g., O'Hara, 1985) and electrical (e.g., Chelidze *et al*., 1999) properties.

8.2.4. How can an exploration geophysicist use the results?

Once the laboratory results on typical reservoir sandstones presented in this thesis are properly calibrated in terms of practical frequency and reservoir temperature, they are ready to guide joint seismic-CSEM explorations. However, brine was used as the pore

fluid in these experiments rather than oil or methane gas which are the targets of interest to the industry.

An exploration geophysicist can apply the joint velocity-resistivity effective medium models developed in Chapter 7 as input to the joint seismic-CSEM inversions if there are no well logging data available as constrains. The inverted resistivity can be plotted against inverted velocity as shown in Figure 6.1. If the inversion results match the well calibrated resistivity-velocity relations based on the laboratory data, this could indicate that the potential reservoir is filled with brine. Another possibility is that the inverted relation will not match that discovered in this thesis; this would be a possible indication of hydrocarbons present in the reservoir, especially if the resistivity is higher than normal. However, the saturation of brine/hydrocarbon must first be taken into consideration. Relationships and theoretical models have already been published which deal with saturation effects on electrical resistivity in sandstones (e.g., Taylor and Barker, 2002; Toumelin and Torres-Verdín, 2005).

Seismic velocity is still the most commonly used parameter in seismic exploration at present but increasing attention has been paid to attenuation which is also related to the petrophysical properties of reservoir rocks. Although the joint resistivity-attenuation relations presented in this thesis are not as clear and straightforward as the joint resistivity-velocity relations, there does exist a correlation between resistivity and attenuation. With our improvement in the understanding of attenuation mechanisms and its relations with petrophysical parameters in the future, a better explanation of the joint resistivity-attenuation relations will be achieved. This could also improve our ability to better characterise reservoir parameters from joint seismic-CSEM surveying.

8.3. Summary

The results reported in Chapters 4 to 7 give for the first time a systematic study of the joint elastic-electrical properties of reservoir sandstones. The results provide insight into wave propagation phenomena in porous rocks and have the potential to constrain joint seismic-CSEM data interpretation and inversion schemes. While the work presented in this thesis makes a major step forward, the full realisation of the results in terms of practical applications will need further work along the lines discussed

above. Nevertheless, the results presented in this thesis must surely be considered a significant step forward in improving the accuracy of the joint inversion of combined elastic-electrical geophysical datasets. This is of major interest to hydrocarbon exploration and other suitable targets for the joint seismic-CSEM survey method.

Appendix A

Petrophysical and mineralogical results for the 67 sandstone samples in this study

Sample	Porosity (%)	Permeability (mD)	Clay (%)				Quartz (%)	Feldspar (%)		*Other minerals (%)
			Illite	Kaolinite	Smectite	Chlorite		K-feldspar	P-feldspar	
W162.0	6.91	0.001	8.53	19.10	0.00	0.00	46.88	3.59	5.28	9.72
W165.6	17.20	217.06	0.00	9.13	0.00	0.00	71.68	0.00	0.00	1.99
W165.6H	17.18	248.20	0.00	9.14	0.00	0.00	71.71	0.00	0.00	1.97
W165.7	16.87	40.85	0.00	3.92	0.00	0.00	77.58	0.60	0.00	1.03
W165.7H	17.55	233.87	0.00	3.89	0.00	0.00	76.91	0.60	0.00	1.05
W166.0	16.03	135.31	0.00	6.74	0.00	0.00	74.17	0.78	0.00	2.27
W166.0H	15.82	185.32	0.00	6.76	0.00	0.00	74.37	0.79	0.00	2.26
W160.15H	12.02	0.12	4.77	11.98	0.00	0.00	64.23	1.30	3.93	1.77
W160.15	12.23	0.04	4.72	11.87	0.00	0.00	63.64	1.29	3.89	2.36
W160.21H	12.21	0.10	5.40	13.19	0.00	0.00	57.55	2.86	3.61	5.17
BEREA	22.30	370.25	1.69	0.00	0.00	0.00	70.49	3.43	0.23	0.95
BP AX	21.20	439.34	2.94	2.90	0.00	0.00	65.42	4.82	1.31	1.41
BP AY	21.35	442.93	2.93	2.88	0.00	0.00	65.10	4.80	1.30	1.64
BP AZ1	22.25	448.10	2.91	2.86	0.00	0.00	64.59	4.76	1.29	1.33
TS	8.36	0.02	13.34	4.62	0.00	2.49	58.31	3.21	5.62	4.05
RB3	12.33	0.06	6.26	0.00	0.00	0.00	63.78	1.48	12.08	4.08
RES1	10.65	0.10	2.92	0.00	0.00	0.00	69.91	3.02	9.79	3.70
WATTSCLIFFE	16.00	8.63	3.40	0.00	0.00	0.00	59.43	6.80	8.68	5.70
RS	15.61	11.71	7.54	5.14	0.00	0.00	40.39	1.67	0.00	29.65
BEESTONE	18.88	114.21	0.54	0.00	0.00	0.00	64.03	13.92	2.60	0.04
E4	14.12	546.03	0.00	0.00	0.00	0.00	80.06	5.36	0.00	0.45
COVERED	17.44	84.91	0.00	0.00	0.00	0.00	58.66	12.90	6.37	4.63
YORK3	10.98	0.11	5.80	0.00	0.00	0.00	68.76	1.64	8.57	4.26
1DYK	12.48	0.27	10.10	2.77	0.00	0.00	62.66	0.00	0.00	11.99
RB2	10.22	0.04	8.99	0.00	0.00	0.16	60.66	1.50	11.80	6.66

1VSF	18.81	3.36	0.00	0.00	0.00	0.29	74.47	1.05	0.00	5.39
4SU	9.22	0.02	0.00	0.00	0.00	3.08	61.60	3.79	14.25	8.05
YORK2	10.31	0.98	8.39	0.00	0.00	0.00	62.05	4.70	11.09	3.45
PEAKMOOR	13.74	6.27	1.23	0.00	0.00	0.00	64.18	7.17	7.80	5.88
1SU	10.71	0.10	0.00	0.00	7.98	0.24	63.29	1.97	10.05	5.76
DUKES	14.39	3.03	1.23	0.00	0.00	0.00	62.09	12.43	0.00	9.87
E6	12.75	234.59	0.00	0.00	0.00	0.00	80.57	6.14	0.00	0.54
E3	13.40	297.27	0.00	0.00	0.00	0.00	81.96	4.27	0.00	0.36
E5	12.86	296.96	0.00	0.00	0.00	0.00	81.91	4.89	0.00	0.34
STONERAISE	10.34	28.74	0.00	0.00	0.00	0.00	77.35	11.95	0.00	0.36
SX1	11.57	0.65	0.00	14.64	0.00	0.00	73.56	0.00	0.00	0.23
SX2	10.60	0.03	0.00	14.50	0.00	0.00	73.20	0.00	0.00	1.70
SX3	11.68	0.71	0.00	18.14	0.00	0.00	70.18	0.00	0.00	0.00
SX4	12.28	0.57	0.00	13.21	0.00	0.00	74.34	0.00	0.00	0.17
SX5	12.30	0.62	0.00	17.14	0.00	0.00	70.56	0.00	0.00	0.00
SX6	11.21	0.49	0.00	25.95	0.00	0.00	62.83	0.00	0.00	0.00
SX7	12.37	0.95	0.00	23.71	0.00	0.00	63.93	0.00	0.00	0.00
SX8	12.11	0.37	0.00	12.63	0.00	0.00	75.01	0.00	0.00	0.25
SX9	12.84	0.64	0.00	15.41	0.00	0.00	71.74	0.00	0.00	0.02
SX10	11.62	0.03	0.00	15.72	0.00	0.00	71.37	0.00	0.00	1.28
SX11	11.95	0.23	0.00	18.10	0.00	0.00	69.96	0.00	0.00	0.00
CZ1	14.46	10.41	10.73	0.00	0.00	0.39	42.47	4.48	12.81	14.66
CZ2	16.74	0.37	13.02	0.00	0.00	0.74	27.41	8.73	22.57	10.79
CZ3	24.82	94.58	3.02	4.48	0.00	0.40	46.51	4.51	13.75	2.51
CZ4	13.89	7.94	4.89	0.00	0.00	0.23	31.40	8.13	21.63	19.83
CZ5	28.99	997.49	3.87	0.00	0.00	0.06	32.08	9.72	24.14	1.15
CZ6	11.02	0.12	11.42	2.79	7.67	0.39	15.12	17.58	28.43	5.57
CZ7	7.18	0.01	10.93	4.04	0.00	0.00	35.23	0.00	1.68	40.94
CZ8	3.23	0.003	8.30	0.39	0.00	0.97	42.64	3.05	24.02	17.41

CZ9	6.69	0.01	12.49	5.32	0.00	0.00	38.04	0.00	0.51	36.95
CZ10	15.85	10.22	8.80	1.57	0.00	0.67	39.21	4.46	17.85	11.60
CZ11	12.76	0.27	7.39	0.00	0.00	0.24	15.78	2.38	9.74	51.71
CZ12	18.12	14.61	5.50	4.49	0.00	0.00	46.30	5.57	14.13	5.88
CZ13	16.52	65.13	1.85	0.00	0.00	0.00	30.73	0.00	37.01	13.89
CZ14	2.64	0.04	17.30	1.28	0.00	0.00	58.18	0.00	14.39	6.21
SD1	1.99	0.0001	14.90	0.00	0.00	0.00	34.62	8.80	29.05	10.63
SD2	8.42	0.003	12.17	0.00	0.00	0.58	26.63	10.91	33.07	8.22
SD3	9.19	0.03	4.02	0.00	3.55	0.08	19.94	10.41	46.07	6.73
SD4	3.14	0.0001	10.53	1.38	0.00	2.39	19.70	11.28	38.89	12.69
CX1	4.26	0.004	10.71	0.10	0.00	1.05	45.84	7.07	9.35	21.63
CX2	2.64	0.004	12.92	0.00	0.00	0.89	51.85	9.07	6.99	15.65
CX3	3.83	0.002	18.92	0.00	0.00	1.40	48.72	8.78	9.14	9.21

* Other minerals comprise mostly calcite.

Appendix B

Validity of the electrical resistivity measurements at different frequencies and differential pressures

B.1. Introduction

The circumference resistivity measurement method described in Chapter 3 relies on certain assumptions, most notably that: i) the measured impedance is the real part of the complex electric impedance; ii) the electrical impedance of the test instrumentation is effectively infinite; and iii) the geometric calibration factors are constant at different effective pressures. However the validity of these assumptions needs to be confirmed.

B.2. Effect of measurement frequency

B.2.1. Complex impedance

The electrical resistivity that was measured during the experiments in Chapter 3 is actually the magnitude or modulus of the complex electrical impedance $\overline{Z}$ of the rock sample. The complex impedance $\overline{Z}$ is given by

$$\overline{Z} = Z_R + iZ_I, \tag{B1}$$

where Z_R and Z_I are the real and imaginary parts, respectively, and $i = \sqrt{-1}$. The magnitude (or modulus) Z of the impedance is given by

$$Z = \sqrt{Z_R^2 + Z_I^2}\ . \tag{B2}$$

The measurement is only meaningful if the imaginary part of $\overline{Z}$ is zero or negligible, i.e., as $Z_I \rightarrow 0$ then $Z \rightarrow Z_R$. While this may be the case at low frequencies, at higher frequencies, particularly at frequencies approaching 100 kHz, the imaginary part may become non-negligible (e.g., Olhoeft, 1985). However, even though the imaginary part was not measured, the measured modulus could indicate the presence of frequency dependent effects in the samples as it would become larger as Z_I increases.

Although an attempt was made to assess possible frequency dependent effects in the 67 sandstone samples by recording the modulus at 2 Hz, 440 Hz and 50 kHz, thus covering the frequency range used in CSEM and well logging, it became apparent that the 50 kHz data were unrepresentative of the true sample properties because of variable instrument impedance effects (see below).

B.2.2. Variable instrument impedance

The following theoretical analysis demonstrates that the test instrumentation has a variable electrical impedance and this leads to inaccurate measurements of sample resistivity at 50 kHz, but does not affect those at 2 Hz and 440 Hz.

The electrical resistivity measurement equipment (mainly the Fluke scopemeter and cables) can be represented by an equivalent electrical circuit comprising a capacitor (Ce) in parallel with a resistor (Re) as shown in Figure B1. The impedance of the capacitor (Z_C, in Ohm) is a function of current frequency given by

$$Z_C = \frac{-i}{\omega C_e}, \tag{B3}$$

where ω is the angular frequency and C_e is the capacitance (in Farad) of the capacitor Ce. The impedance of the equipment (Z_e) can then be expressed as a function of Z_C and the resistance R_e (in Ohm) of the resistor Re

$$\frac{1}{Z_e} = \frac{1}{Z_C} + \frac{1}{R_e}. \tag{B4}$$

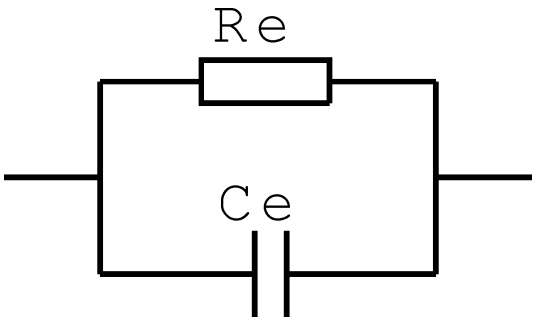

Figure B1. Equivalent circuit of the resistivity measurement equipment. Re and Ce correspond to the resistor and capacitor respectively.

Figure B2 shows how the magnitude of the complex impedance of the measurement equipment varies with current frequency from 2 Hz to 50 kHz, assuming some reasonable values for R_e and C_e. It shows that the equipment impedance is very high at low frequencies then starts to reduce significantly above about 500 Hz. The result is that above about 500 Hz, a non-negligible electrical current will flow in the test equipment which is effectively arranged in parallel with the rock sample (Figure B3). The ideal (assumed) situation is that all the applied electric current will flow through the sample so that the voltage measured across the sample gives the sample impedance. However, at higher frequencies this is not the case; the measured voltage

will include the effect of the sample and the equipment as indicated in Figure B3. This leads to an underestimate of the true rock resistivity at higher frequencies. This can be verified as follows.

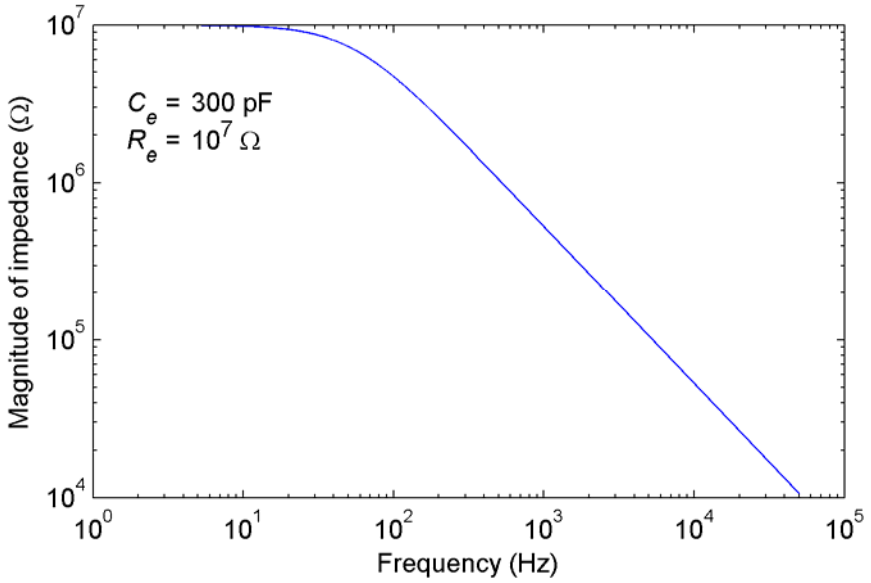

Figure B2. Variation of the equipment impedance with current frequency. Here, the capacitance of the capacitor and resistance of the resistor are estimated to be 300 pF and 10^7 Ω respectively.

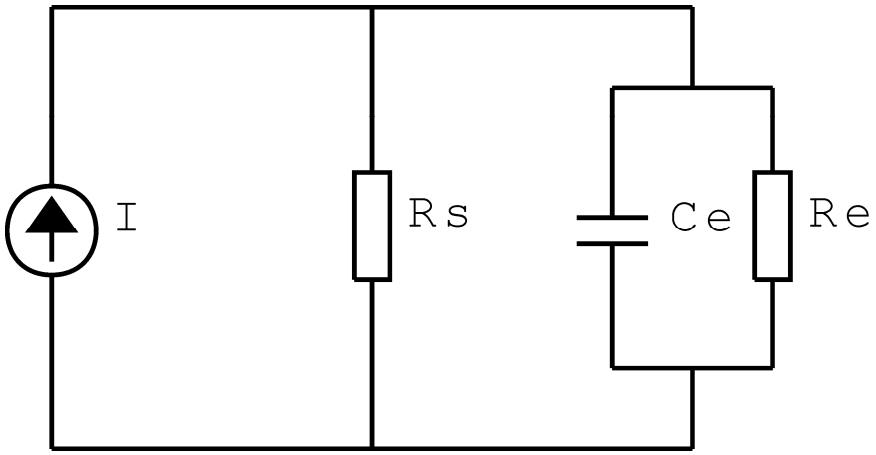

Figure B3. Equivalent circuit of the resistivity measurements on a rock sample of resistance Rs showing the instrument effect. I corresponds to the constant current source.

Assume the sandstone sample in Figure B3 is a pure resistor so that the total impedance (Z_t) of the circuit is

$$\frac{1}{Z_t} = \frac{1}{Z_e} + \frac{1}{R_s}. \qquad \text{(B5)}$$

The voltage measured over the sample according to Ohm's law is

$$V_{meas} = Z_t I \,, \tag{B6}$$

and the measured resistance (R_{meas}) of the sample is calculated to be

$$R_{meas} = \frac{V_{meas}}{I} = Z_t \,. \tag{B7}$$

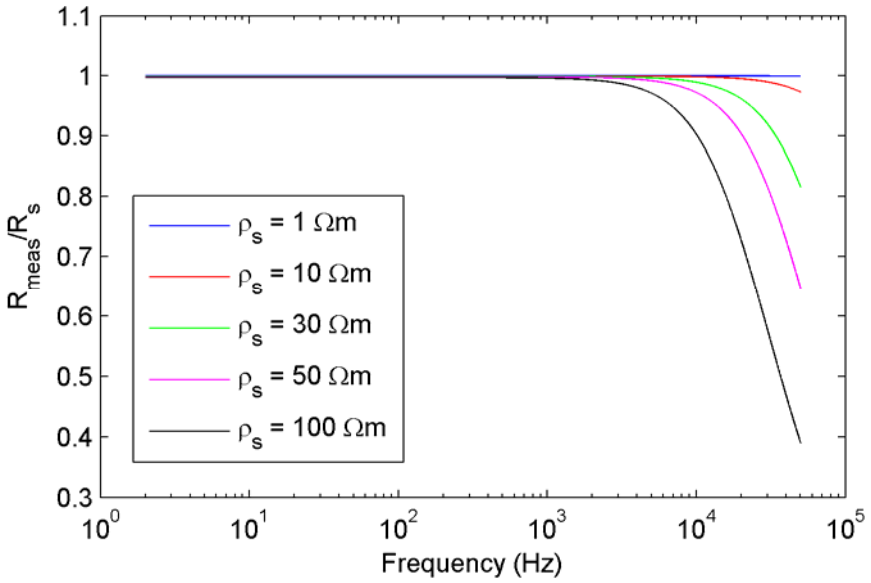

Figure B4. The ratio of measured sample resistance (R_{meas}) to the actual sample resistance (R_s) as a function of frequency on a series of samples with varying resistivity ρ_s, where $R_s = 250\rho_s$.

Figure B4 shows the ratio of the measured sample resistance R_{meas} to the actual sample resistance R_s as a function a frequency with sample resistivity ranging from 1 Ωm to 100 Ωm; this range covers most of the sample resistivities observed in this study. Figure B4 shows that the measured sample resistance in general becomes lower than the actual sample resistance with increasing current frequency and with increasing sample resistivity (resistance). However, at 2 Hz and 440 Hz in particular, the deviation of the measured sample resistance from the actual sample resistance is negligible for all cases, confirming that resistivity measured at these two frequencies are representative of the actual resistivity of the sample. However, the resistivity data at 50 kHz are significantly affected by the equipment impedance and therefore lack the required accuracy (they may be less than 50% of the true value according to Figure B4).

B.3. Effect of measurement pressure

It was assumed that the geometric factors calibrating measured resistance to the sample resistivity are constant at all differential pressures. However a slight change of the sample dimensions would be expected with elevated pressure requiring the geometric factors to be re-determined accordingly. It is therefore necessary to test whether this constant geometric factors assumption is valid.

Best (1992) showed that for consolidated sandstones sample length (axial) varies by less than about 0.3% at differential pressures from 0.1 to 60 MPa. Hence, we would expect a resistivity measurement error of no more than 0.5% due to changes in geometric factors in our sandstone samples by calculating resistivity from the varying geometric factors using a finite element method (Adler and Lionheart, 2006) as shown in Figure B5. This is taken into account in the overall accuracy of the circumference method of ± 2% quoted in Chapter 3.

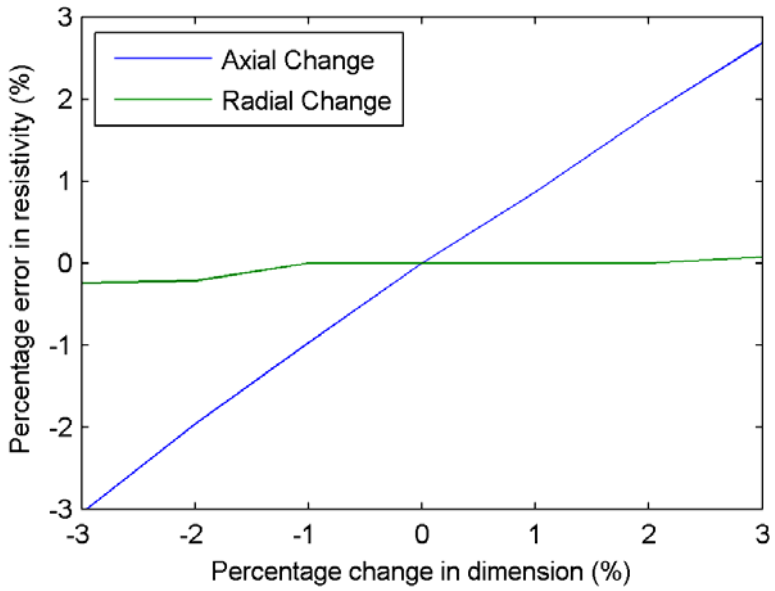

Figure B5. The resistivity error induced by the change of the sample dimensions. The error corresponds to the deviation in resistivity calculated using a finite element model from that using constant geometric factors.

B.4. Conclusions

It has been shown that the measurement frequency does not affect the resistivity at 2 Hz and 440 Hz due to the equipment impedance but does at 50 kHz. The error associated with using constant geometric calibration factors at all differential

pressures are small, but finite, and are therefore taken into account. Hence, only the 2 Hz electrical data relevant to CSEM were analysed in Chapters 4 – 7; these values were almost identical to those at 440 Hz, which are included in Appendix D for completeness.

A more sophisticated measurement system will be required to study electrical frequency-dependent effects in future.

Appendix C

Regression coefficients in equation 5.1 for the elastic and electrical properties of the 63 sandstone samples

Sample	*Vp*			1000/*Qp*			*Vs*			1000/*Qs*			*ρ*		
	A	*B*	*C*	*A*	*B*	*C*	*A*	*B*	*C*	*A*	*B*	*C*	*A*	*B*	*C*
W162.0	4508.838	327.838	0.037	19.386	-19.488	0.081	2640.976	262.912	0.043	34.149	-19.342	0.057	33.893	11.381	0.043
W165.6	4332.183	253.581	0.064	18.792	-27.230	0.034	2741.454	221.791	0.048	45.074	-57.327	0.106	6.174	0.523	0.030
W165.6H	4461.239	275.326	0.067	40.131	-33.305	0.047	2644.703	237.982	0.037	72.228	-87.246	0.064	6.677	0.655	0.062
W165.7	4136.808	312.801	0.033	40.065	-31.396	0.044	2689.816	221.766	0.027	99.032	-17.898	0.047	6.495	0.735	0.050
W165.7H	4311.097	376.665	0.041	39.461	-42.290	0.036	2715.735	321.763	0.034	86.847	-56.335	0.084	6.383	0.607	0.083
W166.0	4440.900	286.481	0.061	32.403	-29.718	0.067	2774.009	277.147	0.062	33.360	-76.060	0.120	7.093	0.592	0.058
W166.0H	4556.202	319.289	0.054	19.425	-28.449	0.071	2784.910	290.251	0.069	35.225	-84.424	0.119	8.223	1.007	0.043
W160.15H	4509.801	500.998	0.058	20.305	-45.458	0.069	2655.344	452.308	0.061	44.350	-77.819	0.099	17.712	4.308	0.053
W160.15	4334.578	451.393	0.046	19.208	-34.257	0.048	2661.658	382.598	0.049	48.272	-96.444	0.065	16.603	4.444	0.040
W160.21H	4470.701	497.380	0.052	22.224	-38.995	0.065	2679.983	466.619	0.052	27.886	-62.164	0.070	18.117	4.864	0.046
TS	4620.812	498.212	0.049	18.374	-38.006	0.082	2827.746	430.559	0.060	28.922	-47.262	0.075	30.176	11.514	0.043
RB3	4319.598	715.585	0.053	19.298	-58.374	0.066	2650.019	704.947	0.058	35.875	-127.266	0.100	21.559	8.824	0.047
RES1	4595.922	604.994	0.053	20.468	-56.587	0.095	2849.238	526.165	0.062	31.298	-84.481	0.107	21.613	6.585	0.039
WATTSCLIFFE	4158.516	458.881	0.038	32.970	-42.649	0.063	2534.455	370.882	0.042	40.086	-138.337	0.102	8.320	1.540	0.048
RS	4510.066	620.933	0.060	19.465	-66.297	0.083	2665.937	495.475	0.058	31.572	-55.437	0.082	9.433	1.651	0.056
BEESTONE	4127.665	526.243	0.062	19.986	-45.543	0.063	2452.907	446.046	0.063	29.251	-55.791	0.051	6.032	0.950	0.035
E4	4776.476	216.971	0.063	6.272	-15.928	0.057	3085.864	153.938	0.069	22.116	-19.281	0.047	7.926	0.524	0.041
COVERED	4211.251	656.377	0.044	18.367	-54.551	0.062	2482.780	555.423	0.061	46.738	-77.220	0.054	5.119	0.731	0.044
YORK3	4666.753	500.253	0.048	14.711	-36.933	0.074	2905.076	440.107	0.054	28.578	-52.938	0.068	27.342	9.625	0.039
1DYK	4376.248	583.780	0.058	16.781	-49.934	0.069	2709.903	554.994	0.067	31.849	-90.511	0.096	20.596	6.746	0.044
RB2	4285.462	888.042	0.072	24.862	-76.628	0.102	2570.998	745.901	0.064	40.007	-78.312	0.087	32.898	18.855	0.054
1VSF	3857.729	590.484	0.056	27.119	-72.245	0.086	2254.311	404.534	0.043	34.914	-76.222	0.066	5.132	0.761	0.033
4SU	4481.509	740.676	0.050	16.629	-49.336	0.054	2739.017	677.872	0.055	31.382	-61.443	0.056	33.033	15.840	0.043
YORK2	4591.734	563.245	0.049	72.577	-102.306	0.071	2979.086	904.811	0.042	92.373	-122.596	0.071	25.849	9.603	0.041
PEAKMOOR	4287.540	473.343	0.035	40.504	-48.592	0.041	2600.486	358.158	0.035	58.019	-124.067	0.094	11.411	2.347	0.034
1SU	4634.270	878.292	0.056	22.652	-71.051	0.073	2647.522	723.347	0.040	28.144	-81.386	0.035	31.656	16.251	0.043
DUKES	4322.978	549.994	0.061	12.173	-52.324	0.082	2587.166	461.655	0.051	48.035	-136.910	0.093	13.927	4.006	0.054
E6	4752.516	210.515	0.049	18.256	-17.490	0.059	3001.251	160.623	0.049	34.288	-24.267	0.041	9.201	0.812	0.044
E3	4672.871	172.947	0.040	1.605	-15.374	0.023	3062.621	129.583	0.052	25.651	-9.835	0.045	8.651	0.677	0.042
E5	4807.869	174.398	0.047	9.352	-12.496	0.045	3119.909	124.594	0.062	12.202	-12.816	0.031	10.404	0.665	0.064
STONERAISE	4895.342	448.404	0.066	27.927	-38.972	0.052	3067.201	418.830	0.070	35.511	-51.847	0.077	25.234	6.717	0.063
SX1	4109.259	550.683	0.051	60.785	-148.653	0.105	2749.856	492.728	0.033	55.036	-69.347	0.043	32.244	14.686	0.042
SX2	4643.027	480.935	0.025	21.944	-53.604	0.051	2935.282	396.305	0.023	42.843	-108.990	0.061	67.591	29.789	0.034
SX3	4656.868	600.824	0.047	45.088	-91.671	0.052	3004.949	582.417	0.056	67.109	-146.271	0.065	40.680	22.377	0.028
SX4	4531.610	703.194	0.070	100.725	-85.402	0.082	2938.834	756.511	0.046	86.957	-36.571	0.061	31.922	16.071	0.037
SX5	4577.048	567.483	0.046	46.118	-90.734	0.062	2798.651	531.141	0.031	62.897	-30.769	0.140	27.654	11.879	0.043

SX6	4625.445	566.177	0.041	46.784	-196.979	0.116	2969.557	647.251	0.058	72.278	-110.280	0.051	36.710	17.316	0.027
SX7	4575.133	640.519	0.057	58.897	-56.587	0.052	2684.413	953.143	0.068	68.192	-28.964	0.038	28.974	13.012	0.039
SX8	4754.607	431.946	0.037	34.113	-62.285	0.013	2930.411	342.774	0.038	82.785	-55.851	0.070	35.248	13.819	0.049
SX9	4765.918	443.185	0.020	52.324	-60.374	0.057	2975.231	341.092	0.026	82.333	-90.239	.068	30.893	10.908	0.027
SX10	4477.737	453.587	0.032	42.671	-84.561	0.048	2889.778	381.395	0.034	61.837	-217.885	0.094	62.161	26.102	0.045
SX11	4693.499	549.817	0.041	57.692	-79.159	0.082	2995.134	545.971	0.044	44.724	-87.260	0.027	42.246	22.879	0.026
CZ1	4446.758	920.298	0.067	10.333	-70.877	0.072	2555.807	738.177	0.064	30.858	-94.823	0.076	7.734	1.709	0.041
CZ2	3806.807	877.448	0.062	28.919	-94.923	0.075	2091.015	508.234	0.045	57.463	-18.051	0.042	3.906	0.887	0.065
CZ3	3856.904	654.594	0.052	40.937	-92.250	0.059	2208.797	620.429	0.045	80.342	-71.209	0.041	3.287	0.562	0.057
CZ4	4179.870	790.687	0.076	18.089	-79.958	0.094	2466.316	753.439	0.096	44.118	-141.525	0.096	6.642	1.239	0.063
CZ5	3264.053	751.740	0.049	20.007	-111.404	0.088	1769.189	591.376	0.050	54.392	-80.867	0.114	1.950	0.266	0.031
CZ6	3853.493	435.946	0.086	27.700	-176.587	0.123	1998.055	249.594	0.074	94.273	-56.754	0.047	23.772	4.529	0.034
CZ7	4781.211	465.840	0.062	31.143	-30.556	0.061	2781.825	274.790	0.070	28.646	-49.221	0.101	36.904	13.081	0.059
CZ8	5543.311	562.880	0.048	0.628	-33.047	0.023	3242.865	528.093	0.044	21.683	-53.267	0.056	148.829	110.127	0.031
CZ9	4991.566	242.626	0.060	72.378	-71.201	0.070	2816.982	235.701	0.055	35.952	-46.372	0.085	47.486	18.380	0.065
CZ10	3935.547	934.796	0.056	18.490	-81.920	0.068	2250.425	586.679	0.046	40.973	-101.133	0.085	5.013	1.127	0.054
CZ11	4487.123	846.230	0.069	54.861	-141.980	0.077	2347.731	576.813	0.060	62.459	-87.643	0.067	13.250	4.549	0.066
CZ12	3752.117	506.082	0.049	22.288	-43.118	0.067	2158.547	493.243	0.069	39.338	-70.941	0.068	4.746	0.681	0.056
CZ13	4230.220	670.333	0.068	44.476	-66.502	0.072	2281.312	559.495	0.067	31.072	-125.577	0.091	4.403	0.542	0.073
CZ14	5432.726	832.494	0.051	7.757	-26.190	0.062	3344.508	945.417	0.059	20.616	-111.475	0.076	152.845	122.924	0.049
SD1	5556.894	311.494	0.048	3.874	-22.097	0.022	3261.661	237.021	0.050	16.383	-18.456	0.025	210.192	107.195	0.043
SD2	4598.748	515.393	0.040	19.857	-31.948	0.089	2623.531	518.826	0.048	28.217	-47.942	0.054	27.935	10.627	0.027
SD3	4572.588	452.533	0.045	15.577	-34.057	0.062	2631.276	338.844	0.048	41.352	-45.630	0.062	22.020	7.424	0.051
SD4	5376.603	336.731	0.040	5.047	-20.387	0.018	3089.325	201.975	0.031	29.376	-38.908	0.080	97.533	40.096	0.043
CX1	5145.804	663.173	0.057	7.413	-35.184	0.076	3025.607	564.048	0.057	25.585	-69.958	0.074	76.386	49.668	0.042
CX2	5300.258	587.386	0.053	13.808	-29.599	0.088	3131.238	599.942	0.062	24.986	-59.731	0.075	99.782	85.183	0.077
CX3	4935.178	588.635	0.063	9.936	-25.829	0.046	2859.476	544.100	0.058	33.456	-59.646	0.071	60.779	40.381	0.054

Appendix D

Joint elastic-electrical measurement results on the 67 sandstone samples in this study

	60 MPa						40 MPa					
Sample	V_p	Q_p	V_s	Q_s	ρ 2 Hz	ρ 440 Hz	V_p	Q_p	V_s	Q_s	ρ 2 Hz	ρ 440 Hz
W162.0	4474	51.4	2621	29.0	32.90	32.11	4430	49.4	2593	27.4	32.10	31.33
W165.6	4332	44.5	2733	22.0	6.09	6.06	4303	39.2	2706	21.8	6.02	5.98
W165.6H	4462	23.9	2621	13.4	6.65	6.64	4433	21.8	2588	13.0	6.64	6.62
W165.7	4096	23.9	2646	10.0	6.45	6.43	4051	21.6	2616	9.8	6.40	6.39
W165.7H	4285	22.6	2670	11.7	6.37	6.36	4223	20.4	2637	11.0	6.37	6.35
W166.0	4440	30.9	2772	31.1	7.08	7.07	4408	28.3	2747	28.9	7.03	7.01
W166.0H	4546	51.3	2787	28.9	8.14	8.13	4516	46.4	2758	27.5	8.05	8.04
W160.15H	4503	48.7	2651	23.2	17.54	17.39	4449	41.6	2607	21.2	17.22	17.01
W160.15	4313	47.2	2646	20.4	16.21	16.03	4248	41.4	2601	17.7	15.73	15.56
W160.21H	4456	43.7	2665	35.5	17.80	17.63	4399	39.4	2615	31.3	17.35	17.16
TS	4602	56.5	2820	34.3	29.35	29.10	4541	47.2	2784	31.9	28.04	27.72
RB3	4295	50.9	2632	28.3	21.03	20.78	4225	41.5	2576	26.2	20.22	19.92
RES1	4575	49.3	2841	32.8	21.01	20.79	4521	45.3	2801	30.3	20.17	19.91
WATTSCLIFFE	4116	29.9	2507	25.7	8.23	8.17	4050	27.1	2460	23.1	8.11	8.05
RS	4503	52.0	2662	31.6	9.36	9.31	4441	43.9	2601	29.8	9.28	9.24
BEESTONE	4123	47.9	2449	30.9	5.92	5.87	4072	42.1	2410	28.5	5.81	5.76
E4	4775	145.9	3085	43.5	7.88	7.87	4754	128.5	3075	39.4	7.83	7.82
COVERED	4168	52.6	2476	20.4	5.07	5.04	4094	42.2	2424	17.6	4.99	4.97
YORK3	4644	69.3	2893	34.2	26.43	26.12	4585	57.4	2845	31.2	25.24	24.94
1DYK	4364	58.7	2706	31.5	20.10	19.88	4313	48.1	2664	29.4	19.43	19.21
RB2	4299	42.6	2570	25.4	32.50	31.89	4209	36.6	2495	23.0	30.19	29.63
1VSF	3845	36.9	2227	27.9	5.03	5.01	3786	33.7	2177	24.6	4.93	4.91
4SU	4449	54.4	2717	29.7	31.90	31.44	4376	44.3	2661	26.5	30.08	29.59
YORK2	4573	13.9	2895	10.5	25.06	24.81	4499	12.4	2826	10.2	23.93	23.67
PEAKMOOR	4233	22.5	2559	17.7	11.10	10.98	4163	19.8	2506	16.1	10.84	10.72
1SU	4611	43.5	2582	24.4	30.43	29.92	4534	36.4	2505	23.1	28.83	28.35

DUKES	4318	78.4	2569	21.4	13.80	13.67	4262	70.9	2517	18.9	13.44	13.29
E6	4745	52.6	2995	27.4	9.15	9.13	4717	50.9	2975	25.9	9.05	9.04
E3	4660	177.1	3060	37.7	8.59	8.58	4632	131.3	3041	37.3	8.54	8.52
E5	4800	98.7	3119	70.2	10.39	10.38	4777	85.7	3105	63.9	10.34	10.34
STONERAISE	4896	33.5	3070	28.3	25.12	25.03	4849	30.8	3031	26.0	24.67	24.55
SX1	4094	16.9	2681	16.8	31.14	30.97	4022	15.4	2621	14.6	29.40	29.16
SX2	4538	41.7	2838	22.1	63.53	60.94	4465	33.8	2777	18.7	60.41	58.23
SX3	4618	20.4	2983	14.7	36.44	35.50	4571	17.4	2943	12.4	33.24	32.37
SX4	4537	10.0	2887	11.5	30.22	29.61	4476	9.4	2820	10.9	28.02	27.37
SX5	4548	21.1	2720	16.0	26.73	26.69	4476	17.9	2630	15.8	25.54	25.36
SX6	4586	22.4	2961	13.3	33.33	32.79	4507	19.6	2891	11.2	31.03	30.61
SX7	4564	16.5	2658	14.1	27.74	27.57	4496	14.7	2618	13.3	26.28	26.05
SX8	4712	16.1	2895	12.1	34.39	34.05	4650	13.9	2858	11.4	33.35	32.84
SX9	4631	18.6	2899	12.1	28.70	28.37	4562	16.9	2859	11.1	27.21	26.92
SX10	4411	21.6	2843	17.0	60.76	58.86	4357	17.6	2792	14.6	57.44	55.87
SX11	4646	17.5	2958	16.2	37.28	36.15	4587	16.1	2902	13.6	34.18	33.37
CZ1	4437	91.1	2544	31.4	7.62	7.59	4378	67.7	2495	28.4	7.38	7.35
CZ2	3795	34.5	2060	17.0	3.90	3.85	3720	29.1	2005	16.4	3.83	3.78
CZ3	3834	23.2	2166	11.5	3.27	3.26	3769	20.1	2097	10.7	3.23	3.21
CZ4	4182	57.4	2474	22.8	6.62	6.51	4130	49.2	2442	20.8	6.54	6.43
CZ5	3233	52.7	1736	19.0	1.91	1.90	3147	39.3	1687	17.5	1.87	1.86
CZ6	3865	35.1	1995	10.1	23.21	23.10	3825	33.7	1985	9.9	22.60	22.49
CZ7	4771	31.5	2780	35.4	36.38	34.62	4739	29.2	2762	33.7	35.95	34.27
CZ8	5510	110.1	3202	42.0	131.75	126.85	5466	76.2	3159	37.1	117.92	112.77
CZ9	4992	14.0	2811	27.9	47.10	45.70	4961	12.6	2787	26.8	46.21	44.90
CZ10	3910	52.0	2212	25.4	4.96	4.91	3827	40.6	2156	21.7	4.90	4.84
CZ11	4484	18.2	2336	15.5	13.14	12.73	4425	15.7	2290	14.9	12.97	12.65
CZ12	3734	45.2	2158	24.3	4.71	4.65	3667	37.9	2116	22.9	4.68	4.62
CZ13	4223	22.6	2274	33.3	4.40	4.37	4181	20.2	2239	28.3	4.37	4.34

CZ14	5396	125.6	3320	46.4	147.60	135.37	5317	96.0	3252	38.4	133.39	122.39
SD1	5540	101.4	3247	47.4	200.90	190.10	5511	79.7	3234	46.0	192.73	181.67
SD2	4553	51.8	2598	33.1	25.76	24.59	4491	46.9	2541	30.1	24.34	23.37
SD3	4547	62.8	2613	23.8	21.81	21.19	4490	52.1	2583	22.0	20.82	20.41
SD4	5348	83.3	3059	34.5	94.23	89.13	5305	66.9	3032	32.3	90.85	87.09
CX1	5127	127.6	3005	37.6	71.49	69.83	5075	108.3	2968	34.4	68.24	66.48
CX2	5275	75.8	3118	39.1	99.66	90.57	5233	65.4	3079	36.0	94.27	84.08
CX3	4920	85.1	2837	29.4	58.81	57.61	4887	71.4	2816	26.5	56.56	55.47
	26 MPa						20 MPa					
Sample	V_p	Q_p	V_s	Q_s	ρ 2 Hz	ρ 440 Hz	V_p	Q_p	V_s	Q_s	ρ 2 Hz	ρ 440 Hz
W162.0	4385	46.0	2556	25.6	30.28	29.58	4349	43.0	2530	24.9	28.93	28.29
W165.6	4286	33.6	2670	20.7	5.94	5.90	4268	29.9	2661	19.4	5.88	5.85
W165.6H	4415	20.2	2556	11.0	6.54	6.53	4385	19.0	2529	10.3	6.50	6.49
W165.7	4007	19.9	2584	9.6	6.31	6.29	3976	19.0	2558	9.5	6.21	6.19
W165.7H	4181	17.7	2595	10.7	6.32	6.32	4155	16.6	2547	10.2	6.27	6.26
W166.0	4378	26.5	2712	26.4	6.95	6.93	4358	25.1	2697	24.4	6.91	6.89
W166.0H	4472	41.8	2733	25.1	7.89	7.88	4451	37.8	2712	23.3	7.79	7.77
W160.15H	4386	35.8	2559	19.7	16.55	16.36	4363	31.6	2525	17.9	16.20	16.03
W160.15	4195	34.6	2555	14.9	15.02	14.81	4160	30.6	2518	13.4	14.61	14.42
W160.21H	4336	34.4	2556	25.0	16.63	16.45	4306	30.7	2520	23.5	16.13	15.94
BEREA	3845	44.0	2342	22.4	2.66	2.63	3801	36.6	2302	21.1	2.60	2.59
BP AX	3738	33.2	2220	19.1	2.83	2.82	3699	29.4	2189	16.9	2.75	2.76
BP AY	3609	37.2	2124	18.9	2.91	2.90	3566	33.3	2096	17.8	2.86	2.90
BP AZ1	3874	36.4	2241	19.1	2.50	2.49	3829	29.5	2216	15.0	2.45	2.49
TS	4479	43.9	2735	27.2	26.26	26.00	4440	39.0	2696	25.5	25.33	25.05
RB3	4132	32.3	2483	21.4	18.89	18.61	4076	28.8	2438	18.5	18.10	17.85
RES1	4435	38.6	2740	26.6	19.22	18.96	4391	35.7	2692	24.1	18.62	18.36
WATTSCLIFFE	3982	23.7	2409	19.4	7.88	7.81	3949	22.4	2379	17.0	7.72	7.66

RS	4367	36.5	2555	25.5	9.05	9.01	4330	31.6	2511	23.7	8.88	8.84
BEESTONE	4019	34.9	2360	22.0	5.64	5.58	3976	29.9	2328	20.6	5.56	5.51
E4	4731	100.5	3058	35.3	7.75	7.74	4717	86.3	3047	34.0	7.70	7.68
COVERED	3999	33.5	2368	15.1	4.89	4.86	3944	30.1	2316	14.0	4.81	4.78
YORK3	4522	49.3	2798	26.2	23.87	23.56	4480	42.7	2758	23.7	22.92	22.62
1DYK	4242	39.4	2608	25.4	18.41	18.19	4201	34.2	2568	21.7	17.76	17.53
RB2	4121	31.7	2414	20.6	28.16	27.62	4074	28.6	2375	18.5	26.84	26.43
1VSF	3715	28.5	2125	19.9	4.82	4.80	3670	24.5	2083	18.1	4.73	4.71
4SU	4277	35.1	2574	21.7	27.70	27.22	4212	29.6	2514	19.2	26.35	25.89
YORK2	4428	11.0	2689	8.9	22.52	22.27	4380	10.4	2467	8.3	21.60	21.38
PEAKMOOR	4094	17.6	2450	14.0	10.45	10.33	4056	16.0	2425	12.9	10.21	10.09
1SU	4426	30.2	2402	17.4	26.35	25.92	4356	26.3	2317	12.9	24.81	24.41
DUKES	4208	54.8	2473	16.1	12.91	12.76	4164	45.6	2416	14.6	12.61	12.45
E6	4695	46.3	2954	23.4	8.96	8.94	4676	41.7	2941	22.0	8.86	8.84
E3	4616	97.9	3027	34.8	8.43	8.42	4600	88.0	3020	33.6	8.35	8.34
E5	4759	76.0	3096	55.8	10.30	10.29	4739	69.8	3087	51.4	10.21	10.21
STONERAISE	4813	26.7	2989	23.0	23.90	23.76	4776	24.1	2968	21.3	23.35	23.18
SX1	3951	13.9	2528	12.9	27.56	27.05	3909	13.0	2512	12.1	25.85	25.63
SX2	4387	27.0	2714	15.3	55.24	53.61	4357	24.5	2685	13.5	52.21	50.90
SX3	4480	14.8	2872	10.6	29.81	29.41	4416	12.9	2823	9.0	27.80	27.58
SX4	4392	9.1	2707	10.7	25.81	25.19	4370	8.6	2640	10.1	24.25	23.74
SX5	4401	16.0	2587	15.6	23.74	23.58	4358	14.0	2513	15.5	22.59	22.44
SX6	4422	17.3	2821	9.4	28.03	27.75	4384	15.4	2771	8.9	26.67	26.40
SX7	4418	13.9	2562	12.8	24.27	24.07	4374	13.2	2448	12.3	23.03	22.82
SX8	4597	12.5	2791	10.9	31.60	30.90	4555	12.4	2772	10.4	30.12	29.44
SX9	4500	15.0	2798	10.4	25.43	25.23	4467	14.1	2771	9.3	24.50	24.38
SX10	4278	15.2	2730	11.6	53.77	52.55	4236	13.1	2694	10.3	51.56	50.39
SX11	4500	14.9	2826	11.2	30.36	29.94	4452	13.7	2761	10.7	28.54	28.07
CZ1	4280	48.2	2411	22.1	7.12	7.07	4204	36.1	2347	19.8	7.00	6.94

CZ2	3618	22.4	1932	15.7	3.74	3.71	3559	20.1	1894	15.4	3.66	3.63
CZ3	3687	16.2	2033	9.5	3.16	3.15	3627	14.4	1955	8.9	3.11	3.09
CZ4	4062	38.1	2395	18.2	6.39	6.30	4009	32.5	2358	15.1	6.29	6.22
CZ5	3057	32.1	1626	16.9	1.83	1.82	2986	25.9	1549	16.1	1.81	1.80
CZ6	3800	30.1	1960	9.2	21.94	21.80	3775	24.1	1944	8.5	21.54	21.33
CZ7	4688	26.8	2735	30.3	34.06	32.70	4645	24.9	2714	28.4	32.73	31.72
CZ8	5386	53.9	3079	28.9	101.45	98.94	5329	46.2	3022	25.4	90.19	88.62
CZ9	4937	11.8	2761	23.8	44.07	42.59	4919	11.3	2736	22.1	42.44	41.25
CZ10	3716	30.7	2074	18.1	4.74	4.68	3634	25.4	2025	17.0	4.61	4.57
CZ11	4335	13.5	2228	12.5	12.43	12.13	4280	12.0	2169	12.0	12.01	11.76
CZ12	3604	33.0	2072	20.3	4.59	4.53	3566	30.3	2043	16.9	4.51	4.46
CZ13	4112	18.0	2183	22.4	4.33	4.29	4061	16.5	2139	19.1	4.28	4.24
CZ14	5214	73.9	3144	27.9	118.33	109.47	5127	64.5	3054	22.0	108.32	100.83
SD1	5467	61.2	3200	28.1	175.67	166.37	5437	54.1	3171	35.6	163.48	154.60
SD2	4414	42.0	2471	24.5	22.62	21.76	4362	40.3	2423	23.1	21.49	20.80
SD3	4428	44.4	2529	19.5	19.99	19.44	4392	40.0	2501	18.5	19.36	18.72
SD4	5261	55.5	2998	27.7	85.14	82.07	5226	52.0	2982	26.8	80.28	77.59
CX1	4999	85.0	2900	28.7	60.83	59.36	4931	65.5	2843	23.6	53.05	51.76
CX2	5151	56.9	3010	29.5	89.23	79.87	5099	53.1	2959	26.2	82.01	72.32
CX3	4825	59.0	2737	23.3	51.63	50.51	4774	48.0	2689	21.5	47.65	46.62
	15 MPa						8 MPa					
Sample	V_p	Q_p	V_s	Q_s	ρ 2 Hz	ρ 440 Hz	V_p	Q_p	V_s	Q_s	ρ 2 Hz	ρ 440 Hz
W162.0	4323	39.9	2501	23.9	27.76	27.18	4263	33.8	2455	21.4	25.95	25.43
W165.6	4232	28.8	2644	17.4	5.84	5.80	4180	25.3	2586	14.4	5.77	5.73
W165.6H	4367	17.5	2514	14.1	6.41	6.40	4297	15.9	2466	8.0	6.28	6.27
W165.7	3949	17.9	2541	9.2	6.14	6.12	3896	16.0	2513	9.0	6.01	5.99
W165.7H	4105	15.9	2507	9.9	6.20	6.18	4036	14.0	2479	8.6	6.08	6.06
W166.0	4336	23.2	2674	22.5	6.86	6.84	4261	20.0	2602	15.9	6.71	6.70

W166.0H	4417	34.7	2690	20.4	7.69	7.67	4346	28.0	2614	14.7	7.51	7.50
W160.15H	4308	27.5	2484	16.6	15.87	15.68	4188	21.4	2374	12.5	14.86	14.68
W160.15	4113	28.0	2486	12.2	14.23	14.04	4016	23.5	2400	9.4	13.37	13.19
W160.21H	4248	26.9	2474	20.7	15.71	15.50	4139	22.1	2369	15.6	14.74	14.55
BEREA	3732	29.7	2241	16.7	2.55	2.60	3551	17.5	1966	10.2	2.52	2.48
BP AX	3637	24.9	2134	15.7	2.77	2.78	3469	16.43	1968	12.4	2.77	2.82
BP AY	3524	29.9	2065	14.0	2.86	2.89	3376	19.0	1924	10.3	2.84	2.81
BP AZ1	3768	24.0	2156	11.8	2.46	2.48	3589	15.2	2062	9.1	2.42	2.38
TS	4392	34.3	2662	22.9	24.30	24.02	4280	26.1	2558	18.1	21.91	21.68
RB3	4002	25.4	2356	16.2	17.25	17.01	3846	18.4	2203	10.7	15.47	15.26
RES1	4334	29.1	2656	21.2	17.99	17.77	4196	21.3	2524	14.8	16.77	16.54
WATTSCLIFFE	3907	20.5	2336	14.7	7.59	7.52	3814	16.9	2268	9.8	7.27	7.22
RS	4270	26.0	2474	21.4	8.71	8.67	4118	18.6	2348	16.5	8.39	8.34
BEESTONE	3930	27.1	2290	18.1	5.49	5.44	3802	21.0	2179	15.1	5.31	5.27
E4	4695	77.7	3035	32.3	7.64	7.63	4643	60.9	2996	28.0	7.55	7.54
COVERED	3877	25.4	2273	12.3	4.74	4.70	3747	19.3	2137	10.3	4.61	4.58
YORK3	4428	38.9	2712	21.4	21.96	21.65	4323	28.2	2617	16.8	20.28	19.99
1DYK	4138	29.2	2512	19.2	17.11	16.90	4007	21.8	2382	13.5	15.83	15.63
RB2	4023	25.1	2301	16.7	24.70	24.30	3768	16.9	2115	12.6	20.51	20.17
1VSF	3615	21.9	2047	16.2	4.67	4.65	3476	15.7	1966	12.4	4.55	4.53
4SU	4139	26.3	2449	17.4	24.93	24.48	3982	20.5	2300	14.1	21.67	21.29
YORK2	4348	9.5	2475	7.3	20.75	20.52	4201	7.6	2345	6.2	18.88	18.68
PEAKMOOR	4013	15.1	2396	11.7	10.00	9.90	3925	13.2	2324	8.5	9.64	9.53
1SU	4265	21.2	2252	13.2	23.21	22.83	4071	16.1	2126	11.4	20.16	19.85
DUKES	4112	35.3	2372	12.4	12.19	12.04	3981	25.5	2279	8.8	11.31	11.18
E6	4654	38.8	2929	21.3	8.78	8.76	4609	34.5	2890	19.3	8.63	8.61
E3	4574	78.4	3005	32.5	8.28	8.27	4548	69.9	2975	30.9	8.17	8.16
E5	4725	62.8	3068	50.3	10.14	10.14	4687	55.3	3044	45.0	10.01	10.00
STONERAISE	4736	21.5	2930	19.8	22.70	22.54	4626	18.8	2822	15.6	21.16	21.03

SX1	3878	10.9	2441	10.9	24.48	24.29	3730	8.0	2372	9.6	21.78	21.60
SX2	4318	21.7	2666	11.4	49.73	48.64	4246	17.2	2601	9.1	45.02	44.03
SX3	4362	11.3	2739	8.6	25.92	25.65	4245	9.5	2637	6.4	22.73	22.00
SX4	4310	7.9	2546	10.0	22.65	22.22	4120	6.9	2417	9.1	19.89	19.57
SX5	4300	12.0	2446	15.0	21.43	21.26	4179	9.9	2391	13.7	19.22	19.10
SX6	4340	12.3	2714	8.6	25.39	25.15	4209	8.0	2556	6.7	22.74	22.56
SX7	4318	11.3	2288	11.7	21.78	21.60	4160	10.5	2149	11.2	19.46	19.32
SX8	4503	12.0	2745	9.8	28.07	27.49	4435	10.9	2673	8.7	26.09	25.66
SX9	4440	12.9	2737	8.9	23.61	23.52	4385	11.0	2701	7.4	22.10	22.00
SX10	4204	12.3	2675	9.3	49.84	48.82	4126	9.9	2595	6.0	43.56	42.79
SX11	4397	12.5	2725	9.7	26.70	26.40	4296	10.1	2610	8.7	23.62	23.42
CZ1	4126	29.6	2285	16.2	6.89	6.84	3904	19.9	2109	12.1	6.47	6.39
CZ2	3470	17.2	1832	14.9	3.58	3.55	3264	12.2	1737	14.2	3.37	3.35
CZ3	3569	13.0	1870	8.4	3.05	3.04	3422	10.1	1782	7.6	2.93	2.92
CZ4	3937	28.1	2297	13.1	6.17	6.10	3744	17.8	2114	9.1	5.89	5.83
CZ5	2915	20.3	1467	14.6	1.79	1.78	2753	13.3	1381	11.5	1.74	1.73
CZ6	3748	17.2	1913	8.0	21.02	20.80	3630	10.7	1860	7.6	20.34	20.12
CZ7	4597	23.0	2688	25.9	31.58	30.65	4496	20.0	2623	19.7	28.78	28.03
CZ8	5266	40.7	2965	22.4	77.69	76.77	5164	36.2	2876	17.9	64.35	63.71
CZ9	4905	10.4	2720	21.3	40.69	39.51	4837	8.8	2663	16.7	36.56	35.69
CZ10	3541	21.2	1941	15.0	4.52	4.48	3335	15.1	1848	10.7	4.28	4.24
CZ11	4204	9.9	2123	10.5	11.57	11.35	3995	7.6	1988	8.8	10.57	10.37
CZ12	3523	26.9	1982	15.3	4.45	4.40	3402	20.9	1872	12.5	4.31	4.27
CZ13	3992	15.3	2076	16.6	4.22	4.19	3839	12.1	1954	10.8	4.10	4.07
CZ14	5048	58.6	2959	18.1	94.21	86.59	4876	41.4	2755	12.3	69.29	65.91
SD1	5408	51.1	3147	33.5	152.62	144.54	5344	44.9	3105	32.5	135.02	128.49
SD2	4324	36.2	2380	20.0	21.00	20.27	4220	28.0	2265	16.9	19.31	18.65
SD3	4350	34.6	2474	17.1	18.77	17.91	4252	27.4	2398	14.4	16.96	16.33
SD4	5192	48.8	2966	25.7	75.85	73.35	5132	43.9	2931	19.8	69.60	67.23

CX1	4871	52.7	2779	20.7	49.05	47.85	4725	37.8	2669	15.6	41.56	40.59
CX2	5035	48.2	2895	22.8	71.98	65.13	4917	34.8	2765	17.3	53.87	49.20
CX3	4693	42.8	2627	18.0	41.22	40.45	4583	36.6	2520	14.9	35.28	34.52

References

Adler A. and Lionheart W.R.B. 2006. Uses and abuses of EIDORS: an extensible software base for EIT. *Physiological Measurement* **27**, S25–S42.

Al-Mjeni R., Günzel F., Jing X., Grattoni C.A. and Zimmerman R.W. 2002. The influence of clay fraction on the complex impedance of shaly sands. Symbolic Computational Algebra 2002-29.

Alvarez R. 1973. Effects of atmospheric moisture on rock resistivity. *Journal of Geophysical Research* **78**, 1769-1779.

Archie G.E. 1942. The electrical resistivity log as an aid in determining some reservoir characteristics. *Transactions of the American Institute of Mining, Metallurgical and Petroleum Engineers* **146**, 54-62.

Baines S.J. and Worden R.H. 2004. Geological storage of carbon dioxide. *Geological Society of London Special Publications*, **233**, 1-6.

Barker R.D. and Worthington P.F. 1973. Some hydrogeophysical properties of the Bunter Sandstone of northwest England. *Geoexploration* **11**, 151-170.

Batzle M.L., Han D. and Hofmann R. 2006. Fluid mobility and frequency-dependent seismic velocity-direct measurements. *Geophysics* **71**, N1-N9.

Berryman J. 1980a. Long-wavelength propagation in composite elastic media I. Spherical inclusions. *Journal of the Acoustical Society of America* **68**, 1809-1819.

Berryman J. 1980b. Long-wavelength propagation in composite elastic media II. Ellipsoidal inclusions. *Journal of the Acoustical Society of America* **68**, 1820-1831.

Berryman J. 1992. Single-scattering approximations for coefficients in Biot's equations of poroelasticity. *Journal of the Acoustical Society of America* **91**, 551-571.

Berryman J. 1995. Mixture theories for rock properties, In: *A Handbook of Physical Constants*, (eds T.J. Ahrens), pp. 205-228. American Geophysical Union, Washington D.C.

Best A.I. 1992. *The prediction of the reservoir properties of sedimentary rocks from seismic measurements*. PhD thesis, University of Reading.

Best A.I. and McCann C. 1995. Seismic attenuation and pore-fluid viscosity in clay-rich reservoir sandstones. *Geophysics* **60**, 1386-1397.

Best A.I. and Sams M.S. 1997. Compressional wave velocity and attenuation at ultrasonic and sonic frequencies in near-surface sedimentary rocks. *Geophysical Prospecting* **45**, 327-344.

Best A.I., Huggett Q.J. and Harris A.J.K. 2001. Comparison of in situ and laboratory acoustic measurements on Lough Hyne marine sediments. *The Journal of the Acoustical Society of America* **110**, 695-709.

Best A.I., McCann C. and Sothcott J. 1994. The relationships between the velocities, attenuations and petrophysical properties of reservoir sedimentary rocks. *Geophysical Prospecting* **42**, 151-178.

Biot M.A. 1956a. Theory of propagation of elastic waves in a fluid saturated porous solid. 1: Low-frequency range. *Journal of the Acoustical Society of America* **28**, 168–178.

Biot M.A. 1956b. Theory of propagation of elastic waves in a fluid saturated porous solid. 2: Higher-frequency range. *Journal of the Acoustical Society of America* **28**, 179–191.

Börner F.D. and Schön J.H. 1995. Low frequency complex conductivity measurements of microcrack properties. *Surveys in Geophysics* **16**, 121-135.

Bourbie T. and Zinszner B. 1985. Hydraulic and acoustic properties as a function of porosity in Fontainebleau sandstone. *Journal of Geophysical Research* **90**, 11524-11532.

Brace W.F. and Orange A.S. 1968. Further studies of the effects of pressure on electrical resistivities of rocks. *Journal of Geophysical Research* **73**, 5407-5420.

Brace W.F., Orange A.S. and Madden T.R. 1965. The effect of pressure on the

electrical resistivity of water saturated crystalline rocks. *Journal of Geophysical Research* **70**, 5669-5678.

Brito Dos Santos W.L., Ulrych T.J. and de Lima O.A.L. 1988. A new approach for deriving pseudovelocity logs from resistivity logs. *Geophysical Prospecting* **36**, 83-91.

Bruggeman D.A.G. 1935. Berechnung verschiedener physikalischer konstanten von heterogenen Substanzen. *Annalen der Physik* **24**, 636-679.

Bussian A.E. 1983. Electrical conductance in a porous medium. *Geophysics* **48**, 1258-1268.

Carcione J.M, Ursin B. and Nordskag J.I. 2007. Cross-property relations between electrical conductivity and the seismic velocity of rocks. *Geophysics* **72**, E193-E204.

Carman P.C. 1937. Fluid flow through granular beds. *Trans. Inst. Chem. Eng.* **15**, 150–156.

Carothers J.E. 1968. A statistical study of the formation factor relation. *The Log Analyst* **9**, 13-20.

Carrara E., Mazzacca A., Pece R., Roberti N. and Vanorio T. 1999. Evaluation of porosity and saturation degree by laboratory joint measurements of velocity and resistivity: a model improvement. *Pure and Applied Geophysics* **154**, 211-255.

Carrara E., Pece R. and Roberti N. 1994. Geoelectrical and seismic prospection in hydrogeology: model and master curves for the evaluation of porosity and water saturation. *Pure and Applied Geophysics* **143**, 729-751.

Castagna J.P., Batzle M.L. and Eastwood R.L. 1985. Relationships between compressional-wave and shear-wave velocities. *Geophysics* **50**, 571-581.

Chan C.Y., Buettner H.M., Newmark R. and Mavko G. 2000. Conductivity measurements of sand-clay mixtures: A modified experimental method. *Journal of Environmental and Engineering Geophysics* **5**, 15-26.

Chand S., Minshull T.A., Gei D. and Carcione H.M. 2004. Elastic velocity models for gas-hydrate-bearing sediments-a comparison. *Geophysical Journal International* **159**, 573-590.

Chelidze T.L., Gueguen Y. and Ruffet C. 1999. Electrical spectroscopy of porous rocks: a review-II. Experimental results and interpretation. *Geophysical Journal International* **137**, 16-34.

Chen J. and Dickens T.A. 2008. Effects of uncertainty in rock-physics models on reservoir parameter estimation using seismic amplitude variation with angle and controlled-source electromagnetics data. *Geophysical Prospecting* **57**, 61-74.

Clavier C., Coates G. and Dumanoir J. 1984. Theoretical and experimental bases for the Dual Water model for the interpretation of shaly sands. *Society of Petroleum Engineers* **24**, 153-168.

Cleary C., Chen I.-W. and Lee S.-M. 1980. Self consistent techniques for heterogeneous media. *American Society of Civil Engineers Journal of Engineering, Mechanics Division* **106**, 861-887.

Cohen M.H. 1981. Scale invariance of the low-frequency electrical properties of inhomogeneous materials. *Geophysics* **46**, 1057-1059.

Constable S. and Srnka L.J. 2007. An introduction to marine controlled-source electromagnetic methods for hydrocarbon exploration. *Geophysics* **72**, WA3-WA12.

Daily W.D. and Lin W. 1985. Laboratory-determined transport properties of Berea sandstone. *Geophysics* **50**, 775-784.

Dasios A., Astin T.R. and McCann C. 1998. Increasing confidence in seismic *Q* measurements: a comparison of estimates from sonic and surface seismic data. 68th SEG meeting, New Orleans, USA, Expanded Abstracts, 1080-1083.

de Lima O.A.L. and Sharma M.M. 1990. A grain conductivity approach to shaly sandstones. *Geophysics* **55**, 1347-1356.

de Lima O.A.L. and Sharma M.M. 1992. A generalized Maxwell-Wagner theory for membrane polarization in shaly sands. *Geophysics* **57**, 431-440.

de Lima O.A.L., Clennell M.B., Nery G.G. and Niwas S. 2005. A volumetric approach for the resistivity response of freshwater shaly sandstones. *Geophysics* **70**, F1-F10.

Deng S., Wang X., Li G. and Fan Y. 2006. Experimental and theoretical study of the

electrical conductivity, NMR properties under different salinities and the membrane potential of shaly sandstone. *Journal of Geophysics and Engineering* **3**, 377-385.

Denicol P.S. and Jing X.D. 1998. Effects of water salinity, saturation and clay content on the complex resistivity of sandstone samples. In: *Core-Log Integration*, Vol. 136 (eds P.K. Harvey and M.A. Lovell), pp. 147-157. Special Publications of the Geological Society London.

Domnesteanu P., McCann C. and Sothcott J. 2002. Velocity anisotropy and attenuation of shale in under- and overpressured conditions. *Geophysical Prospecting* **50**, 487-503.

Du Z. and MacGregor L. 2009. Reservoir parameter estimation from joint inversion of marine CSEM and seismic AVO data using the genetic algorithms. 71st EAGE Meeting, Amsterdam, the Netherlands, Expanded Abstracts, X008.

Dvorkin J. and Nur A. 1993. Dynamic poroelasticity: a unified model with the squirt and the Biot mechanisms. *Geophysics* **58**, 524-533.

Dvorkin J. and Nur A. 1996. Elasticity of high-porosity sandstones: Theory for two North Sea datasets. *Geophysics* **61**, 1363–1370.

Dvorkin J., Mavko G. and Nur A. 1995. Squirt flow in fully saturated rocks. *Geophysics* **60**, 97–107.

Dvorkin J., Nolen-Hoeksema R. and Nur A. 1994. The squirt-flow mechanism: macroscopic description. *Geophysics* **59**, 428-438.

Eberhart-Phillips D., Han D.H. and Zoback M.D. 1989. Empirical relationships among seismic velocity, effective pressure, porosity, and clay content in sandstone. *Geophysics* **54**, 82-89.

Edwards R.N. 1997. On the resource evaluation of marine gas hydrate deposits using sea-floor transient electric dipole-dipole method. *Geophysics* **62**, 63-74.

Edwards R.N. and Chave A.D. 1986. A transient electric dipole-dipole method for mapping the conductivity of the seafloor. *Geophysics* **51**, 204-217.

Ellis D.V. 1987. *Well Logging for Earth Scientists*. Elsevier, New York.

Ellis M.H. 2008. *Joint seismic and electrical measurements of gas hydrates in*

continental margin sediments. PhD thesis, University of Southampton.

Ellis M.H., Sinha M.C., Minshull T.A., Sothcott J. and Best A.I. 2010. An anisotropic model for the electrical resistivity of two-phase geological materials. Accepted by *Geophysics*.

Erickson S.N. and Jarrard R.D. 1998. Porosity/formation-factor relationships for high-porosity siliciclastic sediments from Amazon Fan. *Geophysical Research Letters* **25**, 2309-2312.

Evans R.L., Constable S.C., Sinha M.C., Cox C.S. and Unsworth M.J. 1991. Upper crustal structure of the East Pacific Rise near 13°N. *Geophysical Research Letters* **18**, 1917-1920.

Evans R.L., Sinha M.C., Constable S.C. and Unsworth M.J. 1994. On the electrical nature of the axial melt zone at 13°N on the East Pacific Rise. *Journal of Geophysical Research* **99**, 577-588.

Fatt I. 1957. Effect of overburden and reservoir pressure on electrical logging formation factor. *American Association of Petroleum Geologists Bulletin* **41**, 2456-2466.

Feldman Y., Polygalov E., Ermolina I., Polevaya Y. and Tsentsiper B. 2001. Electrode polarization correction in time domain dielectric spectroscopy. *Measurement Science and Technology* **12**, 1355-1364.

Freund D. 1992. Ultrasonic compressional and shear velocities in dry clastic rocks as a function of porosity, clay content, and confining pressure. *Geophysical Journal International* **108**, 125-135.

Frohlich R.K., Fisher J.J. and Summerly E. 1996. Electric-hydraulic conductivity correlation in fracture crystalline bedrock: Central Landfill, Rhode Island, USA. *Journal of Applied Geophysics* **35**, 249-259.

Gardner G.H.F., Wyllie M.R.J. and Droschak D.M. 1964. Effects of pressure and fluid saturation on the attenuation of elastic waves in sands. *Journal of Petroleum Technology* **16**, 189-198.

Garrouch A.A. 2000. Effect of wettability and water saturation on the dielectric constant of hydrocarbons rocks. SPWLA 41st Annual Logging Symposium.

Garrouch A.A. and Sharma M.M. 1994. The influence clay content, salinity, stress, and wettability on the dielectric properties of brine-saturated rocks: 10 Hz to 10 MHz. *Geophysics* **59**, 909-917.

Gassmann F. 1951. Elastic waves through a packing of spheres. *Geophysics* **16**, 673-685.

Geertsma J. and Smit D.C. 1961. Some aspects of elastic wave propagation in fluid-saturated porous solids. *Geophysics* 2**6**, 169-181.

Gelius L.J. and Wang Z. 2008. Modelling production caused changes in conductivity for a siliciclastic reservoir: A differential effective medium approach. *Geophysical Prospecting* **56**, 677–691.

Gist G.A. 1994. Interpreting laboratory velocity measurements in partially gas-saturated rocks. *Geophysics* **59**, 1100-1109.

Glanville C.R. 1959. Laboratory study indicates significant effects of pressure on resistivity of reservoir rock. *Journal of Petroleum Technology* **11**, 20-26.

Glover P.W.J. 2009. What is the cementation exponent? A new interpretation. *The Leading Edge* **28**, 82-85.

Glover P.W.J., Gomez J.B. and Meredith P.G. 2000. Fractures in saturated rocks undergoing triaxial deformation using complex electrical measurements. *Earth and Planetary Science Letters* **183**, 201-213.

Glover P.W.J., Meredith P.G., Sammonds P.R. and Murrell S.A.F. 1994. Ionic surface electrical conductivity in sandstone. *Journal of Geophysical Research* **99**, 21635-21650.

Glover P.W.J., Zadjali I.I. and Frew K.A. 2006. Permeability prediction from MICP and NMR data using an electrokinetic approach. *Geophysics* **71**, F49-F60.

Goetz J.F., Dupal L. and Bowler J. 1979. An investigation into the discrepancies between sonic log and seismic check shot velocities. *Australian Petroleum Exploration Association Journal* **19**, 131-141.

Goldberg D. and Zinszner B. 1989. P-wave attenuation measurements from laboratory resonance and sonic waveform data. *Geophysics* **54**, 76-81.

Gomaa M.M. 2009. Saturation effect on electrical properties of hematitic sandstone in

the audio frequency range using non-polarizing electrodes. *Geophysical Prospecting* **57**, 1091-1100.

Gomez C.T. 2009. *Reservoir characterization combining elastic velocities and electrical resistivity measurements*. PhD thesis, Stanford University.

Gomez-Rivero O. 1977. Some considerations about the possible use of the parameters a and m as a formation evaluation tool through well logs. SPWLA 18th Annual Logging Symposium, 1-24.

Gordon R.B. and Davis L.A. 1968. Velocity and attenuation of seismic waves in imperfectly elastic rock. *Journal of Geophysical Research* **73**, 3917-3935.

Gribben R.J. 1975. *Elementary partial differential equations*. Van Nostrand Reinhold Company, New York.

Hacikoylu P., Dvorkin J. and Mavko G. 2006. Resistivity-velocity transforms revisited. *The Leading Edge* **25**, 1006-1009.

Hamilton E.L. 1972a. Compressional-wave attenuation in marine sediments. G*eophysics* **37**, 620-646.

Hamilton E.L. 1972b. Correlation between Q_s of shear waves and rigidity. *Marine Geology* **13**, M27-M30.

Han D., Nur A. and Morgan F.D. 1986. Effects of porosity and clay content on wave velocities in sandstones. *Geophysics* **51**, 2093-2107.

Harris P., Du Z., MacGregor L., Olsen W., Shu R. and Cooper R. 2009. Joint interpretation of seismic and CSEM data using well log constraints: an example from the Luva Field. *First Break* **27**, 73-81.

Hashin Z. and Shtrikman S. 1962. A variational approach to the theory of the effective magnetic permeability of multiphase materials. *Journal of Applied Physics* **33**, 3125-3131.

Hashin Z. and Shtrikman S. 1963. A variational approach to the elastic behaviour of multi-phase materials. *Journal of the Mechanics and Physics of the solids* **11**, 127-140.

Heigold P.C., Gilkeson R.H., Cartwright K. and Reed P.C. 1979. Aquifer

transmissivity from surficial electrical methods. *Ground Water* **17**, 338-345.

Hermance J.F. 1979. The electrical conductivity of materials containing partial melt, a simple model form Archie's law. *Geophysical Research Letters* **6**, 613-616.

Hill R. 1965. A self consistent mechanics of composite materials, *Journal of the Mechanics and Physics of the solids* **13**, 213-222.

Hornby B.E., Schwartz L.M. and Hudson J.A. 1994. Anisotropic effective-medium modelling of the elastic properties of shales. *Geophysics* **59**, 1570-1581.

Hoversten G.M., Cassassuce F., Gasperikova E., Newman G.A., Chen J., Rubin Y., Hou Z. and Vasco D. 2006. Direct reservoir parameter estimation using joint inversion of marine AVA and CSEM data. *Geophysics* **71**, C1-C13.

Huntley D. 1986. Relations between permeability and electrical resistivity in granular aquifers. *Ground Water* **24**, 466-474.

Jackson P.D., Smith D.T. and Stanford P.N. 1978. Resistivity-porosity-particle shape relationships for marine sands. *Geophysics* **43**, 1250-1268.

Jakobsen M., Hudson J.A., Minshull T.A. and Singh S.C. 2000. Elastic properties of hydrate-bearing sediments using effective medium theory, *Journal of Geophysical Research* **105**, 561-577.

Jing X.D. 1990. *The effects of clay, pressure and temperature on the electrical and hydraulic properties of real and synthetic rocks*. PhD thesis, Imperial College, London.

Jing X.D., Archer J.S. and Daltaban T.S. 1992. Laboratory study of the electrical and hydraulic properties of rocks under simulated reservoir conditions. *Marine and Petroleum Geology* **9**, 115-127.

Jing X.D., Daltaban T.S. and Archer J.S. 1990. Experimental measurements on the effects of pressure and temperature on the electrical properties of real and synthetic rocks. In: *Rock at Great Depth*, Vol. 3 (eds V. Maury and D. Fourmaintraux), pp. 1357-1368. A.A. Balkema, Rotterdam.

Johnson W.L. and Linke W.A. 1978. Some practical applications to improve formation evaluation of sandstones in the Mackenzie delta. SPWLA 19th Annual Logging Symposium, 1978-C.

Johnston D.H. 1987. Physical properties of shale at temperature and pressure. *Geophysics* **52**, 1391-1401.

Johnston D.H. and Toksöz M.N. 1980. Ultrasonic P and S wave attenuation in dry and saturated rocks under pressure. *Journal of Geophysical Research* **85**, 923-936.

Jones P.H. and Buford T.B. 1951. Electric logging applied to ground-water exploration. *Geophysics* **16**, 115-139.

Jones S.M. 1995. Velocities and quality factors of sedimentary rocks at low and high effective pressures. *Geophysical Journal International* **123**, 774-780.

Jones S.M. 1996. *The effects of confining pressure, pore-fluid salinity and saturation on the acoustic properties of sandstones*. PhD thesis, University of Reading.

Jones T. and Nur A. 1983. Velocity and attenuation in sandstone at elevated temperatures and pressures. *Geophysical Research Letters* **10**, 140-143.

Kaselow A. and Shapiro S.A. 2004. Stress sensitivity of elastic moduli and electrical resistivity in porous rocks. *Journal of Geophysics and Engineering* **1**, 1-11.

Keller G.V. 1953. Effect of wettability on the electrical resistivity of sand. *Oil and Gas Journal* **51**, 62-65.

Khaksar A., Griffiths C.M. and McCann C. 1999. Compressional- and shear-wave velocities as a function of confining stress in dry sandstones. *Geophysical Prospecting* **47**, 487-508.

Khalil M.A. and Monterio Santos F.A. 2009. Influence of degree of saturation in the electric resistivity-hydraulic conductivity relationship. *Surveys in Geophysics* **30**, 601-615.

Khazanehdari J. and McCann C. 2005. Acoustic and petrophysical relationships in low-shale sandstone reservoir rocks. *Geophysical Prospecting* **53**, 447-461.

King M.S. and Marsden R.J. 2002. Velocity dispersion between ultrasonic and seismic frequencies in brine-saturated reservoir sandstones. *Geophysics* **67**, 254-258.

Kjartansson E. 1979. Constant Q-wave propagation and attenuation. *Journal of*

Geophysical Research **84**, 4737-4748.

Klimentos T. 1988. *Seismic and petrophysical properties of porous rocks*. PhD thesis, University of Reading.

Klimentos T. 1991. The effects of porosity-permeability-clay content on the velocity of compressional waves. *Geophysics* **56**, 1930-1939.

Klimentos T. and McCann C. 1990. Relationships among compressional wave attenuation, porosity, clay content, and permeability in sandstones. *Geophysics* **55**, 998-1014.

Knight R.J. 1991. Hysteresis in the electrical resistivity of partially saturated sandstones. *Geophysics* **56**, 2139-2147.

Knight R.J. and Dvorkin J. 1992. Seismic and electrical properties of sandstone at low saturations. *Journal of Geophysical Research* **97**, 17425-17432.

Knight R.J. and Endres A.L. 1991. Surface conduction at the hydrocarbon/water interface. SPWLA 32nd Annual Logging Symposium.

Kosinski W.K. and Kelly W.E. 1981. Geoelectric soundings for predicting aquifer properties. *Ground Water* **19**, 163-171.

Kowallis B.J., Jones L.E.A. and Wang H.F. 1984. Velocity-porosity-clay content systematics of poorly consolidated sandstones. *Journal of Geophysical Research* **89**, 10335-10364.

Kozeny J. 1927. Űber kapillare Leitung des Wassers im Boden. *Sitzungsber. Akad. Wiss. Wien* **136**, 271–306.

Landauer R. 1952. The electrical resistance of binary metallic mixtures. *Journal of Applied Physics* **23**, 779-784.

Lee M.W. and Collett T.S. 2006. A method of shaly sand correction for estimating gas hydrate saturations using downhole electrical resistivity log data. U.S. Geological Survey Scientific Investigations Report, 2006-5121, 10p.

Leroy P. and Revil A. 2009. A mechanistic model for the spectral induced polarization of clay materials. *Journal of Geophysical Research* **114**, B10202.

Leroy P., Revil A., Kemna A., Cosenza P. and Ghorbani A. 2008. Complex

conductivity of water-saturated packs of glass beads. *Journal of Colloid and Interface Science* **321**, 103-117.

Longeron D.G., Argaud M.J. and Feraud J.P. 1989. Effect of overburden pressure and the nature and microscopic distribution of fluids on electrical properties of rock samples. *SPE Formation Evaluation* **4**, 194-202.

MacGregor L. and Sinha M. 2000. Use of marine controlled-source electromagnetic sounding for sub-basalt exploration. *Geophysical Prospecting* **48**, 1091-1106.

MacGregor L.M., Constable S.C. and Sinha M.C., 1998. The RAMESSES experiment III: controlled source electromagnetic sounding of the Reykjanes Ridge at 57°45'N. *Geophysical Journal International* **135**, 772-789.

Mahmood S.M., Maerefat N.L. and Chang M.M. 1991. Laboratory measurement of electrical resistivity at reservoir conditions. *SPE Formation Evaluation* **6**, 291-300.

Marion D., Nur A., Yin H. and Han D. 1992. Compressional velocity and porosity in sand-clay mixtures. *Geophysics* **57**, 554-563.

Marketos G. and Best A.I. 2010. Application of the BISQ model to clay squirt flow in reservoir sandstones. *Journal of Geophysical Research* **115**, B06209.

Marks S.G., McCann C. and Sothcott J. 1992. Compressional wave quality factors of reservoir sandstones at 50 Hz and 1 MHz. 54th EAGE meeting, Paris, France, Expanded Abstracts, 338-339.

Mavko G. and Jizba D. 1991. Estimating grain-scale fluid defects on velocity dispersion in rocks. *Geophysics* **56**, 1940-1949.

Mavko G., Mukerji T. and Dvorkin J. 1998. *The rock physics handbook: Tools for seismic analysis in porous media*. Cambridge University Press.

Mavko G.M. and Nur A. 1979. Wave attenuation in partially saturated rocks. *Geophysics* **44**,161-178.

Maxey A.C. 2009. *Borehole methods for controlled source electromagnetic exploration*. PhD thesis, University of Southampton.

Mayr S.I. and Burkhardt H. 2006. Ultrasonic properties of sedimentary rocks: effect of pressure, saturation, frequency and microcracks. *Geophysical Journal*

International **164**, 246-258.

Mazzeo B.A. 2009. Parasitic capacitance influence of potential-sensing electrodes on four-electrode liquid impedance measurements. *Journal of Applied Physics* **105**, 094106.

McCann C. and McCann D.M. 1969. The attenuation of compressional waves in marine sediments. *Geophysics* **34**, 882-892.

McCann C. and Sothcott J. 1992. Laboratory measurement of the seismic properties of sedimentary rocks. In: *Geological Applications of Wire-Line Logs 2*, Vol. 65 (eds A. Hurst, C.M. Griffiths and P.F. Worthington), pp. 285-297. Special Publications of the Geological Society London.

McCann C. and Sothcott J. 2009. Sonic to ultrasonic *Q* of sandstones and limestones: Laboratory measurements at *in situ* pressures. *Geophysics* **74**, WA93-WA101.

Miller S.L M. and Stewart R.R. 1990. Effects of lithology, porosity and shaliness on P- and S-wave velocities from sonic logs. *Canadian Journal of Exploration Geophysics* **26**, 94-103.

Milton G.W. 1981. Bounds on the electromagnetic, elastic and other properties of two-component composites. *Physical Review Letters* **46**, 542-545.

Moss A.K., Jing X.D. and Archer J.S. 2002. Wettability of reservoir rock and fluid systems from complex resistivity measurements. *Journal of Petroleum Science and Engineering* **33**, 75-85.

Mukerji T., Mavko G. and Gomez C. 2009. Cross-property rock physics relations for estimating low-frequency seismic impedance trends from electromagnetic resistivity data. *The Leading Edge* **28**, 94-97.

Murphy III W.F., Winkler K.W. and Kleinberg R.L. 1986. Acoustic relaxation in sedimentary rocks: dependence on grain contacts and fluid saturation. *Geophysics* **51**, 757-766.

Nur A. and Simmons G. 1969. Stress-induced velocity anisotropy in rock: An experimental study. *Journal of Geophysical Research* **74**, 6667-6674.

O'Connell R.J. and Budiansky B. 1977. Viscoelastic properties of fluid-saturated cracked solids. *Journal of Geophysical Research* **82**, 5719-5735.

O'Hara S.G. 1985. Influence of pressure, temperature, and pore fluid on the frequency-dependent attenuation of elastic waves in Berea sandstone. *Physical Review A* **32**, 472-488.

Olhoeft G.R. 1985. Low-frequency electrical properties. *Geophysics* **50**, 2492-2503.

Olhoeft G.R. 1987. Electrical properties from 10^{-3} to 10^{+9} Hz - physics and chemistry. *AIP Conference Proceedings* **154**, 281-298.

Olsen C., Hongdul T. and Fabricius I.L. 2008. Prediction of Archie's cementation factor from porosity and permeability through specific surface. *Geophysics* **73**, E81–E87.

Osborn J.A. 1945. Demagnetizing factors of the general ellipsoid. *Physical Review* **67**, 351-357.

Patnode H.W. and Wyllie M.R.J. 1950. The presence of conductive solids in reservoir rock as a factor in electric log interpretation. *Transactions of the American Institute of Mining, Metallurgical and Petroleum Engineers* **189**, 47-52.

Pickett G.R. 1963. Acoustic character logs and their application in formation evaluation. *Journal of Petroleum technology* **15**, 658-667.

Ponzini G., Ostroman A. and Molinari M. 1983. Empirical relation between electrical transverse resistance and hydraulic transmissivity. *Geoexploration* **22**, 1-15.

Porter C.R. and Carothers J.E. 1970. Formation factor-porosity relation derived from well log data. SPWLA 11th Annual Logging Symposium, 1-19.

Pozar D.M. 1998. *Microwave Engineering*. John Wiley & Sons.

Prasad M. 2003. Velocity-permeability relations within hydraulic units. *Geophysics* **68**, 108-117.

Prasad M. and Manghnani M.H. 1997. Effects of pore and differential pressure on compressional wave velocity and quality factor in Berea and Michigan sandstones. *Geophysics* **62**, 1163-1176.

Pride S.R., Berryman J.G. and Harris J.M. 2004. Seismic attenuation due to wave-induced flow. *Journal of Geophysical Research* **109**, B01201.

Purvance D.T. and Andricevic R. 2000. On the electrical-hydraulic conductivity

correlation in aquifers. *Water Resources Research* **36**, 2905-2913.

Rabaute A., Revil A. and Brosse E. 2003. In situ mineralogy and permeability logs from downhole measurements: Application to a case study in chlorite-coated sandstones. *Journal of Geophysical Research* **108**, 2414-2429.

Reppert P.M., Morgan F.D. and Toksöz M.N. 2000. Dielectric constant determination using ground-penetrating radar reflection coefficients. *Journal of Applied Geophysics* **43**, 189-197.

Reuss A. 1929. Berechnung der Fliessgrenzen von Mischkristallen auf Grund der Plastizitätsbedinggung für Einkristalle. *Zeitschrift für Angewandte Mathematik und Mechanik* **9**, 49-58.

Revil A. 2007. Comment on "Permeability prediction from MICP and NMR data using an electrokinetic approach" (P.W.J. Glover, Zadjali I.I. and Frew K.A. 2006. Geophysics 71, no. 4, F49–F60). *Geophysics* **72**, X3-X4.

Revil A. and Cathles III L.M. 1999 Permeability of shaly sands. *Water Resources Research* **35**, 651-662.

Revil A. and Glover P.W.J. 1997. Theory of ionic-surface electrical conduction in porous media. *Physical Review B* **55**, 1757-1773.

Revil A. and Glover P.W.J. 1998. Nature of surface electrical conductivity in natural sands, sandstones, and clays. *Geophysical Research Letters* **25**, 691-694.

Revil A. and Leroy P. 2001. Hydroelectric coupling in a clayey material. *Geophysical Research Letters* **28**, 1643-1646.

Revil A., Cathles III L.M., Losh S. and Nunn J.A. 1998. Electrical conductivity in shaly sands with geophysical applications. *Journal of Geophysical Research* **103**, 23925-23936.

Ridge M.J. 1983. A combustion method to measure the cation exchange capacity of day minerals. *Log Anal.* **3**, 6-11.

Rink M. and Schopper J.R. 1974. Interface conductivity and its implications to electric logging. SPWLA 15th Annual Logging Symposium, J1-15.

Ruiz F. and Dvorkin J. 2010. Predicting elasticity in nonclastic rocks with a

differential effective medium model. *Geophysics* **75**, E41-E53.

Salem H.S. 2001. Relationship among formation resistivity factor, compressional wave velocity, and porosity for reservoirs saturated with multiphase fluids. *Energy Sources* **23**, 675-685.

Salem H.S. and Chilingarian G.V. 1999. The cementation factor of Archie's equation for shaly sandstone reservoirs. *Journal of Petroleum Science and Engineering* **23**, 83–93.

Saltas V., Vallianatos F., Soupios P., Makris J.P. and Triantis D. 2007. Dielectric and conductivity measurements as proxy method to monitor contamination in sandstone. *Journal of Hazardous Materials* **142**, 520-525.

Sams M.S. and Andrea M. 2001. The effect of clay distribution on the elastic properties of sandstones. *Geophysical Prospecting* **49**, 128-150.

Sams M.S., Neep J.P., Worthington M.H. and King M.S. 1997. The measurement of velocity dispersion and frequency-dependent intrinsic attenuation in sedimentary rocks. *Geophysics* **62**, 1456-1464.

Sams M.S., Worthington M.H., King M.S. and Shams-Khanshir M. 1993. A comparison of laboratory and field measurements of P-wave anisotropy. *Geophysical Prospecting* **41**, 189-206.

Schön, J.H. 1996. *Physical properties of rocks: fundamentals and principles of petrophysics. Handbook of Geophysical Exploration. Section I, Seismic Exploration*, Vol. 18, Pergamon Press, Oxford.

Schwalenberg K., Willoughby E., Mir R. and Edwards R.N. 2005. Marine gas hydrate electromagnetic signatures in Cascadia and their correlation with seismic blank zones. *First Break* **23**, 57-63.

Schwan H.P. 1968. Four-electrode null techniques for impedance measurement with high resolution. *The Review of Scientific Instruments* **39**, 481-485.

Sen P.N. 1980. The dielectric constant and conductivity response of sedimentary rocks. SPE Annual Technical Conference and Exhibition, Dallas, Texas.

Sen P.N. and Goode P.A. 1988. Shaly sand conductivity at low and high salinities. SPWLA 29th Annual Logging Symposium, Paper F.

Sen P.N. and Goode P.A. 1992. Influence of temperature on electrical conductivity on shaly sands. *Geophysics* **57**, 89-96.

Sen P.N., Goode P.A. and Sibbit A. 1988. Electrical conduction in clay bearing sandstones at low and high salinities. *Journal of Applied Physics* **63**, 4832-4840.

Sen P.N., Scala C. and Cohen M.H. 1981. A self-similar model for sedimentary rocks with applications to the dielectric constant of fused glass beads. *Geophysics* **46**, 781-795.

Shatilo A.P., Sondergeld C. and Rai C.S. 1998. Ultrasonic attenuation in Glenn Pool rocks, northeastern Oklahoma. *Geophysics* **63**, 465-478.

Sheng P. 1990. Effective-medium theory of sedimentary rocks. *Physics Reviews B* **41**, 4507-4512.

Sheng P. and Callegari A.J. 1984. Differential effective medium theory of sedimentary rocks. *Applied Physics Letters* **44**, 738-740.

Simandoux P. 1963. Dielectric measurements in porous media and application to shaly formation. *Revue de l'institut Francais du Pétrole* **18**, 193–215.

Sinha M.C. 2010. Survey design and acquisition parameters for marine CSEM prospecting: key principles and considerations. In: *Electromagnetics for Oil Exploration* (eds L.M. MacGregor, K.M. Strack and L. Thomsen). Society of Exploration Geophysicists. In press.

Sinha M.C., Constable S.C., Peirce C., White A., Heinson G., MacGregor L. and Navin D.A. 1998. Magmatic processes at slow spreading ridges: implications of the RAMESSES experiment at 57°45' North on the Mid-Atlantic Ridge. *Geophysical Journal International* **135**, 731-745.

Sinha M.C., Patel P.D., Unsworth M.J., Owen T.R.E. and MacCormack M.G.R. 1990. An active source electromagnetic sounding system for marine use. *Marine Geophysical Research* **12**, 59-68.

Sothcott J., Ellis M.H., Best A.I., Frerichs N.R., Minshull T.A. and Sinha M.C. 2007. Laboratory observations of morphology, velocity, attenuation and resistivity of methane gas hydrate bearing rocks. 77th SEG meeting, San Antonio, USA, Expanded Abstracts, 1530-1533.

Stacey F.D., Gladwin M.T., McKavanagh B., Linde A.T. and Hastie L.M. 1975. Anelastic damping of acoustic and seismic pulses. *Surveys in Geophysics* **2**, 133-151.

Su Q., Feng Q. and Shang Z. 2000. Electrical impedance variation with water saturation in rock. *Geophysics* **65**, 68-75.

Tanner R.S., Udegbunam E.O., McInerney M.J. and Knapp R.M. 1991. Microbially enhanced oil recovery from carbonate reservoirs. *Geomicrobiology Journal* **9**, 169-195.

Taylor S. and Barker R. 2002. Resistivity of partially saturated Triassic Sandstone. *Geophysical Prospecting* **50**, 603-613.

Tenchov G.G. 1998. Evaluation of electrical conductivity of shaly sands using the theory of mixtures. *Journal of Petroleum Science and Engineering* **21**, 263-271.

Thomas E.C. 1976. Determination of Qv from membrane potential measurements on shaly sands. *Trans. Am. Inst. Min. Metall. Pet. Eng.* **261**, 1087-1096.

Timur A., Hempkins W.B. and Worthington A.E. 1972. Porosity and pressure dependence of formation resistivity factor for sandstones. Proc. 4th Formation Evaluation Symposium of Canadian Well Logging Society, Calgary, Alberta, Canada.

Todd T. and Simmons G. 1972. Effect of pore pressure on the velocity of compressional waves in low-porosity rocks. *Journal of Geophysical Research* **77**, 3731-3743.

Toksöz, M.N. and Johnston D.H. 1981. *Seismic wave attenuation*. Society of Exploration Geophysicists, Tulsa, Ok.

Toksöz M.N., Johnston D.H. and Timur A. 1979. Attenuation of seismic wave in dry and saturated rocks: 1. Laboratory measurements. *Geophysics* **44**, 681-690.

Tosaya C. and Nur A. 1982. Effect of diagenesis and clays on compressional velocities in rocks. *Geophysical Research Letters* **9**, 5-8.

Toumelin E. and Torres-Verdín C. 2005. Influence of oil saturation and wettability on rock resistivity measurements: a uniform pore-scale approach. SPWLA 46th Annual Logging Symposium.

Tutuncu A.N., Podio A.L. and Sharma M.M. 1994. An experimental investigation of factors influencing compressional- and shear-wave velocities and attenuations in tight gas sandstone. *Geophysics* **59**, 77-86.

Urish D. 1981. Electrical resistivity-hydraulic conductivity relationships in glacial outwash aquifers. *Water Resources Research* **17**, 1401-1408.

Wang Z. 2001. Fundamentals of seismic rock physics. *Geophysics* **66**, 398-412.

Waxman M.H. and Smits L.J.M. 1968. Electrical conductivities in oil-bearing shaly sands. *Society of Petroleum Engineers Journal* **8**, 107-122.

Winkler K. and Nur A. 1982. Seismic attenuation: effects of pore fluids and frictional sliding. *Geophysics* **47**, l-15.

Winkler K. and Plona T.J. 1982. Techniques for measuring ultrasonic velocity and attenuation spectra in rocks under pressure. *Journal of Geophysical Research* **87**, 10776-10780.

Winkler K.W. 1983. Frequency dependent ultrasonic properties of high-porosity sandstoens. *Journal of Geophysical Research* **88**, 9493-9499.

Winkler K.W. 1985. Dispersion analysis of velocity and attenuation in Berea sandstone. *Journal of Geophysical Research* **90**, 6793-6800.

Winkler K.W. 1986. Estimates of velocity dispersion between seismic and ultrasonic frequencies. *Geophysics* **51**, 183-189.

Winkler K.W. and Murphy III W.F. 1995. Acoustic velocity and attenuation in porous rocks. In: *Rock physics and phase relations: A handbook of physical constants* (eds T.J. Ahrens), pp. 20-34. American Geophysical Union.

Wong P., Koplik J. and Tomanic J.P. 1984. Conductivity and permeability of rocks. *Physical Review B* **30**, 6606-6614.

Worthington P.F. 1977. Influence of matrix conduction upon hydrogeophysical relationships in arenaceous aquifers. *Water Resources Research* **13**, 87-92.

Worthington P.F. 1982. The influence of shale effects upon the electrical resistivity of reservoir rocks. *Geophysical Prospecting* **30**, 673-687.

Worthington P.F. 1993. The uses and abuses of the Archie equations, 1: The

formation factor-porosity relationship. *Journal of Applied Geophysics* **30**, 215-228.

Wu T.T. 1966. The effect of inclusion shape on the elastic moduli of a two phase material. *International Journal of Solids Structures* **2**, 1-8.

Wuenschel P.C. 1965. Dispersive body waves-an experimental study. *Geophysics* **30**, 539-551.

Wyllie M.R.J. and Southwick P.F. 1954. An experimental investigation of the S.P. and resistivity phenomena in dirty sands. *Transactions of the American Institute of Mining, Metallurgical and Petroleum Engineers* **201**, 43-56.

Wyllie M.R.J., Gregory A.R. and Gardner L.W. 1956. Elastic wave velocities in heterogeneous and porous media. *Geophysics* **21**, 41-70.

Wyllie M.R.J., Gregory A.R. and Gardner G.H.F. 1958. An experimental investigation of factors affecting elastic wave velocities in porous media. *Geophysics* **23**, 459-493.

Xu S., King M.S. and Worthington M.H. 1990. Elastic wave propagation and hydraulic properties of cracked rocks. Prec. International Conference Mechanics of Jointed and Faulted Rock, Technical University of Vienna, Austria, April 1990, pp. 651-658.

Xu S. and White R.E. 1995. A new velocity model for clay-sand mixture. *Geophysical Prospecting* **43**, 91-118.

Yin H. 1993. *Acoustic velocity and attenuation of rocks: isotropy, intrinsic anisotropy, and stress induced anisotropy*. Ph.D. thesis, Stanford University.

Young P.D. and Cox C.S. 1981. Electromagnetic active source sounding near the East Pacific Rise. *Geophysical Research Letters* **8**, 1043-1046.

Zavada P. 2002. Relativistic wave equations with fractional derivatives and pseudodifferential operators. *Journal of Applied Mathematics* **2**, 163-197.